Crustal and Upper Mantle Structure for the Pacific Northwest from an Analysis of Short-Period Teleseismic Network Data

by

Shawn Robert Dewberry

A dissertation submitted in partial fulfillment
of the requirements for the degree of

Doctor of Philosophy

University of Washington

1996

Approved by Robert A Crosson
(Chairperson of Supervisory Committee)

Program Authorized
to Offer Degree Geophysics Program

Date June 21, 1996

Doctoral Dissertation

In presenting this dissertation in partial fulfillment of the requirements for the Doctoral degree at the University of Washington, I agree that the Library shall make its copies freely available for inspection. I further agree that extensive copying of this dissertation is allowable only for scholarly purposes, consistent with "fair use" as prescribed in the U.S. Copyright Law. Requests for copying or reproduction of this dissertation may be referred to University Microfilms, 1490 Eisenhower Place, P.O. Box 975, Ann Arbor, MI 48106, to whom the author has granted "the right to reproduce and sell (a) copies of the manuscript in microform and/or (b) printed copies of the manuscript made from microform."

Signature Sharon R Dawberry

Date June 21, 1996

University of Washington

Abstract

Crustal and Upper Mantle Structure for the Pacific Northwest from an Analysis of Short-Period Teleseismic Network Data

by Shawn Robert Dewberry

Chairperson of Supervisory Committee: Professor Robert S. Crosson
Graduate Program in Geophysics

Pacific Northwest seismic hazards are associated with subduction of the oceanic plate and deformation within both plates of the Cascadia subduction zone. Understanding structure in the region is critical to better quantify seismic potential. We have applied a two-step technique to extract local structure from the coda of teleseismic *P* seismograms. This is applied to nearly 300 earthquakes, representing a range in source distances and back azimuths, recorded by the short-period vertical-component Pacific Northwest Seismograph Network. In the first step, event source and common path signatures, estimated from the sum of all seismograms recording a given event, are removed. Next, deconvolved waveforms from individual stations are stacked in order to identify coherent, yet subtle *P*-coda phases. These phases are interpreted as first order reverberations between the free surface and interfaces at depth. Forward modeling techniques are applied to the stacked waveforms for a number stations, where modeling constraint is provided by prediction of relative arrival times, amplitudes, and moveouts with distance and back azimuth. A prominent modeling result for station MBW in the north Cascades is a non-planar, 5-8 km thick, high-velocity layer/low-velocity layer sequence which lies 3.6 km beneath the surface. This feature correlates with a similar structure 20 km to the west, previously identified from a north-south refraction/reflection profile. The continental moho at this station is modeled at 47 km depth, possibly dipping to the east. Station SPW in the Puget Basin is modeled with a shallow, high-velocity south-dipping basement at a

depth of 1.5 km which is interpreted as Crescent Formation. In the eastern Olympic Peninsula at station HDW, the Crescent Formation is modeled as extending from the surface to 8.0 km depth. Its base dips eastward and is underthrust by low velocity rock, possibly Olympic core rock. In the western Olympic Peninsula, modeling of the oceanic moho depth, strike and dip at five stations provides evidence for deviations from previous inferred structural geometry. These include a moho dipping at less than 11° and the superposition of 2 small-scale undulations with fold axes trending parallel to the greater arch structure.

Table of Contents

List of Figures

List of Tables

Acknowledgments

The work performed during the course of my research was positively influenced by a number of people. This was manifest as direct assistance through constructive criticisms and suggestions, as well as intellectual enabling and equipping through course work and hands-on learning. I gratefully acknowledge the contributions of all those who made this research possible. First, I would like to thank my advisor, Robert Crosson, for providing the initial stimulus, generous support, and vital advice essential for the completion of my dissertation. Thanks also to my supervisory committee, Ken Creager, Steve Malone, and John Booker who provided encouragement, useful conversations and critical contributions throughout this endeavor. Additional thanks to Ken Creager for broadening my horizons to include global seismology. Thanks to office mates and fellow graduate students Tom McSweeney, Seth Moran, John VanDecar, Ivar Mundal, Kim Edlund, Sean Walden, Andreas Schultz, George Thomas, John Winchester, and Neill Symons who provided companionship and camaraderie, as well as insightful and lively discourse. Ruth Ludwin contributed in various ways, especially with editing assistance. Rick Benson provided untold help with accessing and retrieving network data. I am indebted to all those who have worked to establish and maintain the Pacific Northwest Seismograph Network and its teleseismic data base. Without their work and diligent efforts, the work in this dissertation would not have been possible. Thanks also to those office staff members, including Lisa Peterson, Connie Wright, and Darlene Goodwin, who patiently helped and met the needs of the department's graduate students. Most importantly, I want thank my wife Mari, for her never ending support and love during my tenure as a graduate student.

Chapter 1

Introduction

1.1 Objectives

Improving the understanding of crustal and upper mantle structure of the greater Cascadia subduction zone (CSZ) has implications for providing insights into the nature of earthquake hazards for the region. Knowledge of shallow structure can provide a sound starting model from which deeper crustal and upper mantle velocity modeling can proceed. Shallow structural constraints may provide insights into the nature of the region's shallow as well as deep crustal seismicity. Additionally, where the Juan de Fuca (JDF) plate can been readily "seen" (such as on the Olympic Peninsula), improved imaging and structural modeling at oceanic moho depths and beyond may provide a better understanding of the nature of coupling between the North America (NA) and JDF plates. The ramifications include furthering the ability to quantify the likelihood and rupture extent of a megathrust subduction earthquake in the CSZ.

A wealth of structural information is contained in the catalog of digital teleseismic *P* waveforms recorded by the Pacific Northwest Seismograph Network (PNSN) over the past 16 years. With PNSN stations covering much of Washington and Oregon, this catalog has the potential for yielding local structural information for a substantial portion of the Pacific Northwest. This study represents the first attempt to utilize the waveforms of this data set to identify, extract, and model local structural signatures. The contributions from local or near-receiver structure are manifest in the *P*-coda of each seismogram. Since earthquake sources are not delta functions in time and the earth is not an elastic homogenous half-space, other structural signatures contribute to the seismogram *P*-coda. The first objective of this study is to apply a viable technique for extracting (deconvolving) station impulse response functions from the *P* waveforms of teleseisms recorded by short-period, vertical-component instruments of the PNSN. The method of seismogram deconvolution considered must effectively isolate source, common path, attenuation, and instrument terms from the receiver impulse response term. The deconvolution method employed in this study will be referred to as the stacking method.

The second objective of this research is waveform modeling of the subsequent receiver impulse responses for selected stations within the PNSN. Waveform modeling provides constraint of shallow and deep *P* wave velocity structure for the region by identifying significant impedance contrast interfaces. Analyzing and modeling data from a number of

different azimuths and distances allows for models with greater structural complexity than simple 1-D models to be investigated. Dipping layers, for example, are discernible with this type of data set. Other issues, including between-station waveform correlation and lateral heterogeneity length scales, can be addressed when analyzing receiver impulse responses from neighboring stations.

1.2 Regional Tectonics

The Juan de Fuca (JDF) plate system is a remanent of the Farallon plate; the latter has been actively converging at the western margin of the NA plate over the past 150 million years [*Riddihough* 1984]. This interaction is responsible for much of the topography (e.g., the Olympic, Coastal and Cascade Ranges) as well as diverse geology in western Washington and Oregon. The existence of the CSZ, created by a down-welling or underthrusting of the JDF system beneath the NA plate, was established by early investigators using magnetic anomaly analysis [e.g., *Vine and Wilson* 1965, *Vine* 1966, *McKenzie and Parker* 1967, *Atwater* 1970], offshore geologic evidence [*Byrne et al.* 1966, *Silver* 1969], and petrologic evidence [*Dickinson* 1970]. *Dickinson* [1970] even produced a crude contour map of the subducting JDF plate. Up to 30 million years before present (Ma), the JDF plate was part of the Farallon plate until the collision and subsequent subduction of the Farallon-Pacific ridge beneath the NA plate [*Atwater* 1970, *Riddihough* 1984]. From magnetic anomaly analysis, *Riddihough* [1984] reconstructed the convergence history between the JDF and NA plates for the past 6.5 million years. The general trend over this time has shown a fairly stationary convergence direction with a gradual reduction in the relative convergence rates by about 40%, to the present 4.0 cm/yr value (see Figure 1.1 for the present-day plate configuration and convergence directions). In addition, the Explorer plate is thought to have become independent from the rest of the JDF system at 4 Ma. Noting that the present rate of plate convergence is near zero, *Riddihough* [1984] suggests that the Explorer plate has become detached from the rest of the down going JDF plate below. The initiation of slab detachment for a segment of the JDF plate to the south beneath Oregon has likewise been suggested by *VanDecar* [1991] from earthquake tomography.

The maximum age of the JDF plate as it enters the CSZ is less than 10 Ma, making it one of the youngest subducting oceanic plates [*Atwater* 1970, *Molnar and Atwater* 1978,

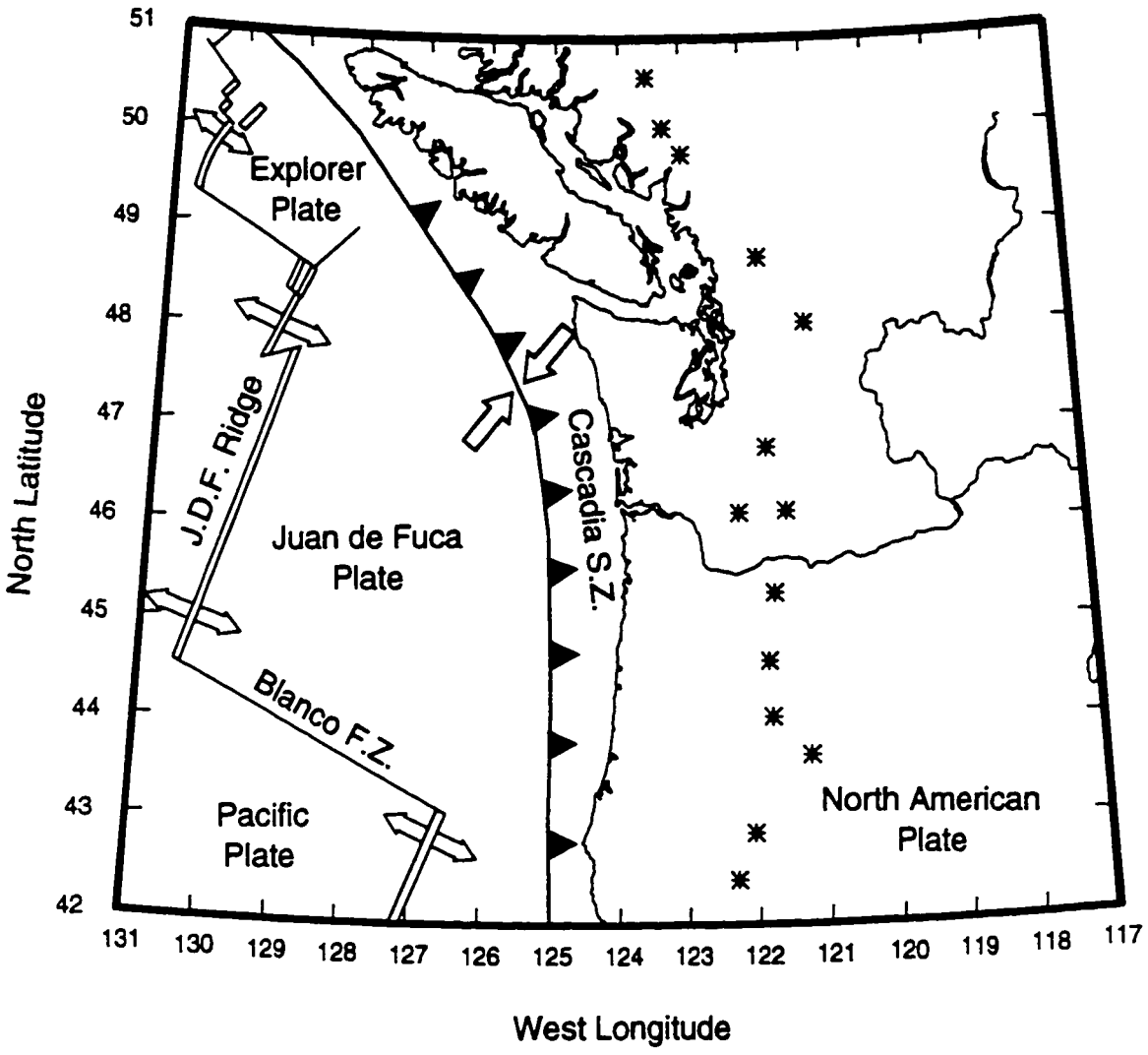

Figure 1.1: Lambert projection map of the tectonic structures in the Cascadia Subduction zone. Asterisks are locations of Cascade volcanoes, solid triangles mark the overthrust plate (North American plate), J.D.F. = Juan de Fuca, F.Z. = fracture zone, S.Z. = subduction zone, and arrows show directions of relative plate motions.

Rogers 1988]. Here the oceanic lithosphere is very thin, less than the 50 km minimum required to create a gravitation instability. Negative buoyancy in a young plate can be obtained by a phase transformation of basalt and gabbro (ρ=2.85 g/cm^3) to eclogite (ρ=3.50 g/cm^3) at depths > 40 km [*Molnar and Atwater* 1978]. The increased body force will manifest as a dip increase at the phase transition depth [*Pennington* 1983]. Some argue this is evidenced by an observed knee in the Benioff zone [*Spence* 1987, *Spence* 1989]. This implies that subduction is driven primarily by the pull of the negatively-buoyant slab below 40 km depth. Does a tear in the down going slab, as suggested by *VanDecar* [1991], then affect the driving forces exerted? A tear could signal a localized cessation of subduction. However, with the lithospheric plates playing an integral part in mantle convection as organizers of the flow structure [*Davies and Richards*, 1992], subduction may not necessarily terminate abruptly. A partial detachment of the slab may simply rearrange the forces acting on and within the subducting plate, altering the dynamics of the system. If partial subduction cessation of the JDF plate is true, how does this affect the potential for megathrust earthquakes in the CSZ? *Heaton and Kanamori* [1984], *Heaton and Hartzell* [1987], and *Rogers* [1988] have shown the CSZ shares many physical properties with other subduction zones which have experienced megathrust earthquakes, suggesting strong coupling between the JDF and NA plates with the possibility of future great earthquakes. Geologic studies from northern California to Vancouver Island, British Columbia of subsurface coastal deposits [*e.g., Atwater* 1987, *Darienzo and Petterson* 1990, *Atwater et al.* 1991, *Atwater* 1992, *Clark and Carver* 1992, *Clague and Bobrowsky* 1994, *Meyers et al.* 1996] and turbidite flows [*Adams* 1990] provide an preponderance of evidence for periodic, large to great subduction earthquakes over the past 5000 years or more.

More recently, the notion of weaker plate coupling has been proposed by *Hyndman and Wang* [1993] and *Dragert et al.* [1994] from modeled heat flow and deformation data that quantifies the down-dip extent (W) of the locked, seismogenic zone. The preferred *Hyndman and Wang* [1993] thermal model for Vancouver Island provides W of length 40 km. For the Olympic Peninsula where the plate is older, more steeply dipping and has more sediment cover, their preferred model has W=100 km. Strain (deformation) rate modeling by *Dragert et al.* [1994] for the southern Vancouver Island margin produced a locked zone of similar dimension, W=60 km. These results are argued by *Hyndman and Wang* [1993] to show relatively weak coupling between the JDF and NA plates. They infer the minimal seismic moment release rate results from the narrow locked zone rather than

large aseismic slip rates. *Pacheco et al.* [1993] studied physical properties of 19 subduction zones (excluding the CSZ) and found a positive correlation between seismogenic zone width (W) and maximum moment magnitude (M_w). They also found a positive correlation between a quantity called the seismic coupling coefficient, α, (ratio of seismic strain rate to total strain rate) and maximum M_w which fit an exponential relation. Their results, if applicable to the CSZ with an average W of ~70 km, indicates an approximate maximum M_w of 8.1-8.7 and α of 0.2-0.6.

Noting the following: (*i*) the maximum size of subduction zone thrust earthquakes globally is limited by the amount of deformation of the overriding plate, (*ii*) subduction zones with $M_w > 8.0$ have forearc deformation rates well below that of the CSZ, and (*iii*) the discovery of nine northwest-southeast trending strike-slip faults offshore Oregon and southern Washington, *McCaffrey and Goldfinger* [1995] like *Hyndman and Wang* [1993] and *Dragert et al.* [1994], argue for a seismogenic zone with limited down-dip extent. In addition, *McCaffrey and Goldfinger* [1995] suggest the observed cross-forearc faults could pose as barriers to slip on the thrust surface, preventing rupture of the entire CSZ thrust surface. Taken together, these studies provide credible evidence for a non-uniform or segmented CSZ which may not be as strongly coupled as previous investigators inferred. Implications are for a maximum $M_w < 9.0$ in the CSZ.

Furthering our understanding of the structure of the plates in the CSZ may facilitate our ability to assess regional earthquake potential, both interplate thrust earthquakes and intraplate crustal earthquakes. In this study, we seek to demonstrate a viable technique for extracting and modeling structural information for the CSZ using teleseismic data recorded by the regional network in an effort to advance our understanding of seismicity and earthquake potential in the region.

1.3 Previous Structural Studies

1.3.1 Shallow Seismic Studies

A number of seismic studies have investigated crustal and upper mantle structure of the Pacific Northwest. The existence of subduction and the plate geometry inferred by early investigators from geologic, petrologic and plate motion data [e.g., *Byrne et al.* 1966, *McKenzie and Parker* 1967, *Silver* 1969, *Dickinson* 1970] have been verified and refined

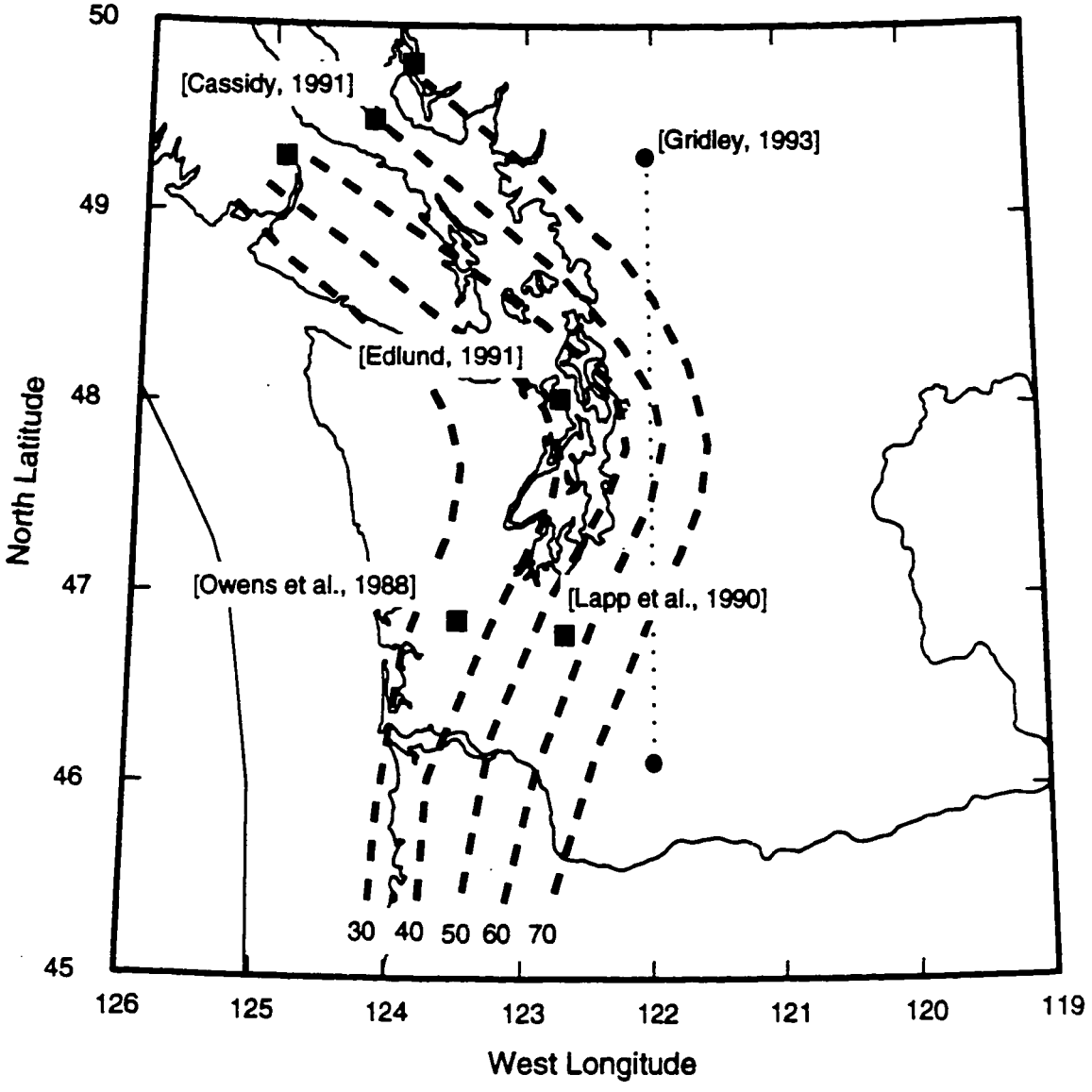

Figure 1.2: Lambert projection map of the Pacific Northwest with depth contours (in km) of the top of the subducting Juan de Fuca plate. The contours are inferred from seismicity [Owens and Crosson 1987], teleseismic receiver function studies, [Owens et al. 1988; Lapp 1990; Cassidy 1991; Edlund 1991] and refraction profile data [Gridley 1993].

using seismic data. Reflection and refraction profiling data, both offshore and onshore, in western Washington and Oregon [e.g., *Berg et al.* 1966, *Shor et al.* 1968, *Rohay 1982, Leaver et al.* 1984, *Taber and Lewis* 1986, *Zervas and Crosson* 1986, *Keach et al.* 1989, *Schultz* 1993, *Gridley* 1993, *Tréhu et al.* 1994, *Johnson et al.* 1994, *Pratt et al.* 1994] have provided constraints on crustal thickness, depths to the JDF oceanic moho, crustal and oceanic mantle *Pn* velocities, as well as local shallow crustal structure. Seismicity and hypocenter distributions [*Crosson* 1976, *Crosson and Owens* 1987, *Taber and Smith* 1985, *Weaver and Baker* 1988] as well as teleseismic receiver function studies [*Langston* 1979, *Owens et al.* 1988, *Lapp et al.* 1990, *Edlund* 1991, *Nábelek et al.* 1993] have provided additional information related to shallow crustal structure, as well as the depth and arched geometry of the subducting JDF plate beneath western Washington and Oregon (Figure 1.2). The *Lees* [1989] 3-D tomographic image of *P* velocity variations in the Puget Sound region has yielded the most comprehensive information to date about the extent of lateral and vertical crustal heterogeneity.

Profiling studies [e.g., *White and Savage* 1965, *Green et al.* 1986, *Clowes et al.* 1987, *Drew and Clowes* 1990] and teleseismic receiver function studies [e.g., *Langston* 1981, *Cassidy* 1991] from Vancouver Island and southwestern British Columbia have provided similar geometric constraints for the subducting JDF plate in the northern part of the CSZ. While less active than western Washington, seismicity and hypocenter distributions in British Columbia [e.g., *Rogers and Horner* 1991] provided additional geometric constraints on the location of the JDF plate. Not surprisingly, the depth cutoffs for crustal seismicity and deep intraslab seismicity for this region of the CSZ is similar to the general distribution observed further south.

1.3.2 Deep Seismic Studies

The lack of seismicity below depths of approximately 100 km [*Crosson and Owens* 1987, *Weaver and Baker* 1988] limits the ability to investigate deeper structure in the CSZ using local seismic data; however, teleseismic data are ideally suited for the task. Investigators inferring deep (depth > ~100 km) structure have exploited a large catalog of teleseismic events recorded by the PNSN to produce *P* velocity tomographic images. *Michaelson and Weaver* [1986] used hand-picked *P*-wave travel-time data to invert for *P* velocity beneath Washington and northern Oregon, utilizing the least-squares technique of

Aki et al. [1977]. *Rasmussen and Humphreys* [1988] applied back-projection tomography to a supplemented *Michaelson and Weaver* [1986] data set. Both studies yielded similar structural results, showing a resolvable image of the subducting JDF slab to depths of 300 km. They found a quasi-planar high velocity anomaly dipping at 45°-60°, with a apparent increase in dip towards the south of the image.

VanDecar [1991] and *Bostock and VanDecar* [1995] revisited this issue with a large data set containing high-quality relative arrival times generated from a multi-channel cross-correlation technique [*VanDecar and Crosson* 1990]. They generated a tomographic image from roughly 45° N to 50° N latitude using an iterative non-linear inversion. With best resolution in the 150-450 km depth range, the resulting images showed a slab signature (positive slowness anomaly) at 150-200 km depth which parallels the shallow slab contours of *Crosson and Owens* [1987]. At greater depths, the positive slowness anomaly is noticeably absent south of 46° N latitude. This feature, which appears contradictory to the results of *Rasmussen and Humphreys* [1988], is interpreted by *VanDecar* [1991] as a "tear" in the subducting slab possibly due to a subduction rate at depth which is greater than the rate at the surface.

1.3.3 Non-seismic Studies

A number of other investigations of non-seismic geophysical data which have provided both large and small scale structural constraints for the CSZ are worth noting. Gravity anomaly data from onshore and offshore western Oregon, Washington and British Columbia [e.g., *Riddihough* 1979, *Finn* 1990] have been used to generate models of crustal and upper mantle density structure across the CSZ. These models provide additional geometrical constraints, such as the dip and the lateral variation of the dip, for the subducted JDF plate. As density and *P* velocity are often assumed to be linearly related (Birch's law), these models are readily comparable with seismic velocity models. *Lees and VanDecar* [1991] used gravity anomaly data to supplement the original *Lees* [1989] travel-time inversion data set to provide a model with improved constraint at shallow depths.

Studies of magnetotelluric and magnetovariational data have identified conductors which correlate with existing crustal and subcrustal geology and velocity models. For example, across Vancouver Island *Kurtz et al.* [1986] identified a eastward dipping

conductive zone which is coincident with a dipping reflective band located above the JDF slab at approximately 30 km depth [*Hyndman et al.* 1990]. Also, the EMSLAB experiment (see *Booker and Chave* [1988] for details), a large scale, regional investigation of the electrical structure of the JDF plate and the corresponding overriding NA plate, identified anomalous conductive features on many length scales. These included a conductive axis below the Cascades that terminates in northern Washington, a "modest" conductor beneath the Oregon Coast Range (at about 45° N) near the depth of a dipping seismic reflector noted by *Keach et al.* [1989], and a subhorizontal conductor at approximately 30 km depth under the western Cascades with conductance several times higher than the previously mentioned feature. Another crustal conductor, termed the SWCC (southern Washington Cascade Conductor), which was first identified by *Stanley et al.* [1987], lies southwest of Mt. Rainier. Imaged from many data sets [e.g., *Stanley et al.* 1987, *Stanley et al.* 1990, *Booker and Chave* 1988, *Egbert and Booker* 1993] the SWCC appears to be closely related to the spatial distribution of crustal seismicity in southwestern Washington [*Stanley et al.* 1996]. Considered a massive unit of highly conductive rock (as opposed to magma or hydrothermal fluids) possible dipping to the east, this structure is hypothesized by *Egbert and Booker* [1993] to represent a section of early subduction zone, analogous in location to the present Olympic Peninsula.

1.4 Structural Goals of this Study

Through the development and implementation of our method for extracting local structure from teleseismic *P* waveforms recorded by short-period, vertical-component instruments of limited dynamic-range, we seek to provide *P* velocity structure information for the broad region covered by the PNSN. Taking into consideration the nature and quality of the data available and the expansion of the PNSN over time, local structural identification constraint for every operational station is not feasible. In fact, the successful waveform modeling performed in this study is limited to a subset of PNSN stations. Still, the results of our analysis supplement existing regional and local structural information. This study not only provides a consistency check for regions where previous studies have developed structural models, such as the north Cascades [e.g., *Gridley* 1993], but also contributes constraints for other regions not yet studied in detail. With a large, fairly uniformly spaced network, our method of receiver impulse response extraction coupled

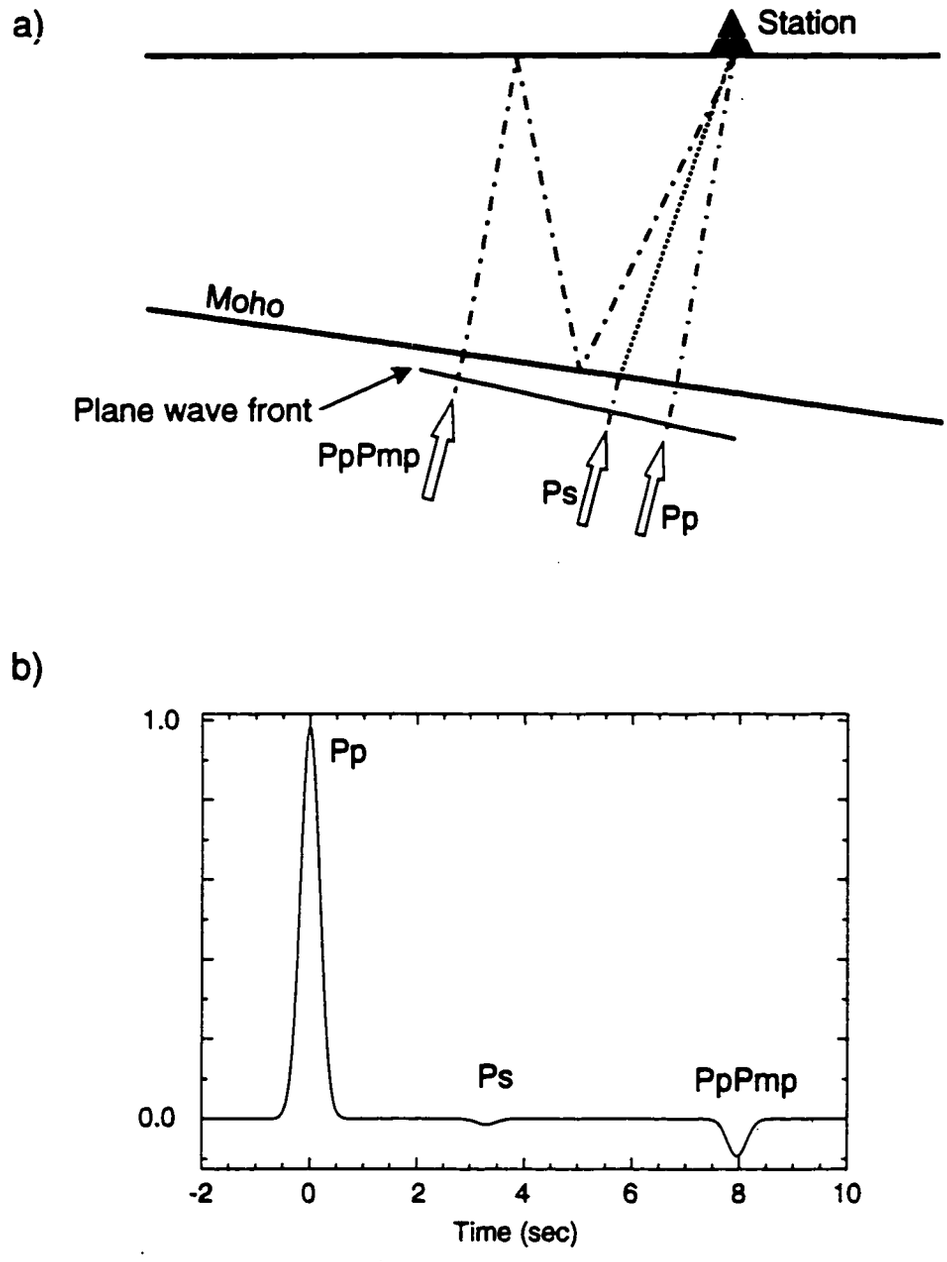

Figure 1.3: a) Ray paths for direct (Pp) and the first two secondary arrivals expected: Ps = P-S converted phase at moho, PpPmp = first order multiple between free surface and moho. b) Synthetics for the single dipping crustal layer model in a) showing relative arrival times and amplitudes of the two secondary phases shown in a).

with waveform modeling promises to be a useful means for systematically investigating both large and small scale near-receiver structure across any area covered by a seismic array.

1.5 Overview of Procedure

The first step of our procedure includes establishing data selection criteria and compiling a data set which is best suited for our analysis (Chapter 2). The next step involves the determination of how best to isolate the near-receiver structure information using deconvolution to extract receiver impulse response functions (Chapter 3). Near-receiver structure is contained in the coda of the *P* waveform and is assumed to be composed principally of first order reverberations and conversions from the incident plane *P* wave beneath each recording station. These near-receiver reverberations and conversions are manifest in the waveform as small amplitude, secondary *P* coda arrivals. For a single layer over a half-space model, Figure 1.3a shows an example of the ray paths for phases that contribute to the *P* coda waveform. The corresponding synthetic waveform in Figure 1.3b demonstrates the small amplitudes of the secondary arrivals relative to the direct arrival. They are on the order of 10-20% of the direct *P* arrival amplitude. Optimal signal enhancement (noise reduction) in the *P* coda through waveform stacking is the final step of the data reduction (Chapter 3). This allows for *P* coda phases to be identified and their statistical significance to be assessed. After the data are processed, stacked waveforms from individual stations which are found to have persistent and significant *P* coda phases are modeled using forward modeling methods and interpreted (Chapter 4). A summary of the procedure, modeling results, and conclusions follow (Chapter 5).

Chapter 2

Teleseismic Waveform Data

2.1 Pacific Northwest Seismograph Network Data

The PNSN has acquired real-time digital waveform data, sampled nominally at 100 samples/sec, from over 100 stations since March 1980 (149 stations as of October, 1994). The network consists almost entirely of short-period, vertical-component stations (see Figure 2.1 and Appendix A.1 for station locations), although five broadband, three-component stations (sampled at 50 samples/sec) were added starting in April of 1993. Data from the short-period stations are telemetered to the University of Washington via telephone, radio or microwave transmission to a central data-processing computer. The network data acquisition normally operates in a triggered mode in an effort to minimize the accumulation and storage of useless, transient event data. A "permanent" record of the digital data is made on computer disk only if an event is detected, as determined when certain conditions of a triggering algorithm are met. The triggering conditions include: (*i*) exceeding a standard STA/LTA (short term average/long term average) threshold for a fixed length of time at any given station, and (*ii*) having a minimum number of stations within a single subnet (the PNSN is divided into a number of overlapping subnets) that exceed the STA/LTA threshold. Running in a triggered mode, the network detects and records local, regional, and teleseismic events. Detected events include both seismic and non-seismic sources (e.g., chemical and nuclear blasts, rockfalls, lightning, and aircraft). After locations are determined by a network analyst, the trace data are archived to computer disk and magnetic tape. To minimize disk and tape storage, teleseisms have been routinely decimated by a factor of two (or four) following the application of a low pass anti-aliasing filter. Decimation does not adversely affect the teleseismic data as the new 25 Hz (or 12.5 Hz) Nyquist frequency is well above the 1.0-2.0 Hz upper limit of the band-limited teleseismic source. *Ludwin et al.* [1994] provide a thorough discussion of the network operation, data acquisition, event triggering, data management and routine data analysis.

Several different types of 1.0-Hz velocity instruments have been deployed within the network during its operation. All have similar response characteristics at 1.0 Hz, although the gains may vary considerably at this frequency. Any limitations or differential effects different instrument types might impose on a study involving teleseismic waveform analysis should be addressed. Two potential problems are immediately apparent. The first, variable gain settings from station to station, should not be problematic as all

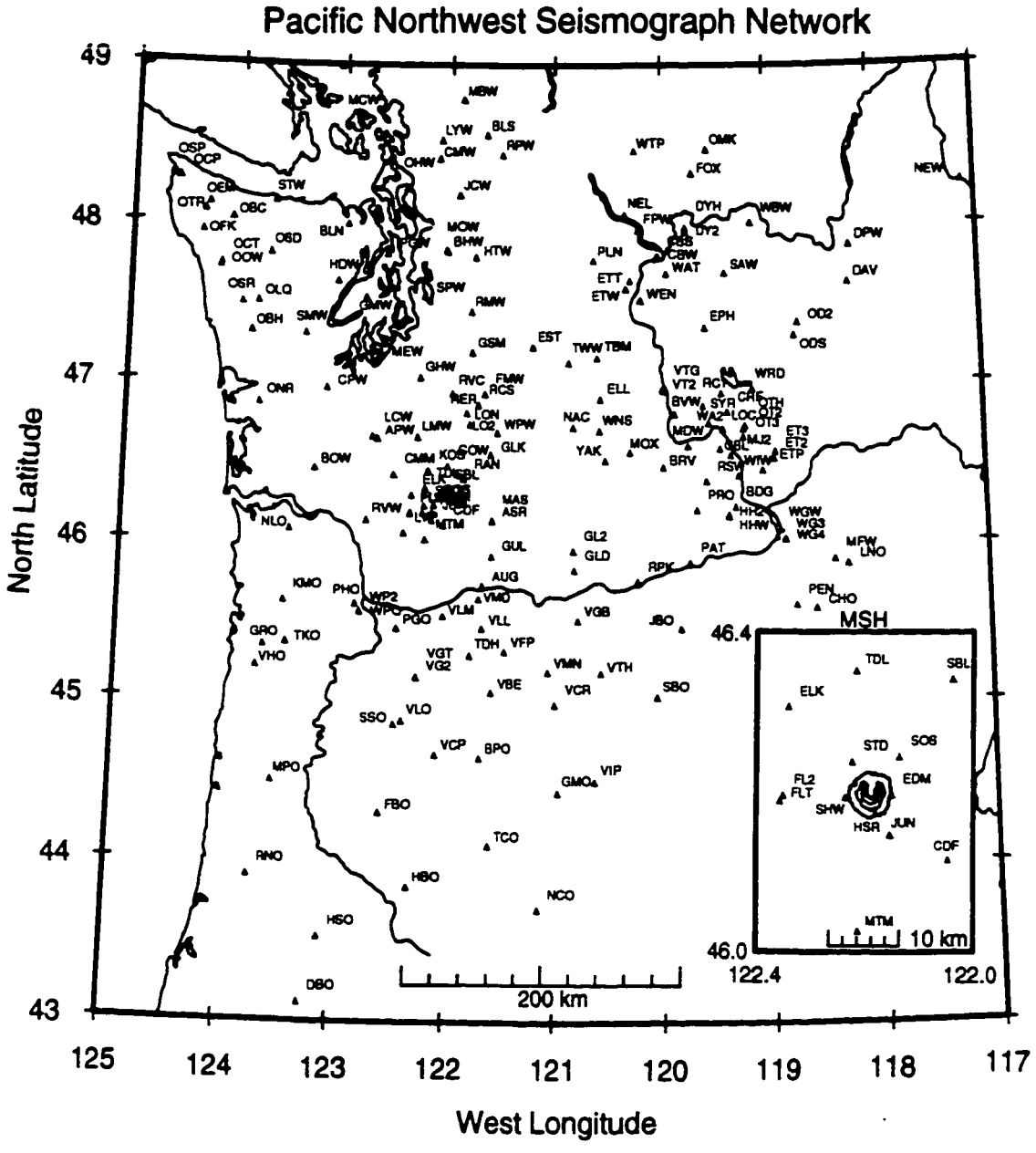

Figure 2.1: Stations of the Pacific Northwest Seismograph Network (PNSN) recording during the period 1980 through 1993. Appendix A.1 gives station location details as well as installation dates for individual stations. MSH=Mt. St. Helens.

seismogram amplitudes are normalized during our waveform analysis. The second, variations in response curves between different instruments, should not produce relative waveform distortions as the frequencies involved are beyond the band-limited teleseismic source. However, the limited dynamic-range of the telemetry system can pose a significant waveform distortion problem, namely clipping. This problem cannot be remedied, and any recorded events with a significant number of stations containing clipped waveforms are not useful for waveform studies. Since clipping is typically associated with larger magnitude ($m_b > 6.5$) earthquakes, some of the highest signal-to-noise ratio events are unfortunately unusable for this waveform analysis study.

2.2 Data Selection

For the period of January 1980 through December 1993, the PNSN digitally recorded over 5400 teleseismic events. These events were checked against the National Earthquake Information Center (NEIC) catalog to verify origin times and hypocenter locations using the same procedure as *VanDecar* [1991]. From this procedure, a total of 4254 PNSN events with *P* arrivals were identified. 4102 of these events were at epicentral distances corresponding to mantle *P*-phases, while the remainder were at epicentral distances corresponding to core *P*-phases (e.g., *PKP* and *PKiKP*). The locations of these teleseisms in terms of distance (Δ) and back azimuth (BAZ) from the PNSN center are shown in Figures 2.2a and 2.2b after *VanDecar* [1991]. Back azimuth is defined here as the azimuthal direction from receiver to event as measured clockwise from north.

The initial data set considered for this study was extracted from the above pool of 4254 events, using a two-step selection process. The first step applied a set of general selection criteria similar to those commonly used in teleseismic receiver function studies. These included: (*i*) an epicentral distance range (Δ) of 40°-95°, (*ii*) a minimum focal depth cutoff of 100 km, and (*iii*) a minimum magnitude cutoff of $m_b = 5.3$. The first condition avoids seismograms complicated by either turning or bottoming in the mantle transition zone ($\Delta < 40°$), or interactions with the core ($\Delta > 95°$). The second condition ensures that secondary source arrivals (e.g., *pP* and *sP*) arrive outside of the data window of interest which is approximately 25 sec in length. The third condition excludes events either poorly recorded or with poor signal-to-noise ratio seismograms. Figure 2.3a shows the distribution of the 693 events that met the above selection criteria, with locations grouped

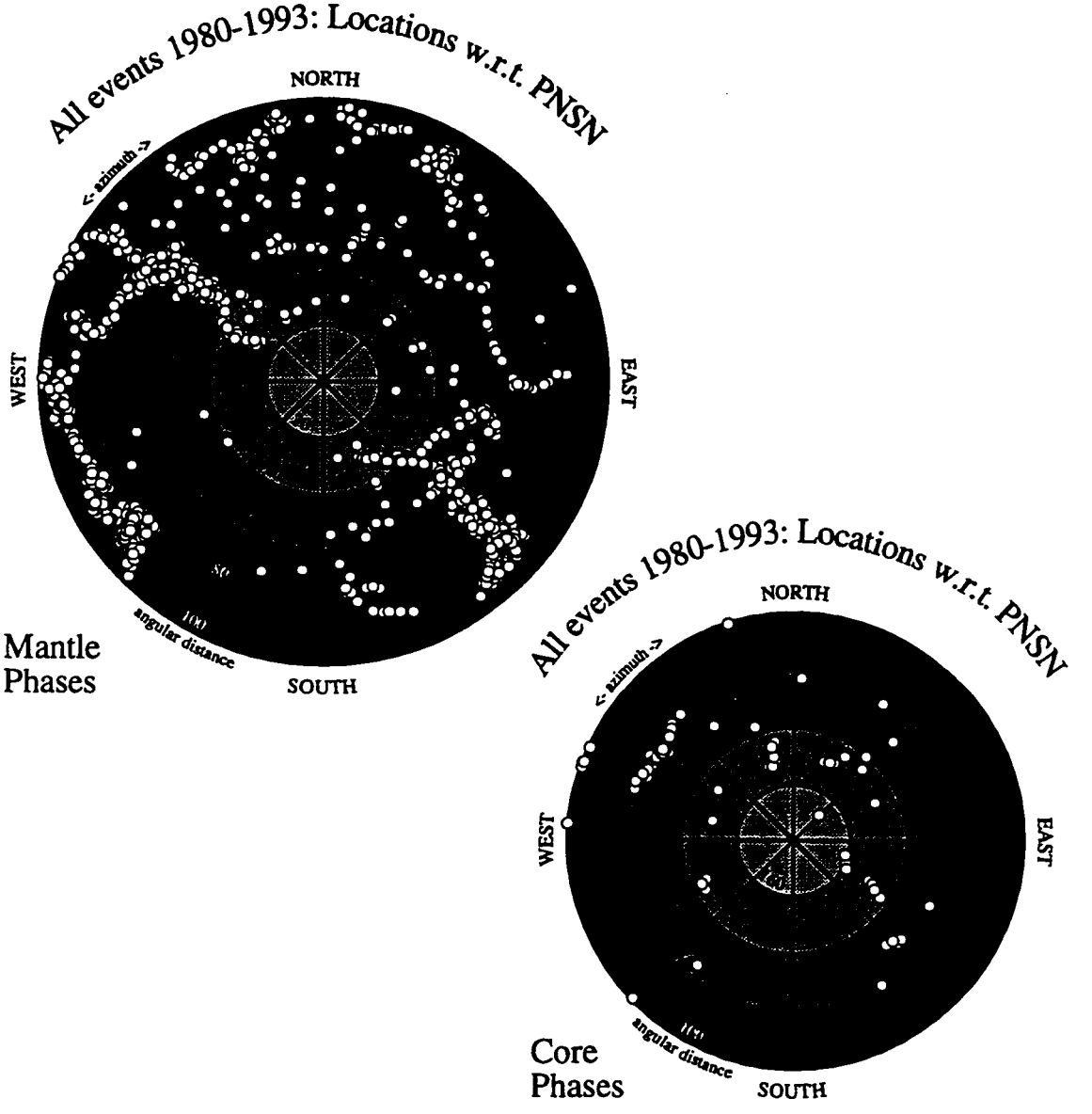

Figure 2.2: Catalog of PNSN teleseisms recorded from 1980 through 1993, showing source locations in terms of distance and backazimuth from the PNSN. The upper plot shows events which turn in the mantle; the lower plot shows those which bottom in the core.

predominantly into three source regions: southeast back azimuths (central and South America), southwest back azimuths (southwest Pacific) and northwest back azimuths (northwest Pacific). This heterogeneous event distribution is ideally suited for this study, as the clustering of events into narrow ranges of back azimuth allows for stacking receiver impulse response functions following deconvolution. In addition, this event distribution is well suited for investigating variations in the receiver impulse response functions as functions of both back azimuth and distance.

The second step of the event selection process involved assessing the quality and acceptability of the larger pool of 693 events targeted in the first step. The initial pool of candidate events was partitioned into ten subgroups by back azimuth, following the trends of the distribution seen in Figure 2.3a. For subgroups with large numbers of events (e.g., events from southeast back azimuths), further partitioning by distance was performed. Events from each of the subgroups were downloaded from magnetic tape individually to disk. Then trace data for each event was visually inspected using the seismogram display and phase picking software *xped*, an X-windows package developed by R. S. Crosson, M. Woolf and E. Crosson. Any event found to have emergent, long or complicated first arrivals, too-short trigger lengths, excessive waveform distortion (e.g., transient noise, spikes or clipped signals), or a poor signal-to-noise ratio was deemed unusable and discarded. Also during the visual inspection, traces for an individual event were aligned on the direct *P* arrival by inspection as part of the initial processing. Any events with fewer than 25 successfully aligned traces (stations) were also discarded; these often included events with poor signal-to-noise. The signal-to-noise ratio was determined for every trace of a given event by comparing the root-mean-square (rms) amplitude of a 5 sec window about the first significant pulse of the *P* arrival with that of similar window taken from the pre-signal noise. An arbitrary value of 4.0 for the rms amplitude ratio was selected as the minimum acceptable level. Typical events in the final data set had on the average 40 successfully aligned, good signal-to-noise stations, with some of the larger events having as many as 100 aligned stations.

2.3 Final Data Set

The final data set resulting from this two-stage selection process consists of 294 events. Their spatial distribution with respect to the PNSN is shown in Figure 2.3b. A

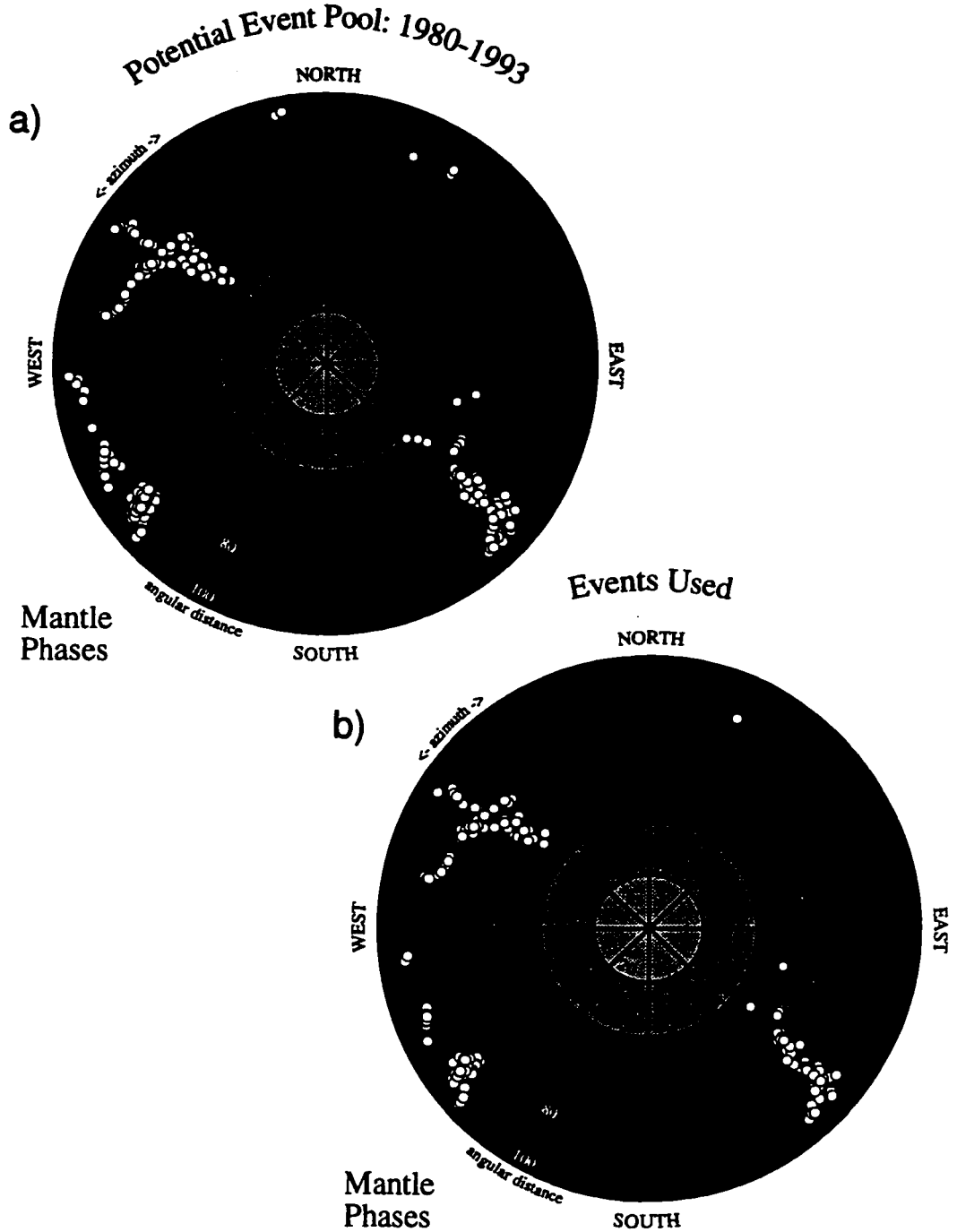

Figure 2.3: (a) Subset of teleseisms recorded by the PNSN which met the minimum event depth and distance criteria for this study. (b) Final data set used in this study.

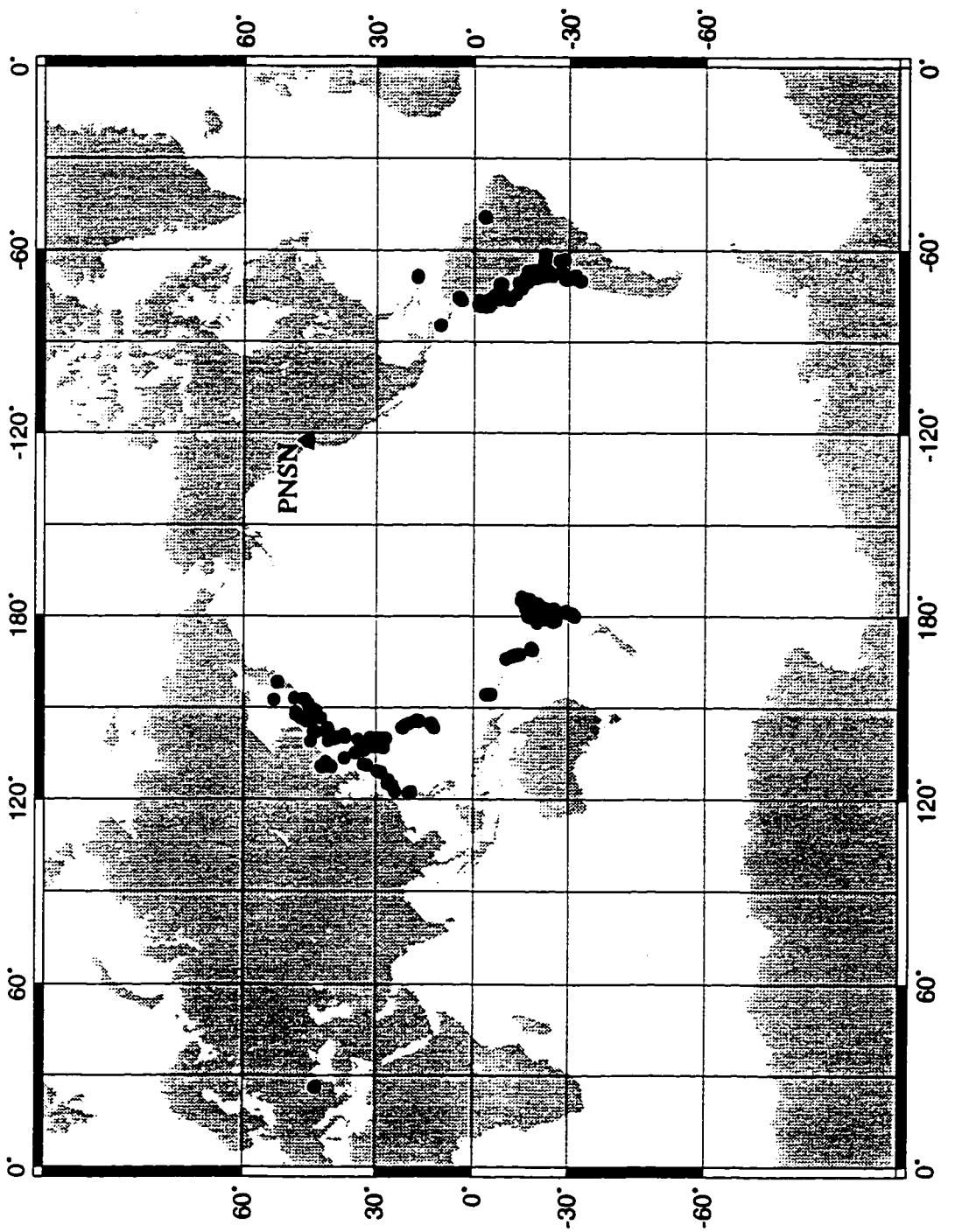

Figure 2.4: Final data set epicenter locations for this study along with the PNSN.

complete listing of these events with source parameters, including distance and back azimuth, can be found in Appendix A.2. This data set includes 1 event from the northeast (NE), 79 events from the southeast (SE), 129 events from the southwest (SW), and 89 events from the northwest (NW). Figure 2.4 gives the geographic distribution of the final data set epicenters. As shown in Figure 2.3b, the source distribution of this data set allows for the investigation of variations in the *P* waveforms (analyzed in Chapter 3) as functions of distance (Δ) and back azimuth (BAZ). The redundancies in source locations for events in this data set are used to enhance waveform signal-to-noise ratios through time-domain stacking. We do not expect all of the redundant source location events to have *P* arrivals with the same duration and pulse shape. In fact, some source normalization procedure must be applied to the data before direct comparisons of waveforms from different events from similar source regions can be made. Source normalization, source wavelet estimation, and removal via deconvolution are discussed in Chapter 3.

Chapter 3

Deconvolution and Stacking

3.1 Deconvolution Introduction

A body-wave seismogram, $d(t)$, can be expressed analytically as the convolution of a source wavelet (which includes the source time function, an attenuation operator, near-source structure and mantle structure), $s(t)$, with the impulse response of a layered earth near the receiver (receiver function), $r(t)$:

$$d(t) = s(t) \otimes r(t) \tag{3.1}$$

where $\otimes$ is the convolution operator. The discrete convolution operator is defined by

$$\sum_{k=0}^{n} s(t-k)\, r(k)\,. \tag{3.2}$$

The problem of seismic deconvolution is typically approached in a general two-step fashion. First, the source function $s(t)$ is estimated using some appropriate method. Next, this source function estimate is removed (deconvolved) from the seismogram using some prescribed or preferred procedure. The resulting deconvolved body-wave seismogram consists of a band-limited spike series which includes the direct arrival plus later arrivals corresponding to conversions and multiple reflections from interfaces with significant impedance contrasts beneath the station. The band-limited spike series associated with a particular recording site is often referred to as the vertical impulse response function for that site.

The general deconvolution method employed in this study and described in detail below is conceptually similar to the method used in conventional horizontal receiver function analysis [*Langston* 1979]. However, unlike the horizontal receiver functions, the resulting deconvolved seismograms of this study are vertical-component and are dominated by first-order *P* reflected phases. As an integrity check of our deconvolution procedure, the waveform contents are verified with a cepstral deconvolution method [*Crosson and Dewberry* 1994, *Dewberry and Crosson* 1994].

3.2 Deconvolution: Stacking Method

The stacking method is explicitly a two-step procedure, involving time-domain source estimation followed by source removal or deconvolution. The resulting deconvolved seismogram represents the vertical component of the receiver impulse response for a given site, containing near-receiver structural information. The general method of far-field source estimation by stacking using short-period vertical-component network data has been used by a number of investigators. *Vidale and Houston* [1993] used the stacking method with deep focus teleseisms to investigate source signatures and quantify rupture durations. *Mack* [1969] and *Bostock and VanDecar* [1994] used this method to estimate source wavelets for teleseisms and then deconvolved the resulting source estimates from each seismogram to investigate direct-*P* phase distortion by near-receiver structure. *Houard and Nataf* [1992] and *Vidale and Benz* [1992] used the same approach with short-period vertical-component teleseismic data to investigate variations in deep mantle (D") and outer core structure with mantle (*P*) and core (*PcP* and *ScP*) *P* waveform records, respectively. *Paulssen et al.* [1993] applied the source estimation procedure to broadband teleseismic data.

Our approach to source estimation follows the general approaches of *Houard and Nataf* [1992] and *Vidale and Benz* [1992]. We apply this method to the teleseismic *P* waveforms of our data set (as discussed in Chapter 2) where individual traces are aligned by eye on the first arrival, normalized, and then stacked. The signal-to-noise ratio for each trace is checked using a 5.0 second window about the *P* arrival and a 5.0 second pre-signal window. Any traces with a signal-to-noise ratios < 4.0 or with excessive reverberations in the *P* coda (determined from visual inspection) are excluded from further analysis. In addition, events with fewer than 25 high signal-to-noise ratio traces are excluded from analysis. The subsequent stack (source estimate) contains only those arrivals which add coherently across the network, or those phases with the same apparent velocity as the *P* arrival. Any scattered energy present in the *P* coda of the individual traces is presumably incoherent between stations and cancels in the stack. Thus, the noise level of the stack is diminished by a factor of $\sqrt{n}$, where n is the number of traces going into the stack.

The stack (source estimate) contains the following elements: the far-field source time function, an attenuation operator, near-source and mantle structure, and an average instrument response. In addition, local structure common to most or all sites which adds coherently maps into the stack. This is problematic as the common near-receiver structure

will be removed and lost in deconvolution. For sufficiently deep common structure, this problem can be alleviated by imposing a length constraint on the source estimate or stack (windowing). For shallow common structure, no clear remedy exists. However, including traces from stations which homogeneously sample the region reduces the likelihood of near-receiver structure producing coherent arrivals, as the overall region covered by the PNSN is structurally heterogeneous.

An assessment of the source estimate quality can be made based on the abrupt truncation (or lack thereof) of the stack *P* arrival wavelet. As *Vidale and Houston* [1993] have shown, stacks of short-period network data for deep focus events generally exhibit abrupt *P* arrival onset and termination. While an abrupt terminus argues for reasonable source estimation (the approximation of a finite duration rupture), a complicated terminus may not indicate insufficient noise cancellation due to an insufficient number of traces being stacked. Rather, near-source scattering may generate a prolonged coherent signal in the *P* coda. With a sufficient number of traces being stacked, the stack quality should be adequate regardless of the nature of the signal termination. Applying the 25 trace minimum criterion to the events analyzed appears sufficient to provide adequate stack quality. Figure 3.1 shows two examples of PNSN recorded earthquakes displayed in record sections (events 195 and 80) aligned on the *P* arrivals. Above each record section is the corresponding stack or source estimate. Note that each source estimate exhibits an abrupt onset and termination. The total number of traces producing each source estimate is also noted.

The second step of the stacking method involves deconvolving the source function from each of the traces that went into the stack to extract receiver impulse response functions (receiver functions). Deconvolution in the time domain, from equation (3.1), can be achieved by convolving the seismogram, $d(t)$, with the inverse of the source function, $s^{-1}(t)$:

$$s^{-1}(t) \otimes d(t) = s^{-1}(t) \otimes s(t) \otimes r(t) = r(t). \tag{3.3}$$

While the source function estimate is known, its inverse function is not. To avoid this complication, a frequency domain deconvolution is considered. By transforming to the frequency domain, the deconvolution is performed using spectral division. A waterlevel

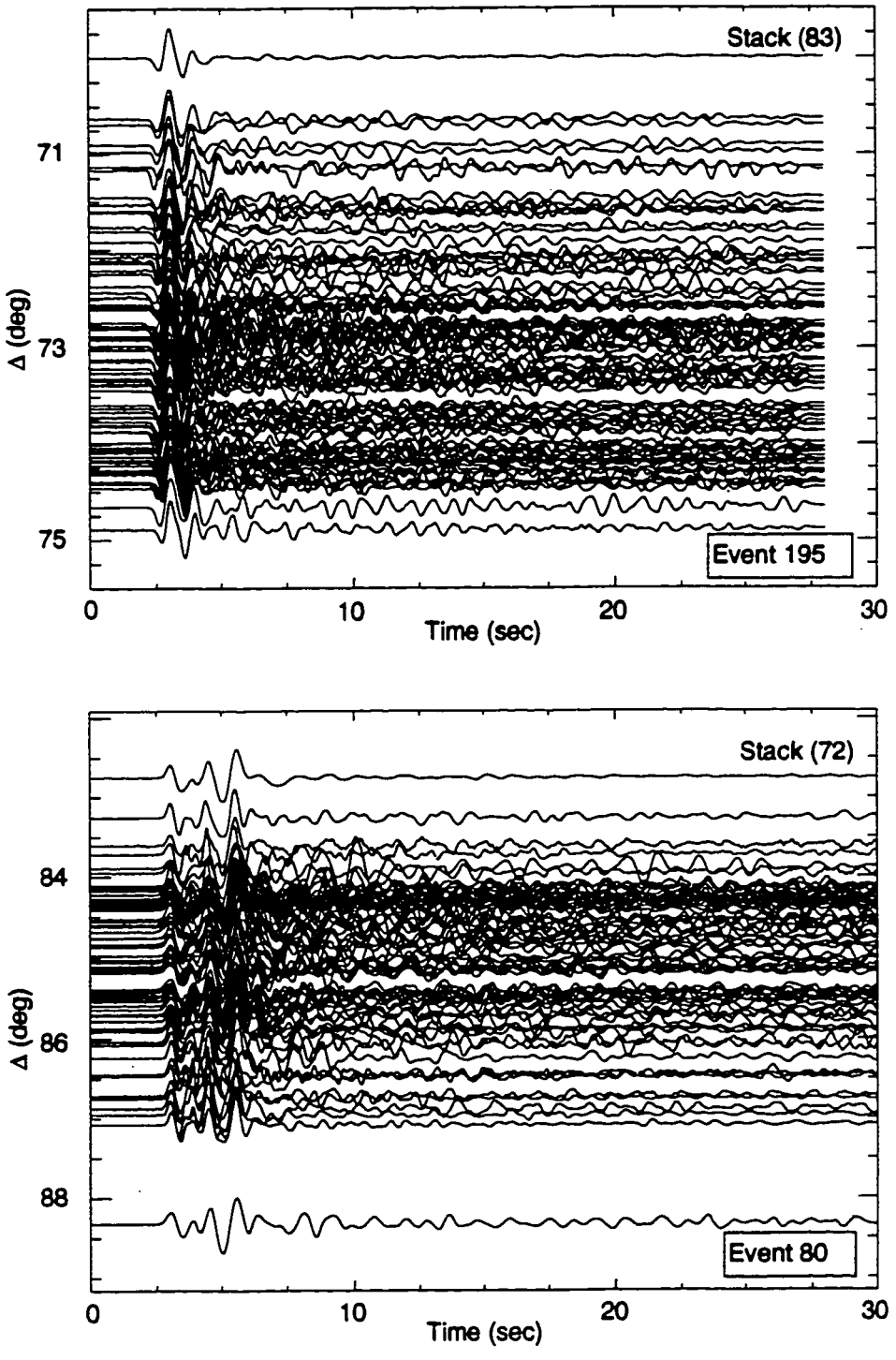

Figure 3.1: Two example event record sections with traces aligned and sorted by distance. The top trace is the corresponding stack (source estimate) for each event.

deconvolution [*Helmberger and Wiggins* 1971, *Clayton and Wiggins* 1976] ensures the spectral division is numerically stable. Additionally, a gaussian filter applied in the frequency domain removes high frequency noise introduced by the deconvolution. With the waterlevel deconvolution, the deconvolved seismogram in the frequency domain then takes the general form:

$$R(\omega) = \frac{D(\omega)\bar{S}(\omega)}{(max\{S(\omega)\bar{S}(\omega), c \cdot max[S(\omega)\bar{S}(\omega)]\})} \cdot G(\omega) \qquad (3.4)$$

where ~ denotes the complex conjugate, c is the waterlevel parameter ($0 \leq c \leq 1$), $S(\omega)$ is the estimated source function, and $G(\omega)$ is a gaussian function. $G(\omega)$ is of the form:

$$G(\omega) = exp(-\omega^2/4\beta^2) \qquad (3.5)$$

where β is the gaussian parameter. For a β value of 4.0, the effective low-pass filter corner frequency is roughly 1.0-2.0 Hz.

The waterlevel parameter, c, assigns the minimum spectral amplitude of $S(\omega)$ as some fraction of the maximum spectral value, $S(\omega)_{max}$. This has the effect of filling holes in the spectrum of $S(\omega)$ where there is little to no source information (although some noise may be present). For a value of $c = 0$, the procedure gives an unrestricted deconvolution of $D(\omega)$ by $S(\omega)$. All of the source effects are removed, providing the "best" estimate of the impulse response. For a value of $c = 1$, the deconvolution gives a scaled version of the cross-correlation of $D(\omega)$ and $S(\omega)$, which is the least squares of the arrival amplitudes [*Helmberger and Wiggins* 1971]. *Clayton and Wiggins* [1976] have demonstrated that the waterlevel parameter can be considered a factor that trades off resolution of travel time with amplitude. Zero waterlevel provides the optimal travel time resolution, and a waterlevel of unity provides the optimal amplitude resolution. *Clayton and Wiggins* [1976] also stipulate that the desired waterlevel should ensure that $c \cdot max[S(\omega)\bar{S}(\omega)]$ is greater than both the noise level and deviations of the source estimate from the true source function. Since making this determination is not practically feasible, the next best approach is to test a range of values, $0.0 \leq c < 1.0$, and compare the resulting impulse responses for each value. Figure 3.2a and 3.2b shows the deconvolved seismograms of

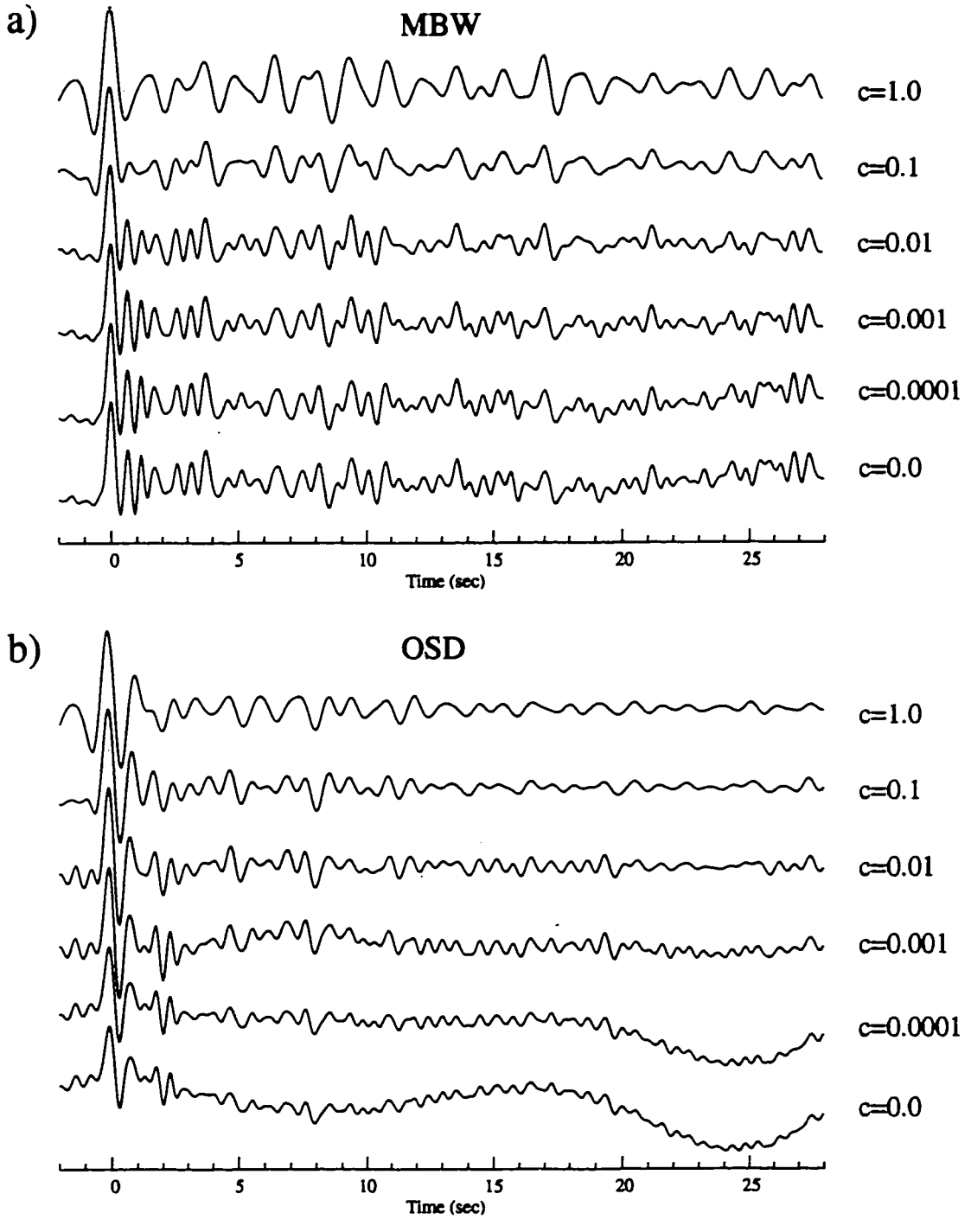

Figure 3.2: Deconvolved seismograms from event 80 for stations (a) MBW and (b) OSD for a range of waterlevel parameters, *c*, using a gaussian parameter of 4.0. Note that the decrease in *c* improves the time resolution of phases in the *P*-coda but also increases the amount of (a) high frequency and (b) low frequency noise.

stations MBW and OSD for event 80 using a range of waterlevel parameters. Note that the decrease in the waterlevel parameter does improve the time resolution of the *P*-coda phases. However, this comes at the expense of increased noise both at high frequencies (figure 3.2a) and low frequencies (figure 3.2b). From these examples, we would select waterlevel parameter values in the range of 0.01 to 0.001 to maintain the best time resolution while maintaining a qualitatively acceptable level of deconvolutional noise.

Noise and signal artifacts can be introduced into the deconvolved seismogram in a number of ways when using the waterlevel deconvolution. Spectral holes at any given frequency in the source estimate, $S(\omega)$, will produce fairly monochromatic noise in the deconvolved seismogram. Figure 3.3 shows examples of this effect using noise-free synthetics and a source estimate with spectral holes at low frequencies (figure 3.3a) and high frequencies (figure 3.3b). Note that the noise mapped into the deconvolved seismograms is monochromatic and generally increases as c decreases. Noise can be introduced over a wider range of frequencies in the higher end of the spectrum when there is a significant spectral roll-off. Additionally, the use of band-limited data will contribute to the deconvolved seismogram in the form of side lobes on individual phase arrivals. Figure 3.4a shows an example where a band-limited source and noise-free synthetics are considered. Side lobes are evident for all $c < 1.0$, with the frequency content increasing as c becomes smaller. Note that a broad gaussian filter has been applied in this case so that effectively no low pass filtering has been applied.

Much of the noise and side lobe artifacts can be mitigated by reducing the width of the gaussian window or low pass filtering the results. Figure 3.4b shows a nice example of side lobe suppression, where a gaussian of 4.0 was applied to the deconvolved data in Figure 3.4b. Much of the undesired signals of the type seen in Figure 3.3b can also be removed in this fashion. Deciding upon an optimal gaussian parameter does depend of the amount and spectral content of deconvolution noise, but may be more dependent of the desired time resolution of the signal and length scale resolution of the responsible structure. For noise problems at low frequencies (as in Figure 3.3b) use of a larger waterlevel parameter is the only effective remedy.

Based on the limited band width of the recording instruments and the intent to resolve structure with wavelengths as long as possible, a gaussian parameter of 4.0 was chosen for the waterlevel deconvolutions performed on our data. The suggestion of testing a range of waterlevel parameters for each seismogram in order to select an optimal value is

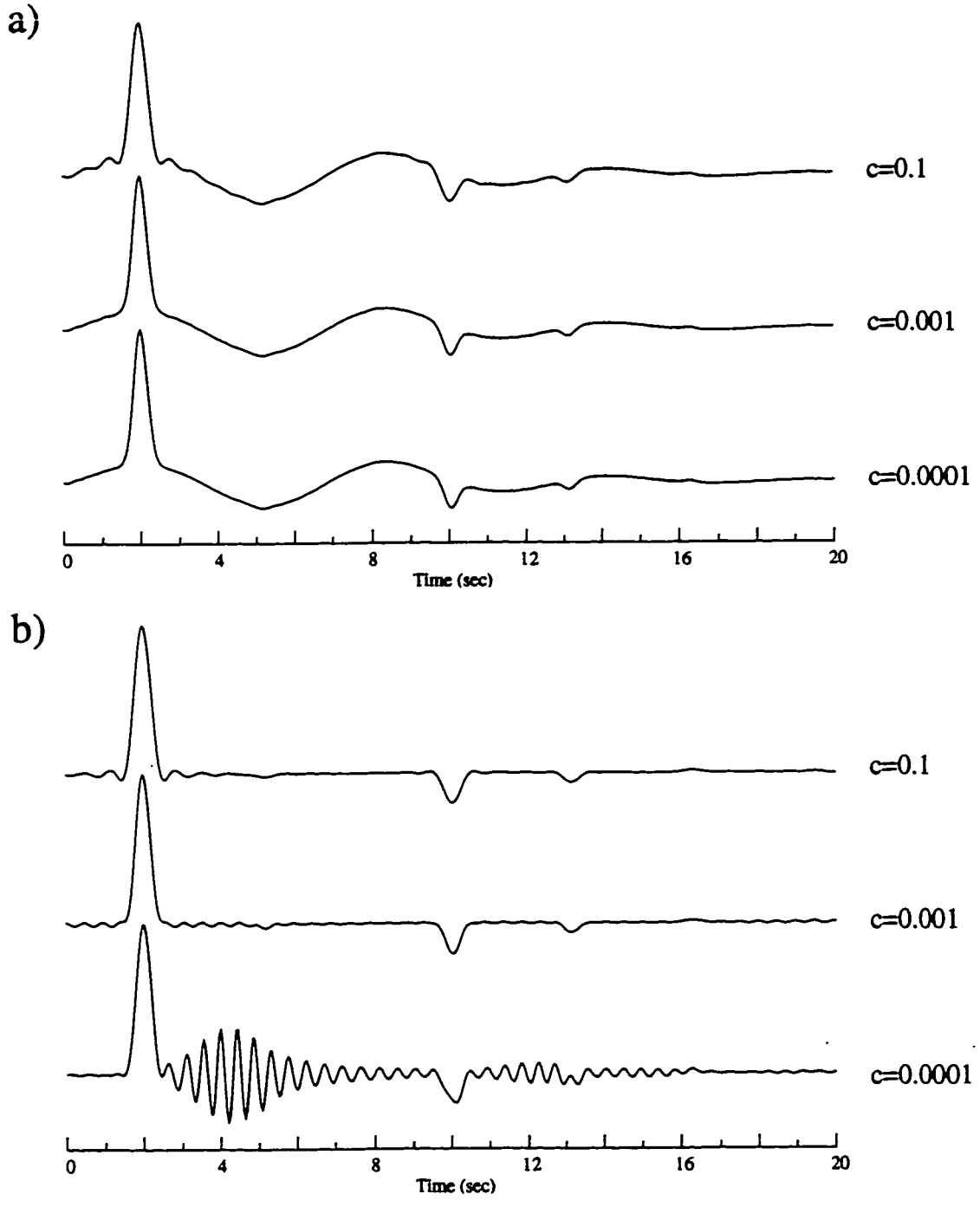

Figure 3.3: Deconvolved seismograms for noise-free synthetics using source estimates with spectral holes at (a) low frequencies, 0.1-0.2 Hz and at (b) higher frequencies, 2.0-3.0 Hz. A gaussian parameter of 4.0 was used for each. Note that these spectral holes produce monchromatic noise in the deconvolved synthetics that increases as the waterlevel, *c*, decreases.

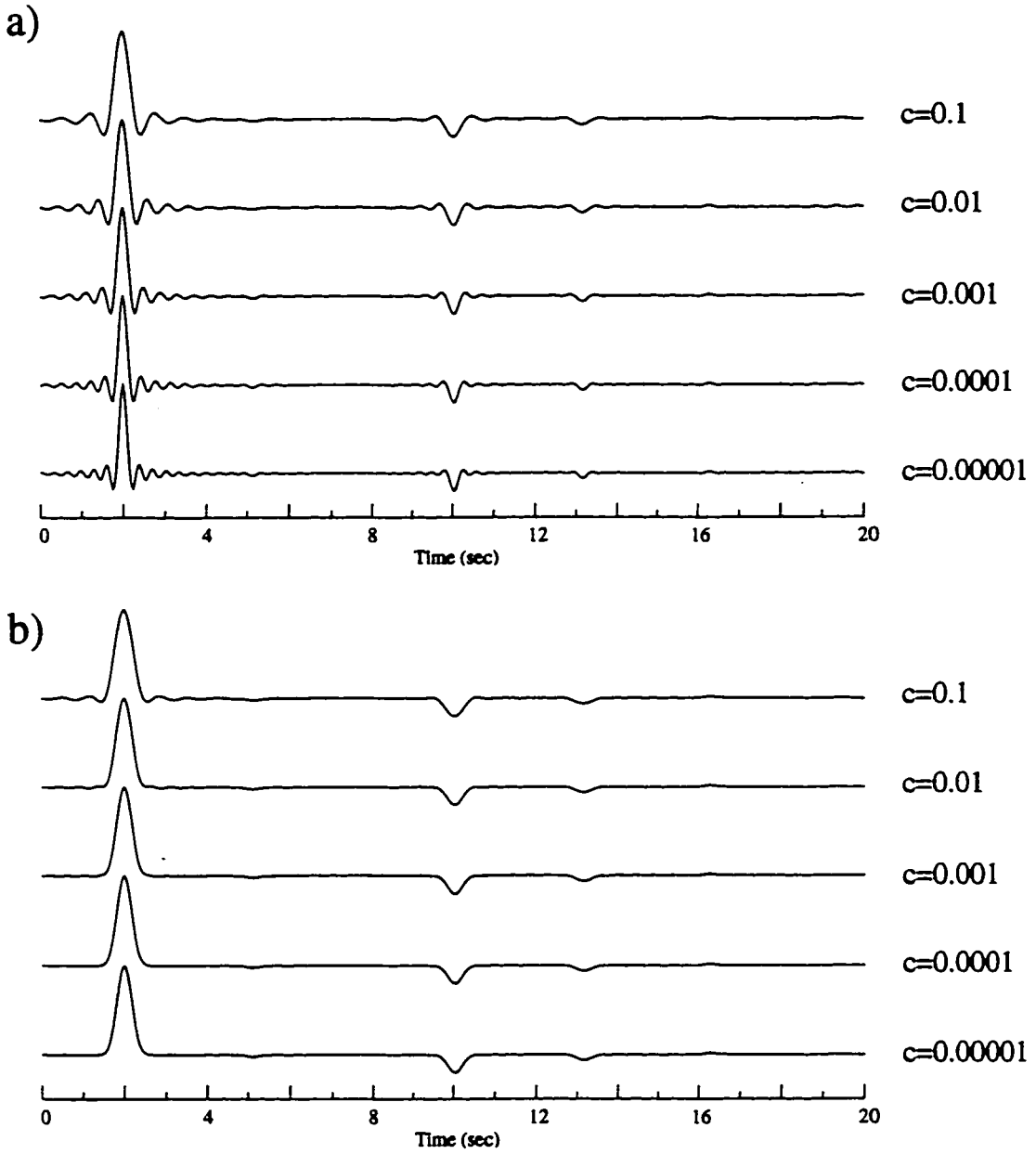

Figure 3.4: Deconvolved seismograms for noise-free, band-limited synthetics using a band-limited source function. (a) A gaussian parameter of 20.0 was used, imposing little filtering. Note that the high-frequency content increases with decreasing *c*. (b) A gaussian parameter of 4.0 was used. Note that filtering removes most of the side lobes at the expense of time resolution.

impractical with the number of seismograms (of the order 10,000) considered. Rather, a subset of events was tested using a range of c values. In the end, a waterlevel parameter of 0.01 was selected for all deconvolutions. This value provided a reasonable compromise between maximum time resolution and minimum noise inclusion, especially low frequency noise. Thus, all of the waterlevel deconvolved seismograms analyzed in this study were produced with these parameter values: $c = 0.01$ and $\beta = 4.0$.

3.3 Deconvolution Verification

To verify the effectiveness of the stacking deconvolution technique, we compared the results of the stacking deconvolution method with those using a cepstral method described by *Crosson and Dewberry* [1994] and *Dewberry and Crosson* [1994]. This comparison was made using a subset of events from SW back azimuths, representing 11 stations recording 15 events confined to a 10° by 10° window in distance and back azimuth. The 15 events selected demonstrated a variety of different source time functions, as determined from the stacking deconvolution source function estimation procedure. To make a direct comparison of the receiver functions produced by each deconvolution procedure, the resulting stacking method deconvolved seismograms for each station are stacked linearly. Figure 3.5 shows a comparison of the resulting waveforms from the two deconvolution methods. All deconvolved waveforms plotted have been normalized and aligned on the direct-*P* arrival. Aside from a slightly higher frequency content for the cepstral method waveforms, the comparison shows generally good waveform agreement. The notable exception is station LON which shows greater *P*-coda phase amplitudes for the cepstral method waveforms.

Having verified comparable performance from each deconvolution procedure, we felt confident that the stacking method was successful in removing the source signature and extracting local structural content from each recorded seismogram.

3.4 Deconvolved Waveform Stacking

After producing deconvolved seismograms, the waveforms were stacked to provide maximum phase enhancement and signal-to-noise reduction. One critical consideration in signal enhancement is the dimensions of the windows in distance (Δ) and back azimuth

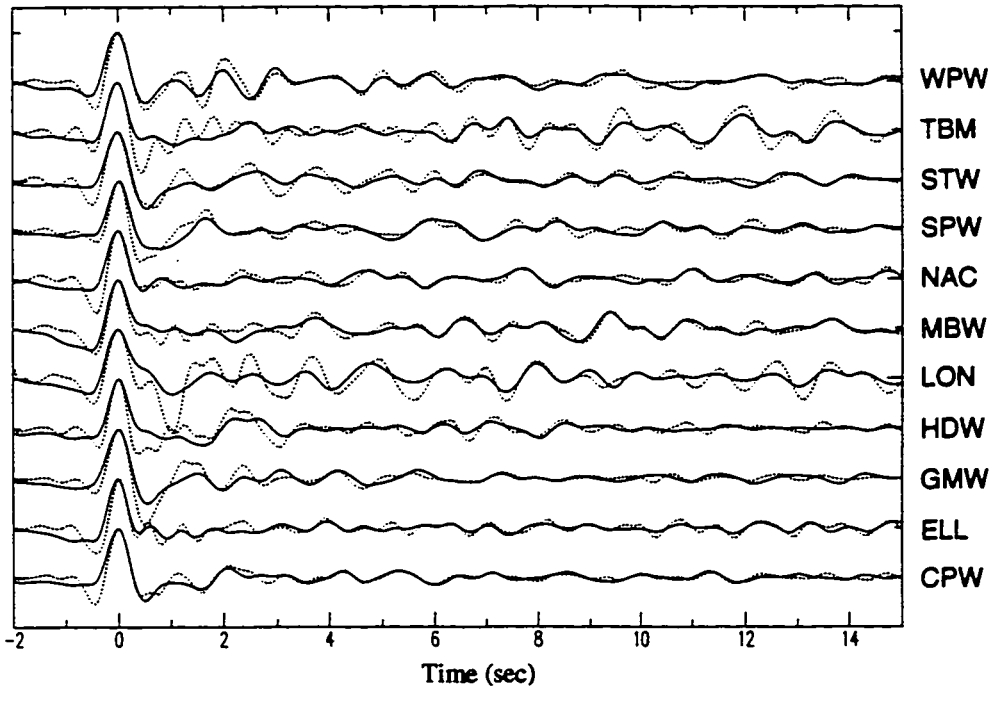

Figure 3.5: Stacking and cepstral deconvolution results comparison for a 15 event, 11 station subset of data from southwestern back azimuths. Station names are noted to the right of the deconvolved waveforms.

(BAZ) over which stacking in performed. In a receiver function study modeling *Ps* phases involving flat lying structures, *Owens* [1984] stacked data over 20° in BAZ and 15° in Δ for Δ > 70° (10° for Δ ≤ 70°). *Cassidy* [1991] revised these to more conservative values of ≤10° for both Δ and BAZ, citing the need to reduce undue amplitude attenuation of *Ps* phases when deep and dipping structures are involved. The use of multiple reverberation phases in this study might indicate the need for stacking ranges over Δ and BAZ even smaller than 10°. However, testing 10° wide stacking windows with synthetic data for an event at Δ=45° using a dipping (at 10°) layer over half-space model with an interface depth of 25 km shows the amplitude variations of stacked data from end member Δ and BAZ are less than ±5% of the amplitudes from the window centers. Even a 10% variation in the end member stacked data amplitudes would be acceptable. To ensure as many traces as possible go into each stack while incurring minimal amplitude attenuation, 10° windows were applied during waveform stacking of the deconvolved data.

Different stacking methods were applied both to enhance certain characteristics of the data and to find optimal noise reduction. The same 10° by 10° windows were applied for each stacking method (see figure 3.6 for window locations and distribution). The stacking methods included the standard linear stack. Along with each linear stack, ±2σ error bounds were determined and plotted to identify statistically significant (to 95% confidence level) coherent *P*-coda phases. In this way, one trace with an outlier phase may leverage the stack amplitude but will also produce greater error bounds (variance). Robust linear methods (e.g., *Andrews et al.* [1972], *Rosenberger and Gasko* [1983]) such as a trimmed mean stack, were also applied to help identify significant phases (and to reduce variances) by removing or down-weighting outliers. The results using linear robust stacking show some stacks with slightly tighter confidence bounds, but on the whole produced no dramatic improvements for that data tested.

*N*th-root stacks (e.g., *McFadden et al.* [1986]) were also applied to the deconvolved data in an effort to improve noise suppression. The advantage of the non-linear *N*th-root stack is that in general where there is no signal the variance decreases as m^N, whereas for the linear stack the reduction is only by an amount m (where m is the number of traces input). Thus, those regions of the stack where only background noise (no signal) exists are greatly reduced with the *N*th-root stack. Because of this noise rejection, the *N*th-root stack produces distortion in the ends of the true signal wavelet, where the signal becomes increasingly inundated by noise. Although distorted and biased to smaller amplitude, the

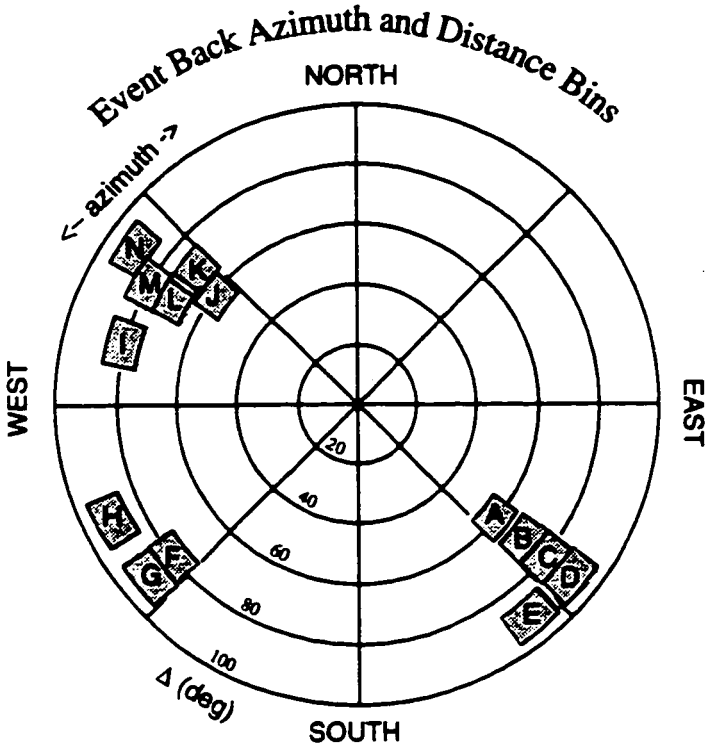

Figure 3.6: Bins of dimension 10 deg by 10 deg used for stacking and modeling deconvolved seismograms. Implicit is the assumption of insignificant waveform amplitude variation over the bin dimensions.

wavelet is not time shifted. As N increases, both phase bias and distortion increase. Accordingly, a small N appears optimal. A value of N=3 was chosen for this data. For those regions in the stack where the signal-to-noise ratio is large, the Nth-root stack results are essentially the same as the linear stack. However, as the signal becomes more buried in the noise, the performance of the Nth-root stack degrades relative to the linear stack. This fact strongly suggests that both linear and non-linear methods should be used in conjunction to provide optimal results for phase identification. Thus, if the same phase is present in stacks produced by each method, its existence is difficult to question.

The linear slant stack was the third signal enhancement technique applied to the waveform data. This method is used commonly in reflection seismology (e.g., *Claerbout* [1976]) and is basically defined as time shifting traces proportional to their distance from some reference point and then summing. It can also be thought of as the sum along a line though a record section. This stacking method allows not only for an increase in the total number (m) of traces going into a stack by adding traces across all Δ for a given stacking window, but also provides a useful diagnostic when a optimal differential ray parameter is identified. The differential ray parameter is simply the slope of the line through the record section over which the sum is taken. The linear slant stacking procedure as applies here assumes a linear moveout of the P-coda phases with Δ. A check of the predicted moveouts from dipping, layered model synthetics shows that the linear moveout assumption is valid. The linear slant stack was applied to waveforms from BAZ's that included a wide range in distances. As implied from the stacking windows of Figure 3.6, this includes only data from NW and SE BAZ's. A range of differential ray parameters (-0.04 to 0.04 sec/deg) were used for linear slant stacking with each station. As with the linear stack, associated $\pm 2\sigma$ error bounds were determined for each slant stack.

Each of the three stacking methods mentioned above was applied to deconvolved data from 46 PNSN stations, stations which included waveforms representing most Δ's and BAZ's. Over half of these stations produced stacks with some significant, coherent P-coda arrivals. Of those, only a fraction showed coherent phases which persisted across a range of both Δ and BAZ, suggesting one or more reflecting interfaces at depth. In the end, stacks from 8 of the stations containing persistent phases were modeled with reasonable success in Chapter 4. Stacked data for these 8 stations are shown below in Figures 3.7-3.22, which include both standard linear stacks and linear slant stacks with $\pm 2\sigma$ error bounds. The 3rd-root stacks for each of these stations can be found in Chapter 4

displayed in comparison plots with the synthetic waveforms generated during the forward modeling procedure.

Stacked data for the 8 stations in Figures 3.7-3.22 show coherent phases with various arrival times, amplitude, polarities, pulse shapes, and moveouts with Δ and BAZ. These different phase characteristics provide various constraints for the structural models. Phase arrival times constrain interface depths. Phase amplitudes provide constraint of interface impedance contrasts, while the polarity indicates whether the discontinuous velocity increases or decreases across the interface. The pulse shape indicates possible phase-shifted arrivals or thin model layers. Phase moveout with Δ and BAZ indicates azimuthal dependent arrival times, suggesting non-horizontal structure. A summary characterization of the phases identified from the stacking results for each station follows below.

Table 3.1: Phase summary from waveform stacking

Station	Early arrival(s)			Later arrival(s)		
	amplitude	wavelet	moveout	amplitude	wavelet	moveout
MBW	large	complex	Δ, BAZ	small	simple	Δ, BAZ
SPW	large	simple	BAZ	medium	simple	Δ
OBH	medium	simple	BAZ	medium	simple	Δ, BAZ
OFK	large	simple	-	medium	simple	Δ, BAZ
OOW	medium	simple	Δ, BAZ	small	simple	Δ, BAZ
OSD	-	-	-	small	simple	Δ, BAZ
OTR	medium	simple	-	small	simple	Δ, BAZ
HDW	medium	complex	Δ, BAZ	-	-	-

Here an early arrival designation is assigned to phases with arrival times ≤ 5.0 sec, large phase amplitudes are defined as ≥ 50% of the direct-*P* arrival, small amplitudes are defined as ≤ 15% of the direct-*P* arrival, and a simple pulse is defined as a single positive or negative polarity pulse. The phases identified in the waveform stacks for each station above are modeled in the subsequent chapter where they are discussed in more detail. Those stations whose stacks contained some coherent *P*-coda arrivals which were not modeled in the following chapter but likely contain significant local structure are identified in Appendix A1 with a superscript dagger.

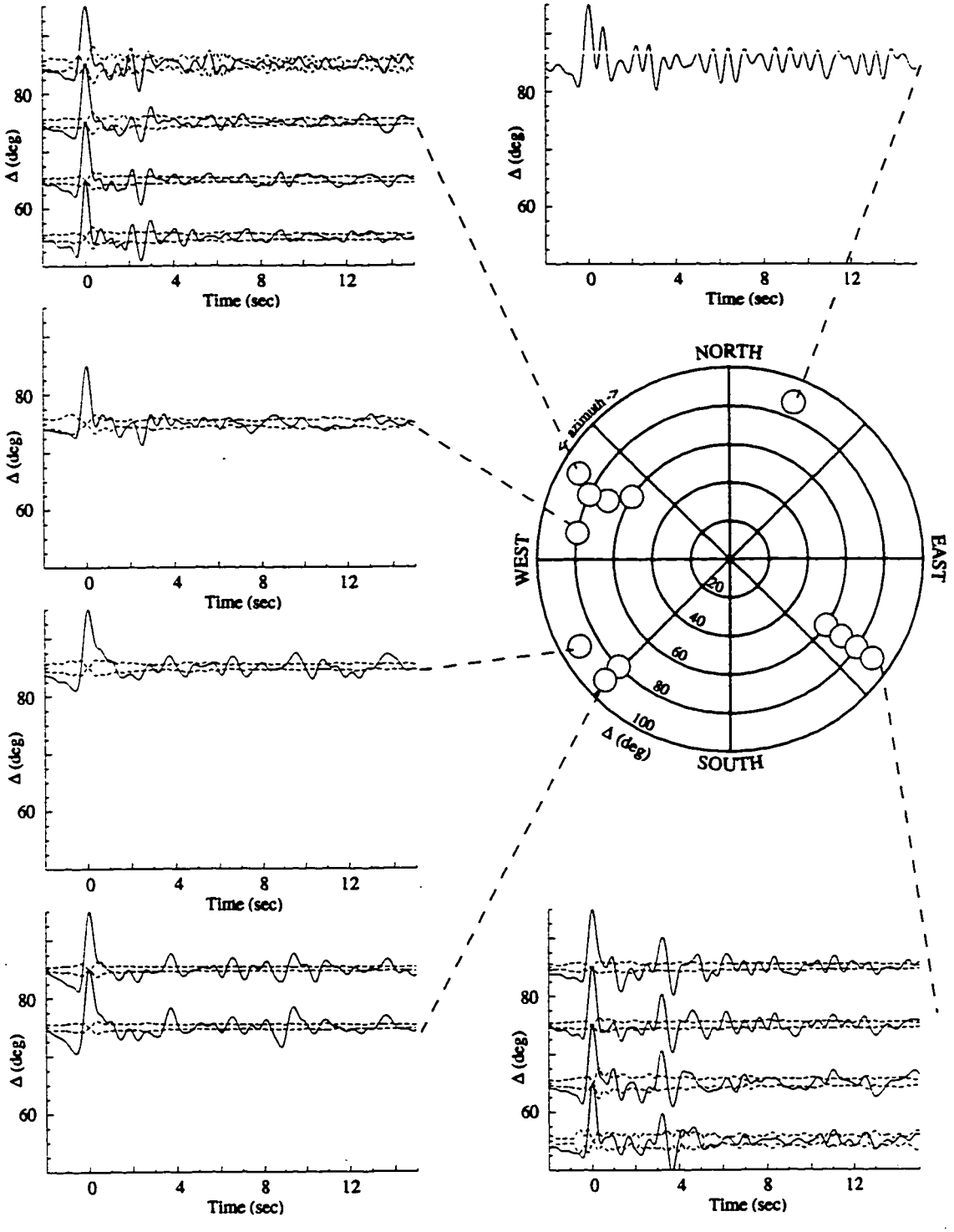

Figure 3.7: Linear stacked deconvolved seismograms for station MBW with stacks (solid lines) and $\pm 2\sigma$ error bounds (dashed lines).

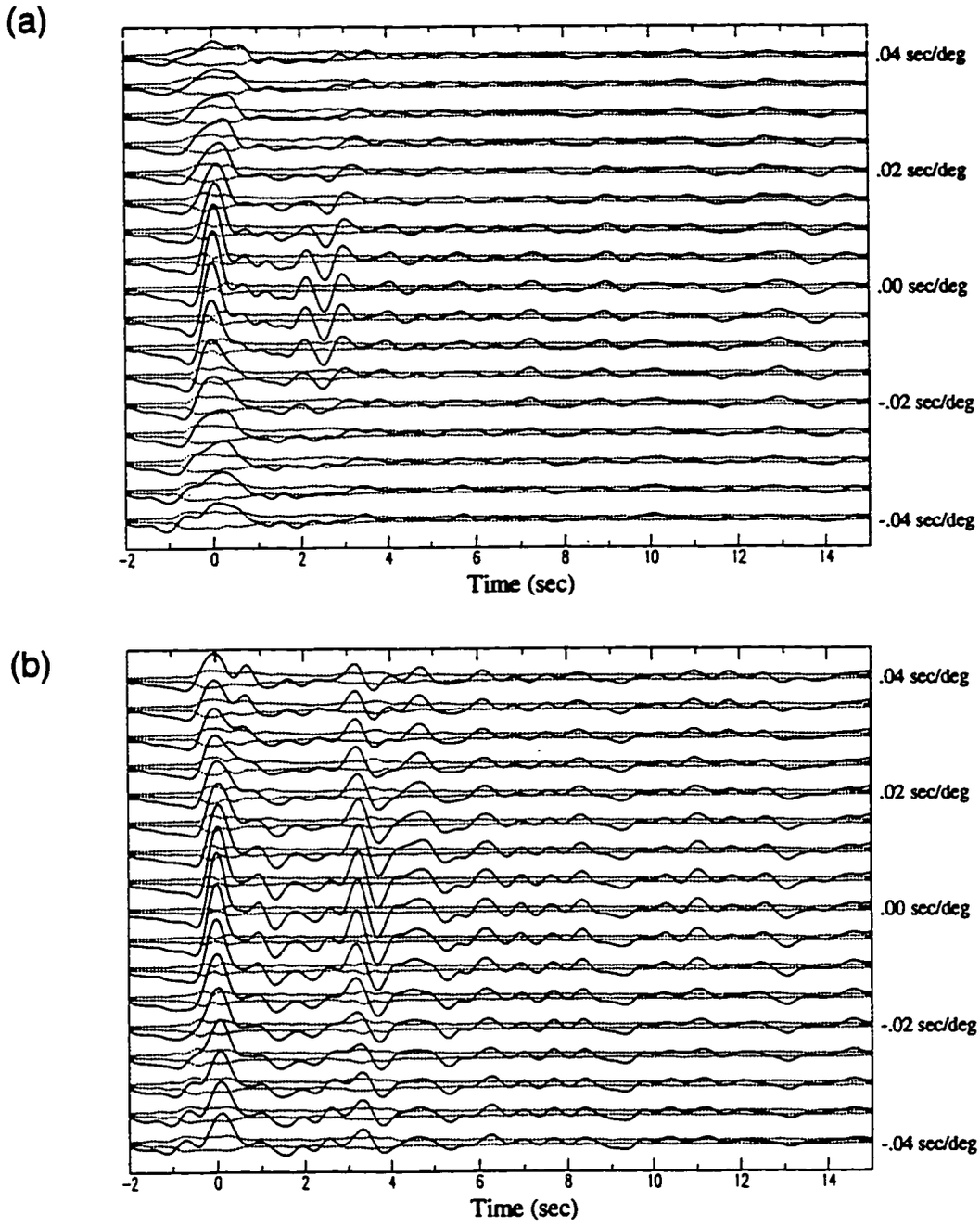

Figure 3.8: Linear slant stacked data for station MBW of (a) NW data and (b) SE data showing stacks (solid lines) and $\pm 2\sigma$ error bounds (dashed lines). Optimal phase enhancement is achieved for a small range of moveouts for both early and later arriving phases.

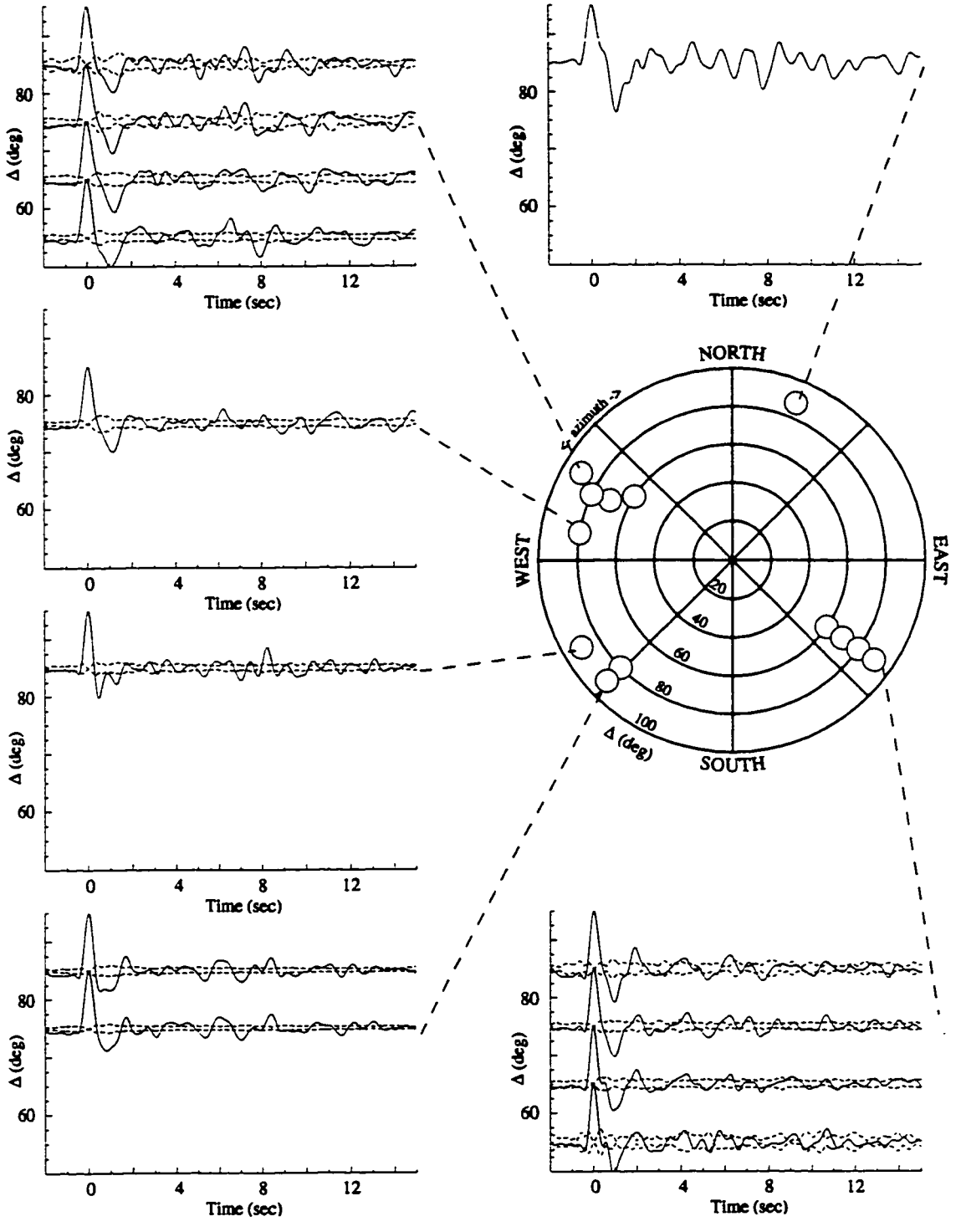

Figure 3.9: Linear stacked deconvolved seismograms for station SPW with stacks (solid lines) and $\pm 2\sigma$ error bounds (dashed lines).

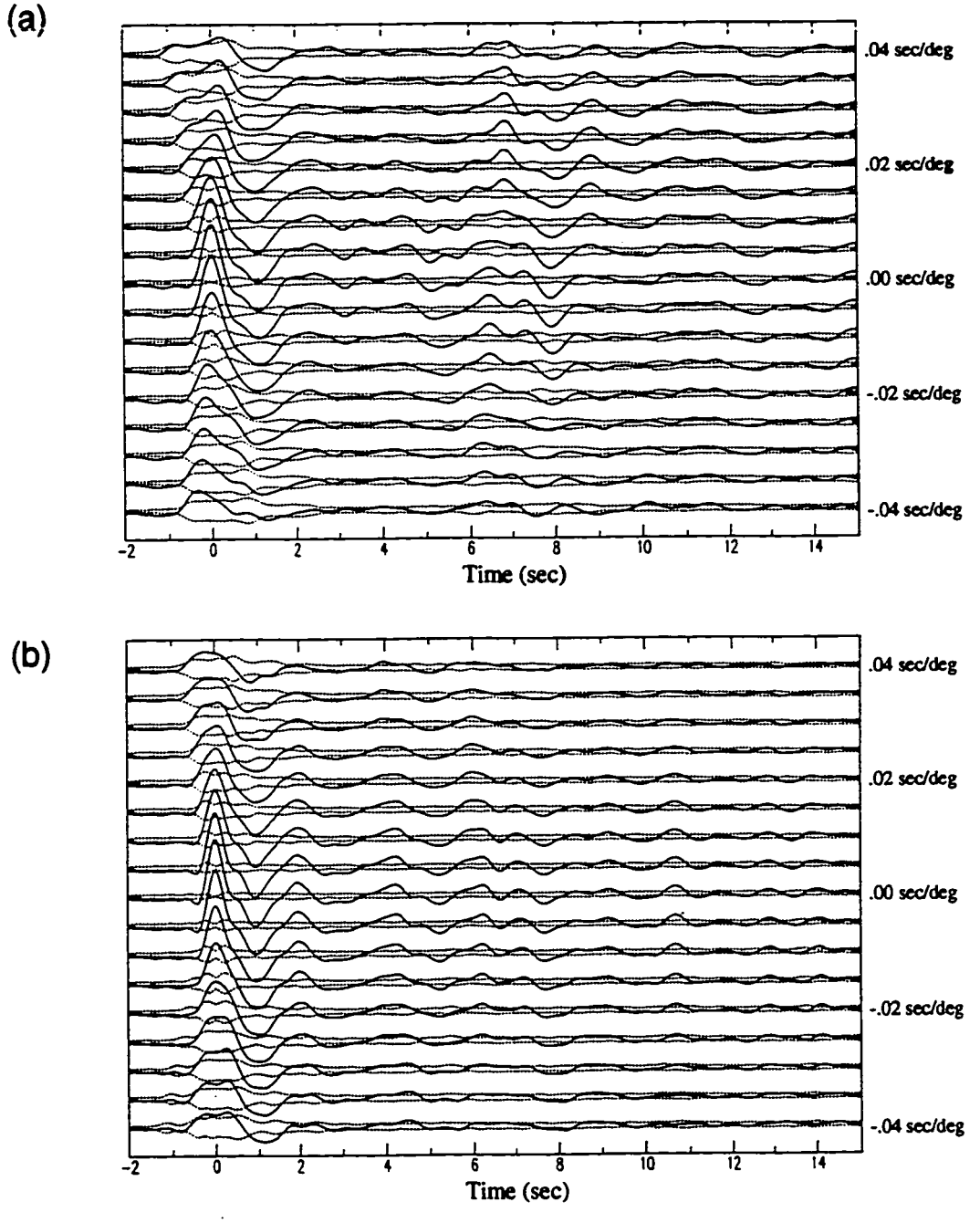

Figure 3.10: Linear slant stacked data for station SPW of (a) NW data and (b) SE data displaying stacks (solid lines) and $\pm 2\sigma$ error bounds (dashed lines). Optimal phase enhancement is achieved for a small range of moveouts for early and later arriving phases.

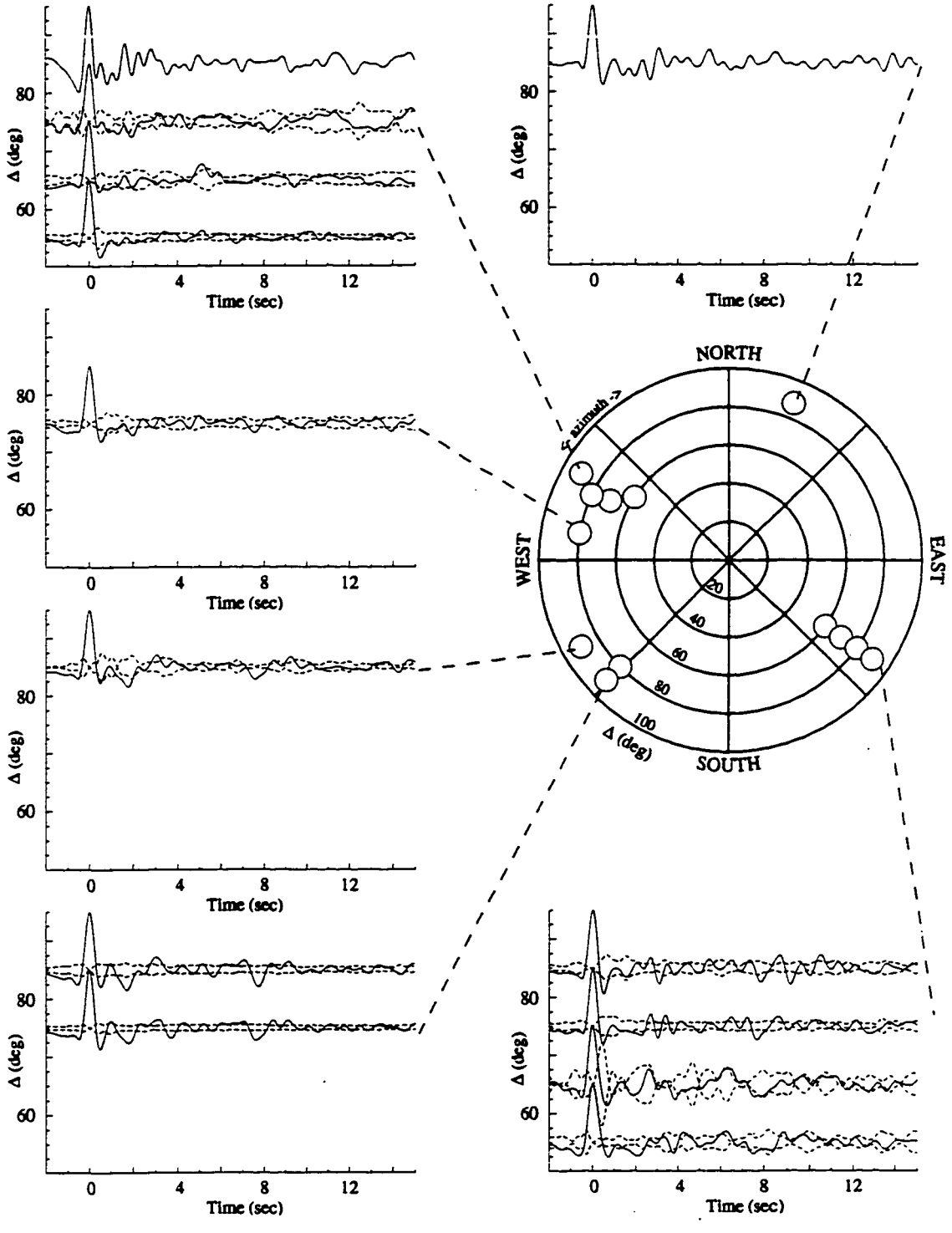

Figure 3.11: Linear stacked deconvolved seismograms for station OBH with stacks (solid lines) and $\pm 2\sigma$ error bounds (dashed lines).

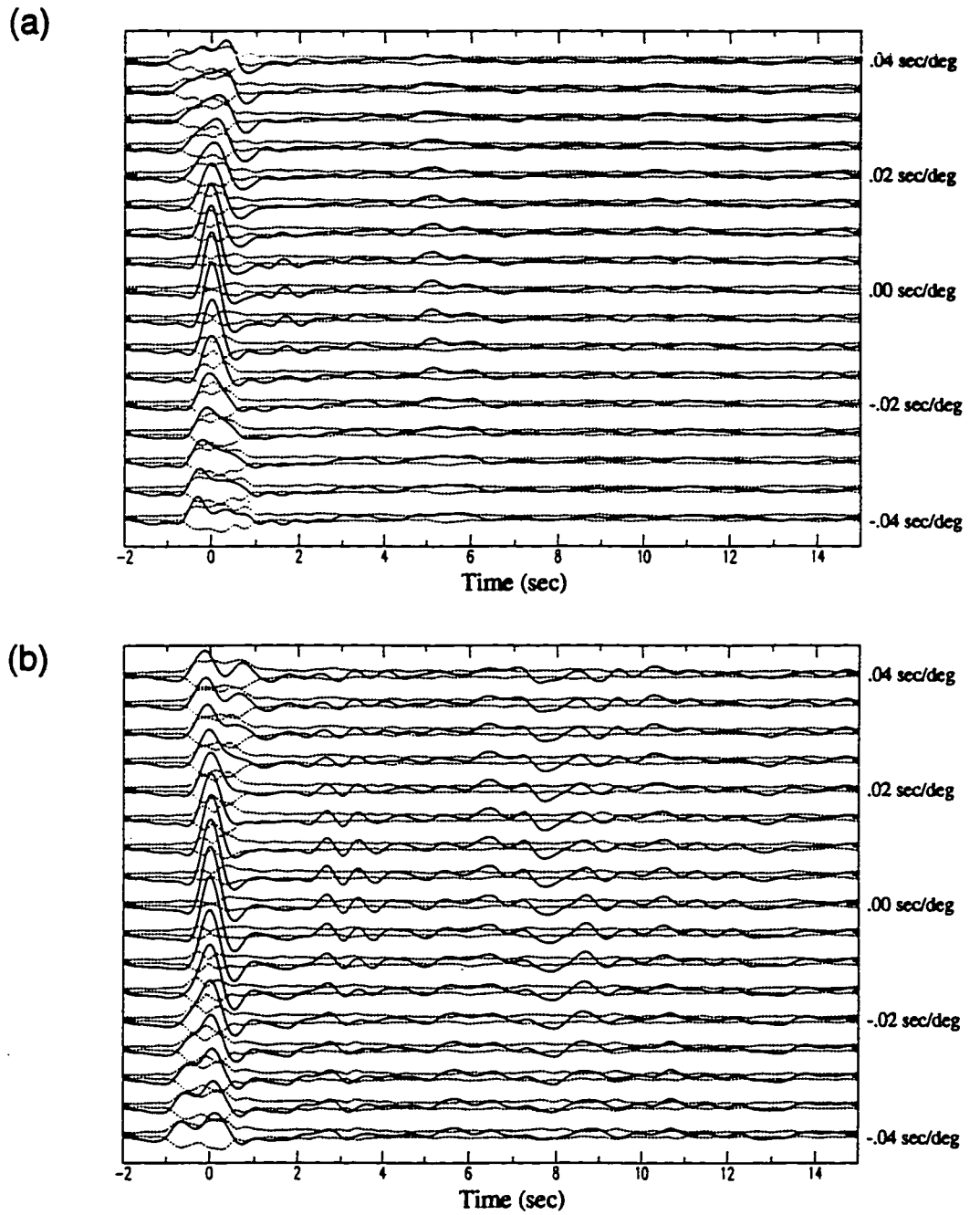

Figure 3.12: Linear slant stacked data for station OBH of (a) NW data and (b) SE data displaying stacks (solid lines) and $\pm 2\sigma$ error bounds (dashed lines). Optimal phase enhancement is achieved for a small range of moveouts for arrivals near 8.0 sec in the SE data.

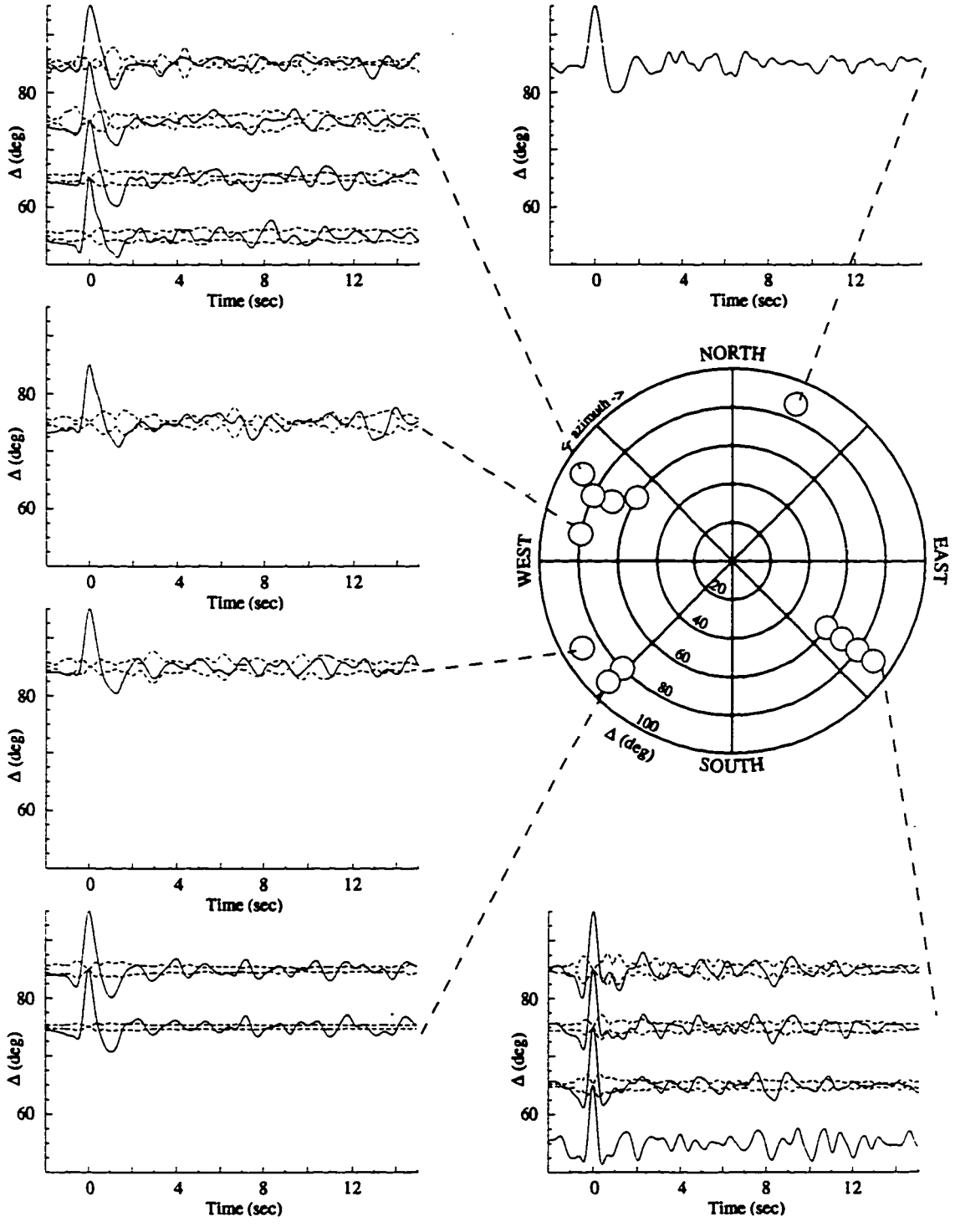

Figure 3.13: Linear stacked deconvolved seismograms for station OFK with stacks (solid lines) and $\pm 2\sigma$ error bounds (dashed lines).

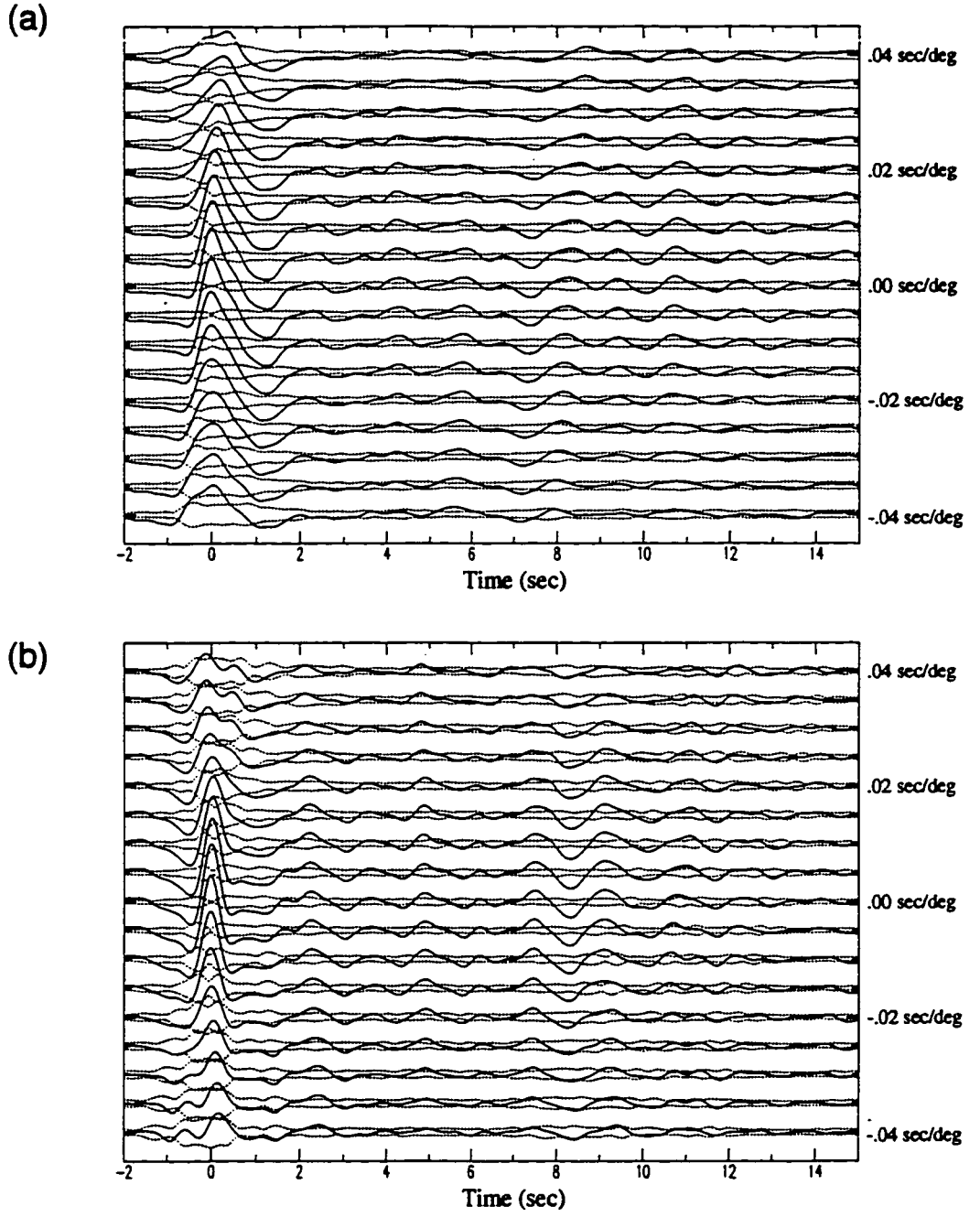

Figure 3.14: Linear slant stacked data for station OFK of (a) NW data and (b) SE data displaying stacks (solid lines) and $\pm 2\sigma$ error bounds (dashed lines). Optimal phase enhancement is achieved for a small range of moveouts for both early and later arriving phases around 8.0 sec.

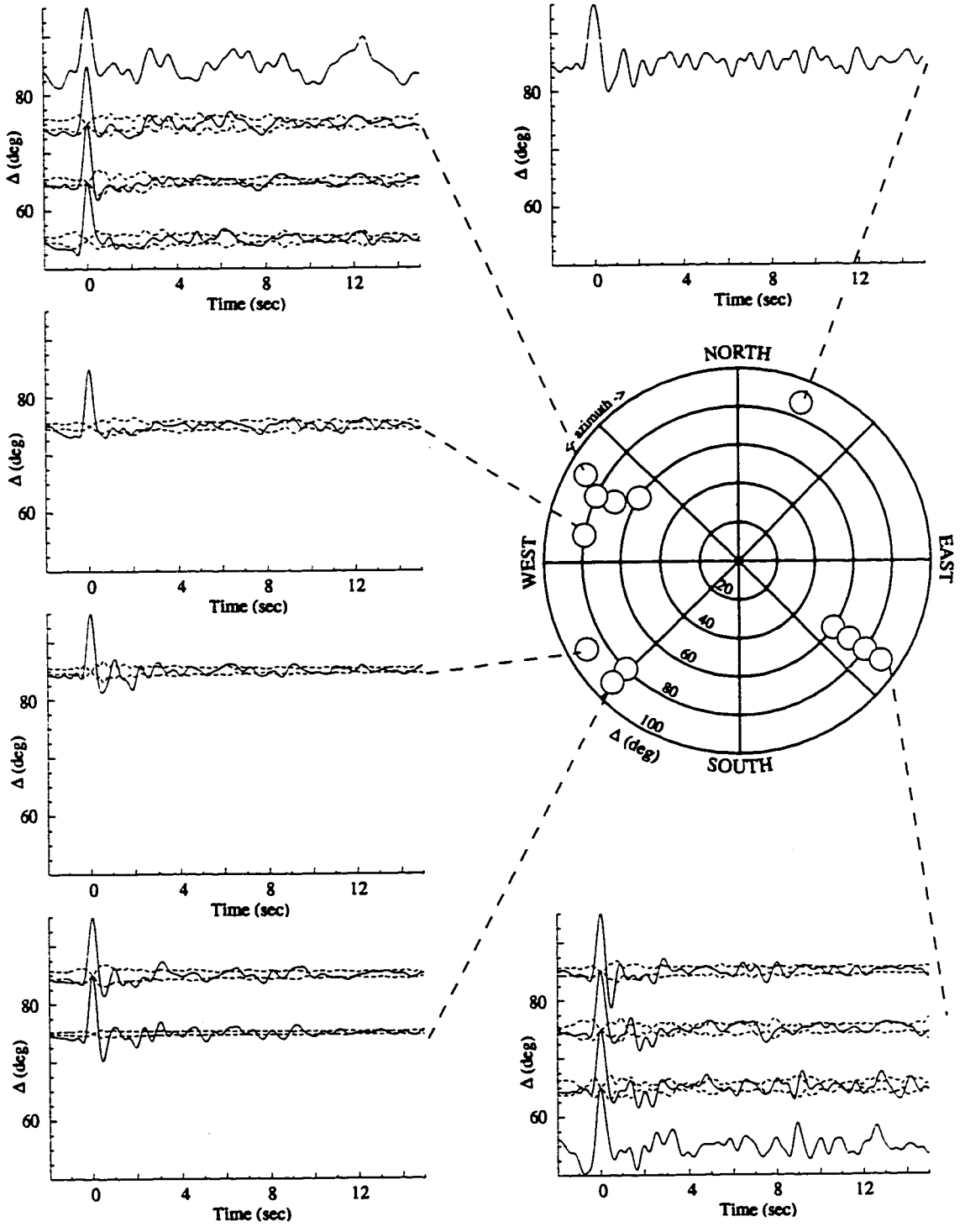

Figure 3.15: Linear stacked deconvolved seismograms for station OOW with stacks (solid lines) and $\pm 2\sigma$ error bounds (dashed lines).

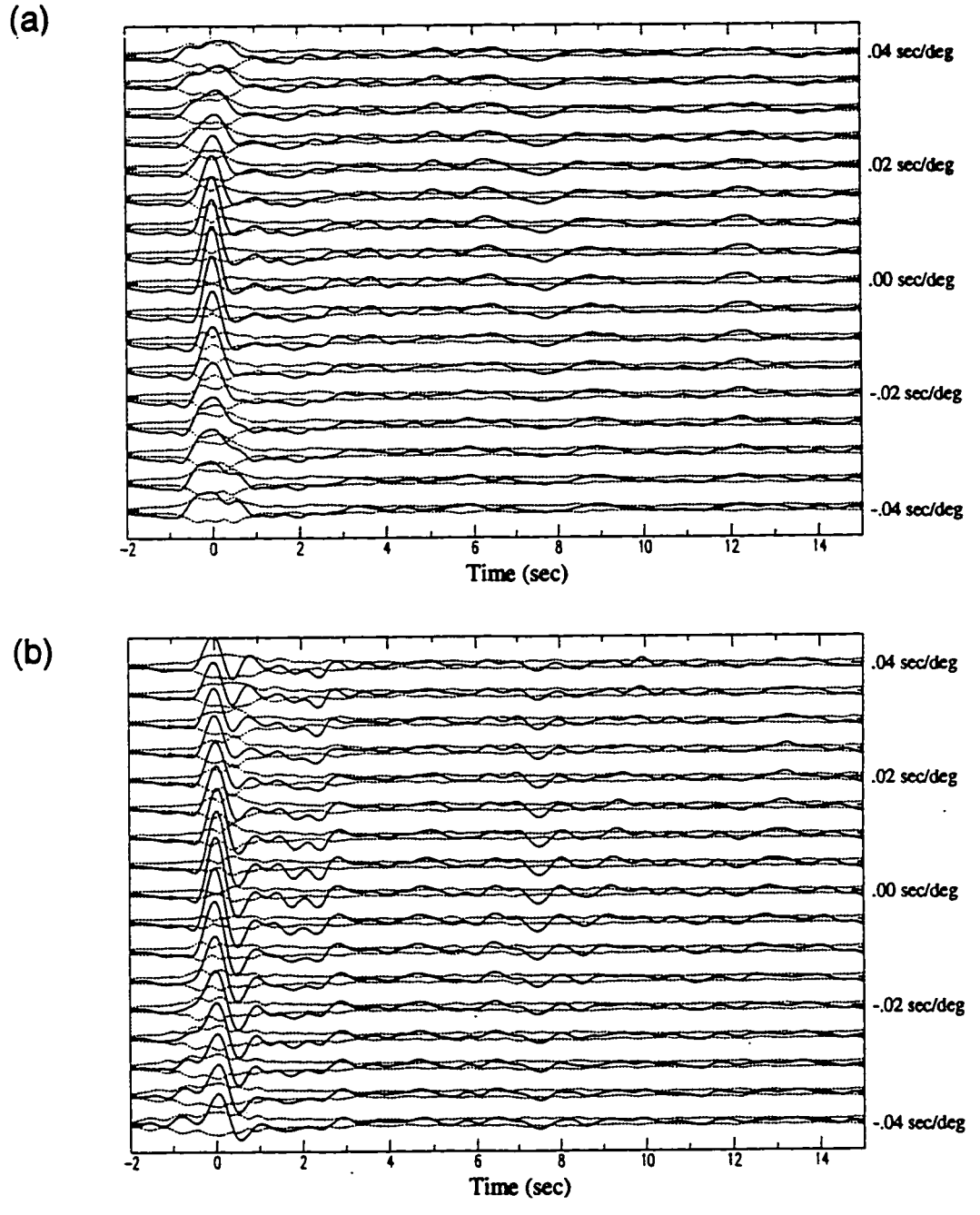

Figure 3.16: Linear slant stacked data for station OOW of (a) NW data and (b) SE data displaying stacks (solid lines) and $\pm 2\sigma$ error bounds (dashed lines). Optimal phase enhancement is achieved for a small range of moveouts for later arriving phases near 7.0-8.0 sec.

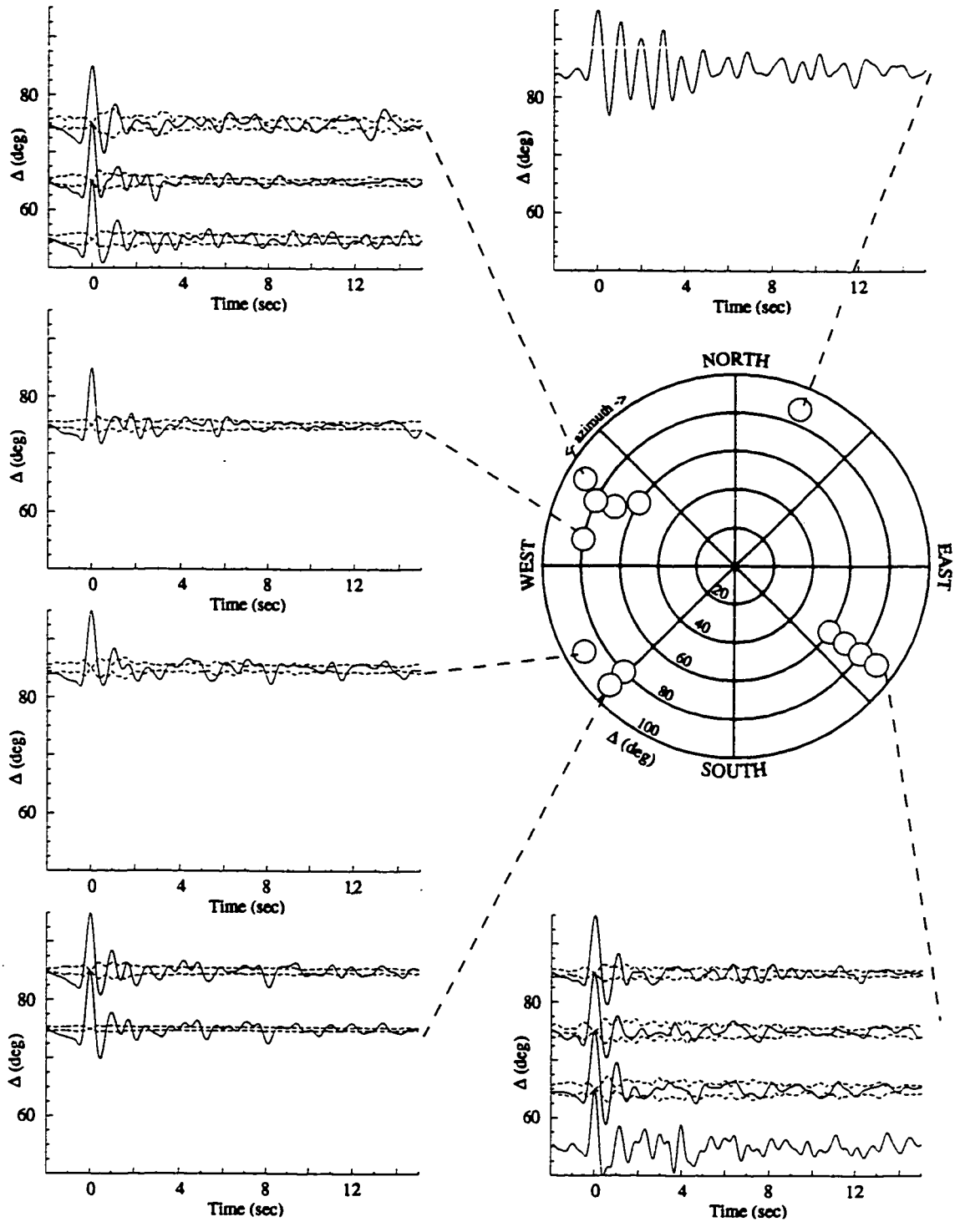

Figure 3.17: Linear stacked deconvolved seismograms for station OSD with stacks (solid lines) and $\pm 2\sigma$ error bounds (dashed lines).

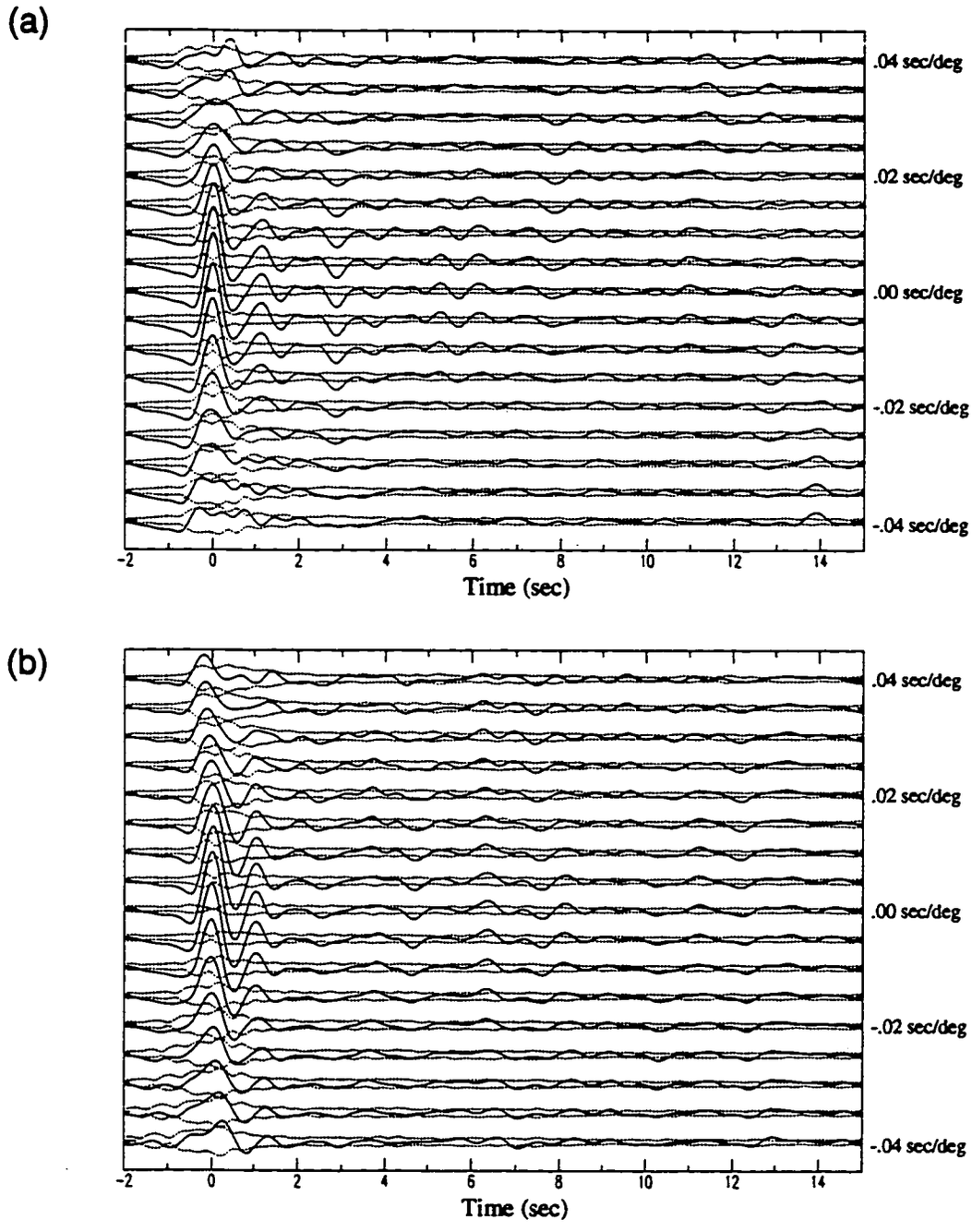

Figure 3.18: Linear slant stacked data for station OSD of (a) NW data and (b) SE data displaying stacks (solid lines) and $\pm 2\sigma$ error bounds (dashed lines). Optimal phase enhancement is achieved for a small range of moveouts for later arriving phases near 8.0 sec.

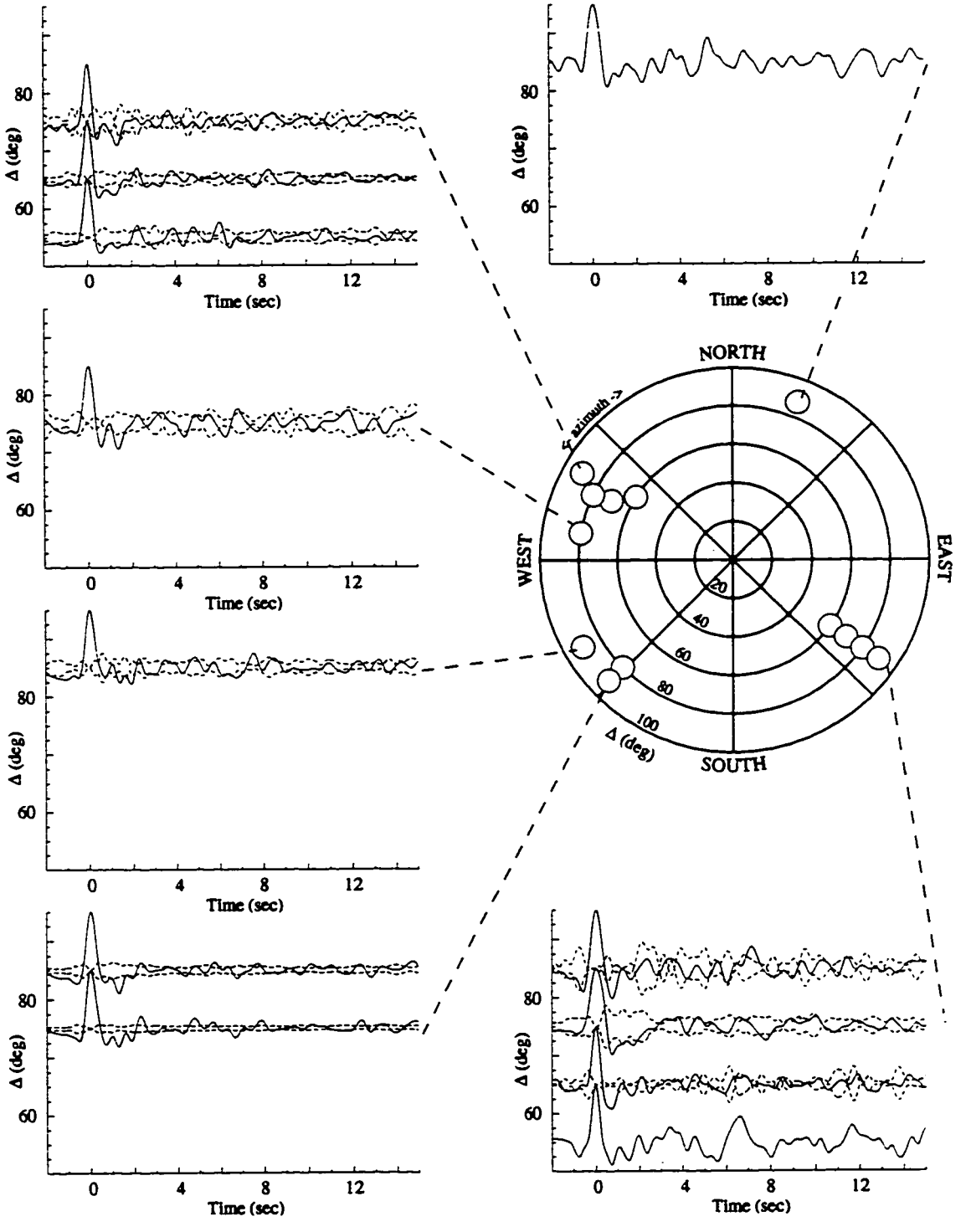

Figure 3.19: Linear stacked deconvolved seismograms for station OTR with stacks (solid lines) and $\pm 2\sigma$ error bounds (dashed lines).

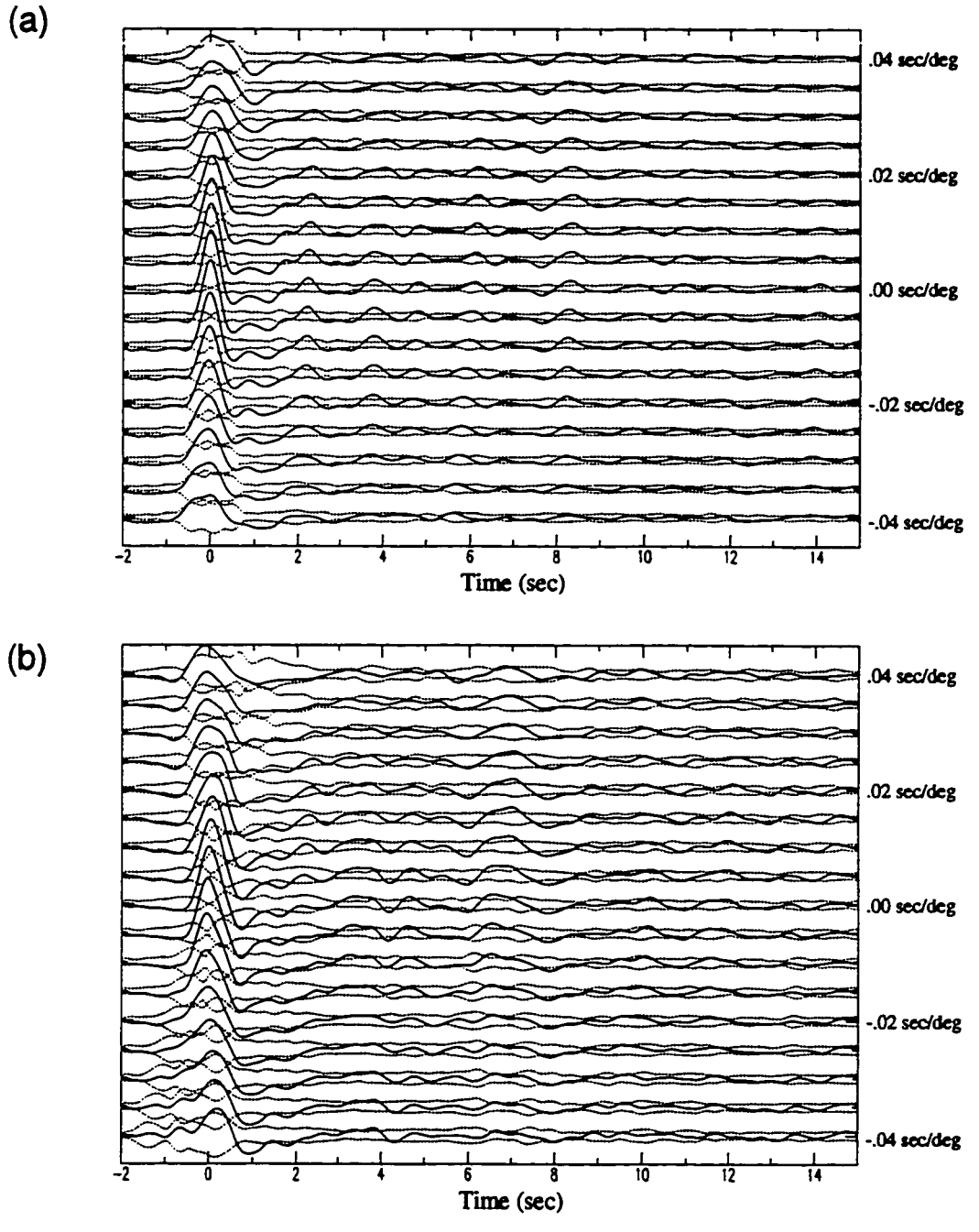

Figure 3.20: Linear slant stacked data for station OTR of (a) NW data and (b) SE data displaying stacks (solid lines) and $\pm 2\sigma$ error bounds (dashed lines). Optimal phase enhancement is achieved for a small range of moveouts for both early and later arriving phases.

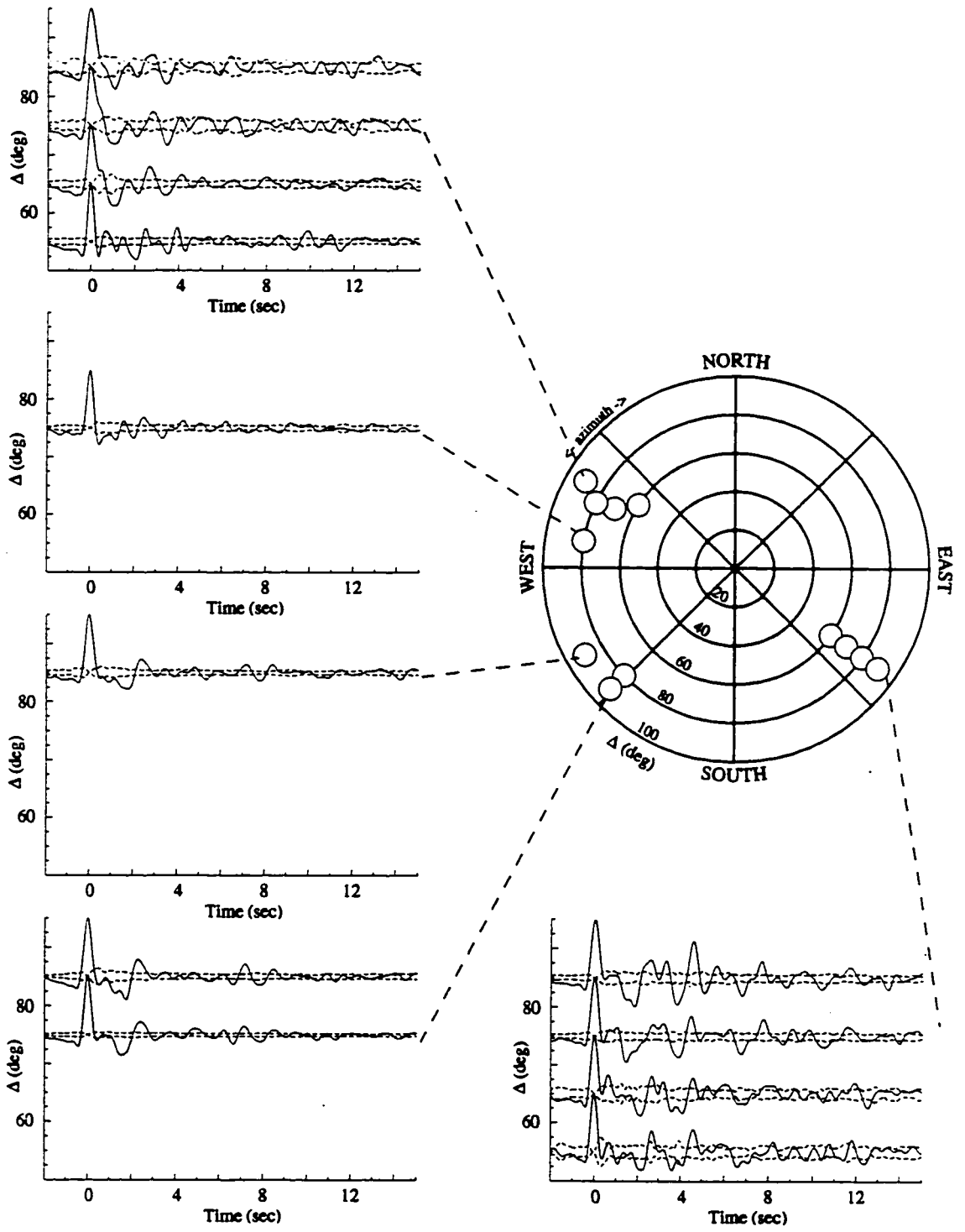

Figure 3.21: Linear stacked deconvolved seismograms for station HDW with stacks (solid lines) and $\pm 2\sigma$ error bounds (dashed lines).

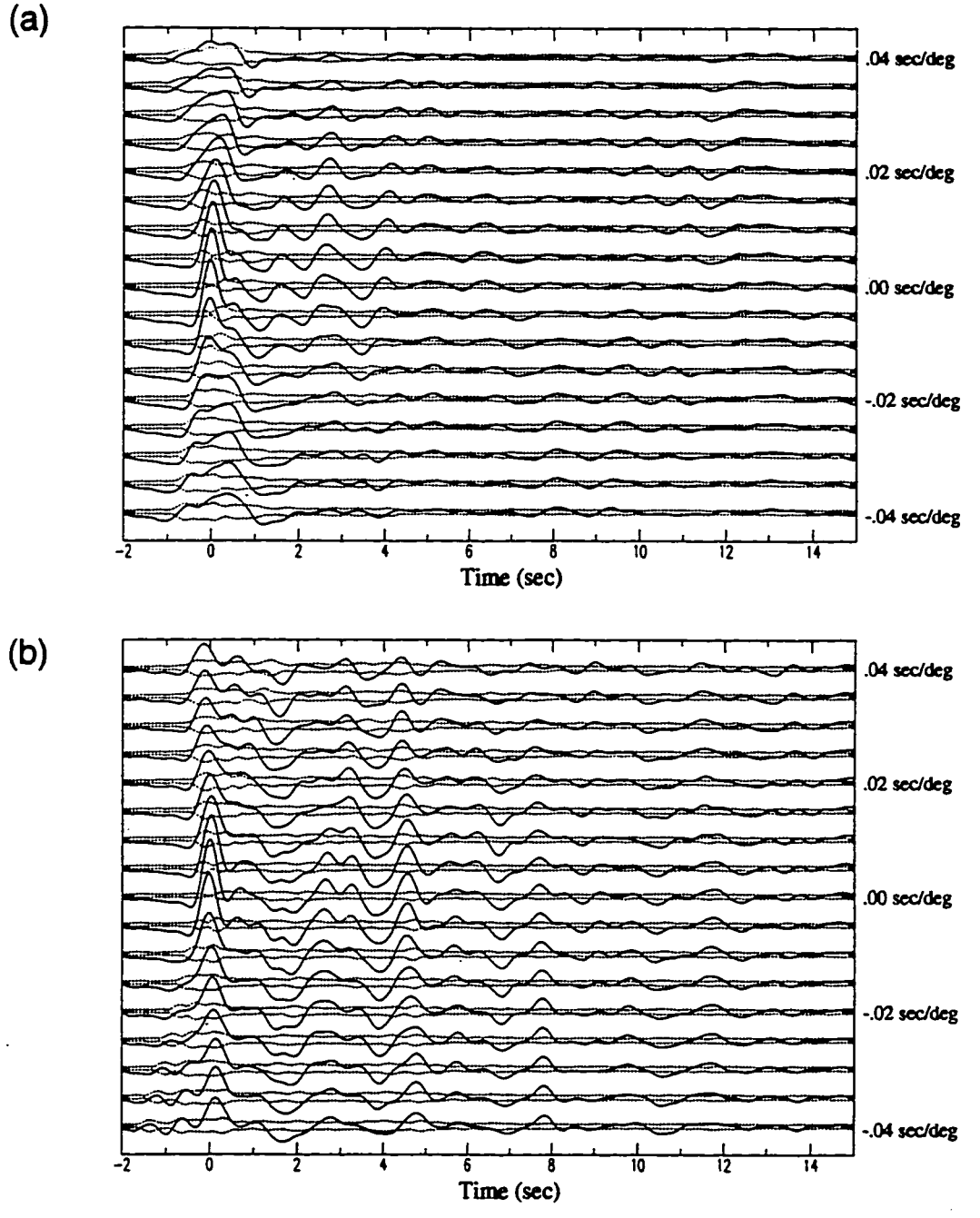

Figure 3.22: Linear slant stacked data for station HDW of (a) NW data and (b) SE data displaying stacks (solid lines) and $\pm 2\sigma$ error bounds (dashed lines). Optimal phase enhancement is achieved for a small range of moveouts for early and later arriving phases.

Chapter 4

Time Domain Forward Modeling

4.1 Introduction

As noted in the previous chapter, much of the stacked, deconvolved seismograms from individual PNSN stations show *P*-coda phases which correlate from event to event and add coherently within given distance and back azimuth ranges. In this chapter, we model the stacked waveforms for a select number of PNSN stations that exhibit *P*-coda phases which persist over much of the distance and back azimuth ranges present in the data set. Forward modeling is performed for 8 stations which contain significant *P*-coda signals above the background noise level. The general aim of the forward modeling is to correctly predict the travel times and amplitudes of the *P*-coda phases (taken with respect to the direct-*P* arrival), including modeling arrival time, amplitude, and pulse shape variations with back azimuth (BAZ) and distance (Δ) or ray parameter. Two fundamental assumptions are made about the nature of the *P* waveforms considered in this study. First, the *P* waveform of each teleseism is assumed to result from the interaction of plane *P* waves incident beneath the PNSN. Second, the major energy contributors to the *P*-coda of the vertical component seismograms are assumed to consist of first order reflected and converted body waves (see Figure 4.1).

The forward modeling methods considered in the following sections provide approximate solutions to the wave equation in two or three dimensions based on ray-theoretical solutions. As a result, these methods are limited in their ability to produce complete waveforms for all types of motion under all geometrical constraints of the velocity structure. However, the first limitation is not of serious consequence as the aim of our waveform modeling is predicting travel times and amplitudes of body waves, which is well within the limitation of a ray-theoretical solution. The second limitation can be avoided either by only allowing for simple model geometries, or by modifying the modeling procedure to correctly handle geometries where the ray-theoretical solutions fail (e.g., caustics and diffractions). More exact wave propagation synthetic seismogram techniques, such as finite element, finite difference, and reflectivity methods, could be used in modeling our data. However, these methods involve numerical solutions which quickly become prohibitive in required run time and storage costs, especially when complex models are considered. In addition, these more exact/complete methods may also be severely limited in the amount of allowable model complexity. The reflectivity method [*Fuchs and Müller* 1971] is an example, where the model parameterization allows

for only flat, homogeneous layers.

Two different methods are used for forward modeling. Each is discussed in detail below. The need for the second forward modeling method arises due to the inability of the first method (with a simplistic velocity model parameterization that includes planar interfaces and homogenous layers) to adequately reproduce observed waveforms for some of the stations considered.

4.2 Forward Modeling: Ray3d

The first forward modeling method considered here is a modified version of the code developed by T. J. Owens [*Owens* 1984] to generate 3-component synthetics for modeling of radial and tangential receiver functions. The code, *ray3d*, employs a fast 3-D ray tracing scheme using geometrical ray theory to generate travel times and amplitudes for the direct-*P* and all first order multiple reflections and conversions. *Ray3d* follows the technique of *Langston* [1977] who investigated the effects of near-source and near-receiver dipping layers on the *P*-wave response of teleseisms. *Langston* [1977] justified the fast 3-D ray tracing procedure by considering analytical first-motion ray solutions produced by *Langston and Helmberger* [1975] for the far-field response of a point dislocation in a horizontally oriented medium. *Langston* [1977] showed that a first-motion approximation to the *Langston and Helmberger* [1975] integral can be made if the source-receiver distance is sufficiently great such that variations in the geometrical ray parameter are small relative to the source time duration. If so, the far-field response can be calculated as if the waves were plane waves. This allows for simple geometrical ray tracing (the first term of asymptotic ray theory) to determine travel times for a given phase. Individual phase displacement amplitudes are determined from reflection and transmission coefficients, which if post-critical can produce a phase shift of $\phi \leq \pi/2$ for a given interaction, plus geometrical spreading (using simple energy flux arguments). We note that the large source-receiver distances inherent in this study ($40^\circ \leq \Delta \leq 95^\circ$) allow for the incident plane wave assumption to be made according to the *Langston* [1977] criterion. Figure 4.1 shows an example velocity model with schematic ray paths for all rays traced by *ray3d*. The ray naming convention is that of *Båth and Steffánsson* [1966]. For the simple flat layer over a half-space model shown in Figure 4.1, the differential travel time between *PpPmp* and *Pp* can be expressed as:

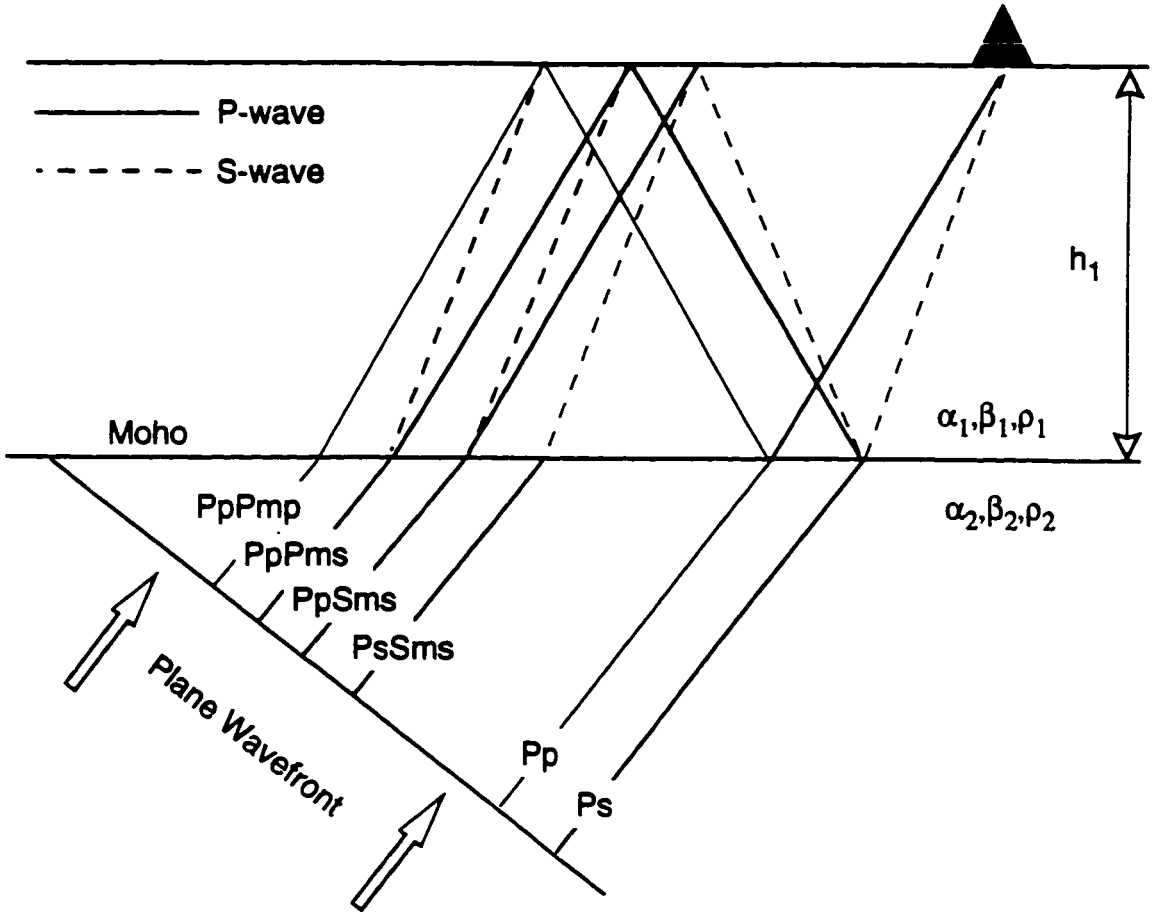

Figure 4.1: Schematic ray diagram showing ray paths for direct and selected first order secondary arrivals for a plane *P*-wave incident beneath a homogeneous planar crustal layer. Ps = P-S converted phase at moho, PpPmp = first order reflection between free surface and moho, etc.

$$T_{PpPmp} - T_{Pp} = \frac{2z}{\alpha_i}\sqrt{(1-\alpha_i^2 p^2)} \qquad (4.1)$$

where α_i is the layer *P* velocity, *z* is the depth to the layer bottom, and *p* is the ray parameter of the incident *P* wave. Note the inherent trade-off between *z* and α_i in equation 4.1. This trade-off can result in a family of models that may reproduce the observed differential travel times. However, the simultaneous modeling of phase amplitudes can reduce the number of acceptable models determined from the travel time data alone by indicating appropriate interface impedance contrasts.

The simplicity of this geometrical ray tracing method allows for rapid synthetic generation, but this comes at the expense of a simplified model parameterization. The inherent limitations of *ray3d* include: (*i*) homogeneous layer velocities, (*ii*) planar interfaces, and (*iii*) certain dipping layer configurations which produce pinch out problems. The planar interface assumption must be considered carefully, especially when considering multiple bounce phases, within the context of lateral sampling of the rays. For the example velocity model of Figure 4.1, we consider the lateral sampling of *Pp* and *PpPmp* for flat and 10° dipping interface cases using a source-receiver distance of 85°, an interface depth of 45 km, layer velocity of 6.1 km/sec, and half-space velocity 8.0 km/sec. The results are shown in Figure 4.2a for each case. For the flat layer case, the lateral sampling has no azimuthal variation so that each of the two phases plot as a circles. The lateral sampling is 12 km for *Pp* and 38 km for *PpPmp*. The dipping layer case shows a skewing to smaller values for the up dip case (10.5 km and 15 km) and larger values for the down dip case (14.5 km and 58 km). Schematics of the ray geometries for both the up-dip and down-dip cases are shown in Figure 4.2b. The lateral sampling of the *PpPmp* phase for both flat and dipping interface models is on the order of the interface depth. For less distant events, the incident angle will be larger, and the lateral sampling increases to more than 1.5 times the interface depth. For waveforms with frequencies on the order of 1.0 Hz, the above lateral sampling of *PpPmp* will be on the order of 3-10 wavelengths. Care then must be taken to assess the validity of the planar interface assumption before blindly applying this modeling technique to any data.

Despite the above limitations, the *ray3d* waveform modeling method is an effective tool for investigating large numbers of models, when relatively simple seismic waveforms

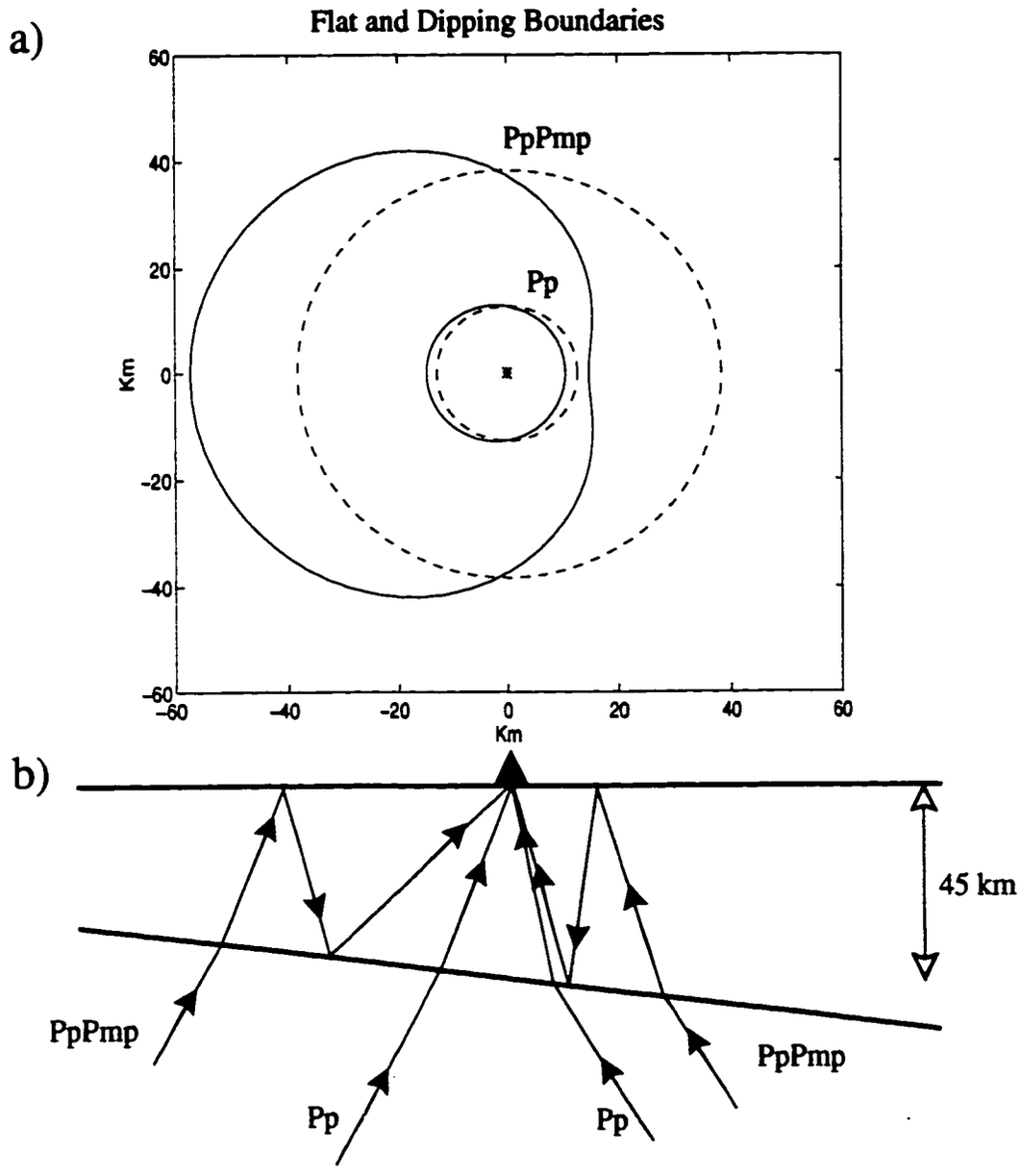

Figure 4.2: (a) Examples of lateral sampling by the direct-*P* and *P*-multiple reflected rays for both a flat (dashed) and dipping (solid) layer interface. (b) Schematic ray diagram with up dip and down dip propagating rays for the dipping layered model used in (a). The interface depth for the models is 45 km, with a source-receiver distance of 85 deg.

are involved. Many investigators [e.g., *Owens et al.* 1988, *Owens and Crosson* 1988, *Lapp et al.* 1990, *Edlund* 1991, *Cassidy and Ellis* 1991] have successfully used this forward modeling procedure to explain azimuthal variations of *Ps* converted phases in broadband radial- and transverse-component teleseismic receiver functions using dipping crustal and/or upper mantle interfaces for stations deployed in western Washington and southern British Columbia.

The model parameterization in *ray3d* is such that each of the i layers is specified by 6 quantities: α_i, β_i, ρ_i, h_i, S_i, and D_i. These represent the *P*-wave velocity, *S*-wave velocity, density, thickness, strike and dip of the ith layer. For an N layer model (including the half-space), there are a total of $6N$-3 free parameters. In practice, the number of free parameters for *ray3d* models considered in this study is on the order $5N$, as a Poisson's ratio of 0.25 (ie., $\alpha_i/\beta_i = \sqrt{3}$) is assumed throughout the forward modeling. Some parameters, such as α_i for certain layers, are assumed to be previously well-constrained. These include upper mantle velocities of 7.7-8.0 km/sec (as determined by previous investigators). Two additional free parameters enter the problem when computing the corresponding non-spike series synthetics for a given model: the source wavelet shape and duration. Each can be reasonably constrained by modeling the shape and duration of the direct-*P* arrivals of the observed waveform data.

4.3 Forward Modeling: Raytopo

The structural limitations associated with the previous simple forward modeling procedure, most notably the assumption of planar interfaces, require an alternative that allows for interface irregularities as well as other complexities. With such an alternative method, models can be investigated where (*i*) the data cannot be reasonably modeled with planar interfaces, (*ii*) the planar interface assumption is highly questionable, or (*iii*) *a priori* evidence suggests that greater structural complexity is required. The existence of interface irregularities, as simple as a step or ramp, can produce variations in phase amplitudes and travel times (as functions of Δ and BAZ) sufficient to explain those observed in the data. Figure 4.3a shows an example of a incident plane *P*-wave beneath an interface with a ramp, taken from *Landers* [1974]. The rays are scattered in the vicinity of the ramp, producing a shadow zone at the ramp "knee" and an interference (focused) zone at the ramp "toe". Figure 4.3b shows the corresponding wave field with the two planar

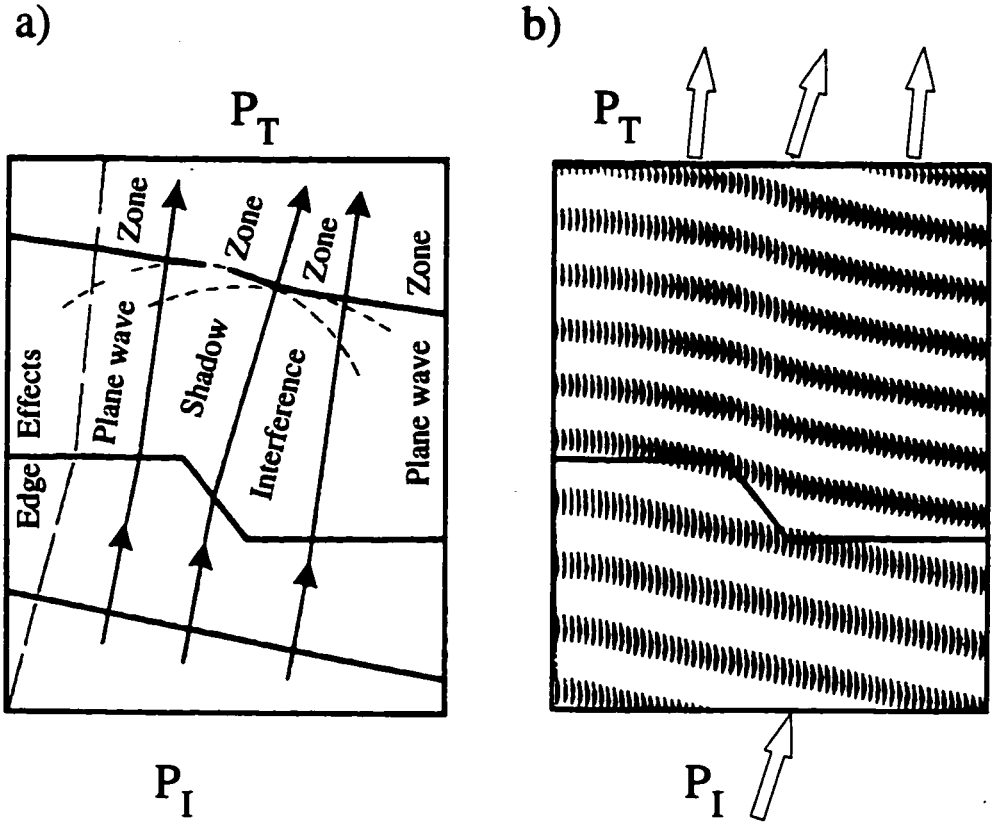

Figure 4.3: (a) Non-normal incident plane *P*-wave scattered by a stepped 2-layer velocity model showing amplitude and travel time variation, and (b) the wave front interpretation of the scattered wave field. Modified from Landers [1974].

branches displaced by the differential travel time related to the ramp height and connected by a smooth transition. Amplitude variations along the wave front are more perceptible in the shadow zone, although amplitudes are increased in the interference zone.

Applied to our problem of modeling differential phase amplitudes and arrival times, we can consider more complex models (like that in Figure 4.3) containing interface structure with wavelengths less than the differential lateral sampling of the phases involved (e.g., *Pp* and *PpPmp*). With this type of parameterization, certain model and ray geometries allow for one phase type to sample the region of the model with the interface irregularity producing ray focusing or scattering, while the others do not. In this fashion, synthetics can be generated that contain greater variations in relative phase amplitudes and arrival times than is possible using models with planar interfaces.

The second forward modeling procedure considered (referred to as *raytopo*) is designed as an extension of the *ray3d* method that provides more complex model parameterization, allowing for non-planar interfaces and heterogeneous layer velocities. Maintaining the *ray3d* assumption of incident plane waves, *raytopo* employs a numerical approximation to construct a plane wave front from individual point sources using Huygen's principle. Rays are shot at take-off angles given by $\sin^{-1}(p\alpha_i)$ from each of the uniformly spaced point sources towards the surface. For a receiver at a specific surface location, x_0, the phase arrival time is determined from those rays which emerge in the vicinity of the receiver. The final travel time is a weighted mean, determined using a weighting window centered at x_0. The window width, w, is dependent to some degree on the point source spacing, d_s, along the incident plane wave front. For most situations, setting $w \geq d_s$ insures that an adequate number of emergent rays fall within the weighting window. The type of window selected is not critical; any bell-shaped function (like a gaussian function) with short tails will produce similar results. In turn, d_s is dependent on the wavelength of the interface irregularity, λ_{int}. To be adequately sampled by the propagating wave, d_s must be less than λ_{int} such that some minimum number of rays traverse the interface irregularity. Testing shows a minimum of 10-20 rays appears sufficient. Figure 4.4 shows a schematic of the construction of an incident plane wave (*PpP*$_l$*p* phase) propagating through a single layer over a half-space model with a ramped interface. Individual point source spacing, d_s is sufficiently dense to sample the interface at the ramp structure of wavelength λ_{int} and produce ray focusing and scattering at the surface. The weighting function (a gaussian function) used to determine travel times and

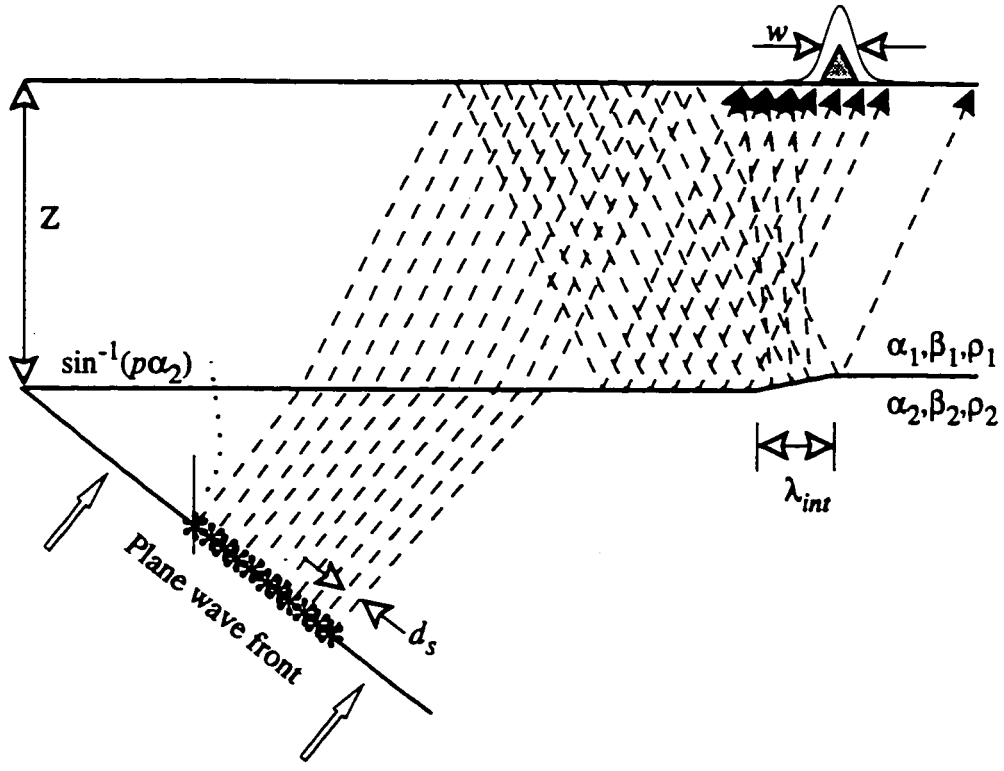

Figure 4.4: Schematic of a velocity model with interface topography showing the construction of an incident plane wave using a set of uniformly spaced point sources with the same take-off angle. Rays shown are for the *PpP1p* phase. Phase travel times and amplitudes are obtained from all rays which emerge at the surface within a certain distance of the recording station, as determined by the weighting window of width *w*. Note the occurrence of both a shadow zone just right of the station and an interference zone to the left of the station. Neither effect is evident if the topography wavelength is less than the point source spacing.

amplitudes for seismograms at given receiver locations is also shown. An implication of using a windowing function to determine travel times is the ability to approximately trace phases into diffraction zones.

The amplitude determination employed with *raytopo* is analogous to the determination of amplitudes using Disk-Ray Theory (DRT) [*Wiggins and Madrid* 1974, *Wiggins* 1976]. The DRT model of wave propagation associates a planar disk of energy (rather than a ray tube) oriented perpendicular to the ray that propagates along the ray path. The superposition of these disks at any time represents a wave front. Each disk intersects the surface and affects an area surrounding the point of emergence. The amplitude response at distance x_0 is determined by summing the effects of each ray's disk where it intersects that distance. Like *Chiang and Braile* [1984], we apply a distance weighting function at x_0 to prevent strong arrivals from large distances from contributing anomalous amplitudes to the seismogram at x_0. As with the travel time determination, this amplitude determination permits amplitudes of phases propagating in the vicinity of a shadow zone and/or caustic to be reasonably approximated. The incident wave front is planar and has a given surface ray (energy) density. The wave front propagates though a model with planar interfaces and emerges at the surface with the same surface area but with a different surface ray density. This is due to velocity variations along the ray paths. The amplitude associated with any given ray in the plane wave front is then given by the product of: (*i*) the reflection and transmission coefficients associated with each interface encountered, (*ii*) the surface conversion coefficient for a vertical-component receiver, and (*iii*) the ratio of the ray density at the receiver and incident wave front. Figure 4.5(a-c) gives a summary of the synthetic construction for a 2-layer irregular interface model, for a event at a distance of 85°, using just the *Pp* and PpP_1p phases. Rays shot from individual point sources along the incident wave front are shown in Figure 4.5a. The corresponding travel times for each point source are plotted for each phase in Figure 4.5b to clearly demonstrate the shadow and interference zones created by the interface topography. Note that these zones occur at different offset distances for each phase. Figure 4.5c shows the resulting synthetics constructed from the travel times and amplitudes associated with each ray emerging in the vicinity using a gaussian weighting function centered at the receiver offset distance. Each seismogram is normalized to a direct arrival amplitude of unity and convolved with a simple source wavelet. The variations in PpP_1p amplitude with offset are clearly observable in the record section of Figure 4.5c.

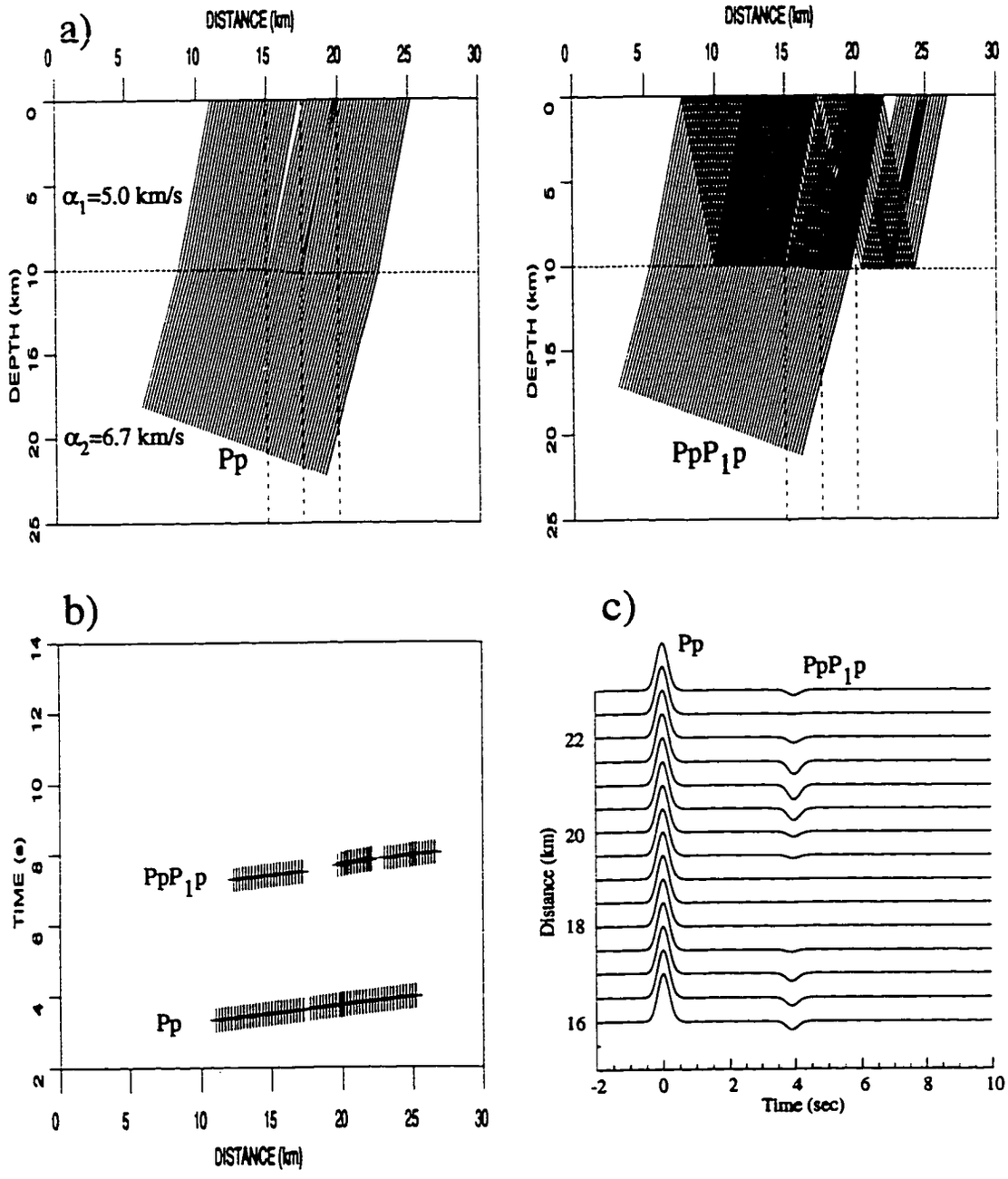

Figure 4.5: (a) A 2-layer model containing a ramped interface with an aspect ratio 1:10. Rays are traced for *Pp* and *PpP1p* for an event 85 deg away. Note that the interface topography produces surface shadow and interference zones at different offsets for each phase. (b) Corresponding travel times for each point source composing the incident plane wave are plotted unreduced to show the effect more clearly for *PpP1p*. (c) Synthetics normalized to *Pp* amplitude showing amplitude variation with offset.

To produce synthetics for models with interface irregularities (as seen in Figure 4.5), ray tracing with travel time and simple amplitude determination must be performed from a large number of individual point sources for each phase considered. The forward modeling software of C. A. Zelt [*Zelt and Smith* 1992], *tramp*, was employed for this task. *Tramp* has a layered, variable block size representation of a 2-D velocity model. A given layer is specified by boundary nodes whose position and number are arbitrary, but all layers must cross the model from left to right without crossing neighboring boundaries. A single node then represents a horizontal boundary. Within a given layer, the *P*-velocity is also specified by an arbitrary number of nodes with arbitrary spacing of upper and lower layer velocity points. The complete velocity field within any given layer is then defined such that the velocity ($\alpha_i(x,z)$) varies linearly both horizontally and vertically between the nearest lateral and vertical node points, respectively. Vertical velocity discontinuities are allowed, while lateral discontinuities are not.

Ray tracing in the above parameterized model is performed using zero-order asymptotic ray theory by numerically solving the following ray tracing equations (*Cerveny et al.* [1977]) when ray paths are near-vertical (as is typically the case with this data set):

$$\frac{dx}{dz} = \tan\theta \tag{4.2}$$

$$\frac{d\theta}{dz} = \frac{(v_z \tan\theta - v_x)}{v} \tag{4.3}$$

with initial conditions x_o, z_o, and θ_o. Here θ is the angle between the tangent to the ray and the z-axis, v is the velocity, and v_x and v_z are the partial derivatives of v with respect to x and z. θ_o is the ray take-off angle and the point (x_o, z_o) is the source location. The ray step length, l, used to solve equations (4.2) and (4.3) varies and is adjusted at each point along the ray path by an amount:

$$l = \frac{av}{|v_x| + |v_z|} \tag{4.4}$$

where a is user-specified. Equation (4.4) optimizes the ray step length by adjusting to small steps where the ray bending is large and then to large steps where the ray bending is small. Solving equations (4.2) and (4.3) takes care of the ray paths within a given block, and the application of Snell's law at each interface completes the ray tracing algorithm.

The amplitude is calculated following zero order asymptotic ray theory and follows in the same general sense as *ray3d*. For any given ray, the final complex amplitude is given as the product of the transmission and reflection coefficients with the geometrical spreading. The general amplitude expression takes the form:

$$A = A_0 q / L \tag{4.5}$$

where A_0 is the initial ray amplitude, q accounts for the energy partitioning at each interface, and L is the geometrical spreading. The energy partitioning coefficient, q, is given (as derived by *Cerveny et al.* [1977], equation (2.58)) by:

$$q = \left(\frac{v_0\rho_0}{v_r\rho_r}\right)^{1/2} \prod_{i=1}^{n} \left(\frac{v'_i\rho'_i}{v_i\rho_i}\right)^{1/2} Z_i \tag{4.6}$$

where:

n = number of boundaries each ray encounters,

v_0, ρ_0 = velocity and density at the source,

v_r, ρ_r = velocity and density at the receiver,

v_i, ρ_i = velocity and density at incidence with the ith interface,

v'_i, ρ'_i = velocity and density at emergence with the ith interface, and

Z_i = Zeoppritz (P-SV reflection/transmission) displacement amplitude coefficients at the ith boundary. Added to the Z_i are the surface conversion coefficients of vertical- and horizontal-component receivers. The geometrical spreading term, L, is discussed in detail by *Zelt and Ellis* [1988]. Because of the way in which we have chosen to implement *tramp* to generate the model response to an incident plane wave, we do not to include their geometrical spreading term in our synthetics. As such, we shall omit the details regarding

the definition of *L*.

Since a number of arbitrary types of rays can be traced using *tramp*, including first order reflected and converted rays, this code can be implemented to trace the same ray types as traced using *ray3d*. This allows for verification of modeling results using each procedure for simple model configurations and continuity in the process of model investigation when progressing to more complex models. An example verification of modeling results from *ray3d* and *raytopo* is given in Figures 4.6a-4.6c. The test model considered is a homogeneous planar layer of thickness 10 km over a half-space. The model velocities and densities are given in Figure 4.6d. Synthetics are generated for events at distances of 55°, 65°, 75°, and 85°containing a total of 10 body phases: *Pp*, *Ps* and 8 first-order multiples. Synthetics for 3 versions of the velocity model were tested: (*i*) a flat boundary interface (Figure 4.6a), (*ii*) a 5° dipping interface with waves propagating down dip (Figure 4.6b), and (*iii*) a 5° dipping interface with waves propagating up dip (Figure 4.6c). The comparisons of the resulting waveforms show the two methods produce comparable results (traces nearly overlay one another). For the three model parameterizations compared, the average amplitude variation between the two methods was less than 3%, with a maximum of 8%. Phase arrival times (the time of the maximum phase amplitude) differed by at most one sample interval, 0.04 sec. This probably reflects differences in the source wavelet convolution procedures; *ray3d* decimates the spike series before wavelet convolution, while *raytopo* decimates after wavelet convolution.

4.4 Data Modeling

4.4.1 Model Synthetic Fitness

When searching through a large number of forward models, whether by trial and error or with a exhaustive grid search through the model parameter space, some quantitative measure of modeling performance or waveform fitness is required to identify "best" models. To quantify how well the synthetics from a given velocity model predict the phase arrival times, amplitudes, moveout with Δ and BAZ, and phase pulse shapes, each synthetic waveform is assigned a misfit value. The assigned misfit is the root-mean-squared (rms) amplitude misfit between the observed and predicted waveforms. The rms misfit is calculated using a time window centered around the arrival time of the *P*-coda phase(s) being modeled. With the rms misfits from all of the synthetics produced for a

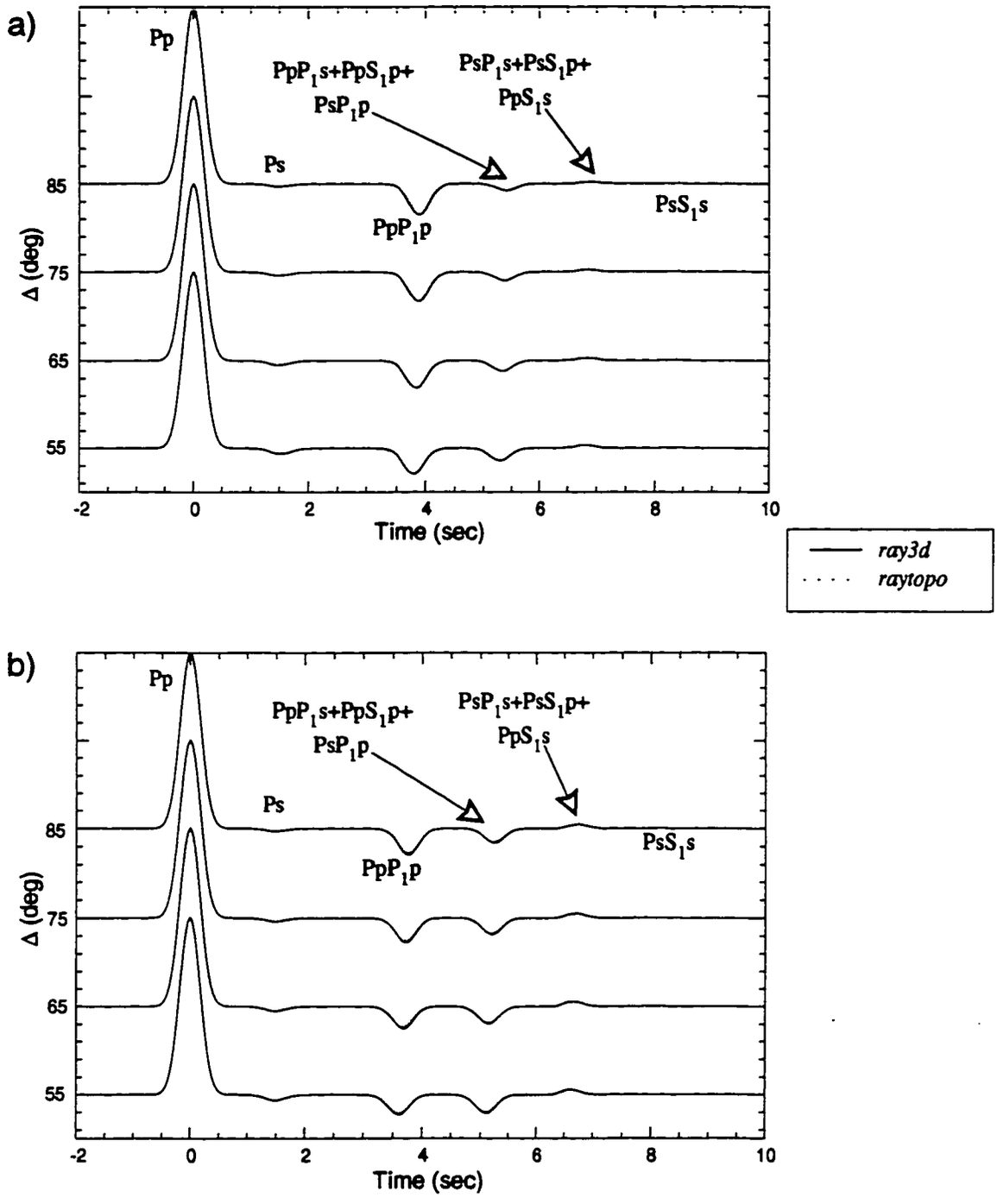

Figure 4.6: a) Comparison of synthetic seismograms for a flat homogeneous layer over a half-space, using *ray3d* (solid traces) and *raytopo* (dashed traces) containing direct, converted and first order multiples. b) Same comparison as in (a) for the top layer dipping at 5 deg and rays traveling down dip.

c)

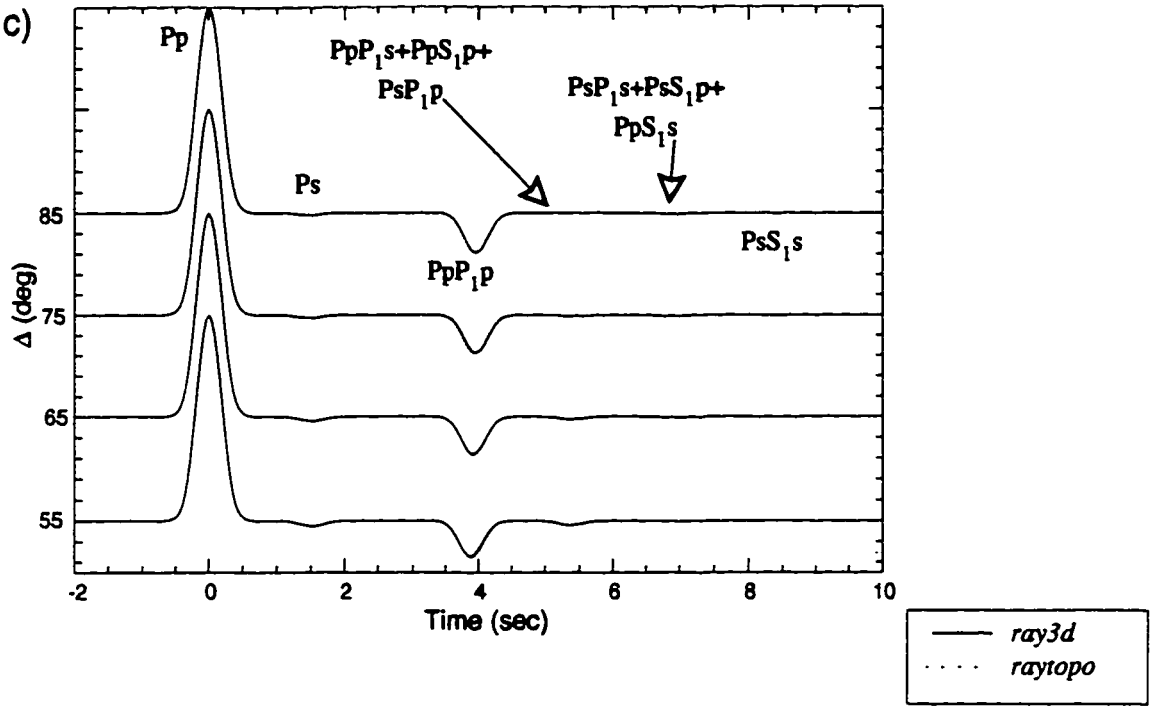

d)

Layer over half-space model	
α_1= 5.00 km/sec	α_2= 6.70 km/sec
β_1= 2.89 km/sec	β_2= 3.87 km/sec
ρ_1= 2.53 g/cm^3	ρ_2= 2.86 g/cm^3
Z_1= 10 km	Z_2 = infinity

Figure 4.6 (cont): c) Same comparison as in (b) for the top layer dipping at 5 deg and rays traveling updip. d) List of model parameters used in (a)-(c).

given model, an overall misfit is assigned to each model as the mean misfit from all of the individual waveforms. For a perfect fit of the synthetics to the observed waveform data, the corresponding overall rms misfit would be zero.

While identifying the model with the minimum overall rms misfit provides the best fitting model from the total number tested, this represents the global minimum of the model parameter subspace searched. Such a misfit minimum is more than likely a mere local minimum for the total model parameter space. Thus, if the initial model subspace considered is too far from the "true" model, the resulting best fitting model may still be a poor fitting model. An initial coarse grid search of the model subspace may help to identify those models which are closer to the "true" model. In the end, a visual comparison of the synthetic waveforms from the minimum misfit model with the stacked data will reveal whether the "best" fitting model adequately fits the data.

4.4.2 Station MBW

Previous Structural Studies: Constraint of crustal and upper mantle structure for the region in the vicinity of PNSN station MBW has been determined from a number of previous seismic studies. *Johnson and Couch* [1970] analyzed two non-reversed, NE-SW trending refraction profiles (azimuths 210° and 223°) extending from Greenbush Lake, British Columbia across the Cascades to roughly the southern Puget Sound. From the travel-time data they found an average *Pn* of 7.96 km/sec and calculated depths to the continental moho (CM) of 30 km, assuming a 2-layer structure. *Rohay* [1982] generated a 1-D velocity model from a refraction travel-time analysis of blast data for the western Cascades. The model is summarized below in Table 4.1.

Table 4.1: *Rohay* [1982] No. Cascades velocity model

Depth (km)	Vp (km/sec)
0.0	5.1
2.0	6.1
11.0	6.4
30.0	7.0
42.0	7.8

The best constrained features of this model are the 6.1 km/sec layer surface at or below 2

km depth and the *Pn* velocity of 7.8-7.9 km/sec. The continental moho depth of 42 km results from assuming an average crustal velocity of 6.4 km/sec.

Zervas and Crosson [1986] determined *Pn* velocities for the region from a time-term analysis of local earthquake data and found significant variations in average P*n* velocity for different regions of Washington. An average *Pn* value of 8.20 km/sec was determined for eastern Washington, while an average *Pn* of 7.79 km/sec was found for western Washington. A *Pn* value of 7.84 km/sec was found beneath the central Cascades. In addition, *Zervas and Crosson* [1986] suggested that the continental moho is a dipping structure, dipping in eastern Washington towards the west at ~1° while dipping towards the east at ~3° in western Washington.

A deep crustal experiment was carried out in 1991 as part of the USGS Earthquake Hazards Reduction and Deep Continental Studies Programs. This included three refraction/wide-angle reflection profiles in western Washington and Oregon. Travel time data from the 325 km N-S profile, situated between the east flank of the Puget Sound and the western foothills of the Cascades (see Figure 1.2), were analyzed and modeled by *Gridley* [1993]. *Gridley* [1993] modeled refracted and reflected arrivals from upper crustal, mid-crustal, and upper mantle layers using the forward modeling code *MacRay* [*Luetgert* 1992] and the inverse modeling code *rayinvr* of C. A. Zelt [*Zelt and Ellis* 1988]. Figure 4.7 shows the upper 20 km of the *Gridley* [1993] final model, including a 3-4 km thick high velocity layer (HVL) at a depth of 4-5 km, above an approximately 3.5 km thick low velocity layer (LVL). Both layers span the northern third (0-150 km) of the profile. The HVL and LVL are identified by reflections from the top and bottom of the HVL and from phases refracted within the HVL ($V_{app} \geq 7.0$ km/sec). A polarity reversal noted in the data which is interpreted as top and bottom HVL reflections suggests an LVL underlies the HVL. The LVL's velocity and thickness are poorly constrained by the data. Gridley interprets the HVL as part of an ophiolite sequence. Figure 4.8 shows the entire final model, with structural constraint to depths of nearly 80 km. Interfaces identified from wide-angle reflections include the continental moho, the top of the JDF oceanic crust, and the oceanic moho. PNSN station MBW is located approximately 20 km east of this profile, and projects onto the *Gridley* [1993] profile near x=30 km.

MBW Shallow Structure: As seen in Figures 3.7 and 3.8, stacked MBW data from SE, SW and NW BAZ's show strong arrivals centered at 3.0-3.5 sec, 3.5-4.0 sec, and 2.5 sec respectively, indicating the presence of shallow structure. These arrivals appear as

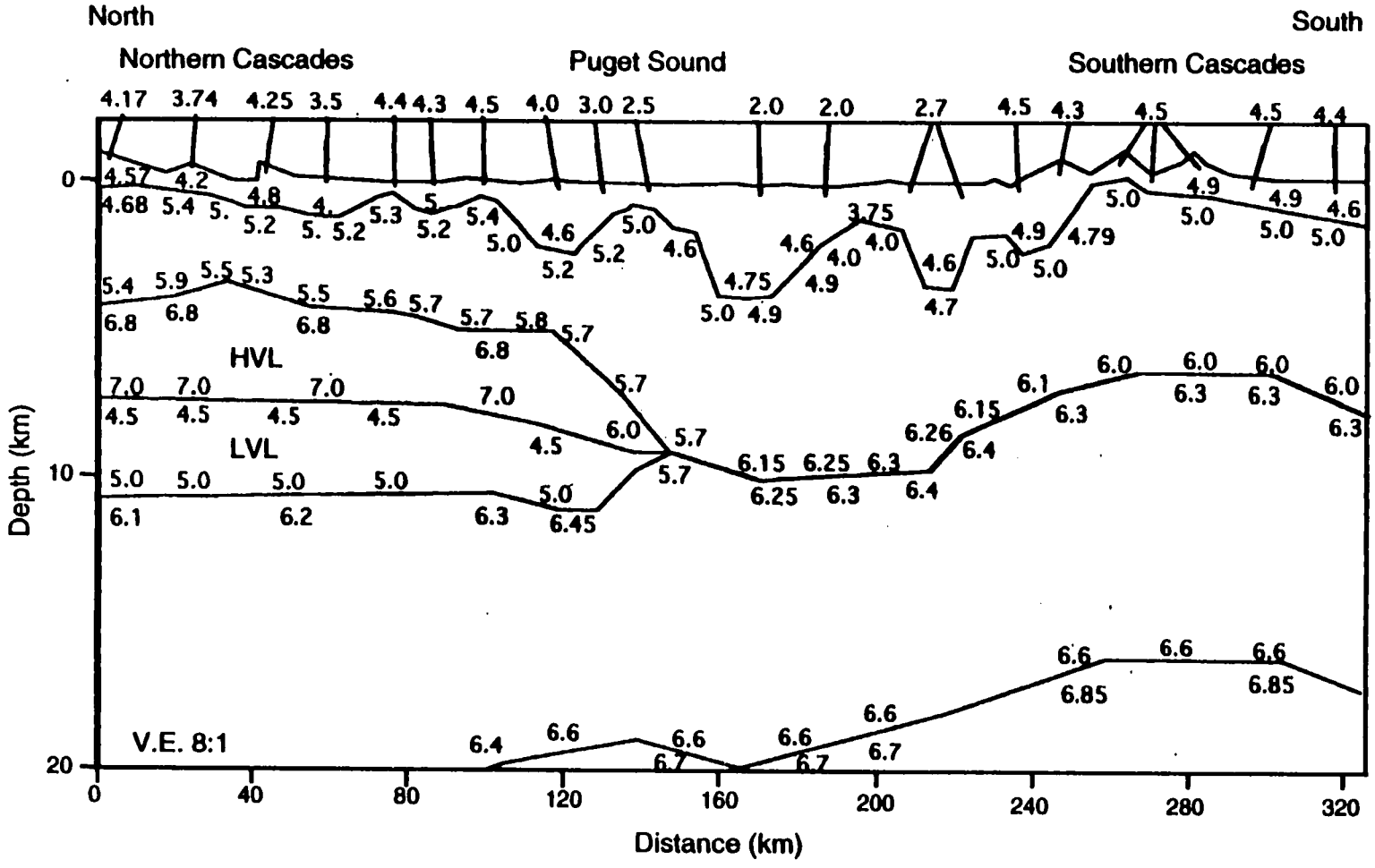

Figure 4.7: A 2-D Cascades upper-crustal *P*-velocity model from the 1991 USGS refraction/wide-angle reflection experiment as determined by Gridley (1993). Note the high and low velocity layers in the northern half of the model.

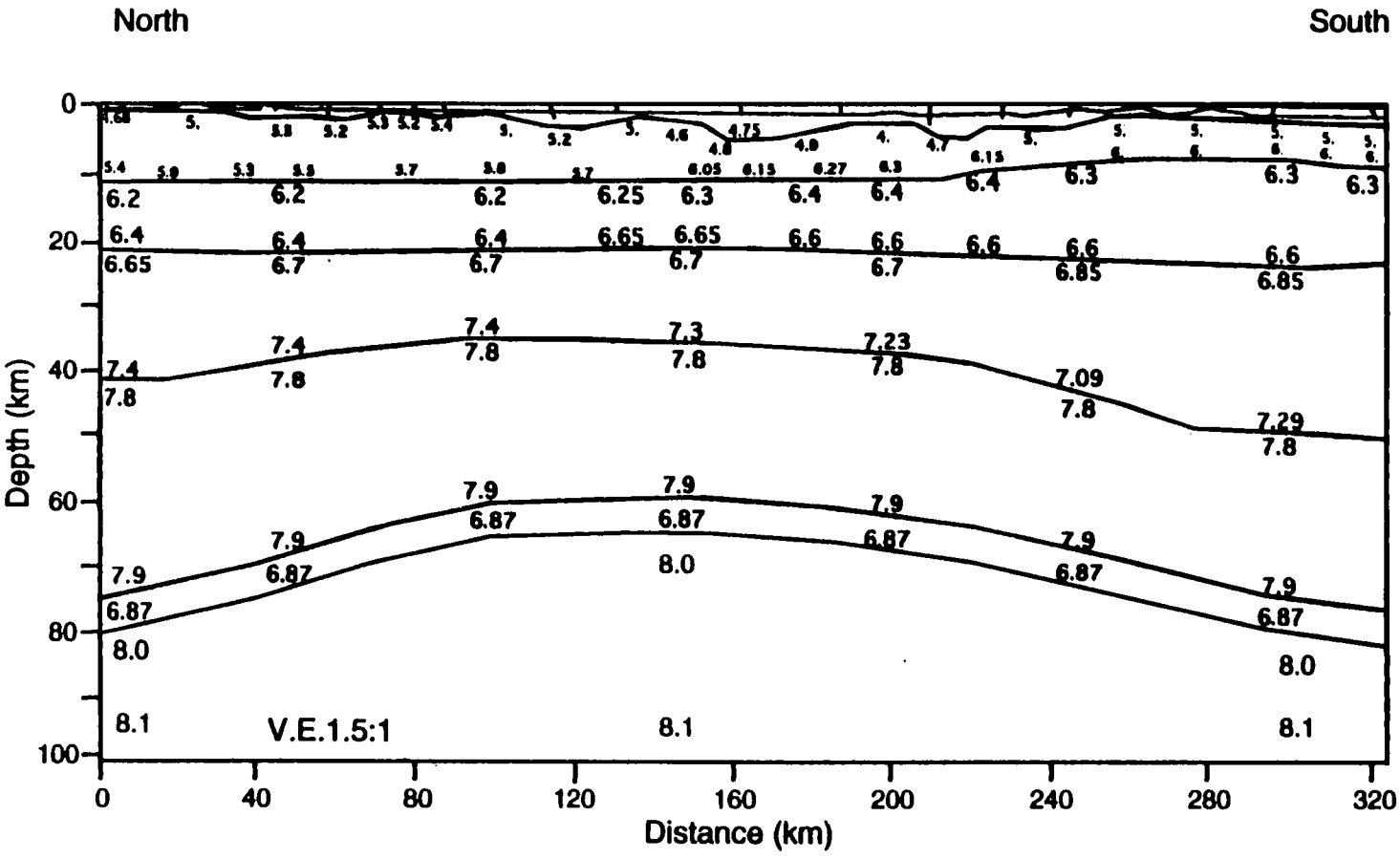

Figure 4.8: Final 2-D Cascade crustal and upper mantle *P*-velocity model from the 1991 USGS refraction/wide-angle reflection experiment. Velocities are in km/sec. From Gridley (1993).

wavelets with a central, negative polarity pulse preceded and followed by smaller positive polarity pulses. The large amplitudes of these arrivals suggest a large impedance contrast, and the arrival time variations with BAZ indicate possible dipping or non-planar structure. A starting shallow model based on the models of *Rohay* [1982] and *Gridley* [1993], which includes a shallow HVL and LVL, is used to model the observed phase arrivals. This starting model consists of 3 homogeneous layers over a half-space. The model parameters are given below in Table 4.2.

Table 4.2: MBW shallow starting model

Layer #	Vp (km/s)	Vs (km/s)	ρ (g/cm^3)	z (km)
1	5.30	3.06	2.60	3.6
2	6.90	3.98	2.80	10.0
3	4.50	2.60	2.50	11.0
4	7.00	4.05	2.86	∞

Initial forward modeling was performed with *ray3d* using this model. The plane layer assumption of *ray3d* applied to the shallow starting model appears feasible as the lateral sampling of multiple bounce rays is at most 1.5-2.0 wavelengths (~10 km). By varying the thickness of layer 2 in the starting model, the phase travel times for the data from each BAZ can be reasonably predicted using flat interface models. The depth to the bottom of layer 2 for each "best" flat interface model are: SE BAZ; z_2 = 10.7 km, SW BAZ; z_2 = 12.1 km, and NW BAZ; z_2 = 6.5 km. Synthetics from these three BAZ dependent models and stacked data are compared in Figure 4.9, with only the significant (observable) synthetic phase arrivals labeled. Note the polarity reversal in the synthetics between phases PpP_2p and PpP_3p, reflections from the top and bottom of the LVL. While the synthetics show a fair agreement in travel time and pulse shape with the data, the phase amplitudes are underestimated by a factor of 2 or more for all Δ's and BAZ's. These three BAZ dependent, flat interface models suggest dipping structure as a means to accommodate the variation in phase arrival time with BAZ. The observed travel time variations with BAZ along with the variation in the three flat model's HVL thickness indicate a south-southeast dipping interface. The slant stacks of SE and NW BAZ data (Fig. 3.8) also indicate dipping structure, as each shows different optimal stacking parameters (moveout with Δ)

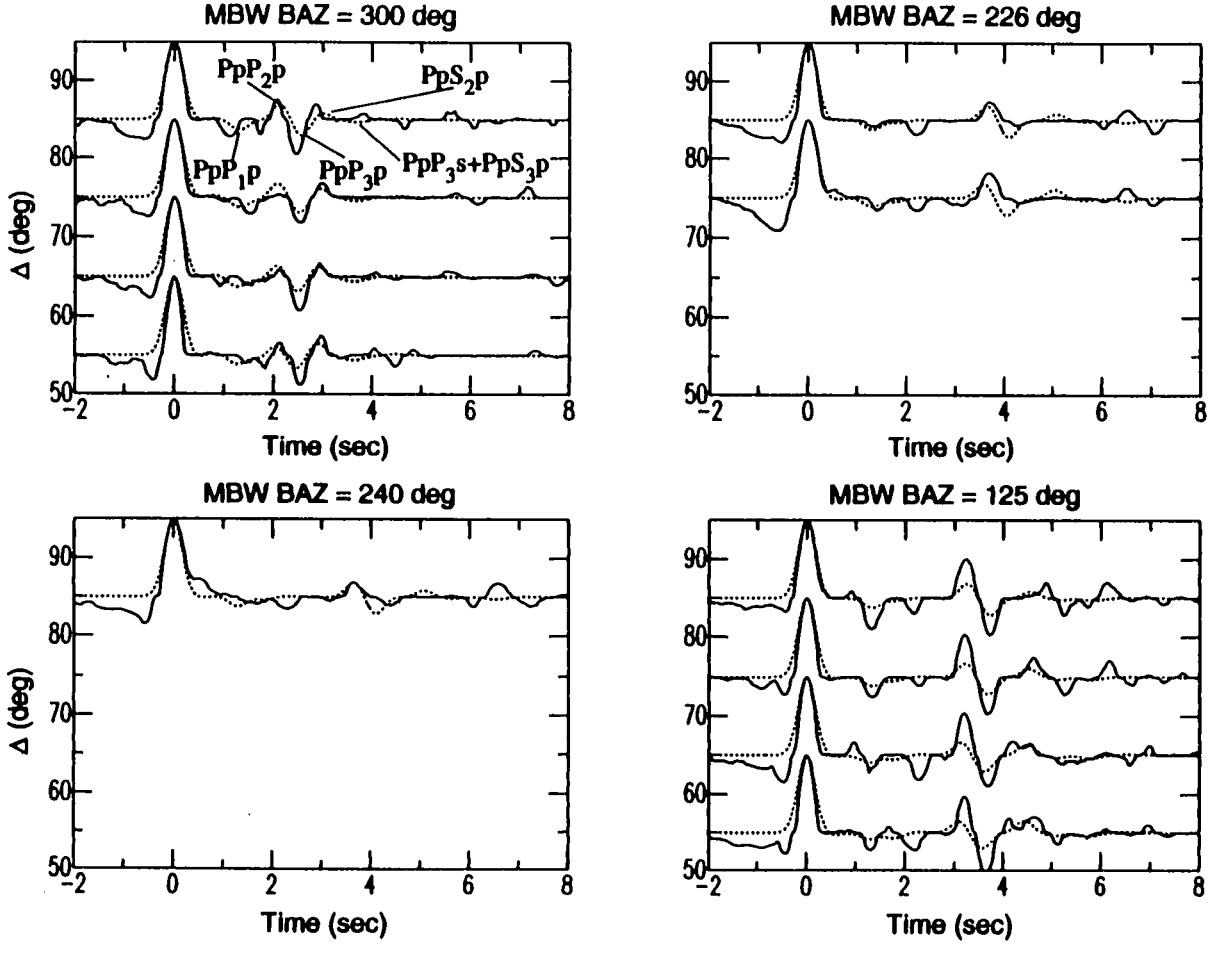

Figure 4.9: Synthetics (dashed lines) for station MBW from the best flat, 1-D homogeneous models compared with the 3rd-root stacked data (solid lines) plotted as record sections. See text for model parameters. Only synthetic phases with significant amplitude (> ~5%) are labeled.

for the phases modeled. The observation of zero to small negative parameter values for the NW BAZ data and zero to small positive parameter values for the SE BAZ data are also consistent with interfaces dipping the to south (versus the north). The dipping interfaces in question include the bottoms of the HVL and LVL.

In general, finding a dipping interface model which fits the stacked data using forward modeling requires either: (*i*) significant *a priori* structural constraint, (*ii*) judicious guessing of model parameters, (*iii*) making an exhaustive search through the entire model parameter space, or (*iv*) some combination of (*i*)-(*iii*). An exhaustive search of the entire model parameter space may provide a definitive best model, however this may be realistically feasible only if the number of model free parameters is reasonably small. For example, the *ray3d* velocity model parameterization allows for as many as $6N$-3 free parameters in an N layered model. Allowing for 5 possible values of each free parameter in a 4 layer model, for example, would require searching through 21^5or 4.08×10^6 grid points. To keep the search within reasonable bounds, certain parameters must be assumed or constrained *a priori*. We have chosen to search a limited subspace of the entire model space by allowing only a few parameters to vary, specifically interface depth, strike and dip. During the course of modeling, interface depths were routinely constrained before the other parameters either though a coarse 3-D grid search or by trial and error testing.

For shallow structure modeling at MBW, the two interfaces (top and bottom of the LVL) are assumed to be coupled such that each has the same strike and dip. The starting model (see table 4.2) with the HVL thickness set to 6.8 km was used to generate models, stepping through dips from 0°-20° in 1° increments and strikes from 0°-350° in 10° increments (756 grid points). Synthetics generated from each model space grid point are judged on their fit to the stacked data using the root-mean-squared (rms) amplitude misfit for the first 8.0 sec of data. Figure 4.10 is a gray scale density plot of the overall model space misfits from the 2-D model grid search. Dark colors (black) are those strike and dip pairs with misfit minima. This density plot indicates the best fitting models of the model space are those with strikes of 0°-30° and dips of 11°-19°. Figure 4.11 shows a comparison of the stacked data and synthetics with model interfaces striking at 10° and dipping at 18°. This comparison shows a reasonable agreement of the SE BAZ synthetics phase arrival times and moveout with Δ, but still underestimates amplitudes. The NW BAZ synthetics show arrivals which are late by ~0.5 sec and a moveout with Δ which is too large, though correct in sign. The SW BAZ synthetics arrivals are also slightly late.

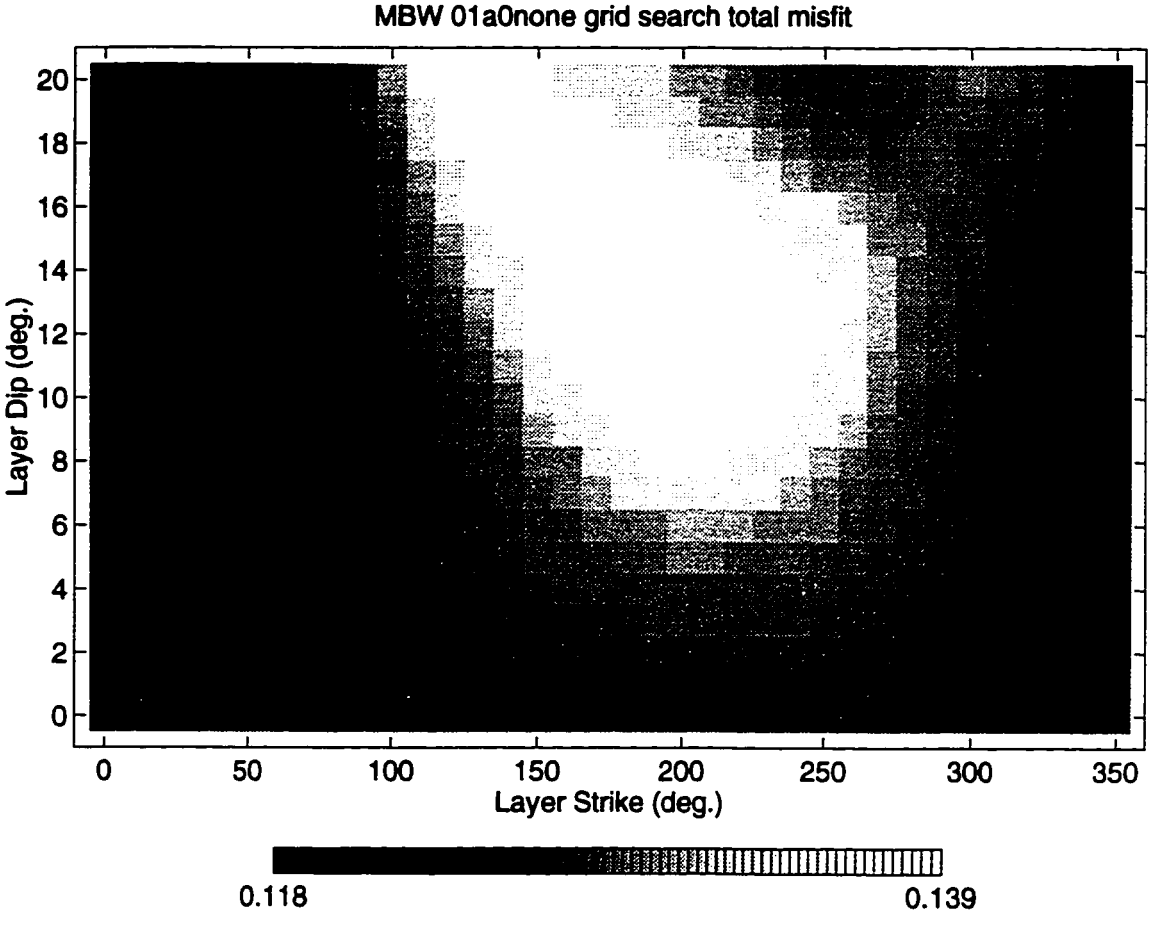

Figure 4.10: Grayscale density plot of model misfit from the grid search of a 2-D model space. Black colored pixels correspond to grid points with misfit minima, or the best fitting models of those tested from the model space. Note that the narrow zone of minima provide qualitative uncertainties for the model strike and dip.

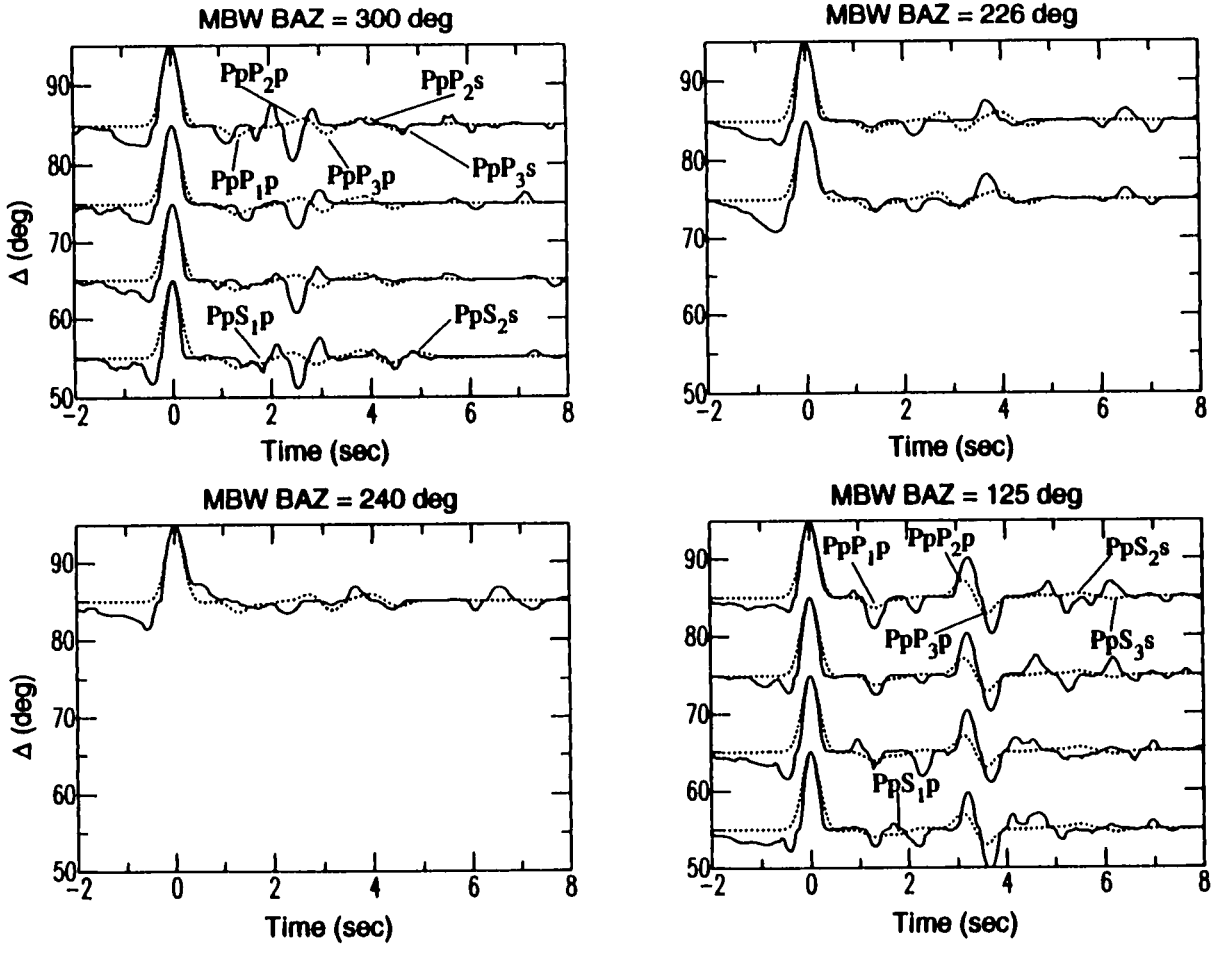

Figure 4.11: Synthetics (dashed lines) for station MBW best dipping layer model as determined from a 2-D model space grid search, compared with 3rd-root stacked data (solid lines) plotted in record sections. The model interfaces here strike at 10 deg and dip at 18 deg. See text for model parameters. Only synthetic phases with significant amplitude (> ~5%) are labeled.

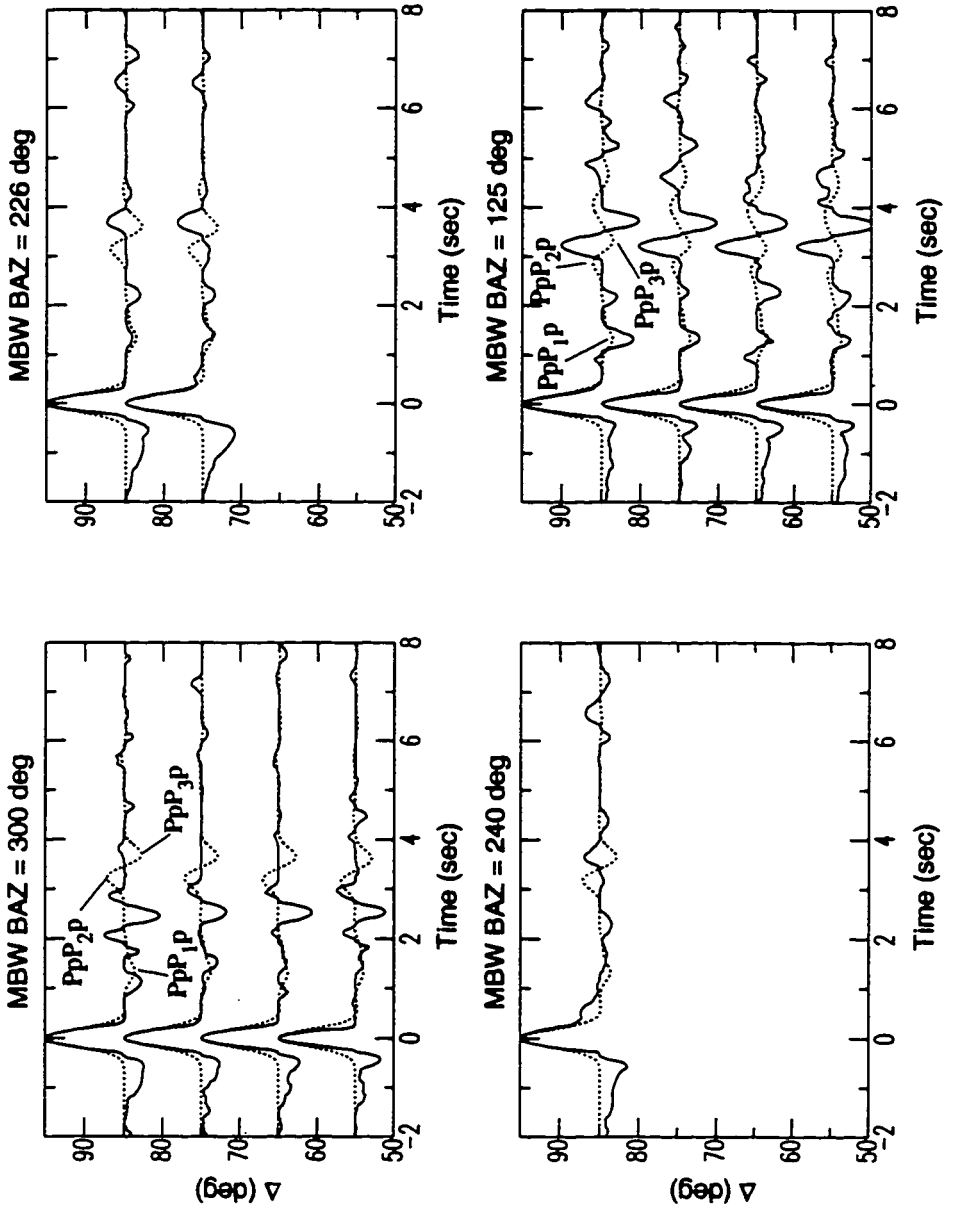

Figure 4.12: Synthetics (dashed lines) for station MBW largest misfit dipping layer model as determined from a 2-D model space grid search, compared with 3rd-root stacked data (solid lines) plotted in record sections. The model interfaces strike at 190 deg and dip at 13 deg. Only synthetic phases with significant amplitude (> ~10%) are labeled. Note that even qualitatively, this is a poor fitting model.

As a check of the integrity and sensitivity of the misfit determination, we compared the stacked data and synthetics with the largest overall misfit. Figure 4.12 shows the stacked data and synthetics with model interfaces striking at 190° and dipping at 13°. Note that the synthetics from all three BAZ's show much poorer agreement with the data than do the synthetics associated with the minimum misfit. This check of minimum and maximum misfit synthetics was routinely made after all model grid searches.

Two significant inadequacies associated with the synthetics generated from the minimum misfit model are: (*i*) the failure to correctly model the phase moveout with distance (Δ), and (*ii*) the consistently under-predicted phase amplitudes. The predicted amplitudes of the PpP_2p and PpP_3p phases are at most 20-25% of the direct-*P* arrival and result from impedance contrasts of 1.72 and 0.56, respectively. To produce amplitudes that rival those observed in the stacked data (~50%) requires impedance contrasts to change by a factor of 2 or more. Such changes are physically questionable and inconsistent with *P*-velocities in the *Gridley* [1993] upper crustal model. Reducing the LVL *P*-velocity to a realistic lower limit of 3.00 km/sec produced synthetics with PpP_2p and PpP_3p amplitudes that are just 28-35% of the direct-*P* arrival. The corresponding grid search model misfit distribution was similar to that for the 4.50 km/sec LVL model, and the minima magnitudes were not significantly different than those from the 4.50 km/sec LVL model. These result indicates that the LVL *P*-velocity from this model parameterization cannot be resolved any better than 3.75±0.75 km/sec and more structure is required to correctly predict the observed phase amplitudes.

More complex structural models with interface topography are considered to address the inadequacies of the previous models' synthetics fitness. This requires the use of the *raytopo* forward modeling procedure. We modified the previous model to include a ramp structure on both the top and bottom of the LVL. The greater phase arrival times for the NW data suggest that the ramp should dip to the south-southeast. This ramp orientation has rays for SE BAZ synthetics propagated up the ramp, while those for NW BAZ synthetics propagated down the ramp. Rays for SW BAZ synthetics propagated along strike (a ramp with no apparent dip). In addition to the interface ramp, the model was allowed to contain vertically heterogeneous velocities, following those of the *Gridley* [1993] model. Depths to the LVL for the ramp model were set to 7.1 km at the ramp top, and 10.8 km at the ramp bottom. A range of ramp dips (5°-20°) and ramp lengths (5-10 km) were used to produce synthetics which were checked for general amplitude and phase

moveout agreement with the stacked data. Of those models tested, the 20° dipping, 10 km length ramp produced the best results. Figure 4.13 shows a comparison of the stacked data with synthetics from this best ramp model, along with the velocity model. The SE BAZ synthetics show good phase arrival time agreement with the stacked data 3.0-3.5 sec arrivals (PpP_3p and PpP_4p) at all distances. The predicted amplitudes of phase PpP_3p fall within the $\pm 2\sigma$ bounds of the linear stack for all Δ. This is true of the PpP_4p phase amplitudes for only the Δ=65° synthetics. The NW BAZ synthetics show general agreement with the pulse shape, though the pulse arrival is slightly late. Predicted amplitudes of phase PpP_3p are within the $\pm 2\sigma$ bounds, while the PpP_4p phase amplitudes are underestimated. The NW BAZ synthetics show a greater phase moveout with Δ than the data. The SW BAZ synthetics show the phase arrivals are too early by ~0.9 sec. However, the pulse shape and predicted phase amplitudes (within the $\pm 2\sigma$ bounds) are in fair agreement with the data.

Shallow Modeling Discussion: The ramped interface model provides better overall fitting synthetics than the previous homogeneous, planar dipping interface models, suggesting that some degree of structural complexity is associated with this location. One of the important products of the ramped model is synthetics with more realistic amplitudes. On the other hand, the poor predicted arrival times of the SW BAZ synthetics from the ramped interface model (Fig. 4.13) indicate additional laterally varying structure. The poor fit of the SW BAZ synthetics is likely due to true 3-D structure, which *raytopo* is unable to model.

The final shallow structural model determined for station MBW confirms and modifies the shallow structural model constrained by Gridley, most notably the existence of an HVL and LVL. The depths to the top of the HVL in each study's model are nearly coincident, but the HVL thickness shows greater variability in our model (3.5-7.2 km). The LVL of the Gridley model is suggested by observed polarity reversals, however the layer thickness and velocity are virtually unconstrained by his data. Reasonable values for each are simply stated [*Gridley* 1993]. Our analysis shows interface velocities in the range 3.00-4.50 km are compatible with the stacked data. An LVL thickness of 1.0 km is required to fit the stacked waveforms. The minimum resolvable layer thickness for data with frequencies of 1.0-2.0 Hz is 1.5 km. Thus, considerable uncertainty is associated with the resolution of the LVL with our data.

The shallow structure imaged beneath station MBW from our forward modeling

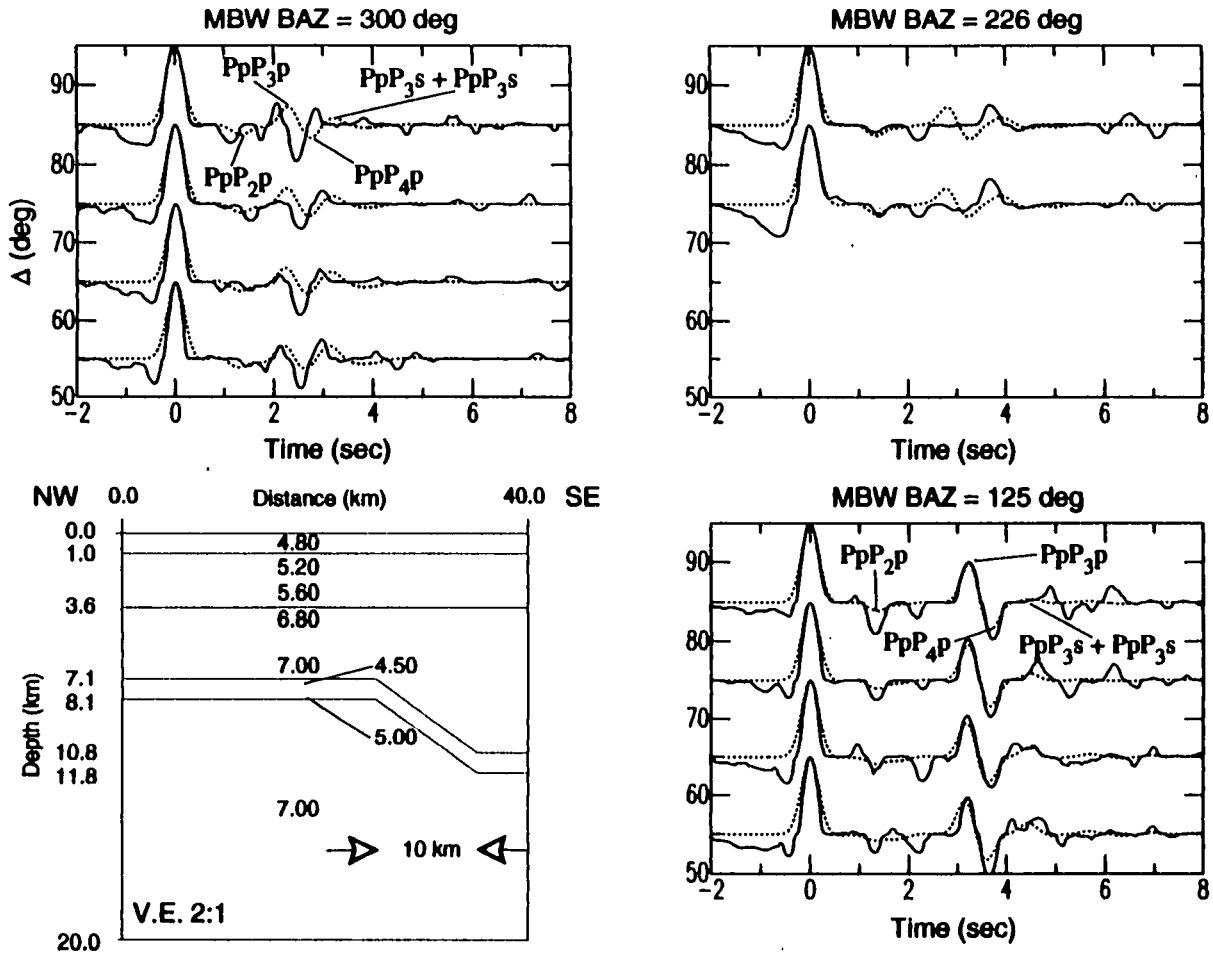

Figure 4.13: Synthetics (dashed lines) for station MBW from an inhomogeneous layered, ramped interface model compared with the 3rd-root stacked data (solid lines) plotted as record sections. Only synthetic phases with significant amplitude (> ~5%) are labeled. The parameterized model is also shown, oriented such that waves arriving from the NW propagate down the ramp, and those arriving from the SE propagate up the ramp.

suggests that the high velocity and low velocity layers determined from Gridley's N-S profile extend laterally off-profile to the east by at least 20 km.

MBW Deep Structure: Deep structure is also indicated in the standard linear stacks and linear slant stacks of MBW data from Figures 3.7 and 3.8. Most noticeable in the stacks is a single negative polarity pulse arriving between 13.1 and 13.7 sec in the SE and NW data. The SW BAZ stacks (226° and 240°) show nothing with a negative polarity of significance arriving in the same time window as the SE and NW data. The appearance of a significant arrival at ~12.2 sec in the 240° BAZ stacks could be the same phase observed later in the SE and SW BAZ data. However, the lack of persistence of this phase in the 226° BAZ stacks tends to de-emphasize its significance. Because of the inconsistency of this phase for the SW BAZ data, we focus our attention solely on the SE and NW data phase.

The amplitude of the NW and SE BAZ phase is ~10% of the direct-*P* arrival. The late relative arrival time and relatively small amplitude suggest that this is a deep crustal or upper mantle phase associated with a moderate impedance contrast interface. In addition, the small phase moveout with BAZ indicates possible gently dipping structure. The observed phase could possibly be a continental moho reflection. A check using a single homogeneous layer over a half-space model with α=6.40 km/sec and z=45.0 km (from *Rohay* [1982] and *Gridley* [1993] average crustal velocities and continental moho depths) reveals the observed phase is consistent with a *PpPmp* phase.

Three previous studies in the region of station MBW provide average crustal velocities and continental moho (CM) depths, which are summarized in Table 4.3 below:

Table 4.3: No. Cascades average crustal velocities and CM depths

Study	∇p (km/s)	z (km)
Crosson [1976]	6.49	41.0
Rohay [1982]	6.40	42.0
Gridley [1993]	6.45	40.0-42.0

Because the relative phase arrival times of the *P*-coda phases are sensitive to the average model velocity above the reflecting interface and the depth to the interface (see equation 4.1), the models tested should contain reasonable average crustal velocities for plausible

interface depth results. The values listed in Table 4.3 provide reasonable constraint for the average crustal *P*-velocity for the region in the vicinity of station MBW.

The close proximity of the *Gridley* [1993] profile to MBW makes the Gridley model a good starting point for a deep, homogeneous layered model. Creating a starting model involved appending additional layers to the shallow starting model of Table 4.2 and adjusting the CM depth to match arrival times. The resulting model velocities and interface depths as listed below in Table 4.4:

Table 4.4: MBW deep starting model

Layer	Vp (km/s)	Vs (km/s)	ρ (g/cm^3)	z (km)
1	4.80	2.77	2.50	1.0
2	5.40	3.12	2.60	3.6
3	6.90	3.98	2.80	9.0
4	4.50	2.60	2.50	10.0
5	6.40	3.67	2.75	21.0
6	6.80	3.93	2.80	46.0
7	7.90	4.56	3.00	∞

For the flat layer case, *ray3d* produces synthetics with *PpPmp* phases arriving from 12.80 sec (Δ=55°) to 13.56 sec (Δ=85°) after the direct-*P* arrival. The *PpPmp* moveout with Δ is 0.023 sec/deg for these synthetics. This positive moveout is larger than the values observed from the linear slant stacks for both the SE and NW BAZ data, -0.01 to 0.01 sec/deg. Allowing the bottom of layer 6 to dip alters the phase moveout with Δ. Down dip propagation increases the moveout with Δ, while up dip propagation decreases the moveout to smaller (even negative) values. To explain the similar, small moveouts for both the SE and NW BAZ slant stacks requires them to be oriented roughly along strike of a planar, steeply dipping CM. Another possibility is the existence of non-planar structure. The lateral sampling of *PpPmp* for the CM at 46 km depth is on the order of 40-60 km or 7-11 wavelengths. A survey of the *Gridley* [1993] model where CM structure is constrained indicates that planar structure is possible. Tentatively allowing for the validity of the assumption, a grid search of the two parameter model space (CM strike and dip)

was made to determine if a simple dipping, homogeneous velocity model could be found. Figure 4.14 shows the overall model space misfits from the 2-D model grid search spanning strikes from 0°-350° and dips from 0°-15°. A misfit window from 8.0-18.0 sec was applied to determine synthetic fitness of the CM phases. The overall misfit minima (7% of the grid points) map to three zones with strikes of 80°-100°, 200°-240°, and 340°-350° and dips of 5°-15°. The first and third strike ranges orient the dipping CM roughly along strike for both the SE and NW BAZ data. The second strike range corresponds to the CM dipping to the NW. A comparison of the corresponding synthetics for the strike=340°, dip=14° model with stacked data (Figure 4.15) shows the SE BAZ synthetics with reasonable agreement in phase travel times and moveout with Δ, but underestimated phase amplitudes. The NW BAZ synthetics have phase arrivals which are early by as much as 2.0 sec, a moveout with Δ which is too large, and phase amplitudes which are small and likely indistinguishable from the background (3.5-5.0% of the direct-*P* arrival) level. While this model is one of the best fitting for the 576 tested in the model space grid search, it does not adequately fit the data. A second minimum misfit model with a strike of 210° and dips of 5° produces SE and NW BAZ synthetics that show a fair agrement with phase arrival times but have excessive moveouts with Δ. The relatively poor fitting "best" model suggests the likelihood of an inadequate starting model, whose fixed model parameters are too far from the "true" model. Varying the CM depth by ±1.0 km produces synthetics with the same overall misfits (magnitude and distribution) as seen in Figure 4.14.

With the general failure of the *ray3d* modeling procedure, the validity of the planar model interface assumption is suspect, and the need for greater structural complexity in the velocity model is apparent. The later phase arrival times of the NW BAZ stacked data (relative to the SE BAZ arrivals) suggest an offset in the CM such that the NW data sample a deeper interface. The revised deep structural model considered is a downward continuation of the ramped shallow model (Fig. 4.13) with the shallow ramp removed. Three vertically heterogeneous layers are appended to this model, with velocities and layer thicknesses following the deep crustal model of *Gridley* [1993]. A ramp structure on the CM with depths on either side of 44.0 and 47.0 km is included to accommodate the longer arrival times for waves traveling from the NW. The CM depths were selected because they provided reasonable agreement with the phase travel times for the stacked data at Δ=85°. Models generated using *raytopo* with ramp dips from 4.0° to 16.0° were compared with the SE and NW BAZ stacked data. Overall model misfits computed from

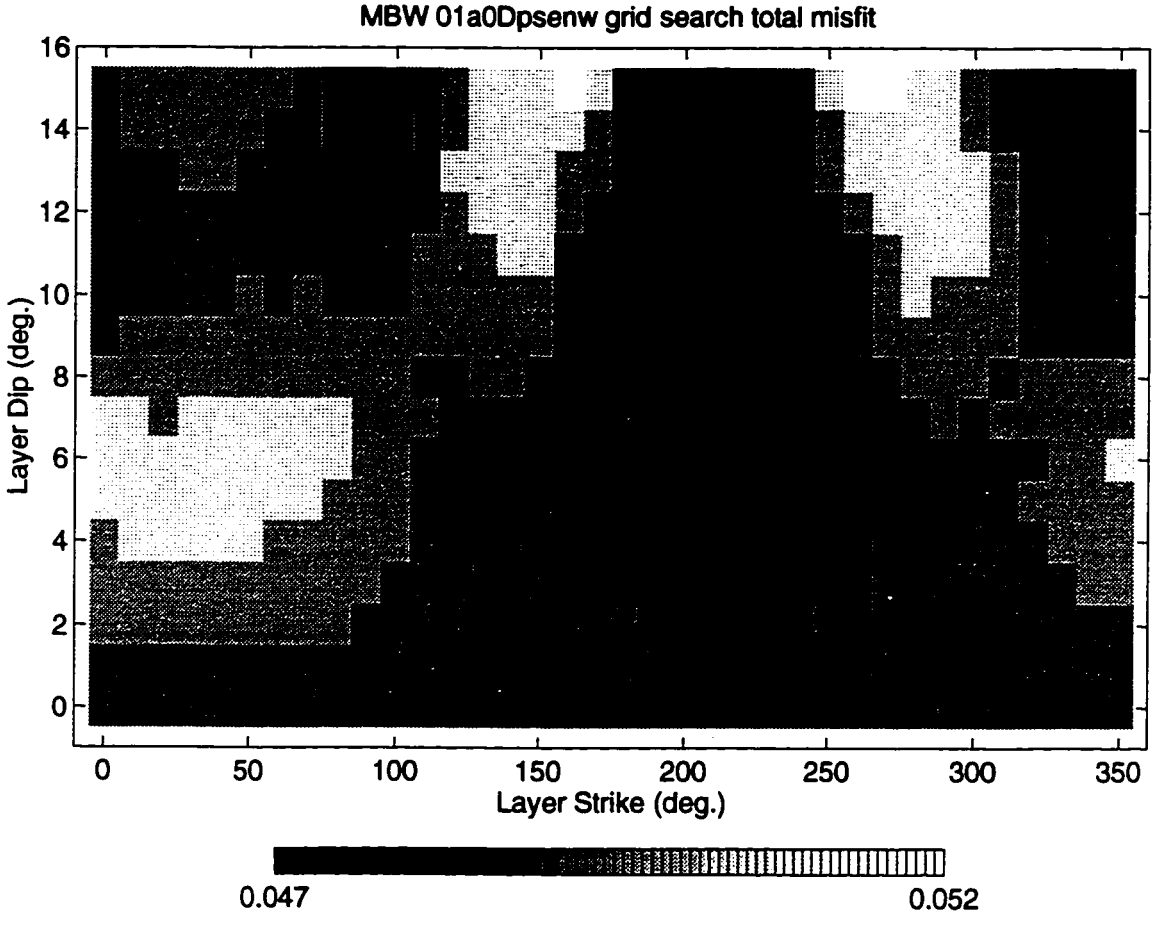

Figure 4.14: Grayscale density plot of model misfit from the grid search of a 2-D model space for the MBW deep layered model. 40 misfit minima exist in three regions of layer strike values. These minima represent strikes and dips with the best fitting models of those tested. Note that the range in overall misfit values is small.

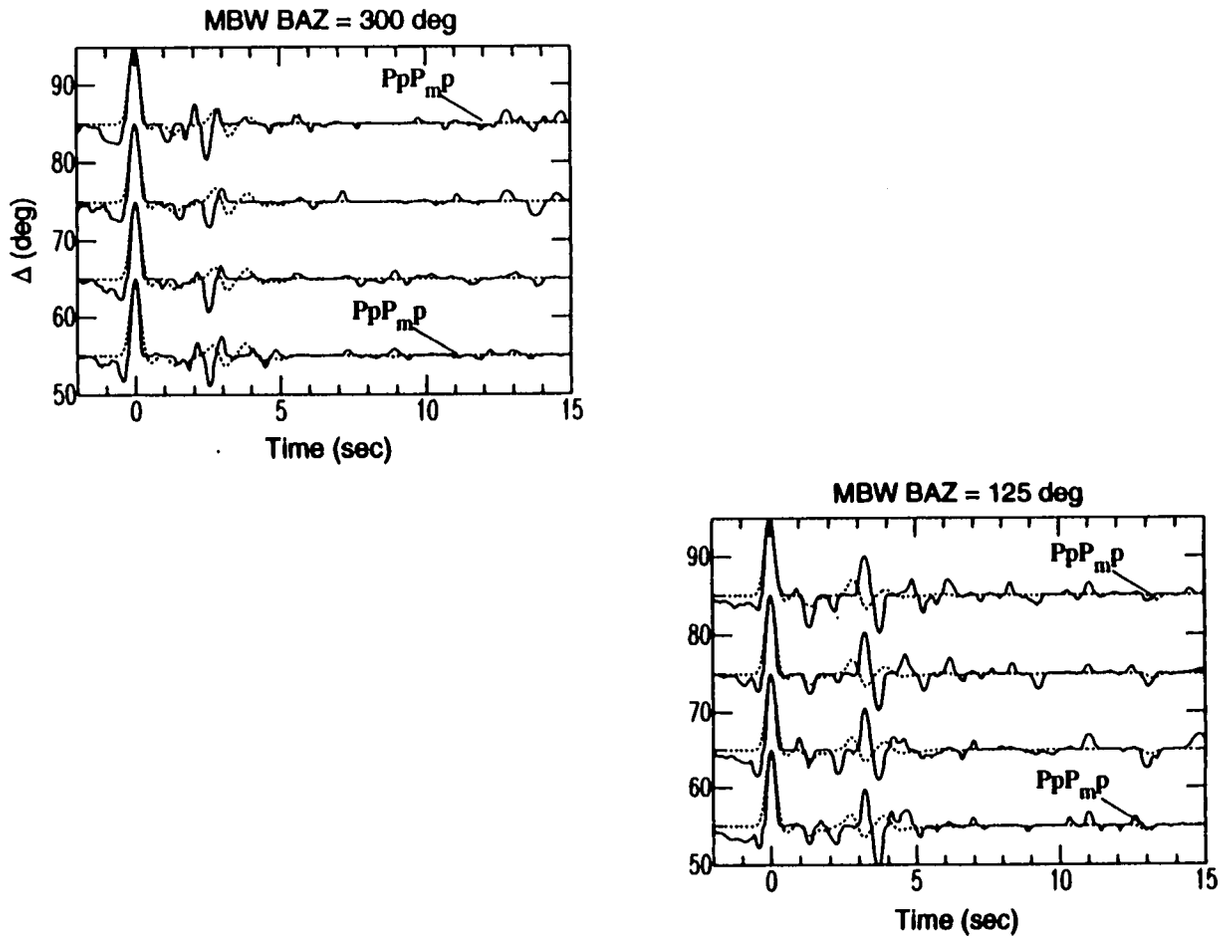

Figure 4.15: Synthetics (dashed lines) for station MBW deep dipping CM model as determined from a 2-D model space grid search, compared with 3rd-root stacked data (solid lines) plotted in record sections. Model CM strike and dip are 340 deg and 14 deg. See Table 4.4 for model parameters. Only synthetic CM phases with significant amplitude (> ~5%) are labeled.

the comparisons of SE and NW BAZ synthetics with the stacked data yielded values of 0.050-0.056 (see Figure 4.14 for a comparison with the homogeneous, dipping layer model). The model with a ramp dip of 8.5° yielded the best fit of those tested (Figure 4.16a). However, this model fits no better than the best planar dipping models previously found. Figure 4.16b shows a comparison of the synthetics for the 8.5° dipping, ramped interface model with the stacked data. The SE BAZ synthetics have the same poor fit as the planar, dipping model (Fig. 4.15), with excessive phase moveout with Δ. The NW BAZ synthetics show larger phase amplitudes than the planar dipping model (a result of ray focusing) and an excessive moveout with Δ. The ramp structure in this model provides marginal improvement in phase amplitudes for the NW BAZ synthetics at the expense of arrival times and moveout. In the end, this model too suffers from the same shortcomings as the best planar dipping models.

Deep Modeling Discussion: The results of the above deep structural modeling for station MBW indicates that greater structural complexity of wavelengths from 3.5-7.0 (the minimum resolvable with 1.0-2.0 Hz data) to 45 km (the lateral sampling of *PpPmp* for a flat CM) must be present. From the limitations of the modeling techniques used, it is difficult to state the exact nature of the structure(s) responsible. Interface curvature and 3-D structure, for example, may play an important role. The possible misidentification of the observed phase arrivals could also be responsible for the shortfalls of the waveform modeling. However, the fair agreement of the *PpPmp* phase arrival times of both the planar dipping and ramped interface models with the data indicates reasonable constraint of the interface depth (46±1 km) for an average crustal *P*-velocity of 6.50 km/sec.

Compared with the simplified 1-D models of Table 4.3, our deep crustal models (planar dipping and ramped interface) indicate that a deeper CM is required to fit the observed phase arrival times. Within the estimated uncertainties for the CM depth (±2%), the greater CM depth of our simple models appears significant. Even with a ±5% depth uncertainty, the minimum depth exceeds those of *Crosson* [1976], *Rohay* [1982], and *Gridley* [1993]. A direct comparison of CM depths inferred from this study and the *Gridley* [1993] profile ~20 km to the west of MBW suggests a possible eastward dipping CM. It is interesting to note that *Schultz* [1993] found an eastward dipping CM (4.4°) under western Washington at a maximum depth of 47±1 km from a NW-SE trending refraction/wide-angle reflection profile through the central Cascades. This has been interpreted by *Schultz and Crosson* [1995] as crustal thickening beneath the Cascade

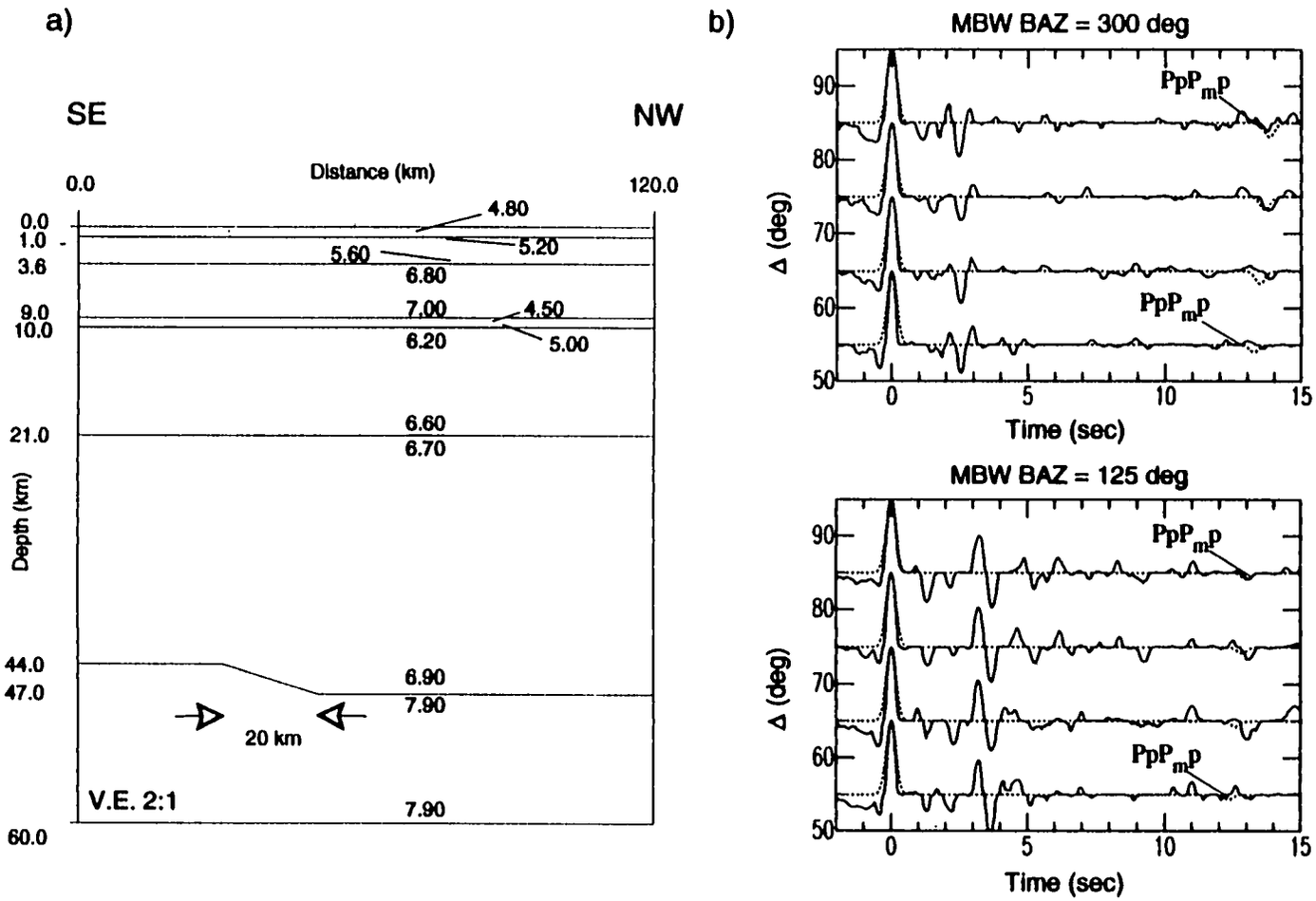

Figure 4.16: (a) Station MBW 2-D ramped interface model parameterization showing *P* velocities and interface depths. The ramp dips at 8.5 deg to the NW. (b) Synthetics (dashed lines) for deep, ramped CM model (as determined from a trial and error search of ramped models) compared with 3rd-root stacked data (solid lines) plotted in record sections.

Range produced by subduction driven magmatic underplating.

4.4.3 Station SPW

Previous Structural Studies: PNSN station SPW is located on the Bailey Peninsula at the south end of Lake Washington. This site, placed on poorly cemented Oligocene sandstone, is south of the inferred surface expression of the east-west trending Seattle fault, as interpreted by *Gower et al.* [1985] from gravity anomaly data and *Bucknam et al.* [1992] from uplifted beach terraces. The gravity anomaly is one of the steepest (100 mgal in 18 km) in the United States. The Seattle fault is interpreted as a thrust fault with downward motion to the north that has produced a deep, sediment filled basin whose base is Coast Range mafic rock (Crescent Formation) [*Finn* 1990]. This fault may be currently active, as suggested by the M_D 5.0 Robinson Point earthquake of January 29, 1995 [*Dewberry and Crosson* 1996]. Recent industry reflection data analyzed by *Johnson et al.* [1994] and *Pratt et al.* [1994] have produced a more detailed image of the Seattle fault at the surface and at depths to 10-12 km. Using different data sets, each group modeled the Seattle fault at depth as dipping to the south at ≤25°. Near the surface, the fault splays into a number of steeply dipping blind, thrust faults with mean dips of ~45-60° [*Johnson et al.* 1994]. The inferred depth to the highly reflective Crescent Formation (CF) in the Seattle basin (north of the fault) is from 7-8 km [*Johnson et al.* 1994] to 9-10 km [*Pratt, personal comm.* 1995]. *Johnson et al.* [1994] infer the CF depth at ~1.0 km south of the surface fault zone (surface fault #4, see *Johnson et al.* [1994] figures 2.A and 2.D) where station SPW is located. These high-resolution studies corroborate the results of *Lees* [1989] showing *P*-velocity anomalies in this vicinity which include a low velocity structure north of the inferred fault surface at depths of 4-6 km and a high velocity structure south of the fault surface at the same depth. Also, the 2-D velocity model of *Gridley* [1993], derived from a N-S profile located 20 km east of station SPW, has an approximately 4.0 km deep basin with surface velocities of 2.0 km/sec at x=160 km, corresponding to the eastern side of the Seattle basin.

General constraint of deep crustal and upper mantle structure for the Puget Sound in the vicinity of station SPW have been provided by *Crosson* [1976] from a 1-D *P*-velocity profile from earthquake data, by *Zervas and Crosson* [1986] with *Pn* velocity of 7.79 km/sec for the Puget Sound, by *Schultz* [1993] with a 2-D, *P*-velocity model for an NW-SE trending profile extending across the Puget Sound to eastern Washington, and by *Gridley* [1993] with a 2-D velocity model from a N-S trending refraction/wide-angle reflection

profile just east of SPW.

Shallow Structure: As seen in Figures 3.9 and 3.10, the stacked SPW waveforms from SE, SW, and NW BAZ's show a large amplitude phase (30-60% of the direct-*P* amplitude) arriving within 1.0 sec of the direct-*P* arrival across all Δ's and BAZ's. The phase is a single, negative polarity pulse that is broader than the direct-*P* arrival. The emergence of this phase beyond the $\pm 2\sigma$ error bounds of the stacks demonstrates the statistical significance of the stacked phase. This phase exhibits very little moveout with Δ (Figure 3.10) as one might expect for a short-lag time arrival. This phase likely represents a very shallow, high impedance contrast crustal interface.

Initial waveform modeling is considered using a planar, layered model that includes a single layer over a half-space. The starting model parameters are derived from applicable existing models and include a low velocity top layer (representing unconsolidated sediments and sedimentary rock) overlaying a higher velocity half-space (Crescent Formation). Table 4.5 below lists the starting model parameters.

Table 4.5: SPW shallow starting model 01A1

Layer #	Vp (km/s)	Vs (km/s)	ρ (g/cm^3)	z (km)
1	3.00	1.73	2.25	1.5
2	6.00	3.46	2.60	∞

The interface depth was first determined by fitting the observed phase arrival times with a search through flat layer models. Then allowing for a dipping layer interface, a gird search of the 2-D model space (strikes 0°-350° and dips 0°-18°) was made to determine the best fitting model. Figure 4.17 shows the overall model misfits from the comparison of this model's synthetics (the first 7.0 sec) with the stacked data from SE, SW and NW BAZ's. The misfit minima (dark colors) fall in a narrow range of strikes (50°-80°) and dips (12°-14°). Figure 4.18 shows a comparison between the synthetics from one of the best fit models (strike=60°, dip=12°) and stacked data. The SE and NW BAZ synthetics have phase arrival times and pulse shapes which agree well with the data, but underestimate the phase amplitudes. The broadened pulse shape for the NW BAZ synthetics results from the superposition of two phases, *PpP1p* and *PpP1s*. The SW synthetics from BAZ=226° show a reasonable agreement with the phase arrival time and amplitude but do not

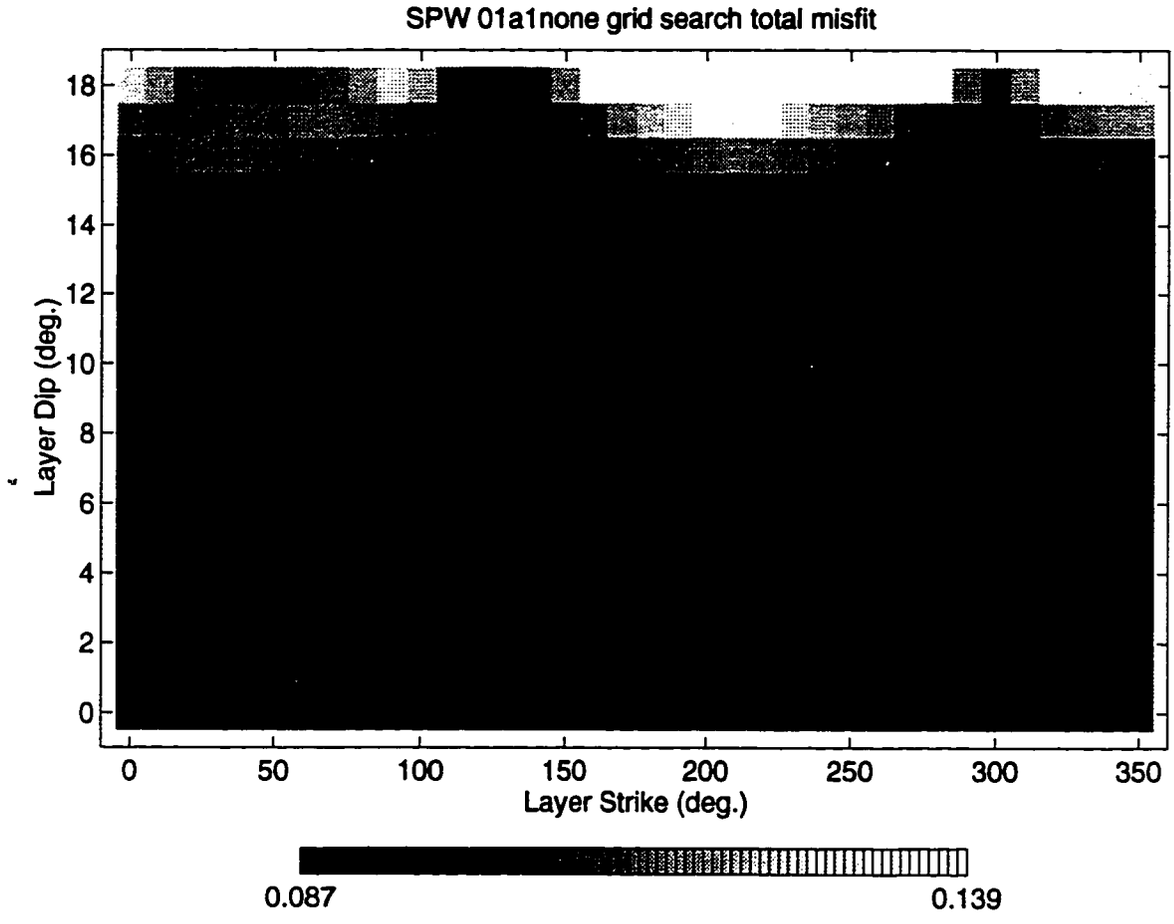

Figure 4.17: Grayscale density plot of model misfit from the grid search of a 2-D model space for the SPW shallow layered model with a top layer *P*-velocity of 3.00 km/sec. Misfit minima are confined to a narrow region of layer strike values.

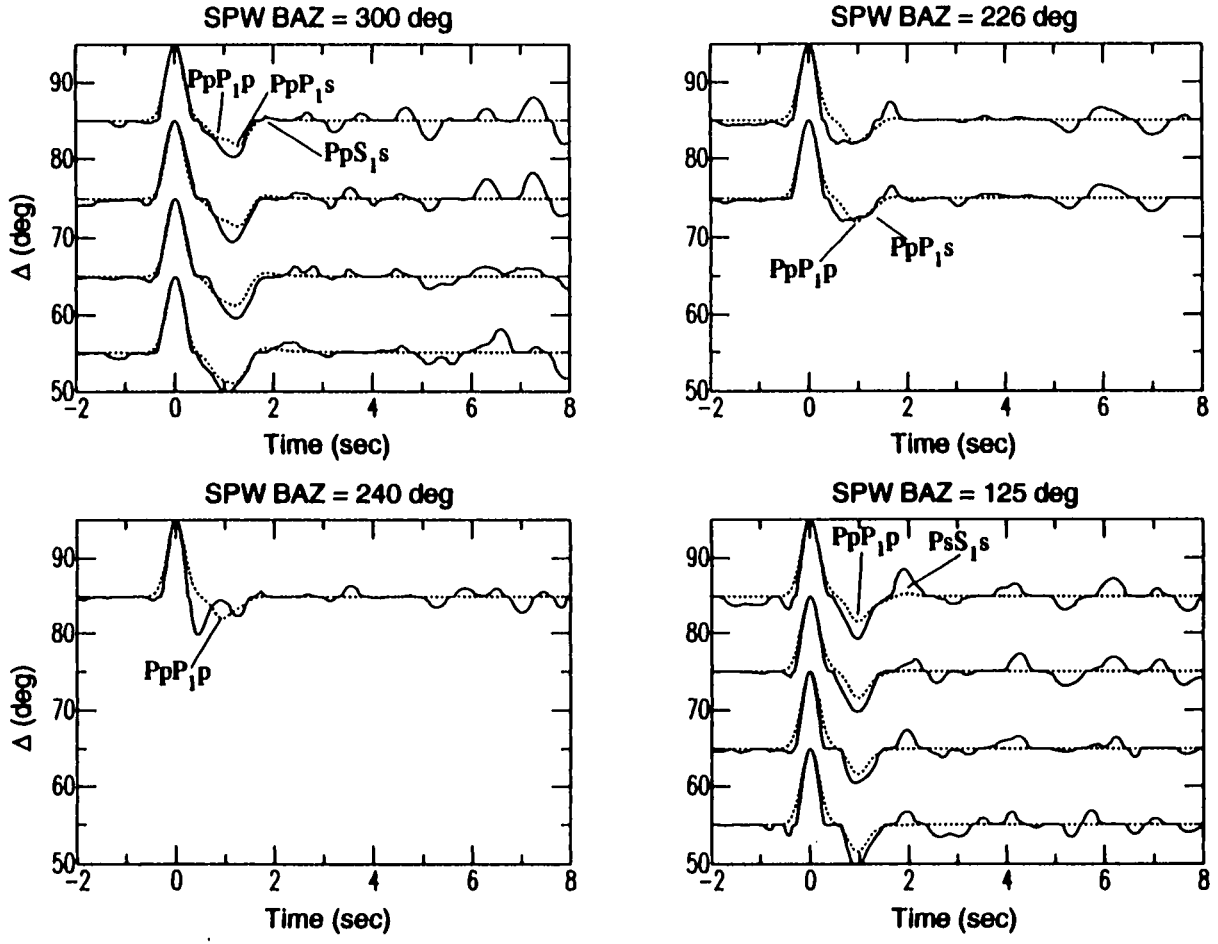

Figure 4.18: Synthetics (dashed lines) for station SPW from the best planar dipping homogeneous model compared with the 3rd-root stacked data (solid lines) plotted as record sections. See text for model parameters. Only synthetic phases with significant amplitude (> ~5%) are labeled.

replicate the broad pulse shape. The agreement of the SW BAZ=240° synthetics with the data is poor. To remedy the phase amplitude deficit of this model's synthetics, the top layer velocity was reduced to 2.50 km/sec. Since layer velocity and thickness trade off (equation 4.1), the layer thickness was in turn reduced to 1.3 km. Figure 4.19 shows the overall misfit of the synthetics for this second model have the same azimuthal distribution as the previous one. The misfit minima fall within strikes of 60°-90° and dips of 10°-11°, however the misfit minima are only slightly smaller (~3.5%) than those from the previous model. A comparison of the best fitting second model (strike=70°, dip=10°) shows that the improved overall fit is the result of larger predicted phase amplitudes (Figure 4.20), which now are generally within the $\pm 2\sigma$ error bounds of the stacked data. Model testing with a top layer velocity of 2.00 km/sec and depth of 1.1 km produced synthetics with overall misfit values (ranging from 0.088 to 0.157) similar to those of the 2.50 km/sec top layer model. The synthetic phase amplitudes for this model showed better agreement with the stacked data but did not replicate the pulse shapes well for the NW and SE BAZ data.

Shallow Modeling Discussion: The small difference between overall misfit minima from each model demonstrates the limited resolution associated with the constraint of the layer parameters (strike, dip, z and Vp). While a surface layer velocity of 2.00 km/sec may be unacceptable on physical grounds, a range of 2.50-3.00 km/sec and layer depth of 1.3-1.5 km are compatible with the results of previous investigators. From the analysis of planar dipping models we find the best fitting synthetics occur when the layer dips to the south-southeast (azimuth 160°±20°) at 12°±2°. These results are in fair agreement with the structural interpretations of *Johnson et al.* [1994] south of the Seattle fault surface expressions. The interface dip, though not well determined in their study, appears relatively gradual. The generally satisfactory waveform modeling results for the planar dipping models removes the need to investigate more complex near-surface velocity models.

SPW Deeper Crustal Structure: Standard linear stacked and linear slant stacked data from SPW (Figures 3.9 and 3.10) also show arrivals at 5.0-5.5 sec for all BAZ's. This is a negative polarity pulse with relative amplitudes of 15-25% of the direct-P exhibiting little moveout with BAZ. The likely structure implied is a relatively flat, mid-crustal interface with a discontinuous velocity increase. The velocity model initially considered for waveform modeling is a downward continuation of the best two-layer model found previously, with an additional crustal layer (Vp=6.70 km/sec, z=14.8 km) appended. The

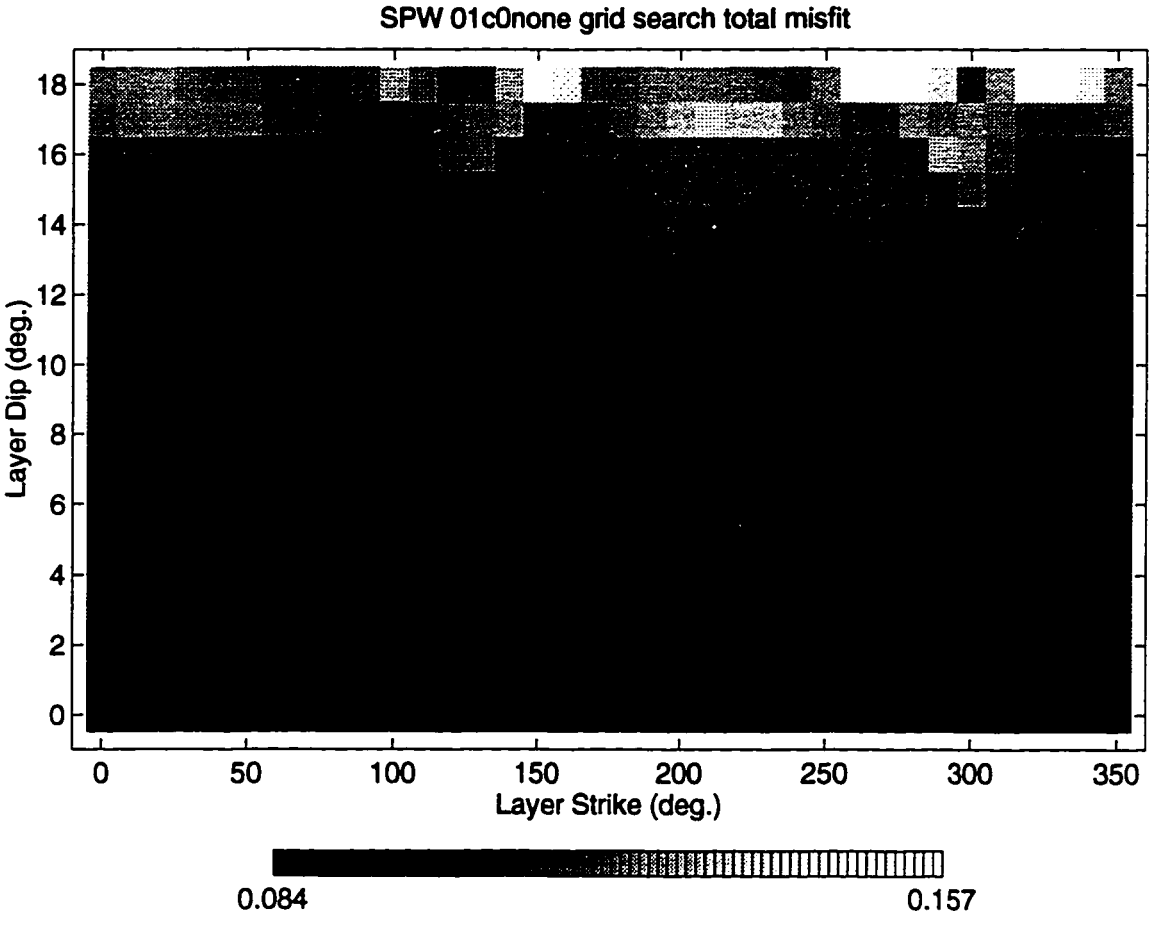

Figure 4.19: Grayscale density plot of model misfit from the grid search of a 2-D model space for the SPW shallow layered model with a reduced top layer velocity and thickness. Misfit minima are confined to a narrow region of layer strike values.

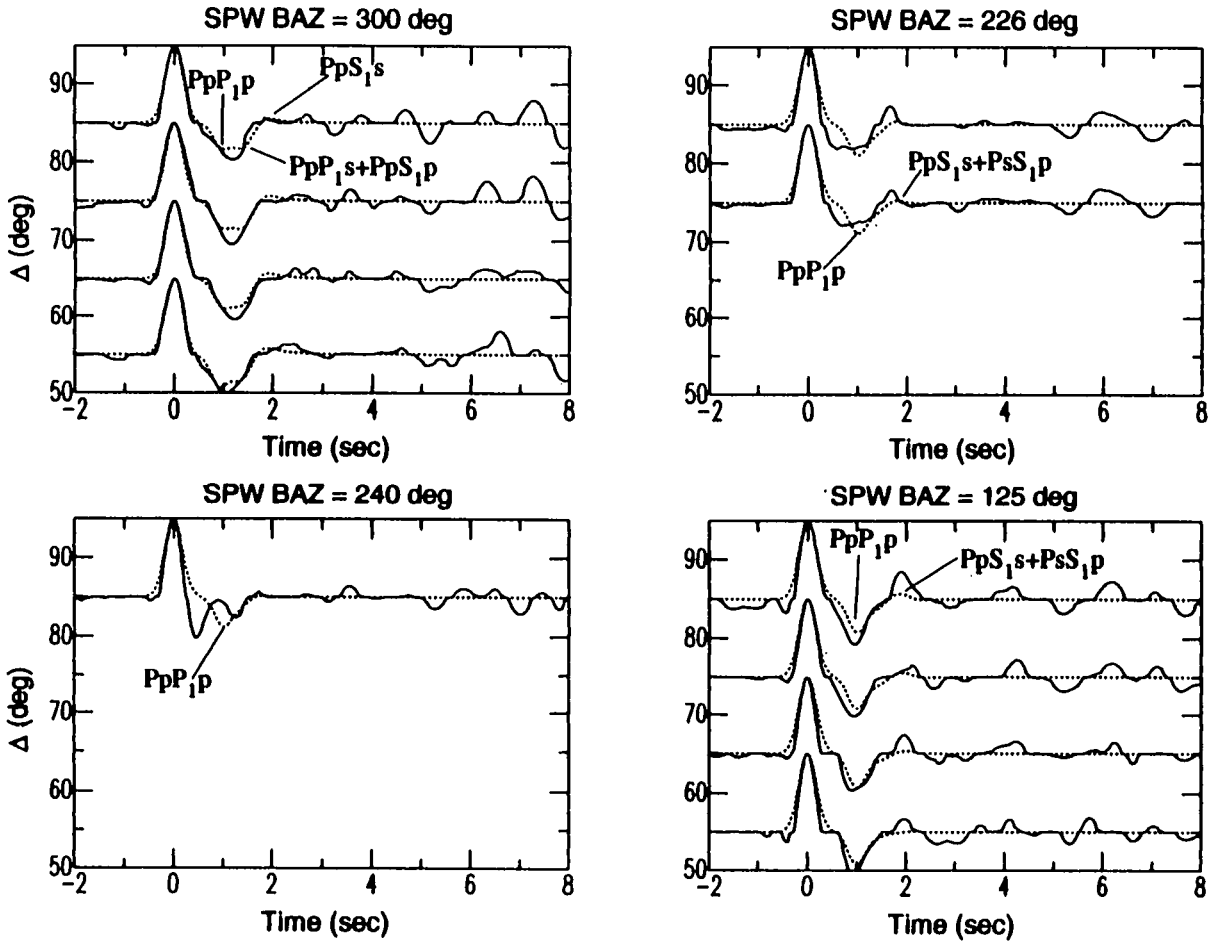

Figure 4.20: Synthetics (dashed lines) for station SPW from the best planar dipping homogeneous model compared with the 3rd-root stacked data (solid lines) plotted as record sections. The top layer velocity and thickness are reduced from the previous model (see text for model parameters). Only synthetic phases with significant amplitude (> ~5%) are labeled.

last layer velocity represents the largest reasonable mid-crustal value for the region (*Lees* [1989], *Schultz* [1993]) and the layer thickness provides appropriate phase arrival times. Assuming a planar, dipping interface, a grid search of the 2-D model space was made for best fitting models. Nearly 40% of the 684 models of the search produced the same misfit, corresponding to all strikes with dips from 0°-7°. Visual inspection of the synthetics from a few of the best fit models show that the overall fit is relatively poor due to the phase amplitude underestimation for synthetics from all BAZ's by a factor of 2-4.

We conclude that this model is not appropriate. Increasing the phase amplitudes requires either: (*i*) the impedance contrast across the interface must increase significantly, or (*ii*) the interface is non-planar, containing a irregularity which can produce ray focusing. The first case would require the bottom layer *Vp* to increase to an upper mantle value (7.80 km/sec), which is unrealistically high at depths of only 15 km. Conversely, reducing the 2nd layer velocity to 5.00 km/sec and thickness to 10.8 km produces appropriate phase amplitudes and arrival times, but these parameters significantly reduce the shallow phase amplitudes and are inconsistent with the work of previous investigators. The second option, interface topography, could produce larger amplitudes through ray focusing, but this is strongly dependent on station location relative to interface structure. As a general rule, not all BAZ's considered here (up dip, down dip and along strike) will "see" the focusing effect (see figure 4.13 for an example with the MBW shallow model).

The selection of an appropriate mid-crustal model remains enigmatic. With the modeling procedures considered in this study, we are unable to adequately model the stacked waveforms using simple models with plausible mid-crustal velocities. Significant local lateral and vertical structural heterogeneity due to the proximity of the Seattle fault and its splays, may likely contribute more signal to the *P*-coda than can be modeled using these tools.

4.4.4 Olympic Peninsula Stations (OBH, OFK, OOW, OSD, OTR, and HDW)

PNSN stations OBH, OFK, OOW, OSD, OTR, and HDW are located on the Olympic Peninsula is a region which includes two main geologic terranes (Figure 4.21). The Olympic core terrane (or Olympic subduction complex) is composed chiefly of marine sedimentary rocks (shale, siltstone and sandstone), turbidites and minor pillow basalts of Eocene to middle Miocene age [*Cady* 1975, *Tabor and Cady* 1978a, *Tabor and Cady* 1978b]. The rocks of the eastern part of the Olympic core have undergone two different middle to high-grade metamorphic events at about 30-40 Ma and 17-19 Ma [*Cady* 1975,

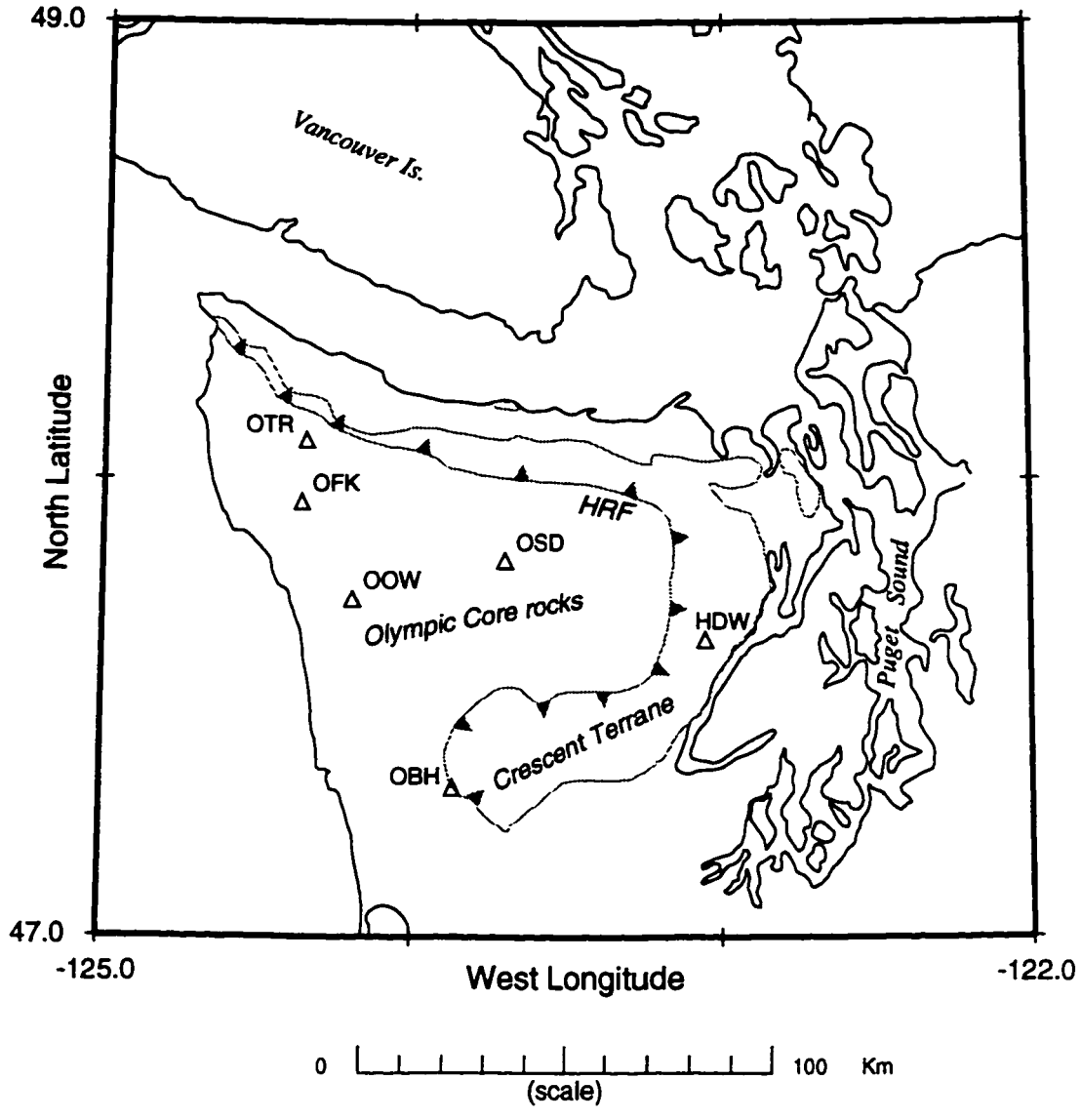

Figure 4.21: Map of Olympic Peninsula stations for which wavefrom modeling was performed. Also show are the two major terranes of the Olympic Peninula; the Crescent Terrane (units bounded in gray) and the Olympic core rocks. The two terranes are separated by steeply-dipping thrust faults, including the Hurricane Ridge Fault (HRF).

Brandon and Vance 1992], decreasing in grade from east to west. No eclogite or blueschist is found in the eastern core, but the rocks are heavily sheared and in places resemble melanges described in the Franciscan rocks of California [*Tabor and Cady* 1978b]. The east core units form long, irregular arcuate packets that are roughly concave westward. The rocks in the western Olympic core are younger, show less deformation, though folds and faults are common, and are locally continuous stratigraphically. The lithology reflects more shallow water deposition (accreted sediments) to the west.

The second Olympic Peninsula geologic terrane is the Crescent terrane (CT) or Peripheral rocks. The CT consists chiefly of the Crescent Formation (submarine and subaerial basalts up to 16 km thick near the Dosewallips River valley) and the Blue Mountain unit (marine sedimentary) [*Tabor and Cady* 1978a, *Babcock et al.* 1992]. The Crescent Formation, originally identified by *Arnold* [1906] in the Crescent Bay area, forms a horseshoe shaped unit which bounds the Olympic core rocks to the west. The rocks of the CT are separated from the core rocks by steeply dipping thrust faults, including the Hurricane Ridge and Calawah Faults, and the Southwestern fault zone [*Tabor and Cady* 1978b]. The early-to-middle Eocene-aged Crescent Formation (48-50 Ma) is the most voluminous of the Coast Range volcanic sequences that stretch from southern British Columbia to central Oregon. Originally postulated to be an accreted arc of basaltic seamounts [e.g., *Cady* 1975], the Crescent Formation is currently postulated to originate from an extrusion in a shallow rift basin in close proximity to the North American margin, the result of a mantle plume in the forearc of the subduction zone coupled with greater convergence obliquity [*Babcock et al.* 1992].

Previous structural studies: Constraint of velocity structure in the greater Olympic Peninsula region has been determined from a number of seismic studies. Offshore reflection profiles analyzed by *Shor et al.* [1968] put the oceanic moho at a depth of 18 km ~50 km west of Grays Harbor. *Taber* [1983] analyzed travel-time data from two reversed refraction profiles across the Olympic Peninsula. An E-W onshore-offshore profile from just south of Grays Harbor to Centralia tied into the *Shor et al.* [1968] profiles provided firm determination of the following: (*i*) an oceanic lithosphere dipping eastward at 9°±2°, (*ii*) a confirmation of slab continuity from the continental margin to the Puget Sound, and (*iii*) the location of the slab bend (knee) beneath the margin to within ±5 km. Mapping the Benioff zone in the vicinity of the profile verified the first two structural constraints (inferred slab dip = 11°). The second *Taber* [1983] profile, of length 280 km, trended NW-

SE extending from the JDF strait (between Clallam Bay and Striped Peak) to Elk Lake. The subsequent modeling provided the following results: (*i*) a moho dipping to the southwest (at depths of 30-40 km from NW to SE), (*ii*) a *Pn* of 7.90 km/sec (verified by *Zervas and Crosson* [1986]), and (*iii*) a mid-crustal refractor with V_p=6.70 km/sec under the core rocks with depths of 12-18 km from NW to SE, interpreted as possible Crescent Formation. *Taber* [1983] noted that the NW-SE profile model emphasizes the apparent rapid transitions in the Olympic crustal terranes.

The *Lees* [1989] tomographic study of *P*-velocity in the greater Puget Sound (with 5 km grid spacing) included the eastern-most Olympic Peninsula to PNSN stations BLN and HDW. Lees' resulting model showed higher velocities for the 6.0-9.0 km depth layer, interpreted as Crescent basalts (from BLN to HDW and GMW). The high velocity feature continues to greater depths (9.0-12.0 km) and possibly further east, indicating an eastward dipping structure. The next layer (z=12.0-16.0 km) shows high velocities of the Crescent basalts further south (to the southern end of Hood canal) and an indication of the low velocity Olympic core rocks to the west underthrusting the Crescent basalts. From a 2-D MT survey across the eastern Olympic Peninsula, *Aprea* [1996] identified a highly resistive surface unit ~20 km wide, thickening to the east, also interpreted as the Crescent basalts.

Structural constraint at oceanic and continental moho depths, including the existence of an arched subduction slab in the vicinity of the Olympic Peninsula and beyond, are provided from Benioff zone cross-sections [*Crosson and Owens* 1987, *Weaver and Baker* 1988], single station teleseismic receiver functions [*Owens et al.* 1988, *Lapp et al.* 1990, *Edlund* 1991, *Cassidy* 1991], a onshore-offshore reflection/refraction profile near Corvallis, Oregon [*Tréhu et al.* 1994; 1995], and a membrane deformation study [*Chiao* 1991]. The inferred slab geometry from southern British Columbia to northern Oregon is shown in Figure 1.2. Firm structural constraint of the slab geometry in the Olympic Peninsula is noticeably absent; contours are simply interpolated. The analysis of stacked waveforms from the 6 Olympic stations (see Fig. 4.21) considered below should provide some insights into the structure of this area.

Station OBH: Standard linear stacks and linear slant stacks of OBH data (Figures 3.11 and 3.12) show two distinct arrivals, which add coherently over many of the BAZ's at ~2.0 sec and 7.0-8.0 sec. Both arrivals are most prominent in the stacked data from BAZ=226°-280°, with phase amplitudes well beyond the $\pm 2\sigma$ error bounds. This is likely due in part

to the large number of good signal-to-noise waveforms for events from these source regions. The NW BAZ=300° stacks show just one stack (Δ=55°) with a statistically significant phase arriving at 6.5-7.5 sec, smaller in amplitude than those from other BAZ's. Because of the lack of statistically significant phases, data from this BAZ will be down-weighted or removed from the overall model fitness determination. The NW BAZ=280° stack however, does show a significant arrival at 7.0-7.5 sec. The negative polarity and lapse time arrival identify the 7.0-8.0 sec phase as a likely oceanic moho (OM) phase. The OM depth in the western Olympic Peninsula is expected to be shallow (≤ 30 km).

A starting model based on the refraction models of *Taber* [1983] was used for forward modeling. Table 4.6 lists the parameters of the homogeneous, three-layer starting model. This model has an average crustal velocity of 6.34 km/sec and a moho depth of 25.5 km.

Table 4.6: OBH starting model TS2

Layer #	Vp (km/s)	Vs (km/s)	ρ (g/cm^3)	z (km)
1	5.90	3.41	2.55	11.5
2	6.70	3.87	2.80	25.5
3	8.00	3.46	3.36	∞

The relatively high velocity of the top layer reflects the proximity of this station to the Crescent Terrane (see Figure 4.21). Noting the *a priori* constraint of a dipping interface, forward modeling using the *ray3d* method was used to find the best fitting dipping OM model (assuming a planar interface). An initial coarse 3-D grid search was made to determine the interface depth. This was followed by a model 2-D grid search through interface strikes and dips ranging from 0°-350° and 0°-18° respectively, provided the overall misfits show in Figure 4.22. Here the rms amplitude misfit window is set between 8.0 and 15.0 sec and includes only those stacks with significant phases (ie. this excludes BAZ=300° data). Models with strikes from 20°-80° and dips from 2°-10° provide the best fit to the data. Synthetics for the model striking at 70° and dipping at 4° are compared with the stacked data in Figure 4.23 and show the dominate synthetic phase is *PpPmp*. The SW BAZ synthetics have good phase arrival time agreement with the data but underestimate amplitudes (by 35-50%). The SE BAZ synthetics also show fairly good arrival time

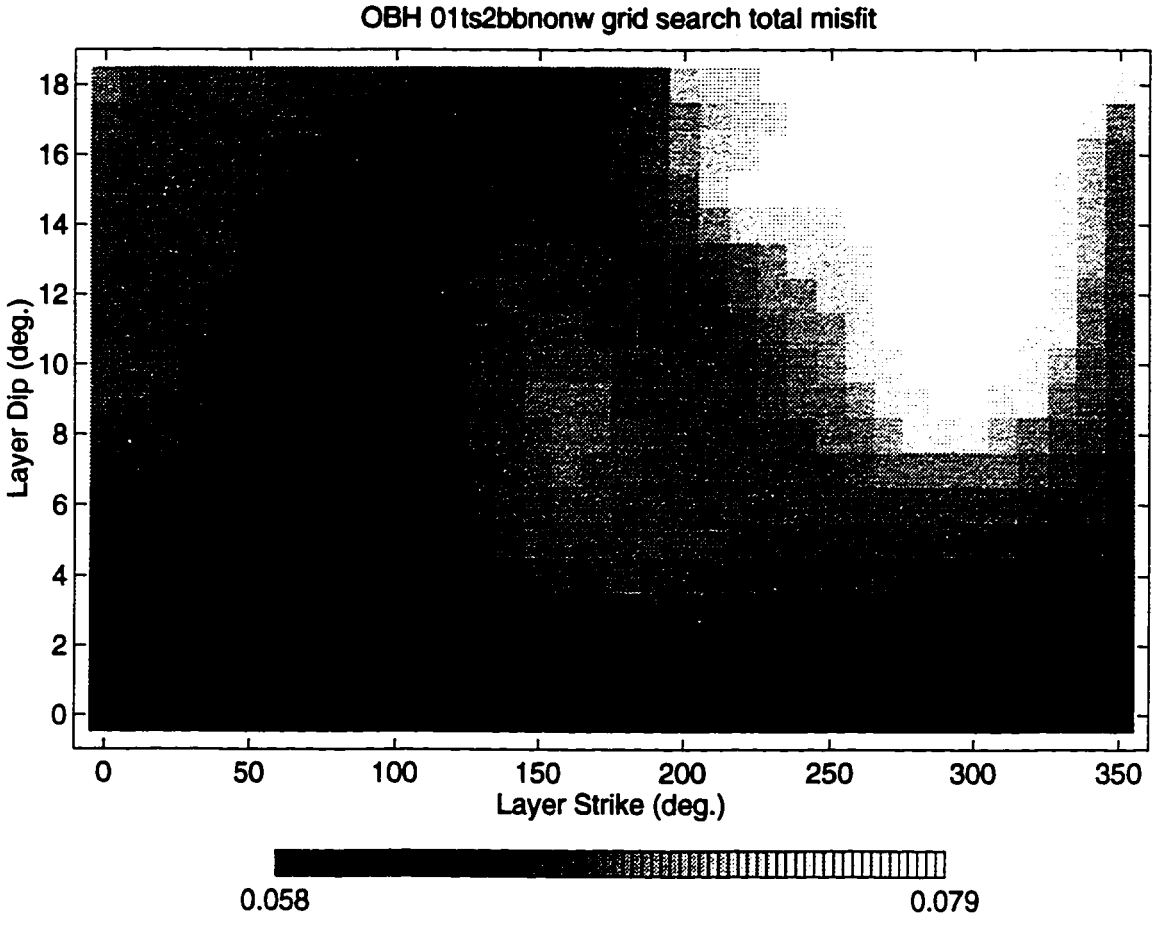

Figure 4.22: Grayscale density plot of model misfit from the grid search of a 2-D model space for the starting OBH layered model, with oceanic moho at a depth of 25.5 km. Misfit minima are confined to a narrow region.

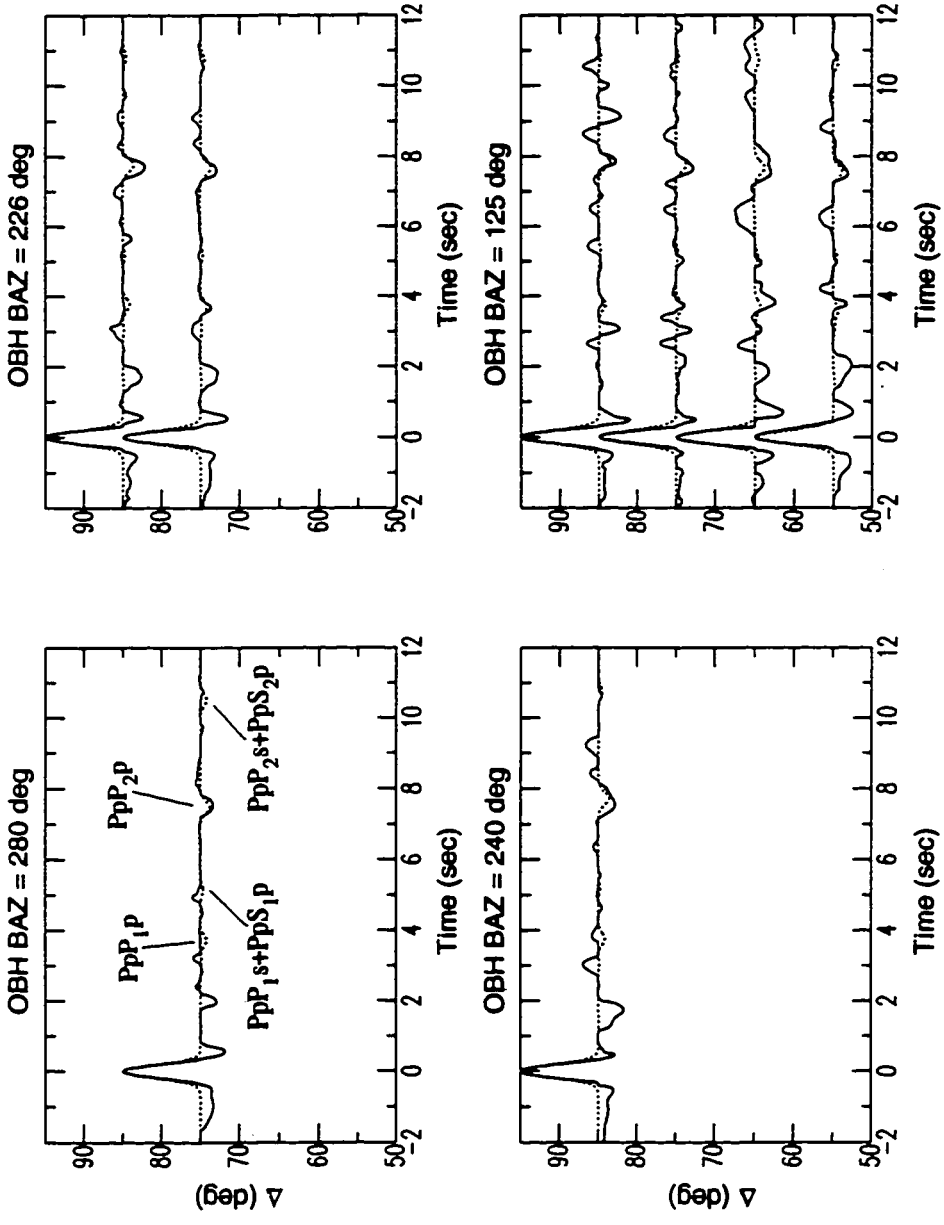

Figure 4.23: Synthetics (dashed lines) for station OBH from the best planar dipping OM model compared with the 3rd-root stacked data (solid lines) plotted as record sections. See text for model parameters. Only synthetic phases with significant amplitude (> ~5%) are labeled.

agreement, and the predicted moveout with Δ (0.01 sec/deg) is also in agreement with that observed. Phase amplitudes of the SE BAZ synthetics are also slightly underestimated (by 30-40%). The phase arrival for synthetics from BAZ=280° is ~0.2 sec early, with the amplitude underestimated by 28%. For all BAZ's, the predicted phase amplitudes fall outside of the $\pm 2\sigma$ bounds associated with each linear stack.

On the whole, this model parameterization provides reasonable predicted arrival times and phase moveouts with Δ for the stacked data that demonstrate clear, significant phases. The strike and dip ranges for the misfit minima provide qualitative uncertainty estimates for these values. A summary of best fitting parameters for this model are: strike=50±30° and dip=6±4°.

A second model with an additional surface layer was tested. The top layer was introduced in an effort to model the observed early-arriving phases. The specific model parameters are listed in Table 4.7 below. This modified model has an average crustal

Table 4.7: Second OBH layered model TS8

Layer #	Vp (km/s)	Vs (km/s)	ρ (g/cm^3)	z (km)
1	4.00	2.31	2.30	3.5
2	5.90	3.41	2.55	10.0
3	6.70	3.87	2.80	24.0
4	8.00	3.46	3.36	∞

velocity of 6.09 km/sec and OM depth of 24.0 km. The average crustal velocity is somewhat low for this region (*Taber* [1983]) and can be considered a end member of possible values.

A grid search of the model space for a dipping OM was made as before. The overall misfit distribution (Figure 4.24) shows minima with strikes ranging from 300°-90° and dips ranging from 1°-14°, and an overall misfit trend similar to that in Figure 4.22. A comparison of the synthetics from one of the best fitting models (strike=0° and dip =3°) with the stacked data (Figure 4.25) gives results similar to those from the starting model TS2. A wide range in strikes and dips for the best fitting models demonstrates the relative insensitivity of this parameterization to model variation. Like the previous model,

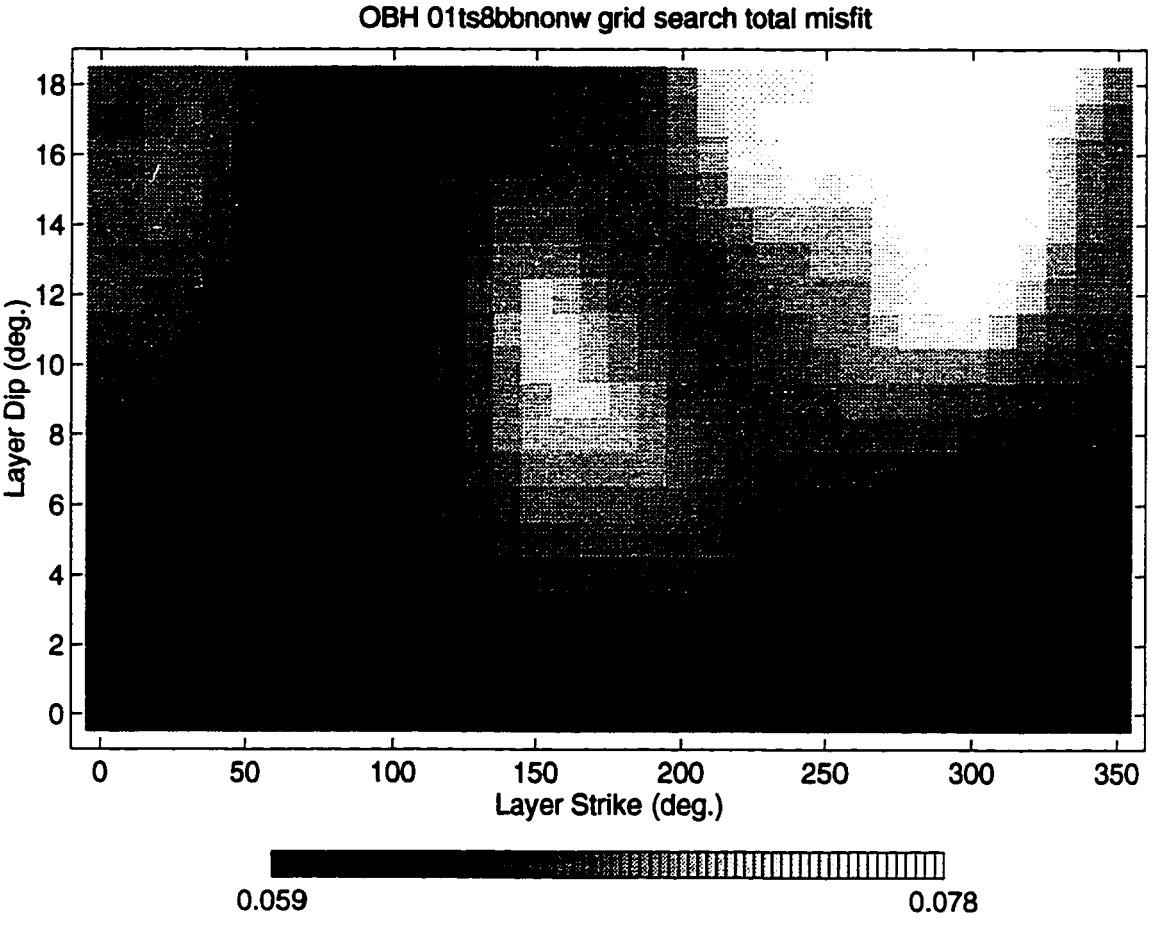

Figure 4.24: Grayscale density plot of model misfit from the grid search of a 2-D model space for the second OBH layered, model with oceanic moho at a depth of 24.0 km. Misfit minima fall in a broader region.

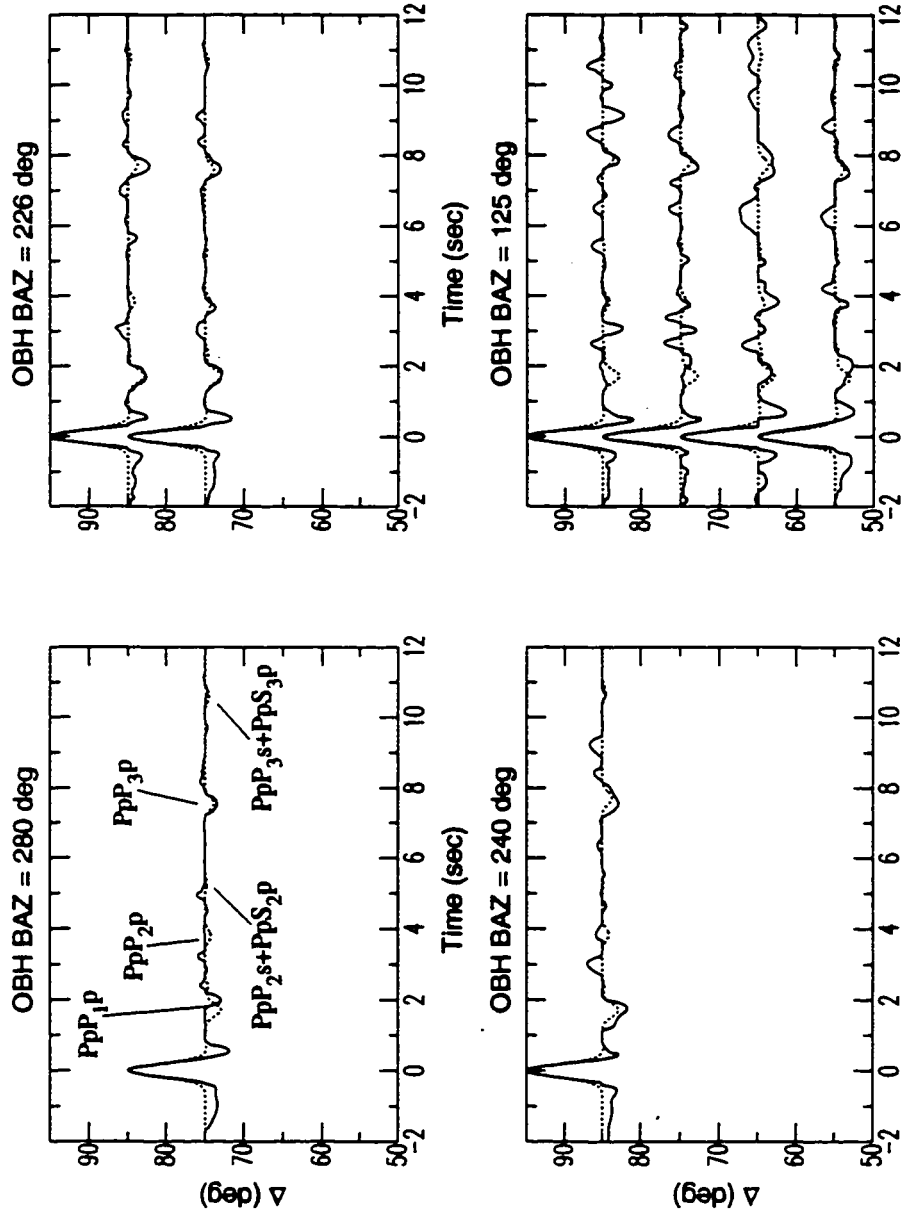

Figure 4.25: Synthetics (dashed lines) for station OBH from the best planar dipping OM model compared with the 3rd-root stacked data (solid lines) plotted as record sections. See text for model parameters. Only synthetic phases with significant amplitude (> ~5%) are labeled.

however the phase amplitudes are underestimated for all BAZ's (Figure 4.25). From the fitness criterion this appears to be as good a model as the starting model, as the misfit minima are not significantly different from those of the starting model). Whether this second parameterization is physically plausible remains to be seen.

To generate synthetic phase amplitudes that rival the observed values requires an even greater impedance contrast at the OM than is found in the two above models. By adding a 1.0 km thick layer with Vp=5.90 km/sec and ρ=2.70 g/cm^3 to either model above the oceanic moho (increasing the impedance contrast by ~15%), adequate phase amplitude for all but the BAZ=226°, Δ=75° synthetics can be achieved. A layer this thin cannot be resolved by this data, but that is not the intent here. The layer thickness is made minimal so as to not significantly change the average crustal velocity while producing a greater impedance contrast. Conversely, increasing mantle Vp and ρ values will produce similar synthetic phase amplitude results. This result suggests that for the planar, layer model parameterization, a large impedance contrast (greater than expected for "standard" deep crustal and upper mantle velocities) is present across the OM beneath station OBH.

A survey of the modeling results for station OBH indicates that the *ray3d* model parameterization, with a planar interface assumption, is reasonably valid. The dipping OM models tested provide a OM at depths of 24.0-25.5 km, dipping to the east-southeast. Each model produced a range of strikes and dips corresponding to misfit minima, with the second model having a larger range for each. An F-test of these best strike and dip variances shows the first model has significantly lower variances for both layer strike and dip. In addition, noting that the first model average crustal velocity ($\overline{V}p$=6.34 km/sec) is more consistent with Taber's value ($\overline{V}p$=6.38 km/sec) we find the first model to be more appealing. From the model misfit minima distribution in Figure 4.22 then we conclude the OM dips at 6±4° to the east-southeast at a strike of 50±30° with a depth of 24.7 km.

Station OFK: Standard linear stacks and linear slant stacks of OFK data (Figures 3.13 and 3.14) show two distinct arrivals, which are coherent over many of the BAZ's, at ~1.0 sec and 7.0-8.0 sec. The 1.0 sec arrival is apparent in the stacks from all BAZ's but the SE, where only the Δ=85° phase amplitude emerges beyond the $\pm 2\sigma$ error bounds. The relatively large amplitude of this arrival suggests a large impedance contrast interface. The 7.0-8.0 sec arrival is indicated as a significant arrival with phase amplitude beyond the $\pm 2\sigma$ error bounds for all but the BAZ=240° stacked data. The slant stacks of NW and SE BAZ data show the second phase has moveouts with Δ from 0.00 to -0.005 sec/deg and

0.01 to -0.005 sec/deg, respectively. A third phase arriving near 3.0 sec is apparent in only half of the standard linear stacks and just in the SE BAZ linear slant stacks.

A starting model based on the Olympic Peninsula refraction models of *Taber* [1983] was used for forward modeling. Table 4.8 lists the parameters of the homogeneous, four-layer starting model. The interface depths and impedance contrasts for layers 1 and 2 were determined by fitting the 1.0 and 3.0 sec phase arrivals using horizontal interface models. The CM depth, z=24.7 km, was determined from a coarse 3-D grid search over strike, dip and depth, as well as trial and error modeling of flat OM models. The average crustal velocity of model 01A1 is 6.14 km/sec. This model has a lower average crustal velocity relative to the OBH model ($\bar{V}p$=6.38 km/sec), reflecting the station's location in the western Olympic core rocks (figure 4.21).

Forward modeling using the *ray3d* parameterization was used to find the best fitting

Table 4.8: OFK starting model 01A1

Layer #	Vp (km/s)	Vs (km/s)	ρ (g/cm^3)	z (km)
1	2.50	1.44	2.25	1.5
2	5.20	3.00	2.55	6.5
3	6.70	3.87	2.80	24.7
4	8.00	3.46	3.36	∞

dipping OM model. With the OM depth fixed, a 2-D model grid search was made over OM strike and dip. Results of the model space grid search show misfit minima fall in a range of strikes, 0°-70° and dips, 8°-15° (Figure 4.26). A comparison of the synthetics from one of the misfit minima models (stike=30°, dip=11°) with the stacked data shows general agreement between predicted and observed phase arrival times for the OM reflection, *PpPmp* (Figure 4.27). The predicted moveout with Δ for the SE BAZ data is comparable with the stacked data, however the predicted moveout for the NW BAZ is too large. In light of the fact that the confidence in the BAZ=300° stacked data phase arrivals is just above the ±2σ error bounds, the poor model moveout prediction is not as serious as if it had involved the SE BAZ data. Predicted phase amplitude on the whole underestimate the observed amplitudes by a factor of 1.4 to 4. Additionally, the two early phases at ~1.2 and 3.0 sec show generally good arrival time and amplitude agreement with

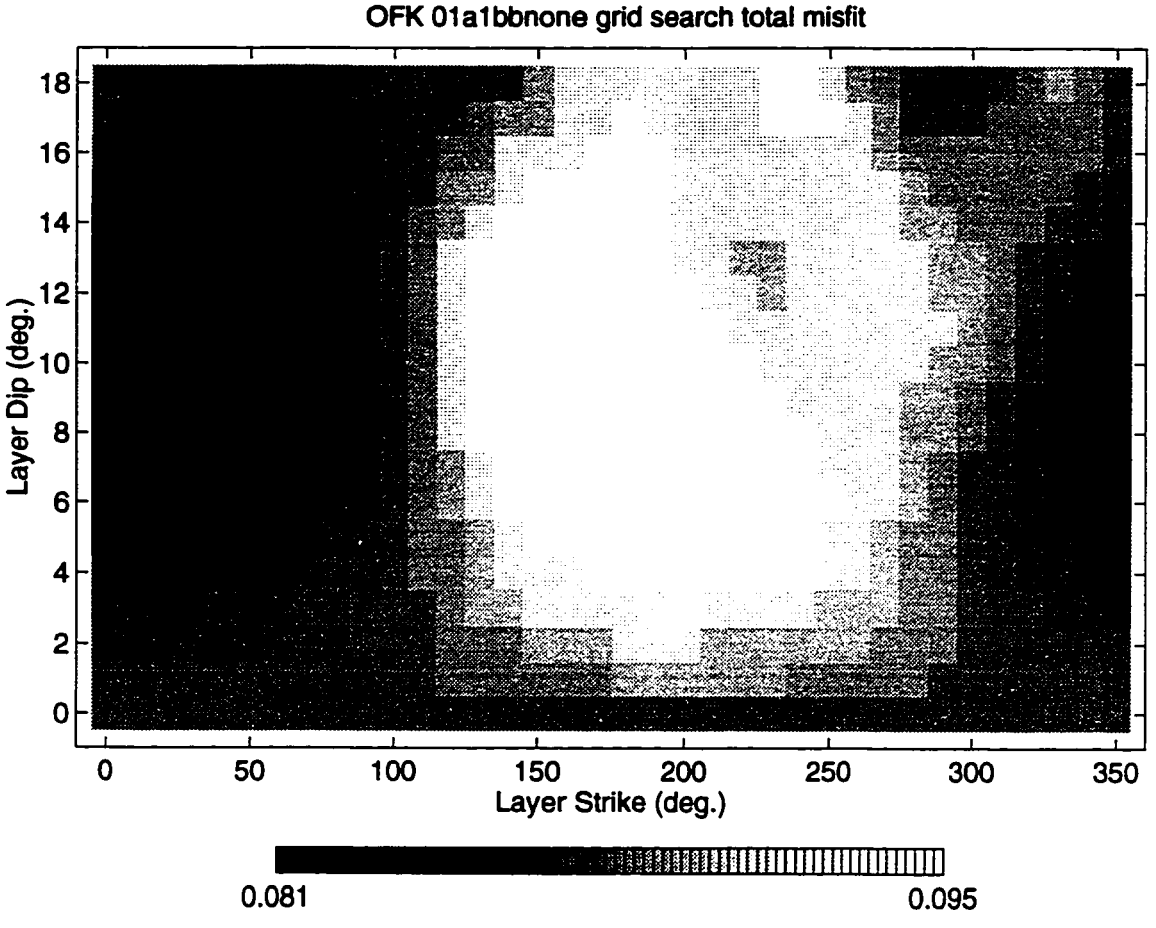

Figure 4.26: Grayscale density plot of model misfit from the grid search of a 2-D model space for the starting OFK layered, model with oceanic moho at a depth of 24.7 km. Misfit minima fall in a broader region.

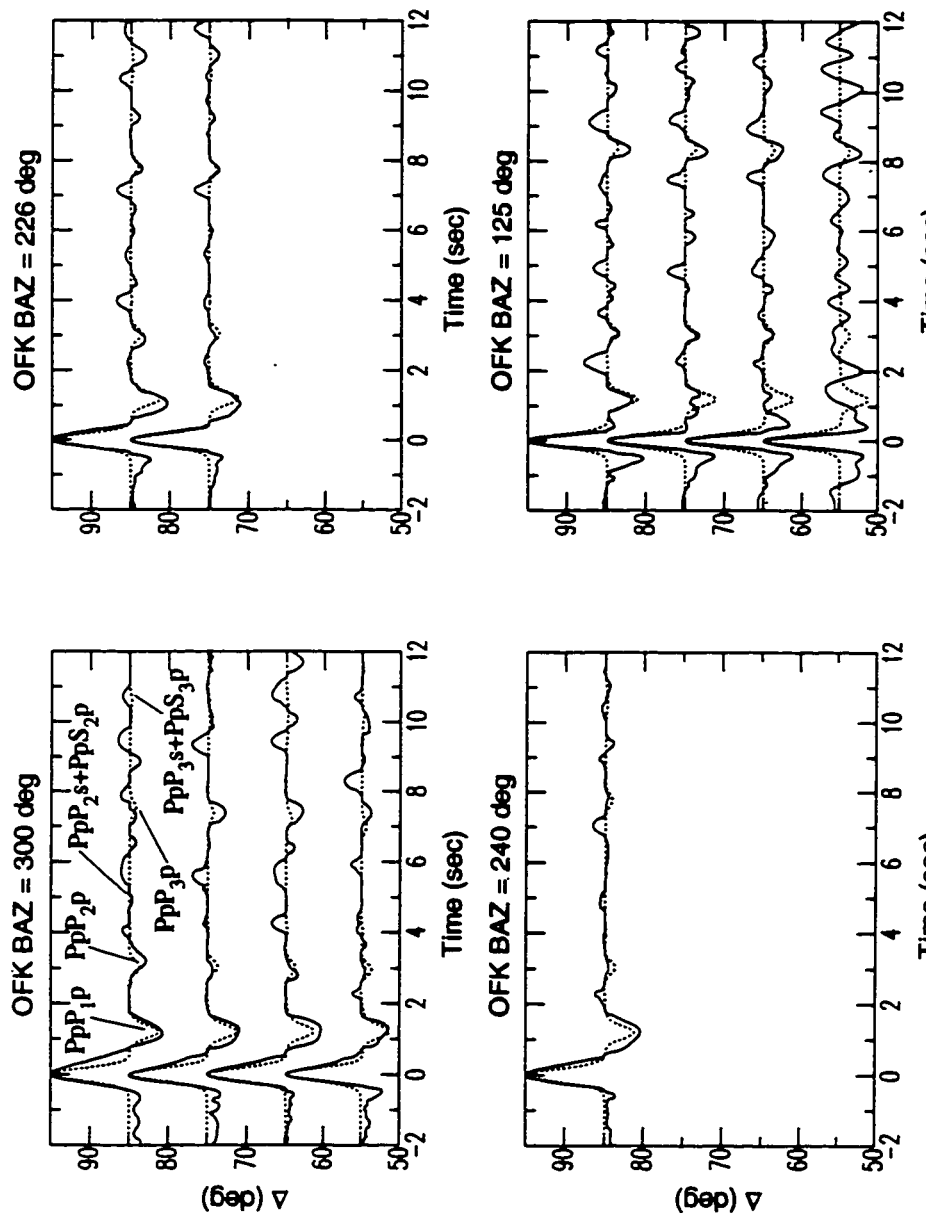

Figure 4.27: Synthetics (dashed lines) for station OFK from the best planar, dipping homogeneous model compared with the 3rd-root stacked data (solid lines) plotted as record sections. See text for model parameters. Only synthetic phases with significant amplitude (> ~5%) are labeled.

those stacked waveforms with statistically significant arrivals (although no attempt has been made to model these phases with anything other than flat model layers).

As was seen with the OBH models, this model produces OM phases with insufficient amplitudes. Like the case for station OBH, the remedy attempted is the introduction of an additional 1 km thick layer on top of the oceanic mantle with a velocity of 5.90 km/sec and density of 2.70 g/cm^3 to increase the impedance contrast (model 01B1). A new 2-D grid search of the model space shows misfit minima in a range of strikes (350°-70°) and dips (9°-15°). The spatial distribution of the misfits is very similar to that of the previous model (Figure 4.28). A comparison of the synthetics from one of the misfit minima models (stike=0°, dip=11°) with stacked data shows an improvement in the predicted phase amplitudes (Figure 4.29) with most falling within the stacked amplitude $\pm 2\sigma$ error bounds. Reducing the layer velocity even further to 5.20 km/sec and density to 2.60 km/sec (impedance contrast increase of 28%), produces synthetic amplitudes that for all BAZ's are within the observed stack $\pm 2\sigma$ error bounds.

The modeling results for station OFK indicate that the *ray3d* model parameterization appears reasonably valid. The dipping OM models tested provide a OM at a depth of 24.7 km, dipping to the east-southeast for a average crustal velocity of 6.14 km/sec. While the model grid searches produced a range of similar strikes and dips corresponding to misfit minima, the improved predicted OM phase amplitudes of the second model (Fig. 4.29) favors it over the starting model. From the model misfit minima distribution of model 01B1, we conclude the OM dips at 12±3° to the east-southeast with a strike of 30±40°.

Station OOW: Standard linear stacks and linear slant stacks of OOW data (Figures 3.15 and 3.16) show an arrival which adds coherently and is apparent from most BAZ's arriving at 7.0-8.0 sec. For those stacks with more than one trace (plotted with error bounds in Figure 3.15), this phase is somewhat weak, but emerges beyond the $\pm 2\sigma$ error bounds for all but the SE BAZ data at Δ=65°. The weak amplitudes and wider error bounds associated with this phase (especially for the NW and SE BAZ data) suggest that the signal-to-noise ratio may be marginal. This phase shows little moveout with BAZ. The linear slant stacks reveal this phase has the same moveout with Δ, between -0.005 sec/deg and 0.01 sec/deg. for both SE and NW BAZ data. The polarity and relative arrival time identify this phase as a likely OM reflection. An early phase at ~2.0 sec is also apparent in the stacks from southern BAZ's. From NW BAZ stacked data, this early phase is difficult to identify.

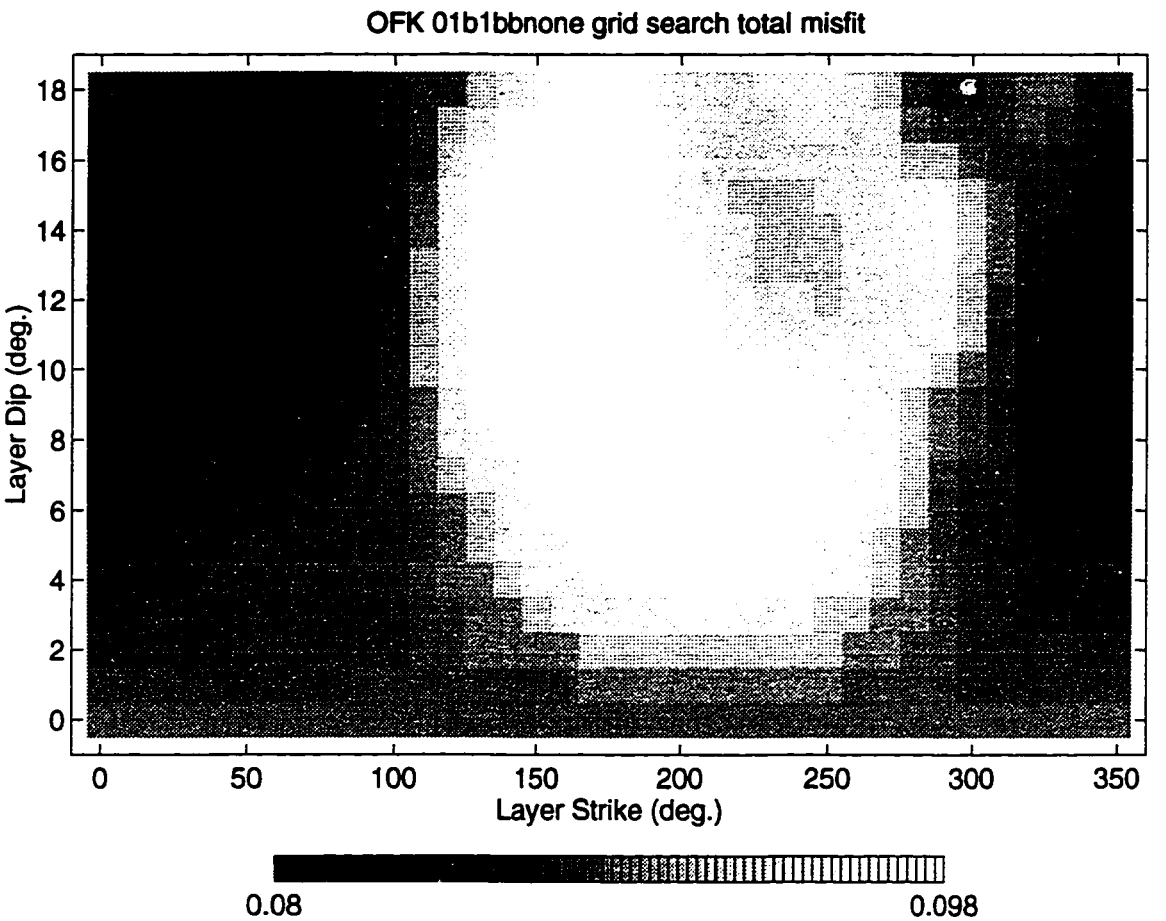

Figure 4.28: Grayscale density plot of model misfit from the grid search of a 2-D model space for the second OFK layered, model with oceanic moho at a depth of 24.7 km. Misfit minima fall in a broader region.

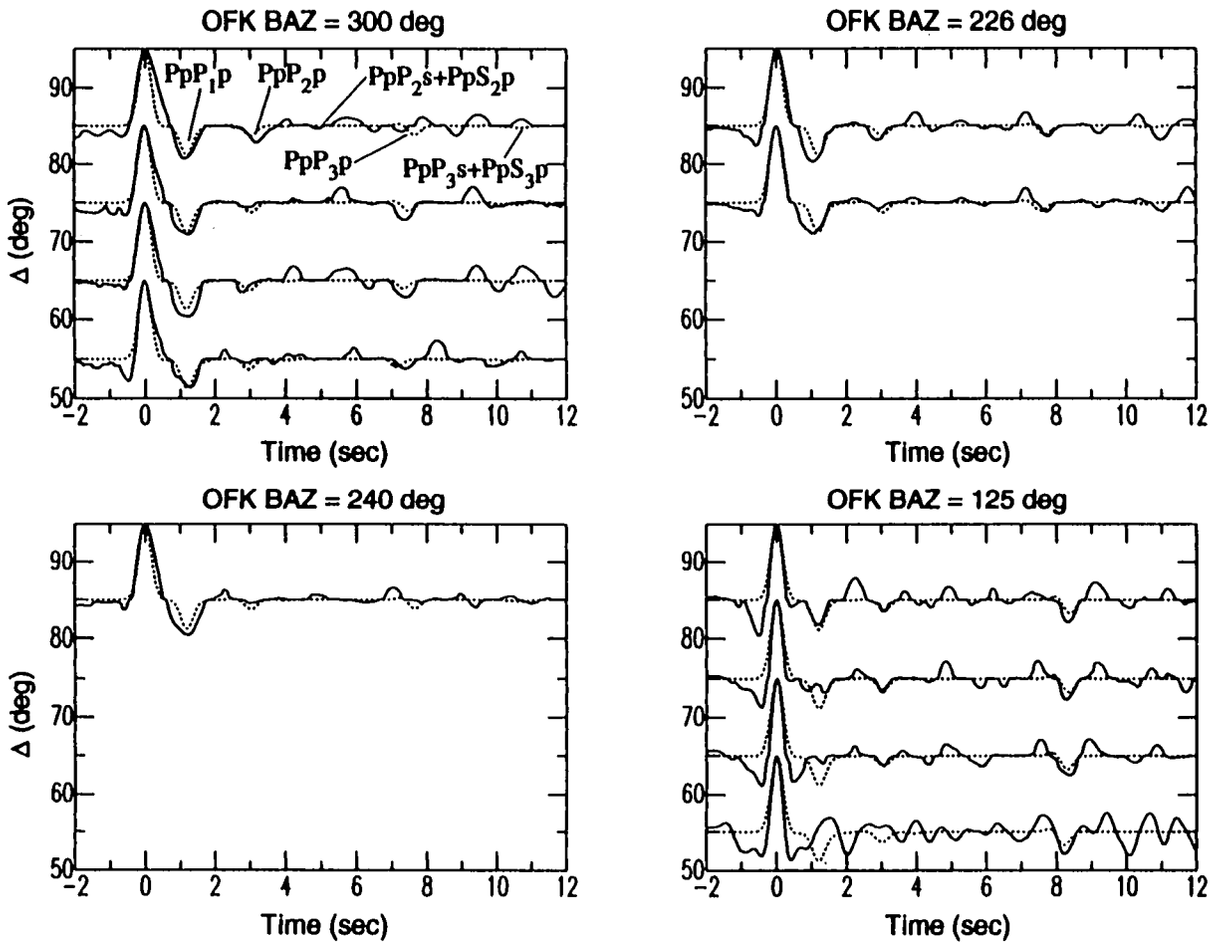

Figure 4.29: Synthetics (dashed lines) for station OFK from the second planar, dipping homogeneous model compared with the 3rd-root stacked data (solid lines) plotted as record sections. See text for model parameters. Only synthetic phases with significant amplitude (> ~5%) are labeled.

The starting model for station OOW is similar to the starting model for station OFK. The model parameters of the homogeneous starting model are given below in Table 4.9. Like station OFK, OOW is located in the western Olympic core rocks (Fig. 4.21) but does

Table 4.9: OOW layered model 01A1

Layer #	Vp (km/s)	Vs (km/s)	ρ (g/cm^3)	z (km)
1	3.00	1.73	2.30	2.7
2	5.20	3.00	2.55	8.5
3	6.70	3.87	2.80	22.0
4	8.00	3.46	3.36	∞

not show the same shallow, strong reflector apparent in the OFK stacked data. As a result, the top layer velocity is set slightly higher at 3.00 km/sec. The thickness of the top layer was determined from a trial and error fitting of the 2.0 sec phase arrival times with a flat layer model (*ray3d*). The average crustal velocity of this model is 5.85 km/sec. This compares with the 5.80 km/sec average determined by *Taber* [1983].

Initial determination of a best fitting dipping OM model was undertaken using *ray3d* with planar interface velocity models. As with previous stations, the OM model depth was constrained first. Then a grid search of the standard 2-D model grid over interface strike and dip was made, producing the overall misfit distribution show in Figure 4.30. These overall model misfits only include misfits from synthetics where the stacked data included more than a single trace (this excludes BAZ=300°, Δ=85° and BAZ=125°, Δ=55° data). The model space misfit minima fall in a range of strikes (between 230°-290°) and dips (between 4°-9°). A comparison of the synthetics associated with a misfit minima (strike=260° and dip=5°) shows good phase arrival time agreement for all BAZ's as well as good phase amplitude replication for all BAZ's (Figure 4.31). The predicted amplitude deviations here are beyond observed amplitudes ±2σ error bounds, for the SE BAZ synthetics at Δ=75°and 85°. Predicted phase amplitudes from the SW BAZ synthetics are the best. The SE BAZ synthetics predict a phase moveout with Δ which is at the upper limit of observed moveout. The predicted phase moveout with Δ of the NW BAZ synthetics (0.008 sec/deg) is also in good agreement with the observed moveout. On the whole, this model does a good job of fitting all general features of this phase in the stacked

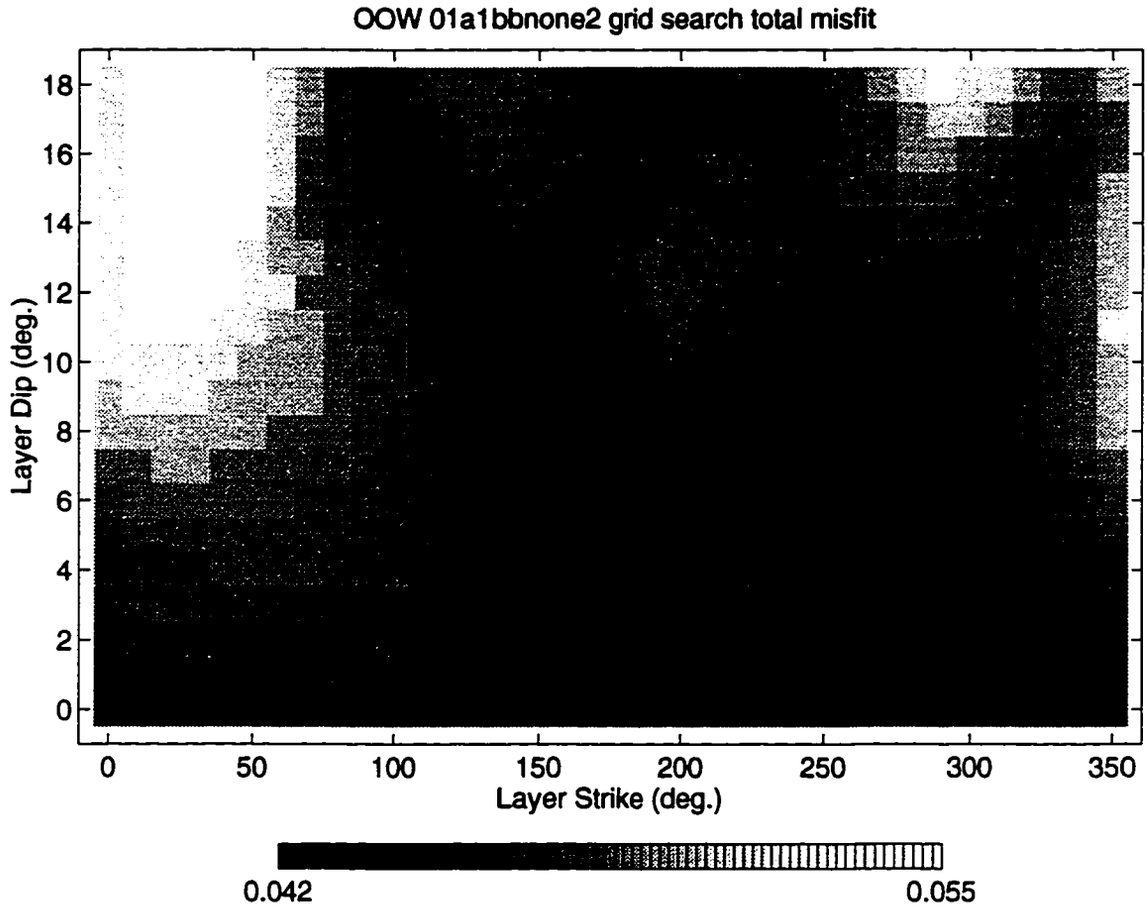

Figure 4.30: Grayscale density plot of model misfit from the grid search of a 2-D model space for the OOW layered, model with oceanic moho at a depth of 22.0 km. Misfit minima fall in a broader region.

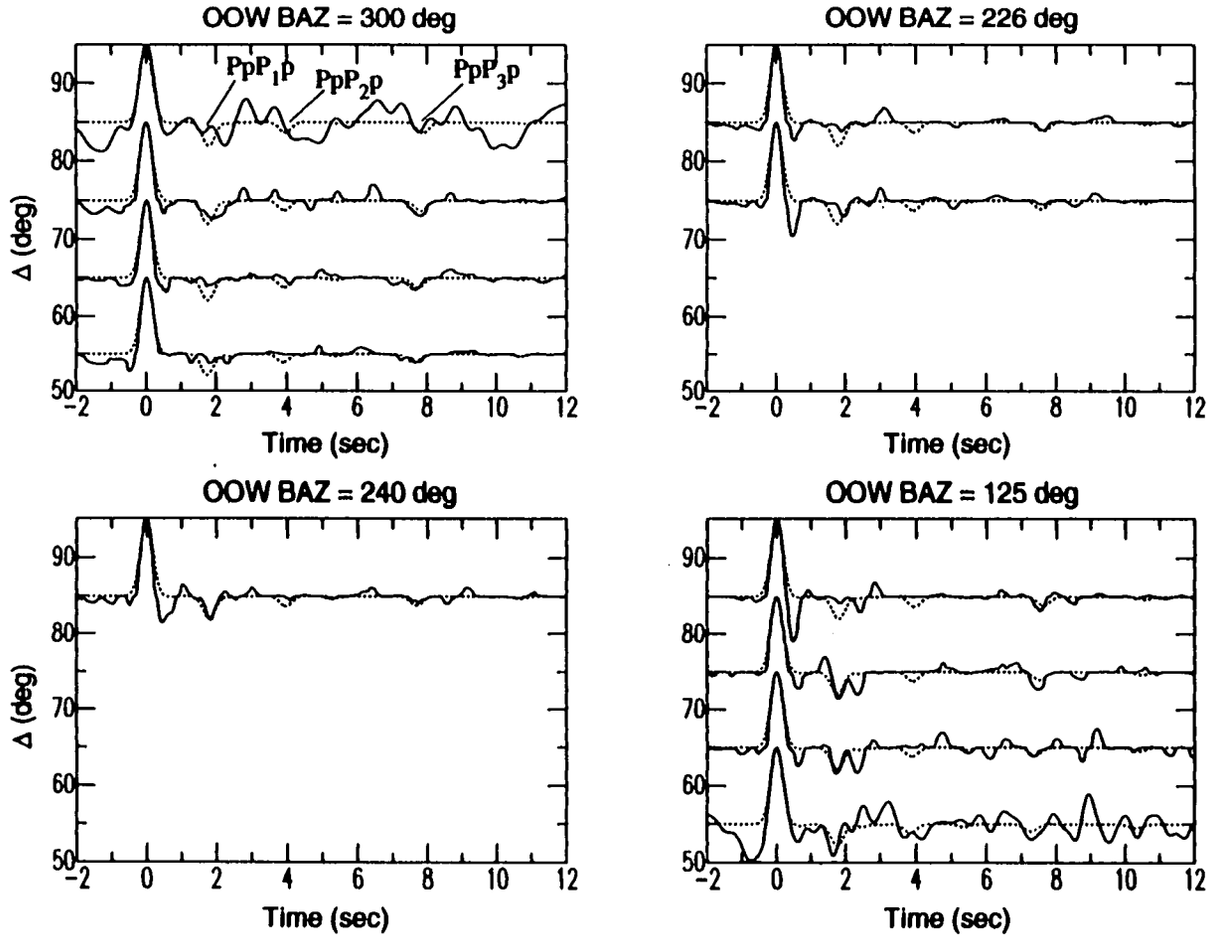

Figure 4.31: Synthetics (dashed lines) for station OOW from the best planar dipping OM model compared with the 3rd-root stacked data (solid lines) plotted as record sections. See text for model parameters. Only synthetic phases with significant amplitude (> ~5%) are labeled.

waveforms. There is no perceived need to consider models which contain additional structural complexity.

A summary of the modeling results for station OOW provides a OM at a depth of 22.0 km dipping at 6.5±2.5° and striking at 260±30° (north-dipping). The average crustal velocity is 5.80 km/sec.

Station OSD: Standard linear stacks and linear slant stacks of OSD data (Figures 3.17 and 3.18) show a number of arrivals which add coherently over most of the BAZ's, arriving at 1.0-2.0 sec, 2.5-3.0 sec, 4.5-5.5 sec, and 7.5-8.0 sec. Arrivals are most prominent is the stacked data from BAZ=226°-280°, showing amplitudes well beyond the $\pm 2\sigma$ error bounds. For stacked data from the SE and NW=300°, the later arrivals are just at or beyond the $\pm 2\sigma$ error bounds. This probably reflects marginal data signal-to-noise ratios. Both later phases exhibit some moveout with Δ and BAZ. The phase arrival travel times, negative polarity, and amplitudes suggest it as a possible OM reflected phase.

Station OSD is centrally located in Olympic core rocks (Fig. 4.21) just north of Mt. Olympus and well east of stations OFK and OOW. From the *Taber* [1983] 1-D velocity model parameterization of the Olympic Peninsula, OSD is associated with more crustal material and a deeper OM at z=30 km. The average crustal velocity is 5.95 km/sec for this portion of Taber's model. The starting model considered for station OSD is similar to the models for station OFK and OOW, but does not contain the low velocity surface layer of the OFK model. Preliminary travel time modeling of the 7.5-8.0 sec arrival indicates a more shallow OM than indicated by *Taber* [1983] at 30 km depth. The model parameters for the subsequent homogeneous starting model are given below in Table 4.10. The average crustal velocity of this model is 5.71 km/sec with the OM at 24.0 km.

Using *ray3d* for forward modeling, a 2-D grid search was made over the standard model

Table 4.10: OSD starting model 01A2

Layer #	Vp (km/s)	Vs (km/s)	ρ (g/cm^3)	z (km)
1	4.00	2.31	2.35	3.0
2	5.20	3.00	2.55	13.5
3	6.70	3.87	2.80	24.0
4	8.00	3.46	3.36	∞

space (OM strike and dip), returning the overall misfit distribution shown in Figure 4.32. This distribution represents model misfits from stacked data that represent the most significant stacked phases. This excludes data from SE BAZ's where the error bounds are largest and the phases are indistinguishable. Figure 4.32 shows misfit minima cluster in a range of strikes from 310°-50° and dips from 3°-8°. A comparison of the synthetics with a misfit minima (strike=0° and dip=5°) shows good arrival time agreement of *PpPmp* phase for all synthetics except BAZ=280°, which is late by 0.25 sec (Figure 4.33). The predicted phase amplitudes from the NW BAZ synthetics are comparable, falling within the stacking $\pm 2\sigma$ error bounds. The SW BAZ synthetics predict smaller amplitudes than those observed. The predicted phase moveout with Δ in the NW BAZ synthetics is consistent with the observed value in the linear slant stacks.

The underestimated SW BAZ phase amplitudes can be remedied, as in the case with stations OBH and OFK, by increasing the impedance contrast across the OM. An increase of 15% to 28% produces adequate amplitudes for the SW BAZ synthetics while keeping the NW BAZ amplitudes within range.

Noting the low average crustal velocity of starting model 01A2 relative that inferred by Taber, a second model with an increased average crustal velocity was considered. This is achieved by increasing the second layer velocity. The model parameters for the second model 01A3 are given below in Table 4.11. This model has an average crustal velocity of

Table 4.11: OSD second model 01A3

Layer #	Vp (km/s)	Vs (km/s)	ρ (g/cm^3)	z (km)
1	4.00	2.31	2.35	3.0
2	5.90	3.41	2.55	15.0
3	6.70	3.87	2.80	25.5
4	8.00	3.46	3.36	∞

6.01 km/sec and a slightly deeper OM at 25.5 km. A grid search over the 2-D model space produced a misfit distribution that is nearly identical to that for the first model. This includes the spatial distribution of the misfit minima (strike 350°-40°, dip 3°-7°) as well as the misfit minima magnitudes (ranging from 0.049 to 0.064). The best fit synthetics from the model (strike=350°, dip = 4°) nearly replicate those from the first model in phase

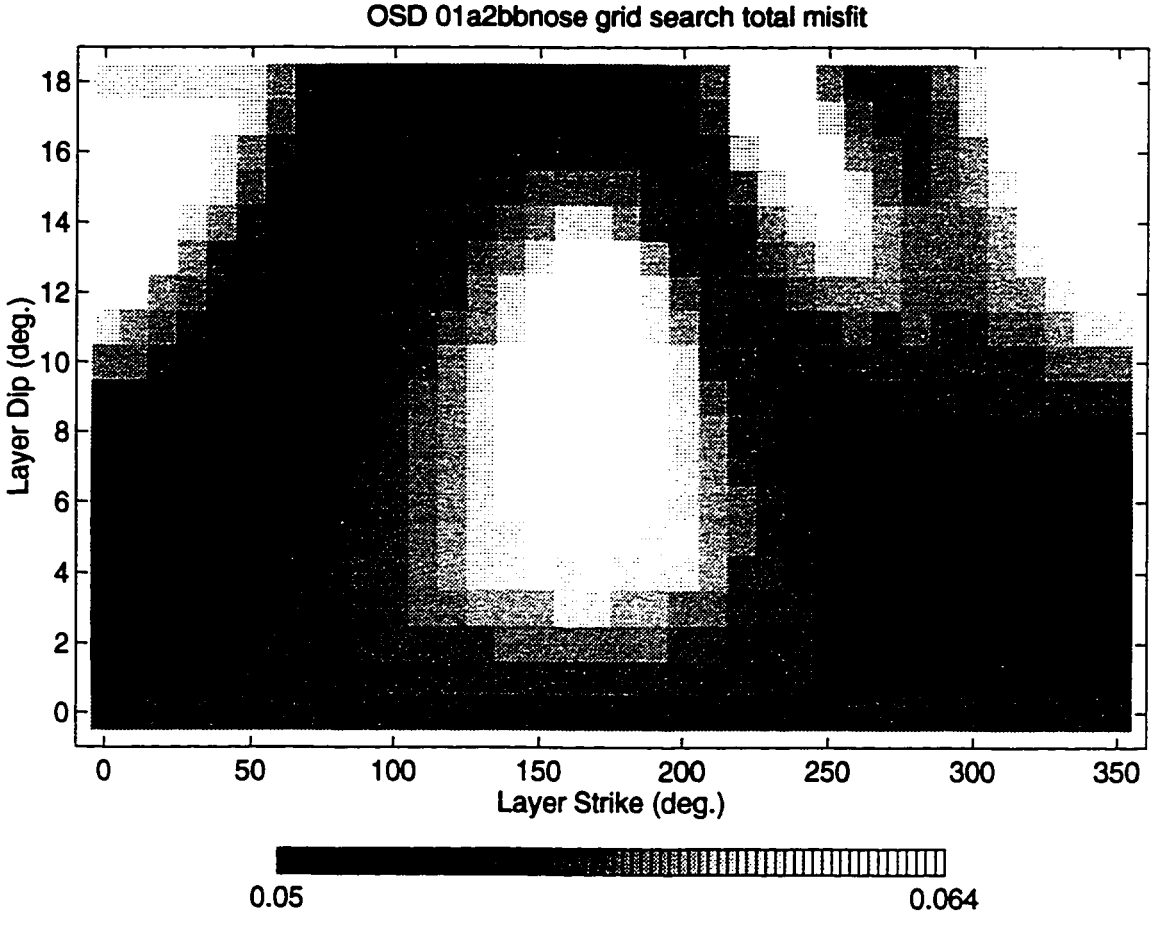

Figure 4.32: Grayscale density plot of model misfit from the grid search of a 2-D model space for the OSD layered, model with oceanic moho at a depth of 24.0 km. Misfit minima fall in a fairly narrow region.

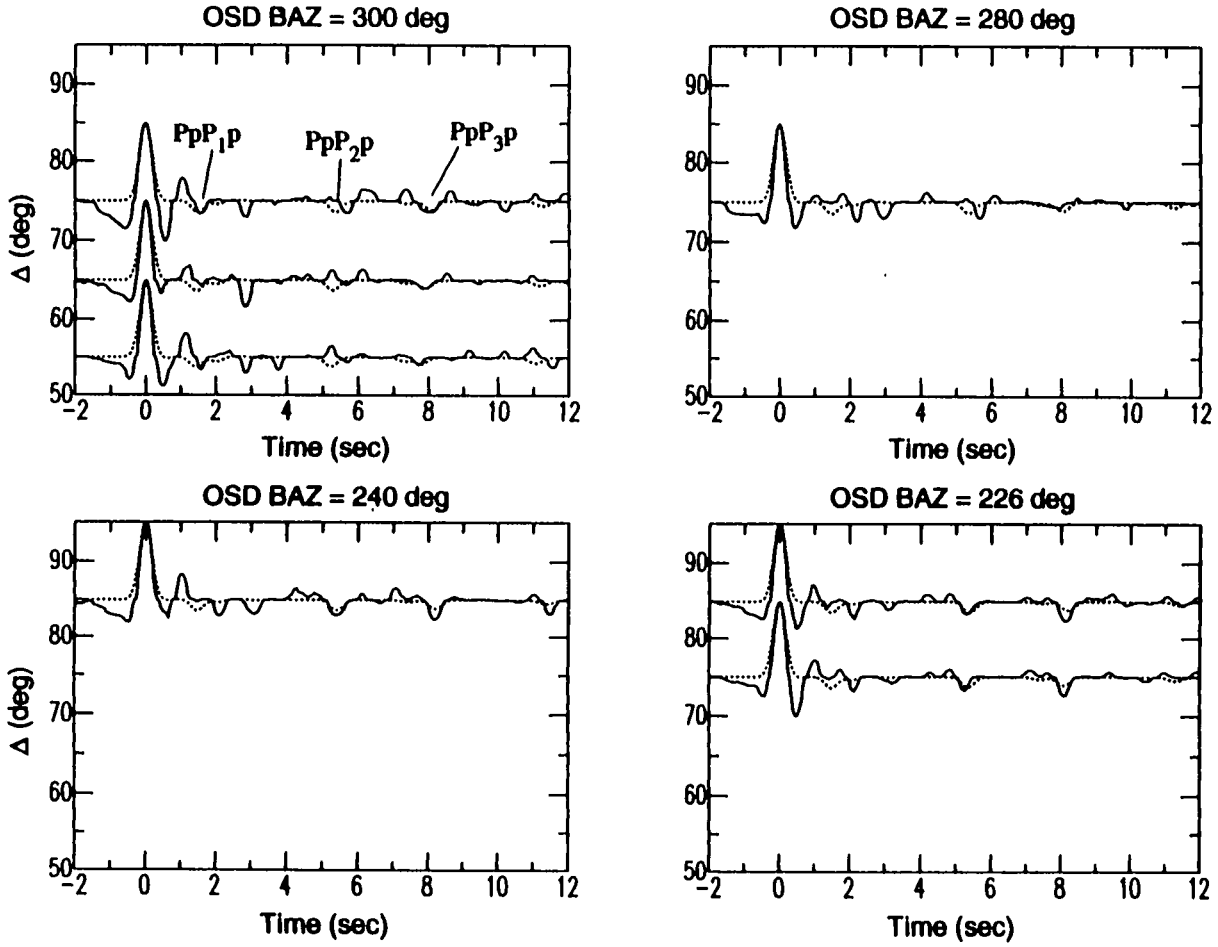

Figure 4.33: Synthetics (dashed lines) for station OSD from the best planar dipping OM model compared with the 3rd-root stacked data (solid lines) plotted as record sections. See text for model parameters. Only synthetic phases with significant amplitude (> ~5%) are labeled.

arrival times, amplitudes and moveouts with BAZ and Δ.

An F-test of the best fitting model strike and dip variances shows both models have equal variances for both layer strike and dip. Coupled with the nearly identical waveforms in the vicinity of the OM arrival from each model, it is difficult to identify a preferred model based on model fit alone. Two additional points to consider in choosing a preferred model are consistency with previous study results and fitting earlier arrivals in the stacked waveforms (ie., the 4.5-5.5 sec arrivals). Here we find a contradiction as the second model has an average crustal velocity that is closer to that inferred by *Taber* [1983], yet the first model predicts phase amplitudes for the PpP_2p phases that are consistent with those observed in the stacked data. With no compelling reason to chose one model over the other, we must conclude neither model is preferred.

In summary, the modeling of stacked waveforms from station OSD using *ray3d* provides a OM with a range in depths, 24.0-25.5 km (average crustal velocities 6.01-5.71 km/sec), dipping at 5±2° and striking at 0±50°. The inferred dip direction of the OM from the forward modeling is to the west. Because of the absence of SE BAZ data and mediocre NW BAZ data modeled, these results are somewhat tenuous compared with those from stations OBH or OFK.

Station OTR: Standard linear stacks and linear slant stacks of OTR data (Figures 3.19 and 3.20) show two arrivals which adds coherently over many of the BAZ's arriving at ~1.0 and 6.5-7.5 sec. Both arrivals is most prominent in the stacked data with BAZ's from 226°-280°, showing phase amplitudes beyond the ±2σ error bounds. For stacked data from the SE, the second arrival is difficult to identify probably due to low signal-to-noise levels. The NW BAZ=300° data show the second arrival just at or below the ±2σ error bounds for all Δ. The NW BAZ linear slant stacks indicate a small positive moveout with Δ and BAZ. The phase arrival travel times, negative polarity, and amplitudes identify the second phase as a possible OM reflected phase.

The starting model listed considered is similar to the OFK model, as these stations are located within 15 km of one another. The model parameters are listed below in Table 4.12. This model has an average crustal velocity of 6.04 km/sec with an OM at 23.7 km

depth. Using *ray3d* for forward modeling, a 2-D grid search over the standard model

Table 4.12: OTR starting model 01A1

Layer #	Vp (km/s)	Vs (km/s)	ρ (g/cm^3)	z (km)
1	3.00	1.44	2.30	2.0
2	5.20	3.00	2.55	7.5
3	6.70	3.87	2.80	23.7
4	8.00	3.46	3.36	∞

space returned the overall misfit distribution shown in Figure 4.34. This distribution reflects model misfits from stacked data that represent the most significant stacked phases and also excludes data from the SE where the error bounds are largest. The misfit minima are located in a narrow, bimodal range in strikes (260°-280° and 340°-350°) and a single range in dips (16°-18°). A comparison of the synthetics for a misfit minima (strike=270° and dip=18°) with stacked data shows fair phase arrival time agreement for all western BAZ's, with the 240° BAZ predicted phases slightly late and the 280° BAZ predicted phases slightly early (Figure 4.35). The synthetics show a fair phase amplitude replication for all BAZ's but BAZ=240° which is underestimated. The predicted phase moveout with Δ of the NW BAZ synthetics of 0.006 sec/deg is smaller than the observed moveout by about a factor of two. A comparison of the synthetics for misfit minima corresponding to a east dipping OM with stacked data provides similar results.

Although the number of misfit minima is small, the best fitting model of those tested was only partially successful in modeling the observed stacked waveforms. This is in part due to the lack of high-quality stacked data from most BAZ's, including the SE BAZ's which would provide better constraint of the modeled parameters. We may not then be as assured about the quality of the strike and dip values identified with this modeling. Noting that other stations (OBH and OSD) where correctly predicted phase arrival times can be made within a small range of depths, we feel the OM depth at station OTR may not be as poorly constrained as the inferred OM strike and dip. In summary, the modeling of OTR stacked data implies a dipping OM with a depth of 23.7 km ($\overline{Vp}$=6.04 km/sec) possibly dipping to the north or east a fairly steep angle (> 15°).

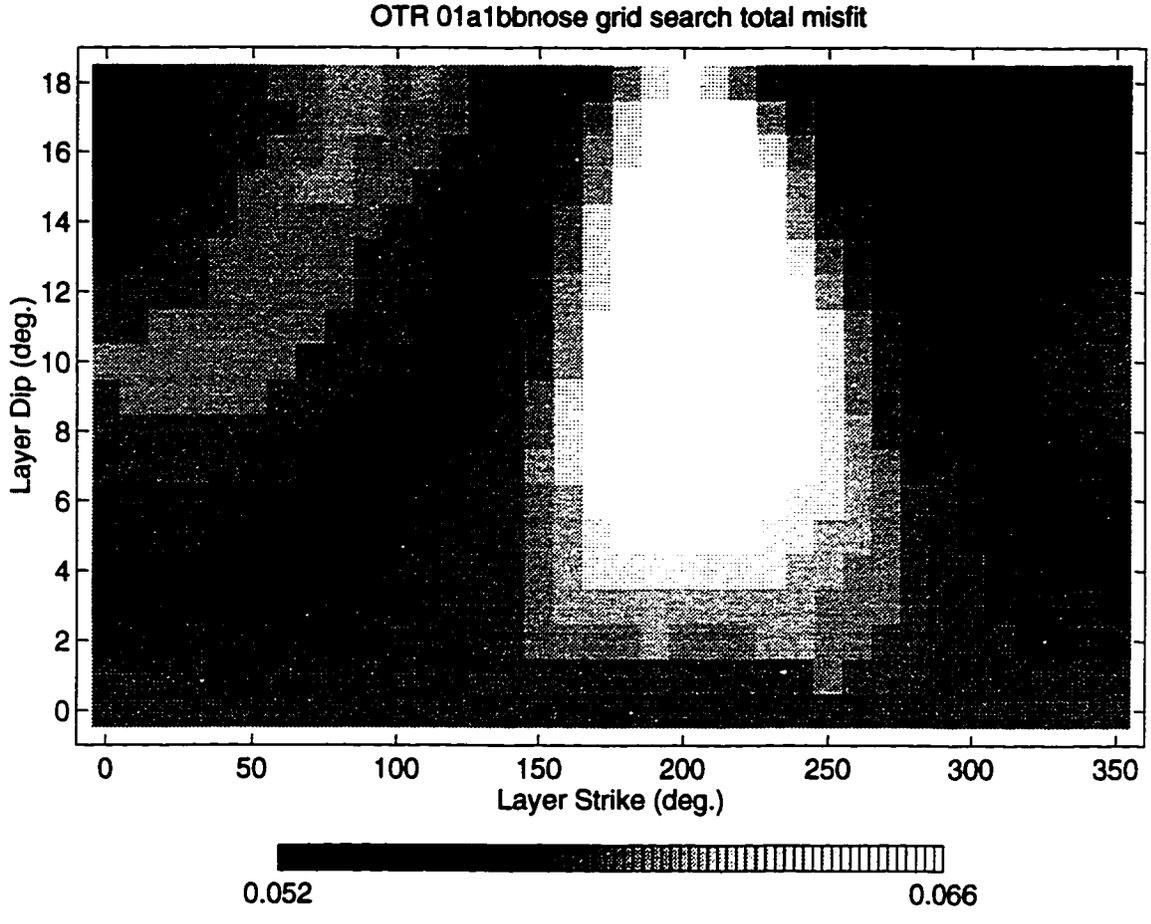

Figure 4.34: Grayscale density plot of model misfit from the grid search of a 2-D model space for the OTR layered, model with oceanic moho at a depth of 23.7 km. Misfit minima fall in a fairly narrow region.

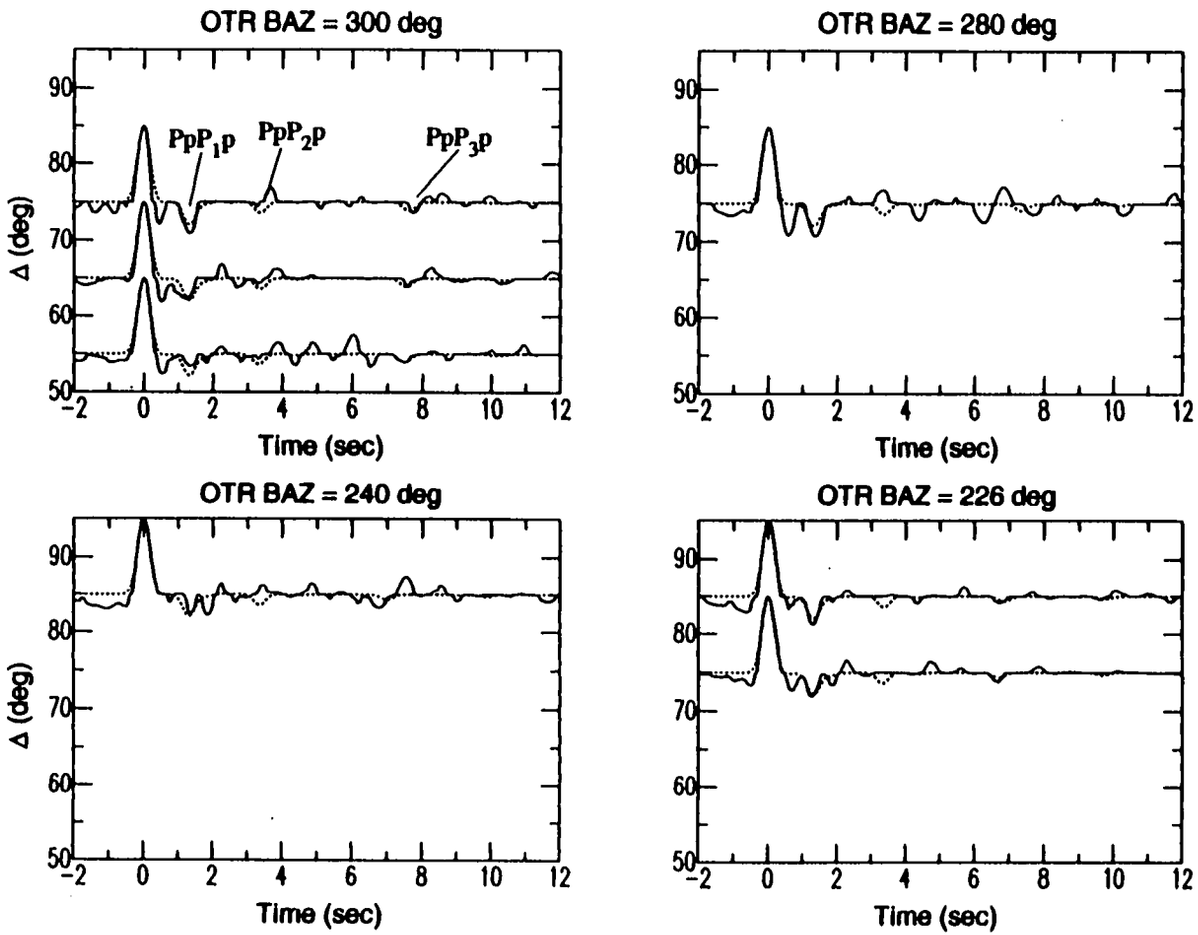

Figure 4.35: Synthetics (dashed lines) for station OTR from the dipping OM model compared with the 3rd-root stacked data (solid lines) plotted as record sections. See text for model parameters. Only synthetic phases with significant amplitude (> ~5%) are labeled.

Station HDW: Standard linear stacks and linear slant stacks of HDW data (Figures 3.21 and 3.22) show a number of phases that add coherently across both BAZ and Δ, but the most pronounced is the wavelet arriving at ~3.0 sec. This arrival has a large negative polarity pulse with smaller positive polarity sidelobes. From the linear slant stacks, the moveout with Δ of this phase for both NW and SE BAZ's is 0.0 ±0.005 sec/deg. This is to be expected for a relatively short lag time arrival. The short lag times of this phase indicate this is most likely the result of a mid-crustal reflector. Noting that HDW is located on top of the Crescent Terrane (see Fig. 4.21), one might suspect crustal structure with a near-surface high-velocity layer overlying a lower velocity layer with the interface between the two dipping towards the east.

The parameters for the homogeneous layered starting model 01A4 are listed in Table 4.13. Using *ray3d* for forward modeling, a 2-D grid search over the standard model space returned the overall misfit distribution shown in Figure 4.36. Here the strike and dip of the interfaces above and below layer 3 were allowed to vary (though not independent of one another). The distribution misfit minima cluster in a narrow region, falling between strikes of 310°-10° and dips of 10°-17°. A comparison of the synthetics from one of the best fitting models (strike=350°, dip=14°) shows phases with reasonable predicted arrivals times (Figure 4.37). This includes the first positive polarity and the negative polarity pulses of the stacked wavelet. Amplitudes of the first part of the wavelet are predicted well by the synthetics; the central negative polarity pulse shows a much greater variation, with fair agreement for SE BAZ data and poor agreement for all western BAZ's. As identified in Figure 4.37, the first two portions of the wavelet represent reflections from the top and bottom of the LVL (layer 3). The second positive polarity pulse in the predicted

Table 4.13: HDW crustal model 01A4

Layer #	Vp (km/s)	Vs (km/s)	ρ (g/cm^3)	z (km)
1	5.00	2.89	2.50	4.0
2	6.00	3.46	2.60	8.0
3	3.00	1.73	2.40	9.5
4	6.00	3.46	2.60	17.5
5	6.70	3.87	2.80	∞

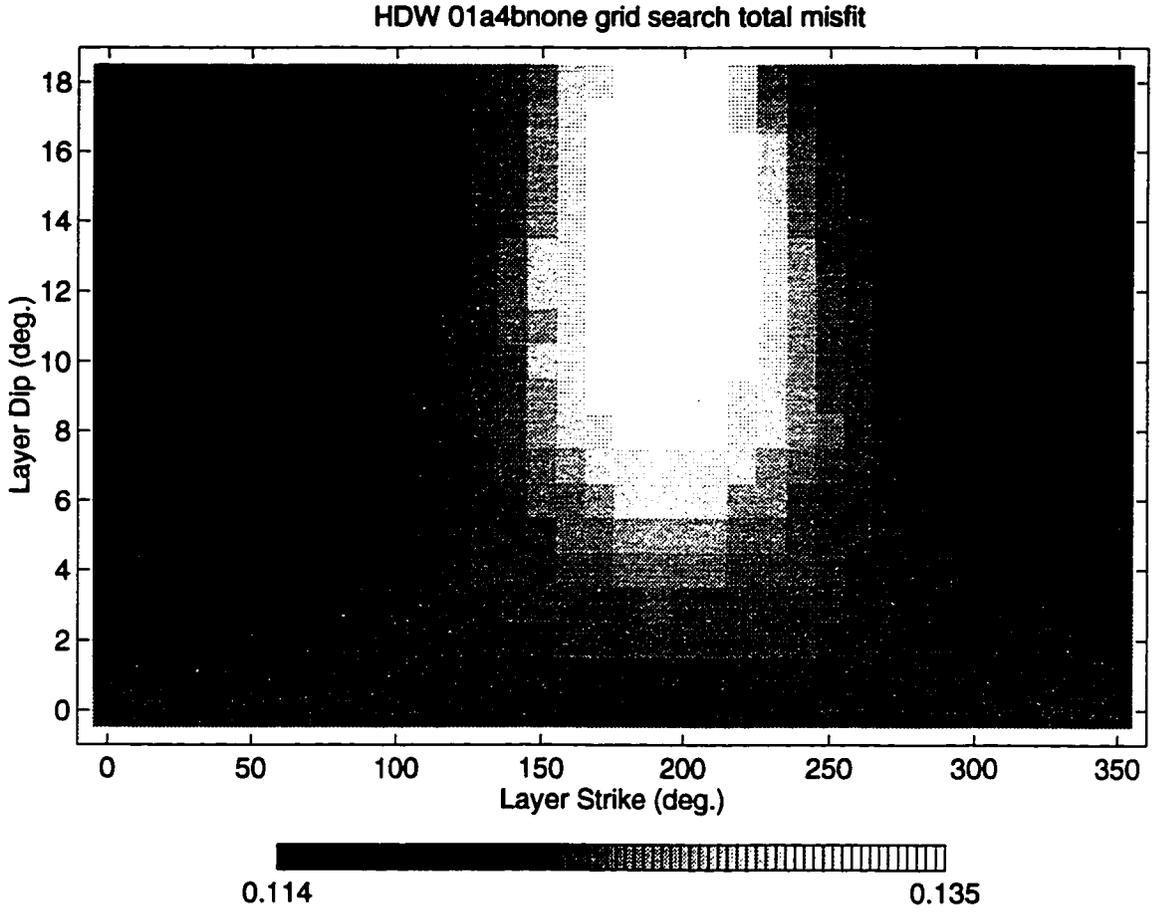

Figure 4.36: Grayscale density plot of model misfit from the grid search of a 2-D model space for the HDW layered, model with crustal structure to 17 km depth. Misfit minima fall in a fairly narrow region.

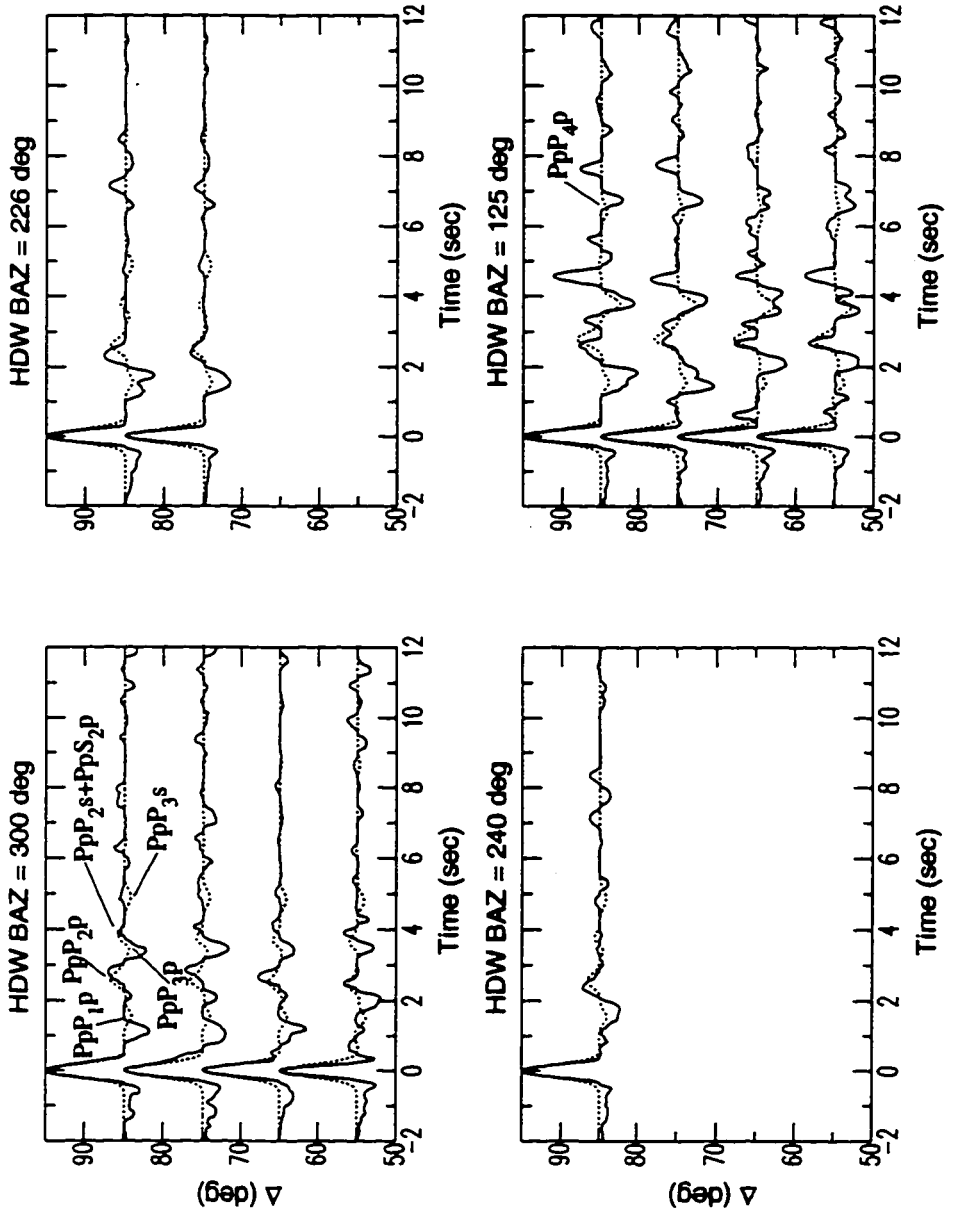

Figure 4.37: Synthetics (dashed lines) for station HDW from the best planar dipping crustal model compared with the 3rd-root stacked data (solid lines) plotted as record sections. See text for model parameters. Only synthetic phases with significant amplitude (> ~5%) are labeled.

wavelet is the superposition of different converted reflections from the top of the LVL. The synthetics do a poor job of replicating the second, large amplitude wavelet sidelobe observed in the SE BAZ data.

For such a simple parameterization, the fit of the synthetics is modest. The generally favorable modeling results attained here suggest that this parameterization (simple, planar dipping layers) to first order is quite reasonable. A summary of the forward modeling finds our best fitting model with 8 km of high velocity material overlying a 1.5 km thick LVL with interfaces dipping to the east (striking from 310°-10°) at 10°-17°. The thickness of the LVL is just within the resolution limit of the deconvolved data at frequencies from 1.0-2.0 Hz.

4.5 Modeling Interpretation

The modeling results for stations MBW and SPW have already been discussed in the sections where the waveform modeling and analysis was performed (sections 4.4.2 and 4.4.3). In brief, the velocity models for each of these stations contain structures which correlate with structures identified by previous investigators. At station MBW this includes a shallow, dipping crustal HVL/LVL sequence of overall thickness 4.5-8.2 km and an inferred east dipping CM at a depth of 47 km uncertainties of the order ±1.0 km. At station SPW, the structure constrained includes a shallow (z=1.3-1.5 km) strong impedance contrast interface which dips to the south-southeast at ~12°. This interface is interpreted as the top of the Crescent Formation south of the surface expression of the Seattle fault.

From the Olympic Peninsula, waveforms were modeled from 5 stations (OBH, OFK, OOW, OSD, and OTR) in an effort to identify and model the oceanic moho (OM). In each case, dipping plane layered models were considered. A summary of OM depth, strike and dip for each station is given in Figure 4.38. Also plotted at each station are vectors representing the *PpPmp* ray lateral sampling. By and large, the simplistic model parameterization yielded models which reasonably explained the arrival times, amplitudes and moveouts of observed phases identified as likely OM reflections (*PpPmp*). Greatest confidence is placed on the modeling results for stations OBH and OFK which had the highest signal-to-noise waveforms. Slightly less confidence is placed on the modeling results for station OOW because of slightly lower waveform signal-to-noise. Modeling

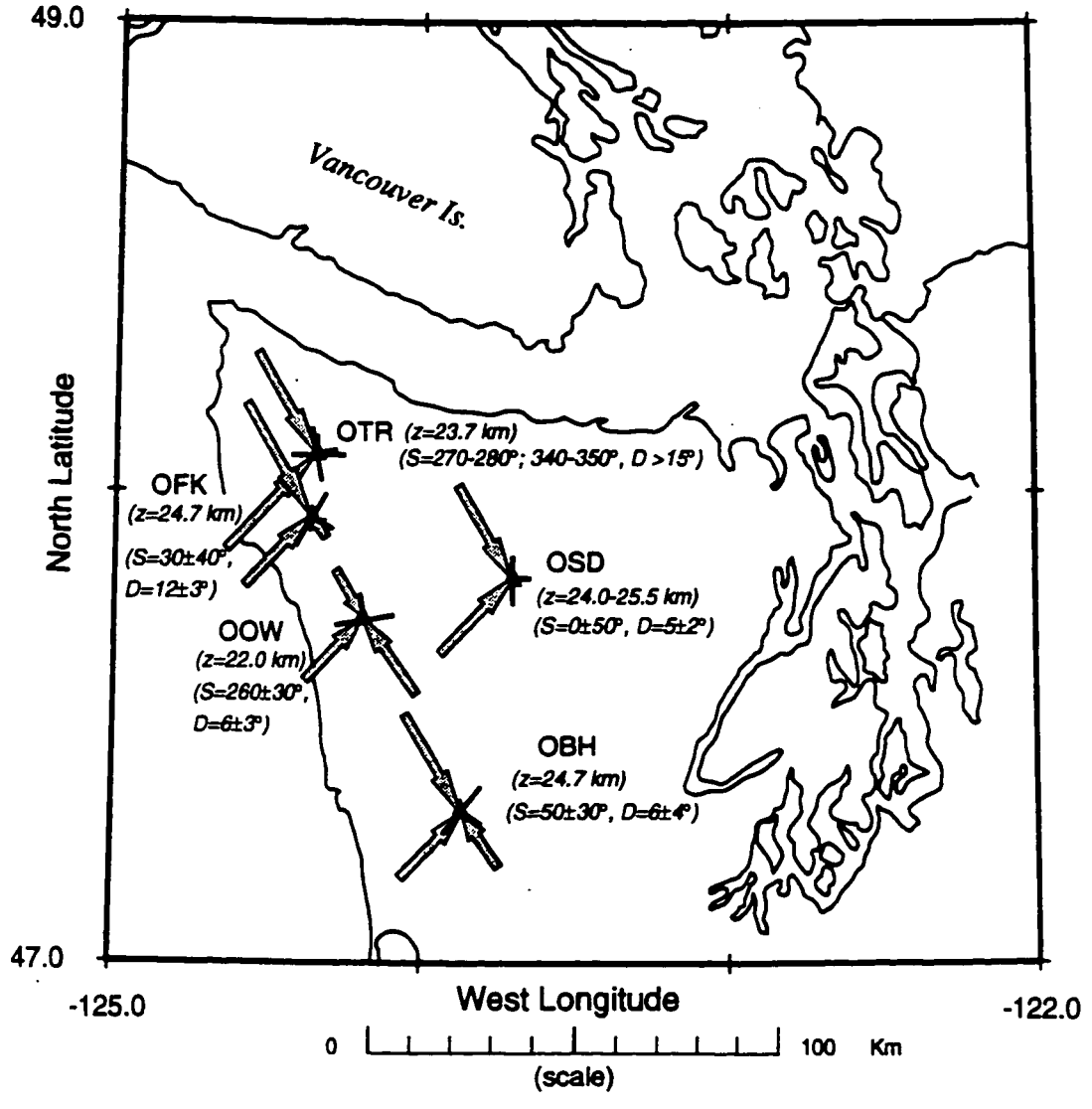

Figure 4.38: Map of Olympic Peninsula stations for which wavefrom modeling was performed showing resulting parameters: oceanic moho depth, strike and dip. Also shown is the approximate lateral sampling of phase PpPmp for each station.

results for stations OSD and OTR are given the least confidence due to marginal signal-to-noise waveforms and the lack of model constraint from eastern BAZ's. Still further doubt is cast on the OTR model constraints due to the overlapping lateral sampling of the SW BAZ model *PpPmp* rays with other rays *PpPmp* from station OFK (Fig. 4.38).

One of the serious difficulties in modeling the phase identified as *PpPmp* at the Olympic sites was the inability to replicate the phase amplitudes with reasonable crustal (6.70 km/sec) and upper mantle (8.00 km/sec) velocities at the oceanic moho. Three stations in particular only achieved proper amplitudes after the *P*-velocity contrast (ΔVp) was increased from 1.30 km/sec to 2.10 km/sec (stations OBH, OFK, and OSD) by either adding a thin LVL to the bottom of the crust, or increasing the upper mantle velocity. Physically plausible interpretations, whether structural or otherwise, which explain either remain elusive.

Deep crustal low velocity zones (LVZ) have been identified above the subducting JDF plate beneath Vancouver Island (the E reflective zone) [e.g, *Green et al.* 1986, *Hyndman et al.* 1990, *Cassidy and Ellis* 1991] and suggested beneath central Oregon [*Tréhu et al.* 1995]. At both of these locations, the identified LVZ's are located at least 4-6 km above the oceanic moho. These LVZ's have been interpreted as possible underplated sediments or oceanic crust, conductive fluids trapped in porous materials bounded by an impenetrable boundary, and a shear zone. Our data modeling are somewhat incompatible with the observed LVZ characteristics at these other two study locations. Aside from the layer depth relative to the oceanic moho, the LVL inferred in our study has a larger velocity contrast than observed from Vancouver Island (ΔVp=0.8 km/sec [*Drew and Clowes* 1990], ΔVs=1.0 km/sec [*Cassidy* 1991]). The discrepancies between these observations and the values of our models imply that the structure identified with out data may not be the same as the deep crustal LVZ's beneath Vancouver Island and Oregon.

Another possibility is the misidentification of a deep crustal LVZ as the OM, as was the case with the initial identification of the E reflective zone beneath Vancouver Island [*Green et al.* 1986]. However, this is unlikely as the velocity contrasts noted above (ΔVp=0.8 km/sec and ΔVs=1.0 km/sec) are not sufficient to produce the observed amplitudes, and we see no clearly coherent arrivals following those currently being modeled that would represent the "true" OM. Moreover, the OM depths determined from our modeling are consistent with the depth to the Benioff zone beneath the western Olympic Peninsula (Figure 4.39).

a)

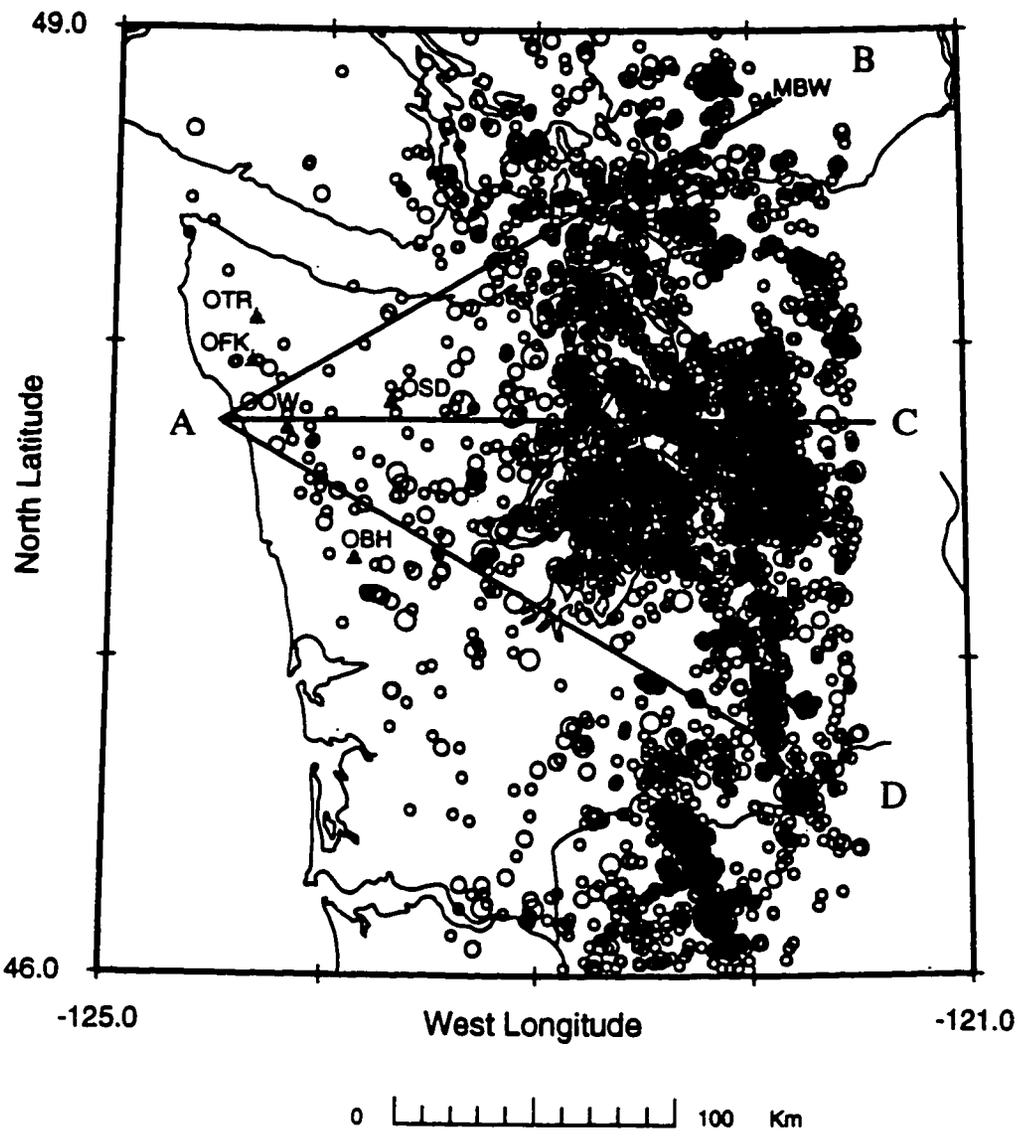

Figure 4.39: (a) Earthquake epicenters for events with M_D > 1.0 from 1980-1995 to latitude 121.5 °W . Cross-sections along profiles A-B, A-C, and A-D are shown in (b-d).

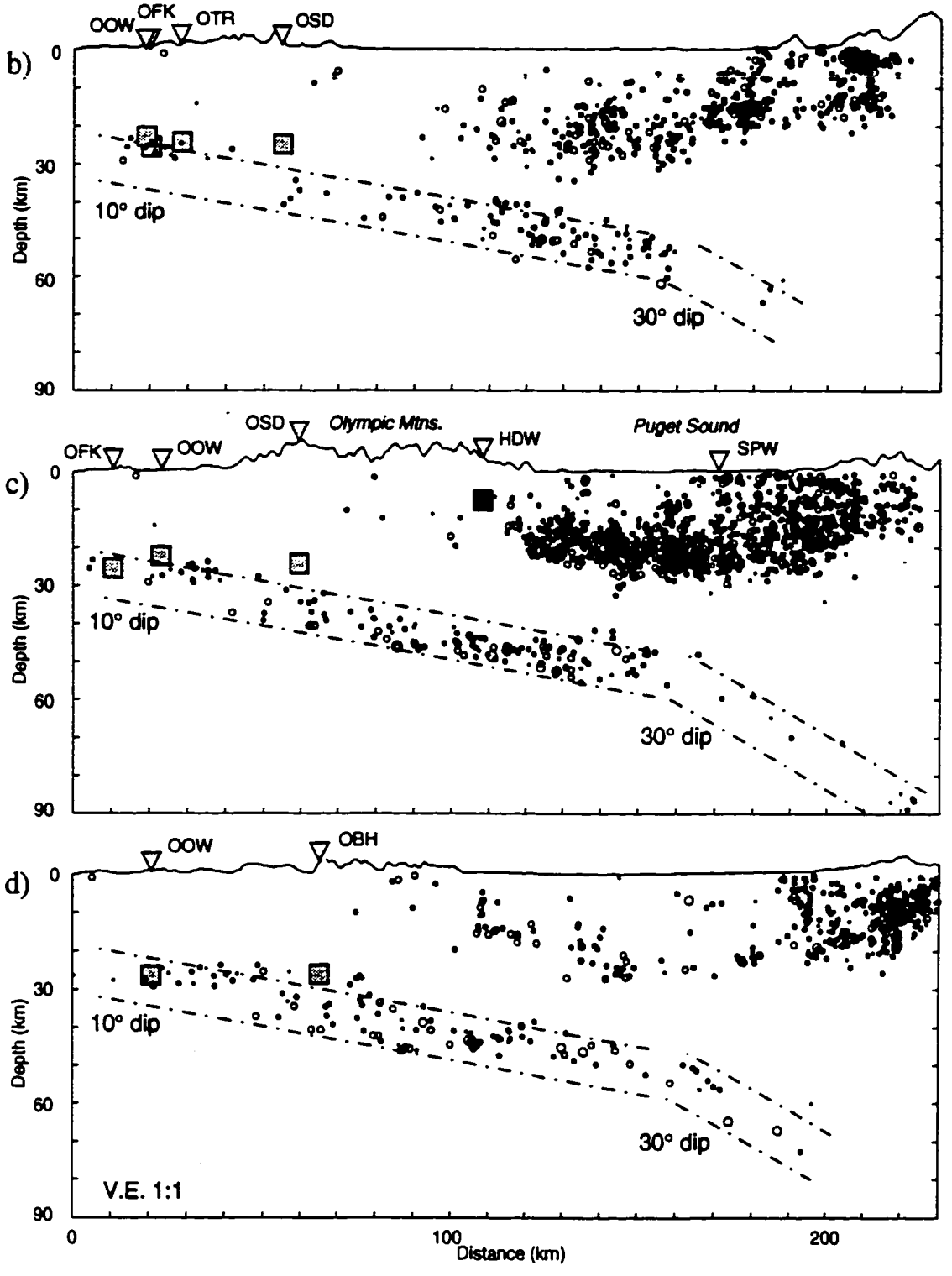

Figure 4.39 (cont): Cross-sections across the Olympic Peninsula and Puget Sound showing hypocenters for events along the profiles shown in (a) with inferred OM depths and Crescent Formation depths (gray boxes).

The presence of pore fluids along thrust faults in the oceanic crust that extend into the upper mantle could provide a mechanism for lowering the oceanic moho impedance contrast. Such faults have been observed in seismic data from the Indian Ocean, where pre-existing normal faults formed at the spreading center have been reactivated by intraplate compression [*Bull and Scrutton* 1990].

Upper mantle anisotropy from olivine crystal alignment seems unlikely, as the slow olivine direction is in the vertical direction while the fast olivine direction is parallel to the ridge spreading direction [*Kendall* 1994]. Still other explanations for the large observed phase amplitudes include: phase amplitude distortion incurred during deconvolution, deconvolutional noise, and local interface geometry or structure which produces strong energy focusing.

The OM strikes and dips determined for the 5 Olympic stations (Figure 4.38) exhibit trends which are parallel to or subparallel to the inferred trend of the arched slab for 3 stations (OBH, OSD, and OTR) and nearly normal for the others. The first three sites, moving south to north, show an OM dipping to the southeast at 6±2° (OBH), then the east at 5±2° (OSD), and finally to the north or east at >15°(OTR). The strike and dip constraint for OTR is not as good as for the other two stations due to limited stacked data and modeling using just western BAZ data. OM parameters constrained for station OFK indicate the slab dips to the east-southeast (with a strike of 30±40°) at 13±4°. For its relative location near or north of the slab arch axis, we would expect the dip direction at OFK to be rotated more to the northeast. However, within the strike uncertainty a northeast dip direction cannot be accommodated. The dip angle at OFK is not significantly different than the 10°-11° value inferred from the Benioff zone (Figure 4.39).

The variation of the OM structure determined from this study may indeed reflect a localized variation of the slab geometry, but could also reflect our inability to find a model that truly represents the OM structure (recalling the inadequate synthetic phase amplitudes). For station OOW, the model tested produced the best fitting synthetics of all the stations considered with a narrow range in OM strike (260±40°) and dip (6±3°). The best fitting model however dips to the north which is normal to the general trend of the slab arch at that location. Assuming the phase identified and modeled as *PpPmp* was done so correctly, the good fit and reasonable constraint confidence leads to the conclusion that the structure is real. The deviations in OM strike and dip for stations OFK and OOW from the inferred general arch geometry may represent a localized, small scale interface feature

superposed over the larger scale arch geometry.

Modeling at station HDW on the eastern Olympic Peninsula (see Fig 4.21 for location) produced a crustal model with 8.0 km of high velocity crustal material above a thin (1.5 km) LVL. We interpret this as the Crescent basalts overlying slower velocity, possible underthrust Olympic core sedimentary rocks on an eastward dipping fault. The depth to the Crescent bottom is consistent with the findings of *Johnson et al.* [1996] who interpret the total Crescent thickness ~30 km north of HDW to be at least 10 km. The depth and dip direction are also consistent the interpretation of resistivity by *Aprea* [1996] for a 2-D, east-west resistivity profile just north of HDW.

Chapter 5

Summary and Conclusions

5.1 Study Summary

The goals of this research were two-fold. The primary goal was to obtain better structural constraint at crustal and upper mantle depths in the Cascadia subduction zone using teleseisimic waveform data from the PNSN. This study represented the first attempt to model local structure using a waveform analysis with PNSN data, as opposed to previous methods based exclusively on travel time data [e.g., *Lees* 1989, *VanDecar* 1991]. The second goal, necessitated by the first, was to develop and demonstrate a viable method (from both theoretical and practical viewpoints) for separating near-receiver structure from all other constituents of the individual seismograms in order to produce vertical-component receiver response functions. Subsequent forward modeling of stacked receiver response functions was then used to provide local structural constraint.

To accomplish these goals, a data set was required that provided both high-quality waveforms and a broad source distribution, in terms of distance and azimuth. The more than 5400 earthquakes recorded digitally by the PNSN from 1980-1993 provided a profusion of data from which an optimal group was selected. With this data set, waveforms from a large subset of the total number of PNSN stations could be considered for structural studies, encompassing a much larger study area than previous waveform studies. The latter include single site and linear array receiver function studies, as well as 2-D refraction/wide-angle reflection profile studies. The nature and distribution of teleseismic events within the PNSN catalog along with the selection process of our subsequent data set were described in detail in Chapter 2.

The method for seismogram deconvolution (or receiver response function isolation) considered in Chapter 3, represents the application of traditional horizontal-component receiver function analysis to vertical-component data. This required a source wavelet to be estimated in the time domain before a waterlevel deconvolution could be applied. Confidence in the methodology was bolstered by comparison with a second deconvolution method, the complex cepstral deconvolution [*Crosson and Dewberry* 1994, *Dewberry and Crosson* 1994]. With the deconvolution goal achieved, optimal signal enhancement (noise reduction) in the *P*-coda of the source normalized waveforms was addressed using a number of stacking procedures including standard linear, 3rd-root and linear slant stacks.

With stacked data from 46 network stations which contained significant phases in the *P*-coda at short and/or long relative arrival times, 8 were selected that provided strong

indications for likely success in waveform modeling in Chapter 4. For these sites, models were determined which were found to correlate well with known geologic features, gravity signatures, and existing velocity models, as well as characterize structures until now only inferred.

In the north Cascades just west of Mt. Baker, station MBW was found to have a 5-8 km thick HVL/LVL sequence 3.6 km from the surface dipping to the east-southeast which correlates well with a similar structure identified by *Gridley* [1993] along a north-south profile ~20 km to the west. This provides constraint of the lateral extent of this structure, interpreted as a possible ophiolite sequence. The continental modo is inferred to be at 47 km depth and possibly eastward dipping, corroborating similar findings by *Schultz* [1993] and *Schultz and Crosson* [1995] under the central Cascades.

In the Puget Sound just south of the surface expression of the Seattle fault, waveform modeling at station SPW demonstrates the shallow depth (≤1.5km) to a high velocity, southward dipping basement, interpreted as the Crescent Formation. This correlates well with the gravity data in the area and corroborates the results of *Johnson et al.* [1994].

Waveform modeling results for 5 Olympic Peninsula sites (OBH, OFK, OOW, OSD, and OTR) provide the first direct seismic evidence for a 3-D oceanic moho (OM) in western half of the peninsula. As modeled, the OM depth ranges from 22 to 26 km. OM dips and strikes for three of the sites generally correlate with the inferred arched slab geometry, while the other two deviate significantly from the arching trend. The latter two sites are interpreted as revealing localized OM structure. A modified version of the general depth contours of the slab (originally Figure 1.2) determined by constraints imposed from this study is shown in Figure 5.1. To accommodate the modeled OM depths, strikes, and dips at each site, the 20 km depth contour has two smaller scale (~20 km) concave seaward bends superposed between stations OBH and OOW, and between OFK and OTR. These features resemble small scale, eastward dipping anticlinal structures on the OM, with symmetry axes subparallel or parallel to the east-west trending axis of the larger slab signature. These may represent undulations of the OM itself. The slight increase in the east-west trending Bouguer gravity signature between stations OOW and OBH (Figure 5.2) could represent such an undulation. However, the signature could also be dependent on the near surface structure as well. The inferred OM undulations may have resulted from intraplate deformation imposed either previous to, or during, subduction.

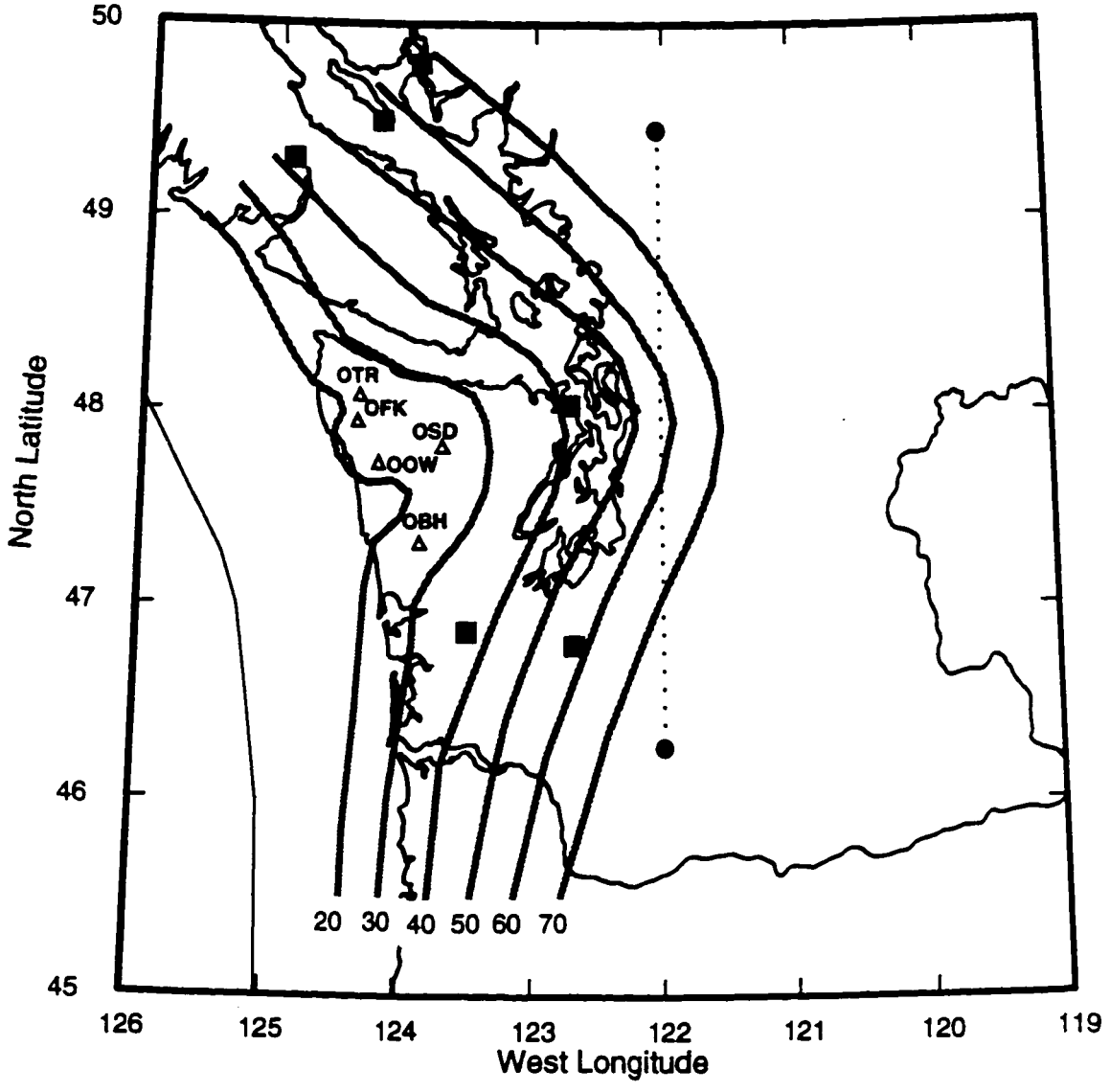

Figure 5.1: Lambert projection map of the Pacific Northwest with revised depth contours (in km) reflecting the results of this study. Filled squares denote receiver function study sites and the dashed line denotes the Gridley [1993] study profile.

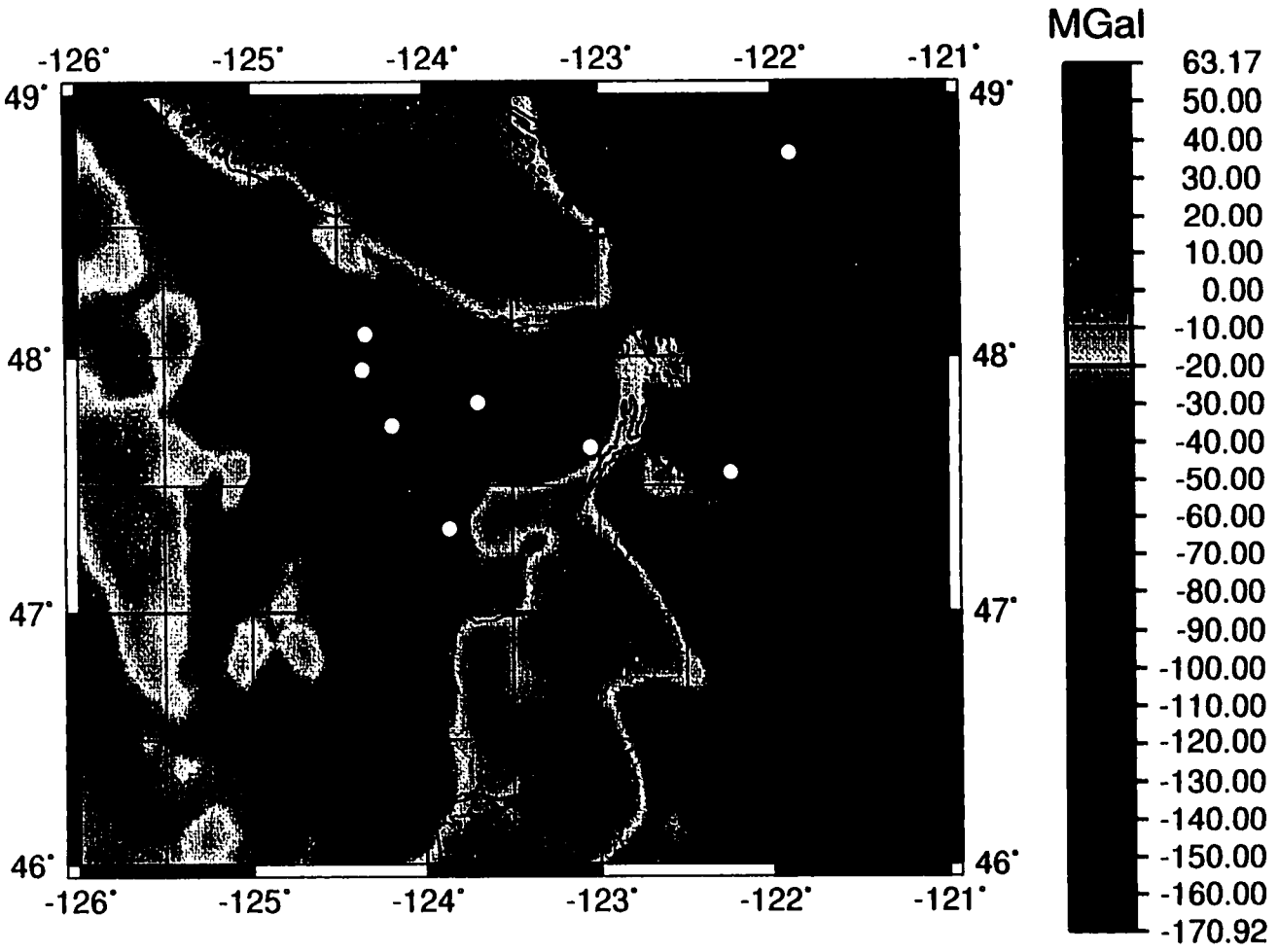

Figure 5.2: Map of the Bouguer gravity anomaly for western Washington and southern British Columbia with a Boubuer reduction density of 2.67 g/cm^3.

On the eastern side of the Olympic Peninsula at station HDW, the Crescent Formation outcrops at the surface and extends to a depth of 8.0 km. The base of the Crescent dips to the east and overlies a thin layer of low velocity material, interpreted as underthrust Olympic core rock. These results correlate with known constraints from seismic data modeling, gravity data, and MT/resistivity modeling.

5.2 Future Work

This work represents a new method for analyzing short-period network waveform data from the vast PNSN digital waveform catalog in order to provide detailed near-receiver, 3-D structural constraint in Washington and Oregon. The general success of this method, as demonstrated in this study, provides another tool for investigating and producing 3-D structural images for the region covered by the PNSN.

Other implementations of this waveform analysis which may yield additional useful structural information for the Pacific Northwest and other regions include: (*i*) the application to intermediate and broadband network data to extract and model longer wavelength structure, (*ii*) the application to 3-component array data intended for traditional receiver function studies, (*iii*) additional modeling of the short period *P*-coda as scattered energy [e.g., *Revenaugh* 1995], (*iv*) modeling waveforms with preserved, true amplitudes rather than normalized amplitudes, (*v*) implementing an efficient and rapid waveform modeling method which allows a large model space to be investigated, and (*vi*) applying an inversion method like that employed by *Owens et al.* [1984], modified to allow dipping structures to find the "best" fitting models.

Bibliography

Adams, J. (1990). Paleoseismicity of the Cascadia subduction zone: Evidence from turbidites off the Oregon-Washington margin, *Tectonics*, **9**, 569-583.

Aki, K., A. Christoffersson, and E.S. Husebye (1977). Determination of the three-dimensional seismic structure of the lithosphere, *J. Geophys. Res.*, **82**, 277-296.

Andrews, D.F., P.J. Bickel, F.R. Hampel, P.J. Huber, W.H. Rogers, and J.W. Tukey (1972). *Robust Estimates of Location: Survey and Advances*, Princeton University Press, Princeton, New Jersey, 373 pp.

Aprea, C.M. (1996). *Implications of the electrical resistivity structure of the Olympic Mountains and Puget Lowland*, Ph.D. thesis, Univ. of Washington, Seattle, Washington, 144 pp.

Arnold, R. (1906). A geologic reconnaissance of the coast of the Olympic Peninsula, Washington, *Geol. Soc. Am. Bull.*, **17**, 451-468.

Atwater, B.F. (1987). Evidence for great Holocene earthquakes along the outer coast of Washington state, *Science*, **236**, 942-944.

Atwater, B.F. (1992). Geologic evidence for earthquakes during the past 2000 years along the Copalis River, southern coastal Washington, *J. Geophys. Res.*, **97**, 1901-1919.

Atwater, B.F., M. Stulver, and D.K. Yamaguchi (1991). Radiocarbon test of earthquake magnitude at the Cascadia subduction zone, *Nature*, **353**, 156-158.

Atwater, T. (1970). Implications of plate tectonics for the Cenozoic tectonic evolution of western North America, *Geol. Soc. Am. Bull.*, **81**, 3513-3536.

Babcock, R.S., R.F. Burmester, D.C. Engebretson, and A. Warnock (1992). A rifted margin origin for the Crescent basalts and related rocks in the northern coast range volcanic province, Washington and British Columbia, *J. Geophys. Res.*, **97**, 6799-6821.

Båth, M. and R. Steffánsson (1966). *S-P* conversion at the base of the crust, *Ann. Geophys.*, **19**, 119-130.

Berg, J.R., Jr., L. Trembly, D.A. Emilia, J.R. Hutt, J.M. King, L.T. Long, W.R. McKnight, S.K. Sarmah, R. Souders, J.T. Thiruvathukal, and D.A. Vossler (1966). Crustal refraction profile, Oregon Coast Range, *Bull. Seism. Soc. Am.*, **56**, 1357-1362.

Booker, J.R. and A.D. Chave (1988). Introduction to the special section on the EMSLAB-Juan de Fuca experiment, *J. Geophys. Res.*, **94**, 14,093-14,098.

Bostock, M.G. and J.C. VanDecar (1994). The influence of crust and upper mantle heterogeneity on short period waveform distortion, *Phys. E. Planet. Int.*, **83**, 225-247.

Bostock, M.G. and J.C. VanDecar (1995). Upper mantle structure of the northern Cascadia subduction zone, *Can. J. Earth Sci.*, **32**, 1-12.

Brandon, M.T. and J.A. Vance (1992). Zircon fission-track ages for the Olympic subduction complex and adjacent eocene basins, western Washington state, *Washington Division of Geology and Earth Resources Open File Report 92-6*, 71 pp.

Bucknam, R.C., E. Hemphill-Haley, and E.B. Leopold (1992). Abrupt uplift within the past 1700 years at southern Puget Sound, Washington, *Science* **258**, 1611-1614.

Bull, J.M. and R.A. Scrutton (1990). Fault reactivation in the central Indian Ocean and the rheology of oceanic lithosphere, *Nature*, **344**, 855-858.

Byrne, J.V., G.A. Fowler, and N.J. Maloney (1966). Uplift of the continental margin and possible continental accretion off Oregon, *Science*, **154**, 1654-1656.

Cady, W.M. (1975). Tectonic setting of the Tertiary volcanic rocks of the Olympic Peninsula, Washington, *J. Res. U.S. Geol. Surv.*, **3**, 573-582.

Cassidy, J.F. (1991). *Teleseismic receiver function analysis of the crust and upper mantle of southwestern British Columbia*, Ph.D. thesis, Univ. of British Columbia, Vancouver, British Columbia, 174 pp.

Cassidy, J.F. and R.M. Ellis (1991). Shear wave constraints on a deep crustal reflective zone beneath Vancouver Island, *J. Geophys. Res.*, **96**, 19,843-19,851.

Cerveny, V., I.A. Molotkov, and I. Psencik (1977). Ray method in seismology, Univerzita Karlova, Praha, Czechoslovakia, 214 pp.

Chiang, C.S. and L.W. Braile (1984). An example of two-dimensional synthetic seismogram modeling, *Bull. Seism. Soc. Am.*, **74**, 509-519.

Chiao, L.-Y. (1991). *Membrane deformation rate and geometry of subducting slabs*, Ph.D. thesis, Univ. of Washington, Seattle, Washington, 144 pp.

Clague, J.J. and P.T. Bobrowsky (1994). Evidence for a large earthquake and tsunami 100-400 years ago on western Vancouver Island, British Columbia, *Quaternary Res.*, **41**, 176-184.

Claerbout, J.F. (1976). *Fundamentals of geophysical data processing: with applications to petroleum prospecting*, McGraw-Hill, New York, 274 pp.

Clark, S.H., Jr., and G.A. Carver (1992). Late Holocene tectonics and paleoseismicity, southern Cascade subduction zone, *Science*, **255**, 188-192.

Clayton, R.W. and R.A. Wiggins (1976). Source shape estimation and deconvolution of teleseismic bodywaves, *Geophys. J. R. Astr. Soc.*, **47**, 151-177.

Clowes, R.M., C.J. Yorath, and R.D. Hyndman (1987). Reflection mapping across the convergent margin of western Canada, *Geophys. J. R. Astr. Soc.*, **89**, 79-84.

Crosson, R.S. (1976). Crustal structure modeling of earthquake data 2. Velocity structure of the Puget Sound region, Washington. *J. Geophys. Res.*, **81**, 3047-3054.

Crosson, R. S. and S. R. Dewberry (1994). Receiver function estimation from short-period regional network teleseismic data using cepstral deconvolution (abstract), *EOS Trans.*, **75**, 485.

Crosson, R.S. and T.J. Owens (1987). Slab geometry of the Cascadia subduction zone beneath Washington from earthquakes hypocenters and teleseismic converted waves, *Geophys. Res. Lett.*, **14**, 824-827.

Darienzo, M.E. and C.D. Peterson (1990). Episodic tectonic subsidence of late Holocene salt marshes, northern Oregon central Cascadia margin, *Tectonics*, **9**, 1-22.

Davies, G.F. and M.A. Richards (1992). Mantle convection, *J. Geol.*, **100**, 151-206.

Dewberry, S. R. and R. S. Crosson (1994). Comparison of stacking and cepstral deconvolution in estimation of receiver functions from short-period regional network teleseismic data (abstract), *EOS Trans.*, **75**, 485.

Dewberry, S.R. and R.S. Crosson (1996). The M_D 5.0 earthquake of 29 January 1995 in the Puget Lowland of western Washington: An event on the Seattle fault?, *Bull. Seism. Soc. Am.*, **86** (in press).

Dickinson, W.R. (1970). Relations of andesites, granites, and derivative sandstones to arc-trench tectonics, *Rev. Geophys.*, **8**, 813-860.

Dragert, H., R.D. Hyndman, G.C. Rogers, and K. Wang (1994). Current deformation and the width of the seismogenic zone of the northern Cascadia subduction thrust, *J. Geophys. Res.*, **99**, 653-668.

Drew, J.J. and R.M. Clowes (1990). A re-interpretation of the seismic structure across the active subduction zone of western Canada, in *Studies of Lateral Heterogeneous Structures using Seismic Refraction and Reflection Data*, edited by A. G. Green, Geol. Survey of Canada, 89-13, 115-132.

Edlund, K.M. (1991). *Geometric constraints for the Cascadia subduction zone beneath Indian Island, Washington from teleseismic receiver function analysis*, M.S. thesis, Univ. of Washington, Seattle, Washington, 80 pp.

Egbert, G.D. and J.R. Booker (1993). Imaging crustal structure in southwestern Washington with small magnetometer arrays, *J. Geophys. Res.*, **98**, 15,967-15,985.

Finn, C. (1990). Geophysical constraints on Washington convergent margin structure, *J. Geophys. Res.*, **95**, 19,533-19,546.

Fuchs, K. and G. Müller (1971). Computation of synthetic seismograms with the reflectivity method and comparison with observations, *Geophys. J. R. Ast. Soc.*, **23**, 417-433.

Gower H.D., J.C. Yount, and R.S. Crosson (1985). Seismotectonic map of the Puget Sound region, Washington, *U.S. Geol. Surv., Misc. Inv. Ser. Map I*-1613.

Green, A.G., R.M. Clowes, C.J. Yorath, C. Spencer, E.R. Kanasewich, M.T. Brandon, and A. Sutherland Brown, (1986). Seismic reflection imaging of the subducting Juan de Fuca plate, *Nature*, **319**, 210-213.

Gridley, J.M. (1993). *Crustal structure of western Washington State*, Ph.D. thesis, Univ. of Texas, El Paso, Texas, 232 pp.

Heaton,T.H. and S.H. Hartzell (1987). Earthquake hazards on the Cascadia subduction zone, *Science*, **236**, 162-168.

Heaton, T.H. and H. Kanamori (1984). Seismic potential associated with subduction in the northwestern United States, *Bull. Seism. Soc. Am.*, **74**, 933-941.

Helmberger, D. and R.A. Wiggins (1971). Upper mantle structure of midwestern United States, *J. Geophys. Res.*, **76**, 3229-3245.

Houard, S. and H.C. Nataf (1992). Further evidence for the 'Lay discontinuity' beneath northern Siberia and the North Atlantic from short-period P-waves recorded in France, *Phys. E. Plan. Int.*, **72**, 264-275.

Hyndman, R.D. and K. Wang (1993). Thermal constraints on the zone of major thrust earthquake failure: the Cascadia subduction zone, *J. Geophys. Res.*, **98**, 2039-2060.

Hyndman, R.D., C.J. Yorath, R.M. Clowes, and E.E. Davis (1990). The northern Cascadia subduction zone at Vancouver Island: seismic structure and tectonic history, *Can. J. Earth Sci.*, **27**, 313-329.

Johnson, S.H. and R.W. Couch (1970). Crustal structure in the north Cascade mountains of Washington and British Columbia from seismic refraction measurements, *Bull. Seism. Soc. Am.*, **60**, 1259-1269.

Johnson, S.Y., C.J. Potter, and J.M. Armentrout (1994). Origin and evolution of the Seattle fault and Seattle basin, Washington, *Geology*, **22**, 71-74.

Johnson, S.Y., C.J. Potter, J.M. Armentrout, J.J. Miller, C. Finn, and C.S. Weaver (1996). The southern Whidbey Island fault, an active structure in the Puget lowland, Washington, *Geol. Soc. Am. Bull.*, **108**, 334-354.

Keach II, R.W., J.E. Oliver, L.D. Brown, and S. Kaufman (1989). Cenozoic active margin and shallow Cascade structure: COCORP results from western Oregon, *Geol. Soc. Am. Bull.*, **101**, 783-794.

Kendall, J.M. (1994). Teleseismic arrivals at a mid-ocean ridge: Effects of mantle melt and anisotropy, *Geophys. Res. Lett.*, **21**, 301-304.

Kurtz, R.D., J.M. DeLaurier, and J.C. Gupta (1986). A magnetotelluric sounding across Vancouver Island detects the subducting Juan de Fuca plate, *Nature*, **213**, 596-599.

Landers, T.E (1974). Elastic scattering of plane P-waves at irregular boundaries in the lower crust, *Earthquake Notes*, **45**, 12-21.

Langston, C.A. (1977). The effect of planar dipping structure on the source and receiver responses for constant ray parameter, *Bull. Seism. Soc. Am.*, **67**, 1029-1050.

Langston, C.A. (1979). Structure under Mount Rainier, Washington, inferred from teleseismic body waves, *J. Geophys. Res.*, **84**, 4749-4762.

Langston, C.A. (1981). Evidence for the subducting lithosphere under southern British Columbia and western Oregon from teleseismic *P* wave conversions, *J. Geophys. Res.*, **86**, 3857-3866.

Langston, C.A. and D.V. Helmberger (1975). A procedure for modeling shallow dislocation sources, *Geophysics*, **42**, 117-130.

Lapp, D.B., T.J. Owens, and R.S. Crosson (1990). P-waveform analysis for local subduction geometry south of Puget Sound, *Pageoph*, **133**, 349-365.

Leaver, D.S., W.D. Mooney, and W.M. Kohler (1984). A seismic refraction study of the Oregon Cascades, *J. Geophys. Res.*, **89**, 3121-3134.

Lees, J.M. (1989). *Seismic tomograhpy in western Washington*, Ph.D. thesis, Univ. of Washington, Seattle, Washington, 173 pp.

Lees, J.M. and J.C. VanDecar (1991). Seismic tomography constrained by Bouguer gravity anomalies: applications in western Washington, *Pure Appl. Geophys.*, **135**, 31-52.

Ludwin, R.S., A.I. Qamar, S.D. Malone, C.Jonientz-Trisler, R.S. Crosson, R. Benson, and S.C. Moran (1994). Earthquake hypocenters in Washington and northern Oregon, 1987-1989, and operations of the Washington Regional Seismograph Network, *Washington Division of Geology and Earth Resources Information Circular 89*, 40 pp.

Luetgert, J.H. (1992). Interactive two-dimensional seismic raytracing for the Macintosh™, *U. S. Geol. Surv. Open-File Rept.* 92-356.

Mack, H. (1969). Nature of short-period P-wave signal variations at LASA, *J. Geophys. Res.*, **74**, 3161-3170.

McCaffrey, R. and C. Goldfinger (1995). Forearc deformation and great subduction zone earthquakes: Implications for Cascadia offshore earthquake potential, *Science*, **267**, 856-859.

McFadden, P.L., B.J. Drummond, and S. Kravis (1986). The *N*th-root stack: Theory, applications and examples, *Geophysics*, **51**, 1879-1892.

McKenzie, D.P. and R.L. Parker (1967). The north Pacific: An example of tectonics on a sphere, *Nature*, **216**, 1276-1280.

Meyers, R.A., D.G. Smith, H.M. Jol, and C.D. Peterson (1996). Evidence for eight great earthquake-subsidence events detected with ground-penetrating radar, Willapa barrier, Washington, *Geology*, **24**, 99-102.

Michaelson, C.A. and C.S. Weaver (1986). Upper mantle structure from teleseismic *P* wave arrivals in Washington and northern Oregon, *J. Geophys. Res.*, **91**, 2077-2094.

Molnar, P. and T. Atwater (1978). Interarc spreading and cordilleran tectonics as alternatives to the age of subducting oceanic lithosphere, *Earth Planet. Sci. Lett.*, **41**, 330-340.

Nábelek, J., X. Q. Li, S. Azevedo, J. Braunmiller, Z. Fabritius, B. Leitner, A. Tréhu, and G. Zandt (1993). A high-resolution image of the Cascadia subduction zone from teleseismic converted phases recorded by a broadband seismic array (abstract), *EOS Trans.*, **74**, 431.

Owens, T.J. (1984). *Determination of crustal and upper mantle structure from analysis of broadband teleseismic P-waveforms*, Ph.D. thesis, Univ. of Utah, Salt Lake City, Utah, 146 pp.

Owens, T.J, G. Zandt, and S.R. Taylor (1984). Seismic evidence for an ancient rift beneath the Cumberland Plateau, Tennessee: A detailed analysis of broadband teleseismic *P* waveforms, *J. Geophys. Res.*, **89**, 7783-7795.

Owens, T.J. and R.S. Crosson (1988). Shallow structure effects on broadband teleseismic *P* waveforms, *Bull. Seism. Soc. Am.*, **78**, 96-108.

Owens, T.J., R.S. Crosson, and M.A. Hendrickson (1988). Constraints on the subduction geometry beneath western Washington from broadband teleseismic waveform modeling, *Bull. Seism. Soc. Am.*, **78**, 1319-1334.

Pacheco, J.F., L.R. Sykes, and C.H. Scholz (1993). Nature of seismic coupling along simple plate boundaries of the subduction type, *J. Geophys. Res.*, **98**, 14,113-14,159.

Paulssen, H., J. Visser and G. Nolet (1993). The crustal structure from teleseismic P-coda -- I. Method, *Geophys. J. Int.*, **112**, 15-25.

Pennington, W.D. (1983). Role of shallow phase changes in the subduction of oceanic crust, *Science*, **220**, 1045-1047.

Pratt, T.L., S.Y. Johnson, C.J. Potter, and W.J. Stephenson (1994). The Puget lowland thrust sheet, (abstract), *EOS Trans.*, **75**, 621.

Rassmussen, J. and E. Humphreys (1988). Tomographic image of the Juan de Fuca plate beneath Washington and Oregon using teleseismic P-wave travel times, *Geophys. Res. Lett.*, **15**, 1417-1420.

Revenaugh, J. (1995). A scattered-wave image of subduction beneath the Transverse Ranges, *Science*, **260**, 1088-1092.

Riddihough, R.P. (1979). Gravity and structure of an active margin -- British Columbia and Washington, *Can. J. Earth Sci.*, **16**, 350-363.

Riddihough, R.P. (1984). Recent movements of the Juan de Fuca plate system, *J. Geophys. Res.*, **89**, 6984-6994.

Rogers, G.C. (1988). An assessment of the megathrust earthquake potential of the Cascadia subduction zone, *Can. J. Earth Sci.*, **25**, 844-852.

Rogers, G.C. and R.B. Horner (1991). An overview of western Canadian seismicity, in *Neotectonics of North America*, editors D.B. Slemmons, E.R. Engdahl, M.D. Zoback, and D.D. Blackwell, Geological Society of America, Boulder, Colorado, Decade Map Vol. 1, 69-76 pp.

Rohay, A.C. (1982). *Crust and mantle structure of the north Cascades Range, Washington*, Ph.D. thesis, Univ. of Washington, Seattle, Washington, 163 pp.

Rosenberger, J.L. and M. Gasko (1983). Comparing location estimators; trimmed means, medians and trimean, in *Understanding Robust and Exploration Data Analysis*, edited by D.C. Hoaglin, F. Mosteller, and J.W. Tukey, John Wiley and Sons, Inc., New York, New York.

Schultz, A.P. (1993). *A 2-D velocity structure for a cross-Cascades profile using earthquake sources*, M.S. thesis, Univ. of Washington, Seattle, Washington, 55 pp.

Schultz, A.P. and R.S. Crosson (1995). Seismic velocity across the central Washington Cascade range from refraction interpretation with earthquake sources, (submitted to *J. Geophys. Res*).

Shor, G.G., Jr., P. Dehlinger, H.K. Kirk, and W.S. French (1968). Seismic refraction studies of Oregon and northern California, *J. Geophys. Res.*, **73**, 2175-2194.

Silver, E.A. (1969). Late Cenozoic underthrusting of the continental margin off northernmost California, *Science*, **166**, 1265-1266.

Spence, W. (1987). Slab pull and the seismotectonics of subducting slabs, *Rev. Geophys.*, **25**, 55-69.

Spence, W. (1989). Stress origins and earthquake potentials in Cascadia, *J. Geophys. Res.*, **94**, 3076-3088.

Stanley, W.D., C. Finn, and J.L. Plesha (1987). Tectonics and conductivity structure in the southern Washington Cascades, *J. Geophys. Res.*, **92**, 10,179-10,193.

Stanley, W.D., W.D. Mooney, and G.S. Fuis (1990). Deep crustal structure of the Cascade Range and surrounding regions from seismic refraction and magnetotelluric data, *J. Geophys. Res.*, **95**, 19,419-19,438.

Stanley, W.D., S.Y. Johnson, A.I. Qamar, C.S. Weaver, and J.M. Williams (1996). Tectonics and seismicity of the southern Washington Cascade Range, *Bull. Seism. Soc.*, **86**, 1-18.

Taber, J.J. (1983). *Crustal structure and seismicity of the Washington continental margin*, Ph.D. thesis, Univ. of Washington, Seattle, Washington, 159 pp.

Taber, J.J. and B.T.R. Lewis (1986). Crustal structure of the Washington continental margin from refraction data, *Bull. Seism. Soc. Am.*, **76**, 1011-1024.

Taber, J.J. and S.W. Smith (1985). Seismicity and focal mechanisms associated with the subduction of the Juan de Fuca plate beneath the Olympic peninsula, Washington, *Bull. Seism. Soc. Am.*, **75**, 237-249.

Tabor, R.W. and W.M. Cady (1978a). Geologic map of the Olympic Peninsula, Washington, *U.S. Geol. Surv., Misc. Inv. Ser. Map I-994.*

Tabor, R.W. and W.M. Cady (1978b). The structure of the Olympic Mountains, Washington -- Analysis of a subduction zone, *U.S. Geol. Surv. Prof. Paper 1033*, 38 pp.

Tréhu, A.M., I Asudeh, T.M. Brocher, J.H. Luetgert, W.D. Mooney, J.L. Nábelek, and Y. Nakamura (1994). Crustal architecture of the Cascadia forearc, *Science*, **266**, 237-243.

Tréhu, A.M, L. Guibiao, E. Maxwell, and C. Goldfinger (1995). A seismic reflection profile across the Cascadia subduction zone offshore central Oregon: New constraints on methane distribution and crustal structure, *J. Geophys. Res.*, **100**, 15,101-15,116.

VanDecar, J.C. (1991). *Upper-mantle structure of the Cascadia subduction zone from non-linear travel-time inversion*, Ph.D. thesis, Univ. of Washington, Seattle, Washington, 165 pp.

VanDecar, J.C. and R.S. Crosson (1990). Determination of teleseismic relative phase arrival times using multi-channel cross-correlation and least squares, *J. Geophys. Res.*, **80**, 150-169.

Vidale, J.E. and H.M. Benz (1992). A sharp and flat section of the core-mantle boundary, *Nature*, **359**, 627-629.

Vidale, J.E. and H. Houston (1993). The depth dependence of earthquake duration and implications for rupture mechanisms, *Nature*, **365**, 45-47.

Vine, F.J. (1966). Spreading of the ocean floor: New evidence, *Science*, **154**, 1405-1415.

Vine, F.J. and J.T. Wilson (1965). Magnetic anomalies over a young oceanic ridge off Vancouver Island, *Science*, **150**, 485-489.

Weaver, C.S. and G.E. Baker (1988). Geometry of the Juan de Fuca plate, *Bull. Seism. Soc. Am.*, **88**, 264-275.

White, W.R.H. and J.C. Savage (1965). A seismic refraction and gravity study of the earth's crust in British Columbia, *Bull. Seism. Soc. Am.*, **55**, 463-486.

Wiggins, R.A. (1976). Body wave amplitude calculations -- II, *Geophys. J. R. Ast. Soc.*, **46**, 1-10.

Wiggins, R.A. and J.A. Madrid (1974). Body wave amplitude calculations, *Geophys. J. R. Ast. Soc.*, **37**, 423-433.

Zelt, C.A. and R.M. Ellis (1988). Practical and efficient ray tracing in two-dimensional media for rapid travel time and amplitude forward modeling, *Can. J. Expl. Geophys.*, **24**, 16-31.

Zelt, C.A. and R.B. Smith (1992). Seismic traveltime inversion for 2-D crustal velocity structure, *Geophys. J. Int.*, **108**, 16-34.

Zervas, C.E. and R.S. Crosson (1986). Pn observations and interpretations in Washington, *Bull. Seism. Soc. Am.*, **76**, 521-546.

Appendix A.1

Station Locations

Locations of PNSN stations in operation during the period 1980-1993 in Washington and Oregon.

Name	Latitude	Longitude	Elev. (km)	Installed (mm/yy)	Approx. Location
APW	46° 39′ 28.00″	122° 39′ 24.30″	0.457	12/80	Alpha Peak
†ASR	46° 09′ 02.40″	121° 35′ 33.60″	1.280	09/82	Stagman Ridge
AUG	45° 44′ 10.00″	121° 40′ 50.00″	0.865	10/81	Augspurger Mt.
BBO	42° 53′ 12.55″	122° 40′ 46.63″	1.671	06/92	Butler Butte
BDG	46° 13′ 59.10″	119° 19′ 03.90″	0.430	03/82	Badger Mt.
BHW	47° 50′ 12.60″	122° 01′ 55.80″	0.198	07/84	Bald Hill
†BLN	48° 00′ 26.50″	122° 58′ 18.64″	0.585	07/70	Blyn Mt.
BLS	48° 34′ 21.00″	121° 40′ 00.00″	1.341	12/84	Lk. Shannon
BOW	46° 28 30.00″	123° 13′ 41.00″	0.870	11/80	Boistfort Mt.
BPO	44° 39′ 06.86″	121° 41′ 19.20″	1.957	09/87	Bald Peter
BRV	46° 29′ 07.20″	119° 59′ 28.20″	0.920	12/83	Black Rock Valley
BVW	46° 48′ 39.60″	119° 52′ 59.40″	0.670	09/86	Beverly
CBS	47° 48′ 17.40″	120° 02′ 30.00″	1.067	12/87	Chelan Butte, So.
CBW	47° 48 25.50″	120° 01′ 57.60″	1.160	07/75	Chelan Butte
CDF	46° 06′ 58.20″	122° 02′ 51.00″	0.780	03/80	Cedar Flats
CHO	45° 35′ 27.00″	118° 34′ 45.00″	1.076	08/86	Cabbage Hill
CMM	46° 26′ 07.00″	122° 30′ 21.00″	0.620	04/80	Crazy Man Mt.
CMW	48° 25′ 25.30″	122° 07′ 08.40″	1.190	06/86	Cultus Mt.
COW	46° 29′ 27.60″	122° 00′ 43.60″	0.305	03/80	Cowlitz River
†CPW	46° 58′ 25.80″	123° 08′ 10.80″	0.792	07/70	Capitol Peak
CRF	46° 49′ 30.00	119° 23′ 13.20″	0.189	07/70	Corfu
DAV	47° 38′ 180.00	118° 13′ 33.60″	0.758	10/75	Davenport
DBO	43° 07′ 09.00″	123° 14′ 34.00″	0.984	08/90	Dodson Butte

(continued)

Name	Latitude	Longitude	Elev. (km)	Installed (mm/yy)	Approx. Location
DPW	47° 52′ 14.30″	118° 12′ 10.20″	0.892	11/86	Davenport
DYH	47° 57′ 37.80″	119° 46′ 09.60″	0.820	07/75	Dyer Hill
DY2	47° 59′ 06.60″	119° 46′ 16.80″	0.890	06/85	Dyer Hill
EDM	46° 11′ 50.40″	122° 09′ 00.00″	1.609	06/80	East Dome, MSH
ELK	46° 18′ 20.00″	122° 20′ 27.00″	1.270	05/80	Elk Rock
ELL	46° 54′ 34.80″	120° 33′ 58.80″	0.789	06/79	Ellensburg
EPH	47° 21′ 22.80″	119° 35′ 45.60″	0.661	03/83	Ephrata
EST	47° 14′ 16.80″	121° 12′ 21.80″	0.756	06/79	Easton
ETP	46° 27′ 53.40″	119° 03′ 32.40″	0.250	06/75	Eltopia
ET2	46° 32′ 06.00″	118° 57′ 01.20″	0.330	04/89	Eltopia
ET3	46° 34′ 38.40″	118° 56′ 15.00″	0.286	0//90	Eltopia
ETT	47° 39′ 18.00″	120° 17′ 36.00″	0.439	07/77	Entiat
ETW	47° 36′ 15.60″	120° 19′ 56.40″	1.477	10/86	Entiat
FBO	44° 18′ 35.60″	122° 34′ 40.20″	1.080	09/91	Farmers Butte
FLT	46° 11′ 21.30″	122° 21′ 22.50″	1.387	12/80	Flat Top
FL2	46° 11′ 47.00″	122° 21′ 01.00″	1.378	08/84	Flat Top
†FMW	46° 56′ 29.60″	121° 40′ 11.30″	1.859	09/72	Mt. Fremont
FOX	48° 19′ 50.00″	119° 42′ 29.00″	0.896	06/85	Fox Mt.
FPW	47° 58′ 09.00″	120° 12′ 46.50″	0.352	7/75	Fields Pt.
GBL	46° 35′ 54.00″	119° 27′ 35.40″	0.330	06/76	Gable Mt.
GHW	47° 02′ 30.00″	122° 16′ 21.00″	0.268	09/75	Garrison Hill
GLD	45° 50′ 13.00″	120° 48′ 46.00″	0.610	01/80	Goldendale
GL2	45° 57′ 35.00″	120° 49′ 22.50″	1.000	09/84	Goldendale
†GLK	46° 33′ 50.20″	121° 36′ 30.70″	1.320	06/81	Glacier Lk.
GMO	44° 26′ 20.80″	120° 57′ 22.30″	1.689	08/87	Grizzlie Mt.

(continued)

Name	Latitude	Longitude	Elev. (km)	Installed (mm/yy)	Approx. Location
†GMW	47° 32′ 52.50″	122° 47′ 10.80″	0.506	02/70	Gold Mt.
GRO	45° 21′ 04.50″	123° 39′ 43.00″	0.945	05/86	Grindstone Mt.
†GSM	47° 12′ 11.40″	121° 47′ 40.20″	1.305	06/70	Grass Mt.
GUL	45° 55′ 27.00″	121° 35′ 44.00″	1.189	07/86	Guler Mt.
HBO	43° 50′ 39.55″	122° 19′ 11.88″	1.615	09/90	Huckleberry Mt.
HDW	47° 38′ 54.60″	123° 03′ 15.20″	1.006	11/79	Hoodsport
HHW	46° 10′ 59.00″	119° 22′ 59.00″	0.415	08/84	Horse Heaven Hills
HH2	46° 10′ 18.00″	119° 23′ 01.00″	0.490	03/87	Horse Heaven Hills
HSO	43° 31′ 33.00″	123° 05′ 24.00″	1.020	09/90	Harness Mt.
HSR	46° 10′ 28.00″	122° 10′ 46.00″	1.720	08/85	South Ridge, MSH
†HTW	47° 48′ 12.50″	121° 46′ 08.65″	0.829	06/75	Haystack Lookout
JBO	45° 27′ 41.68″	119° 50′ 13.28″	0.645	09/82	Jordan Butte
†JCW	48° 11′ 42.70″	121° 55′ 31.07″	0.792	12/82	Jim Creek
JUN	46° 08′ 48.00″	122° 09′ 10.80″	1.049	03/80	June Lk.
KMO	45° 38′ 07.80″	123° 29′ 22.20″	0.975	09/82	Kings Mt.
KOS	46° 27′ 40.80″	122° 11′ 25.80″	0.828	05/81	Kosmos
LCW	46° 40′ 14.40″	122° 42′ 02.80″	0.396	03/92	Lucas Creek
†LMW	46° 40′ 05.40″	122° 17′ 26.40″	1.224	06/75	Ladd Mt.
LNO	45° 52′ 18.60″	118° 17′ 06.60″	0.771	08/86	Lincton Mt.
LOC	46° 43′ 01.20″	119° 25′ 51.00″	0.210	11/82	Locke Is.
LON	46° 45′ 00.00″	121° 48′ 36.00″	0.853	0970	Longmire
†LO2	46° 45′ 00.00″	121° 48′ 36.00″	0.853	03/88	Longmire
LVP	46° 04′ 06.00″	122° 24′ 30.00″	1.170	04/80	Lakeview Peak
LYW	48° 32′ 07.20″	122° 06′ 06.00″	0.107	04/75	Lyman
MAS	46° 08′ 41.00″	121° 35′ 30.70″	1.370	12/80	Mt Adams, So.

(continued)

Name	Latitude	Longitude	Elev. (km)	Installed (mm/yy)	Approx. Location
MBW	48° 47′ 02.40″	121° 53′ 58.80″	1.676	11/72	Mt. Baker
MCW	48° 40′ 46.80″	122° 49′ 56.40″	0.693	11/72	Mt. Constitution
MDW	46° 36′ 47.40″	119° 45′ 39.60″	0.330	01/75	Midway
MEW	47° 12′ 06.62″	122° 38′ 45.60″	0.0970	03/85	McNeil Is.
MFW	45° 54′ 10.80″	118° 24′ 21.00″	0.395	10/71	Milton-Freewater
MJ2	46° 33′ 27.00″	119° 21′ 32.40″	0.146	03/89	May Junction
MOW	47° 50′ 46.90″	122° 02′ 52.90″	0.180	09/79	Monroe
MOX	46° 34′ 38.40″	120° 17′ 53.40″	0.501	10/84	Moxie City
MPO	44° 30′ 17.40″	123° 33′ 00.60″	1.249	08/90	Mary's Peak
†MTM	46° 01′ 31.80″	122° 12′ 42.00″	1.121	03/80	Mt. Mitchell
†NAC	46° 43′ 59.40″	120° 49′ 25.20″	0.728	06/79	Naches
NCO	43° 42′ 14.40″	121° 08′ 18.00″	1.908	09/87	Newberry Crater
NEL	48° 04′ 12.60″	120° 20′ 24.60″	1.500	05/85	Nelson Butte
NEW	48° 15′ 50.00″	117° 07′ 13.00″	0.760	09/75	Newport
NLO	46° 05′ 18.00″	123° 27′ 00.00″	0.900	04/82	Nicolai Mt.
OBC	48° 02′ 07.10″	124° 04′ 39.00″	0.938	07/80	Bonidu Creek
OBH	47° 19′ 34.50″	123° 51′ 57.00″	0.383	07/80	Burnt Hill
OCP	48° 17′ 58.50″	124° 37′ 37.50″	0.487	07/80	Cheela Peak
OCT	47° 44′ 57.00″	124° 10′ 25.80″	0.743	07/80	Mt. Octopus
OD2	47° 23′ 15.60″	118° 42′ 34.80″	0.553	06/89	Odessa
ODS	47° 18′ 24.00″	118° 44′ 42.00″	0.523	08/75	Odessa
OEM	48° 07′ 46.50″	124° 18′ 13.50″	0.712	07/80	Tyee Ridge
OFK	47° 57′ 00.00″	124° 21′ 28.10″	0.134	07/80	Forks
OHW	48° 19′ 24.00″	122° 31′ 54.60″	0.054	05/75	Oak Harbor
OLQ	47° 30′ 58.10″	123° 48′ 31.50″	0.121	07/80	Lk. Quinault

(continued)

Name	Latitude	Longitude	Elev. (km)	Installed (mm/yy)	Approx. Location
OMK	48° 28′ 49.20″	119° 33′ 39.00″	0.421	07/75	Omak
ONR	46° 52′ 37.50″	123° 46′ 16.50″	0.257	07/80	North River
OOW	47° 44′ 03.60″	124° 11′ 10.20″	0.561	06/84	Octupus West
OSD	47° 49′ 15.00″	123° 42′ 06.00″	2.010	10/84	Snow Dome
OSP	48° 17′ 05.46″	124° 35′ 23.30″	0.585	10/83	Sooes Peak
OSR	47° 30′ 20.30″	123° 57′ 42.00″	0.815	09/89	Salmon Ridge
OTH	46° 44′ 20.40″	119° 12′ 59.40″	0.260	06/75	Othello
OT2	46° 43′ 09.60″	119° 14′ 01.80″	0.329	12/88	Othello
OT3	46° 40′ 08.40″	119° 13′ 58.80″	0.322	08/94	Othello
OTR	48° 05′ 08.00″	124° 20′ 39.00″	0.712	06/84	Tyee Ridge
PAT	45° 52′ 55.20″	119° 45′ 08.40″	0.262	04/81	Paterson
PEN	45° 36′ 43.20″	118° 45′ 46.50″	0.430	07/75	Pendleton
PGO	45° 27′ 42.60″	122° 27′ 11.50″	0.253	06/82	Gresham
†PGW	47° 49′ 18.80″	122° 35′ 57.69″	0.122	04/85	Port Gamble
PHO	45° 37′ 07.80″	122° 49′ 50.20″	0.299	04/82	Portland Hills
PLN	47° 47′ 04.80″	120° 37′ 58.82″	0.700	07/77	Plain
PRO	46° 12′ 45.60″	119° 41′ 08.40″	0.553	10/71	Prosser
RAN	46° 24′ 30.00″	121° 51′ 49.00″	1.620	03/80	Randle
RC1	46° 56′ 42.60″	119° 26′ 39.60″	0.485	05/88	Royal City
RCS	46° 52′ 15.60″	121° 43′ 51.96″	2.877	06/89	Camp Schurman
RER	46° 49′ 09.20″	121° 50′ 27.30″	1.756	07/89	Emerald Ridge
†RMW	47° 27′ 34.95″	121° 48′ 19.20″	1.024	07/71	Rattlesnake Mt., W.
RNO	43° 54′ 44.00″	123° 44′ 26.00″	0.875	09/91	Roman Nose
RPK	45° 45′ 42.00″	120° 13′ 50.00″	0.330	08/84	Roosevelt Peak
†RPW	48° 26′ 54.00″	121° 30′ 49.00″	0.850	11/77	Rockport

(continued)

Name	Latitude	Longitude	Elev. (km)	Installed (mm/yy)	Approx. Location
RSW	46° 23′ 40.20″	119° 35′ 28.80″	1.045	07/70	Rattlesnake Mt., E.
RVC	46° 56′ 34.50″	121° 58′ 17.30″	1.000	01/83	Voight Creek
RVW	46° 08′ 58.20″	122° 44′ 37.20″	0.460	02/81	Rose Valley
SAW	47° 42′ 06.00″	119° 24′ 01.80″	0.701	07/75	St. Andrews
SBL	46° 20′ 25.20″	122° 02′ 19.80″	1.665	06/80	Strawberry Lookout
SBO	45° 01′ 42.00″	120° 03′ 33.48″	1.390	09/82	Squaw Butte
SHW	46° 11′ 37.10″	122° 14′ 06.50″	1.425	10/72	MSH
SMW	47° 19′ 10.20″	123° 20′ 30.00″	0.840	03/75	South Mt.
SOS	46° 14′ 38.50″	122° 08′ 12.00″	1.270	06/81	Smith Creek, MSH
SPW	47° 33′ 13.30″	122° 14′ 45.10″	0.008	09/69	Seward Park
SSO	44° 51′ 21.60″	122° 27′ 37.80″	1.242	09/91	Sweet Springs
STD	46° 14′ 16.00″	122° 13′ 21.90″	1.268	05/82	Studebaker Ridge
STW	48° 09′ 02.90″	123° 40′ 13.10″	0.308	06/73	Striped Peak
SYR	46° 51′ 46.80″	119° 37′ 04.20″	0.267	03/69	Smyrna
†TBM	47° 10′ 12.00″	120° 35′ 52.80″	1.006	11/79	Table Mt.
TCO	44° 06′ 21.00″	121° 36′ 01.00″	1.975	08/87	Three Crk. Meadows
TDH	45° 17′ 23.40″	121° 47′ 25.20″	1.541	09/82	Tom,Dick,Harry Mt.
TDL	46° 21′ 03.00″	122° 12′ 57.00″	1.400	11/83	Tradedollar Lk.
TKO	45° 22′ 16.73″	123° 27′ 14.02″	1.024	08/91	Trask Mt.
TWW	47° 08′ 17.40″	120° 52′ 06.00″	1.027	10/86	Teanaway
†VBE	45° 03′ 37.20″	121° 35′ 12.60″	1.544	10/79	Beaver Butte
VCP	44° 40′ 16.20″	122° 05′ 22.20″	1.161	05/80	Cooper's Ridge
†VCR	44° 58′ 58.18″	120° 59′ 17.35″	1.015	08/87	Criterion Ridge
VFP	45° 19′ 05.00″	121° 27′ 54.30″	1.716	10/80	Flag Pt.
VGB	45° 30′ 56.40″	120° 46′ 39.00″	0.729	04/80	Gordon Butte

(continued)

Name	Latitude	Longitude	Elev. (km)	Installed (mm/yy)	Approx. Location
VGT	45° 08′ 59.40″	122° 15′ 55.20″	0.993	04/80	Goat Mt.
VG2	45° 09′ 20.00″	122° 16′ 15.00″	0.823	09/85	Goat Mt.
VHO	45° 13′ 09.00″	123° 43′ 31.20″	0.951	04/80	Mt. Hebo
VIP	44° 30′ 29.40″	120° 37′ 07.80″	1.731	12/79	Ingram Pt.
†VLL	45° 27′ 48.00″	121° 40′ 45.00″	1.195	10/80	Laurance Lk.
VLM	45° 32′ 18.60″	122° 02′ 21.00″	1.150	06/80	Little Larch
VLO	44° 52′ 46.20″	122° 23′ 34.80″	1.351	06/80	Lookout Mt.
VMD	45° 39′ 09.60″	121° 42′ 43.80″	1.317	10/80	Mt. Defiance
VMN	45° 11′ 12.60″	121° 03′ 10.80″	0.555	03/80	Maupin
VTG	46° 57′ 28.80″	119° 59′ 14.40″	0.208	0/770	Vantage
VT2	46° 58′ 02.40″	119° 59′ 57.00″	1.270	09/92	Vantage
VTH	45° 10′ 52.20″	120° 33′ 40.80″	0.773	03/80	The Trough
WA2	46° 45′ 19.20″	119° 33′ 56.40″	0.244	05/78	Wahluke Slope
†WAT	47° 41′ 55.20″	119° 57′ 14.40″	0.821	11/76	Waterville
WBW	48° 01′ 04.20″	119° 08′ 13.80″	0.825	07/75	Wilson Butte
WEN	47° 31′ 46.20″	120° 11′ 39.00″	1.061	07/75	Wenatchee
WGW	46° 02′ 40.80″	118° 55′ 57.60″	0.158	11/70	Wallula Gap
WG2	46° 01′ 50.25″	118° 51′ 19.95″	0.511	04/87	Wallula Gap
WG3	46° 01′ 43.00″	118° 51′ 24.00″	0.480	01/90	Wallula Gap
WG4	46° 01′ 49.20″	118° 51′ 21.00″	0.511	08/92	Wallula Gap
WIW	46° 25 45.60″	119° 17′ 15.60″	0.128	07/70	Wooded Is.
WNS	46° 42′ 37.00″	120° 34′ 30.00″	1.000	07/84	Wenas
WPO	45° 34′ 24.00″	122° 47′ 22.40″	0.334	10/86	West Portland
WP2	45° 33′ 57.20″	122° 47′ 06.90″	0.341	12/88	West Portland
†WPW	46° 41′ 53.40″	121° 32′ 48.00″	1.250	03/80	White Pass

(continued)

Name	Latitude	Longitude	Elev. (km)	Installed (mm/yy)	Approx. Location
WRD	46° 58′ 12.00″	119° 08′ 41.40″	0.375	07/70	Warden
WTP	48° 28′ 16.20″	120° 14′ 52.20″	0.855	08/77	Winthrop
YAK	46° 31′ 43.80″	120° 31′ 14.40″	0.629	11/79	Yakima
YEL	46° 12′ 35.00″	122° 11′ 16.00″	1.750	09/81	Yellow Rock, MSH

MSH = Mt. St. Helens

† denotes stations showing stacks with coherent arrivals not modeled in this study.

Appendix A.2

Event Locations

Event parameters for events used in this study as provided by the NEIC published in the Preliminary Determination of Epicenters (PDE). Also included are the distance and back azimuth of each event with respect to the center of the PNSN.

Event #	Date (y/m/d)	UTC (h:m:s.dsec)	Lat (deg.)	Long (deg.)	Z (km)	m_b	Dist. (deg.)	BAZ (deg.)
1	80/05/26	18:41:42.9	19.364S	69.238W	114	6.1	80.81	131.31
2	80/06/09	20:06:35.0	40.796N	139.860E	165	5.6	67.35	305.87
3	81/01/23	04:58:31.5	42.524N	142.122E	116	6.3	64.51	305.60
4	81/03/26	18:04:44.7	19.370S	68.957W	138	5.8	80.69	130.90
5	81/04/01	18:03:36.5	27.310S	63.320W	554	5.9	90.33	130.87
6	81/05/08	23:34:44.9	42.660N	139.129E	200	6.0	66.47	306.86
7	81/09/14	12:44:29.8	18.320N	68.891W	170	5.9	51.37	106.01
8	81/11/03	07:02:38.6	1.831S	78.436W	129	5.6	61.27	129.56
9	81/11/27	17:21:45.8	42.913N	131.076E	543	5.8	70.13	311.99
10	82/01/04	06:05:01.3	18.014N	145.626E	590	6.1	79.29	284.81
11	82/01/07	08:03:44.6	12.070S	166.707E	156	5.8	86.96	248.97
12	82/02/27	16:16:54.5	22.288N	143.458E	127	5.9	77.66	289.33
13	82/03/21	13:35:03.1	18.586S	175.188W	203	5.9	81.44	231.06
14	82/07/04	01:20:06.8	27.929N	136.967E	536	6.3	77.68	297.65
15	82/09/03	20:14:30.3	23.859S	66.605W	183	5.5	85.90	131.73
16	82/09/15	20:22:55.2	14.493S	70.785W	128	6.0	75.94	129.89
17	82/09/17	13:28:24.8	23.469S	179.852W	546	5.9	87.92	231.85
18	82/11/18	14:57:52.4	1.719S	76.703W	195	6.0	62.10	127.83
19	82/11/27	09:55:38.9	50.205N	147.727E	622	5.6	56.71	309.78
20	82/12/31	03:47:28.5	20.993S	68.464W	118	5.7	82.57	131.59
21	83/01/01	05:31:56.1	16.943S	69.114W	172	5.7	78.86	129.87
22	83/01/10	12:32:21.6	27.237S	63.301W	558	5.7	90.36	131.18

(continued)

Event #	Date (y/m/d)	UTC (h:m:s.dsec)	Lat (deg.)	Long (deg.)	Z (km)	m_b	Dist. (deg.)	BAZ (deg.)
23	83/01/15	00:39:34.2	33.268N	136.040E	435	5.5	74.39	302.05
24	83/02/13	06:35:30.0	13.837N	144.935E	105	5.7	82.75	282.39
25	83/04/12	12:07:54.5	4.843S	78.103W	104	6.5	63.99	131.00
26	83/04/15	00:09:33.3	19.221S	175.469W	227	5.7	82.11	230.93
27	83/04/15	10:08:20.5	5.979S	75.663W	118	5.6	66.23	129.37
28	83/04/26	15:26:40.3	24.647N	122.589E	116	5.7	88.55	305.39
29	83/05/02	09:58:13.8	20.733S	178.475W	596	5.7	84.96	232.40
30	83/06/01	01:59:54.6	17.038S	174.605W	180	6.2	79.85	231.47
31	83/06/21	17:06:51.4	29.718N	129.395E	158	5.9	80.80	303.89
32	83/06/25	15:04:10.4	22.003S	177.451W	278	5.5	85.44	230.89
33	83/07/03	02:49:27.9	20.161N	122.379E	220	6.1	92.20	302.81
34	83/07/21	07:11:33.8	22.193S	68.451W	126	5.5	83.57	132.23
35	83/07/24	23:07:30.9	53.930N	158.372E	180	6.1	49.55	308.56
36	83/08/02	02:17:41.0	20.435N	122.101E	158	6.1	92.14	303.18
37	83/08/25	20:23:33.3	33.509N	131.484E	126	6.1	76.79	305.07
38	83/09/01	20:01:47.0	17.330S	69.932W	105	6.0	78.51	130.59
39	83/09/14	11:25:00.9	18.104N	145.770E	159	6.0	79.59	285.26
40	83/09/16	08:09:26.6	24.032S	179.796W	510	6.0	88.34	231.48
41	83/09/20	08:50:58.3	18.185N	68.474W	101	5.6	51.54	105.51
42	83/10/08	07:45:26.6	44.229N	130.741E	558	5.7	69.35	313.15
43	83/11/29	23:41:07.3	19.503S	177.783W	525	5.7	83.58	232.58
44	83/12/15	04:22:33.4	33.099S	70.120W	100	5.9	91.98	139.26
45	84/01/13	02:29:00.9	3.863S	78.494W	103	5.8	62.96	130.81
46	84/01/19	16:15:16.3	23.642S	178.321W	332	5.8	87.24	230.61
47	84/02/01	07:28:28.7	49.063N	146.590E	573	5.9	58.26	309.43

(continued)

Event #	Date (y/m/d)	UTC (h:m:s.dsec)	Lat (deg.)	Long (deg.)	Z (km)	m_b	Dist. (deg.)	BAZ (deg.)
48	84/02/25	15:29:14.5	16.747S	174.772W	257	5.5	79.70	231.77
49	84/02/26	08:18:19.8	17.316S	70.526W	113	5.8	78.44	131.23
50	84/03/14	11:36:30.9	20.089S	178.073W	570	5.7	84.22	232.46
51	84/04/20	06:31:10.6	50.120N	148.745E	582	6.0	56.28	309.14
52	84/04/22	03:33:00.5	21.866S	179.375W	593	5.7	86.36	232.43
53	84/04/23	21:40:35.5	47.450N	146.692E	414	6.0	59.13	307.24
54	84/04/24	04:11:29.0	30.909N	138.431E	403	6.1	74.65	298.81
55	84/04/25	04:19:32.0	17.311S	177.229W	415	5.7	81.50	233.41
56	84/06/15	14:22:23.0	15.816S	174.831W	247	6.1	78.97	232.35
57	84/06/18	11:20:17.9	15.705S	72.491W	117	5.8	76.08	131.99
58	84/07/03	13:42:00.8	17.735S	178.847W	536	5.7	82.74	234.43
59	84/09/28	03:03:46.8	21.510S	177.796W	364	5.8	85.22	231.43
60	84/10/10	19:05:58.1	20.147S	179.271W	676	5.6	84.92	233.35
61	84/10/15	10:21:07.5	15.860S	173.643W	128	6.5	78.36	231.36
62	84/10/20	17:59:17.0	24.072S	66.832W	192	6.0	85.96	132.02
63	84/10/30	01:05:49.9	17.109S	174.076W	141	6.0	79.63	231.00
64	84/11/01	09:27:39.3	19.790S	175.845W	223	5.7	82.78	230.90
65	84/11/15	05:52:30.5	20.388S	177.421W	348	5.7	84.11	231.79
66	84/11/17	13:45:49.1	18.785S	178.032W	451	6.1	83.14	233.18
67	84/11/22	17:07:36.1	17.779S	178.050W	646	5.9	82.33	233.78
68	84/11/23	18:40:14.4	8.191S	76.130W	122	5.9	67.85	131.06
69	84/12/04	07:43:23.1	22.609N	143.334E	122	5.8	77.51	289.64
70	85/01/26	21:36:10.8	32.545N	131.184E	121	5.8	77.67	304.61
71	85/02/14	08:30:56.6	24.068S	67.881W	139	5.6	85.42	132.82
72	85/03/15	00:16:02.7	20.682S	178.218W	545	5.7	84.78	232.23

(continued)

Event #	Date (y/m/d)	UTC (h:m:s.dsec)	Lat (deg.)	Long (deg.)	Z (km)	m_b	Dist. (deg.)	BAZ (deg.)
73	85/03/27	12:48:12.3	44.335N	146.666E	155	5.9	60.81	304.78
74	85/03/28	16:07:06.8	40.310N	140.362E	166	6.1	66.97	304.77
75	85/04/27	10:11:42.6	21.032S	176.820W	260	5.8	84.31	230.95
76	85/05/01	13:27:56.1	9.196S	71.230W	600	6.0	71.30	127.27
77	85/06/10	15:37:00.9	27.958S	66.995W	151	5.8	89.09	134.29
78	85/08/23	16:35:10.2	24.080S	66.830W	195	5.5	85.96	132.02
79	85/08/24	06:53:14.8	22.021S	177.799W	348	5.5	85.64	231.14
80	85/08/28	20:50:48.3	21.011S	178.981W	625	6.1	85.46	232.62
81	85/09/10	06:39:01.7	27.208N	139.848E	501	5.8	76.43	295.24
82	85/10/04	08:41:37.9	27.558N	139.964E	478	5.6	76.11	295.42
83	85/10/06	12:00:49.2	18.961S	169.432E	273	5.7	90.54	242.49
84	85/10/08	09:47:24.8	22.825S	66.311W	242	5.5	85.19	130.93
85	85/10/12	02:12:57.9	21.656S	176.382W	155	5.9	84.59	230.26
86	85/10/18	04:19:06.4	46.323N	146.272E	271	5.9	59.80	306.78
87	85/10/24	01:48:55.9	31.386S	68.605W	110	5.7	91.18	137.34
88	85/11/19	14:03:34.6	28.666N	128.875E	135	5.5	81.90	303.55
89	85/11/30	03:04:18.8	16.366S	174.197W	165	5.7	79.08	231.52
90	86/02/20	12:16:41.7	22.060S	179.560W	602	5.7	86.62	232.45
91	86/03/05	15:47:06.8	18.813S	169.605E	287	5.6	90.32	242.46
92	86/03/15	11:29:44.3	18.909S	67.391W	243	5.6	81.40	129.58
93	86/04/01	10:13:40.7	18.037S	178.537W	540	5.8	82.81	234.01
94	86/04/30	14:09:39.8	18.036S	69.453W	106	5.5	79.59	130.75
95	86/05/11	01:24:25.7	26.743N	125.205E	194	5.9	85.45	304.83
96	86/05/26	18:40:44.2	21.819S	179.079W	583	6.1	86.17	232.23
97	86/05/26	19:06:15.9	20.190S	178.860E	538	6.4	85.99	234.75

(continued)

Event #	Date (y/m/d)	UTC (h:m:s.dsec)	Lat (deg.)	Long (deg.)	Z (km)	m_b	Dist. (deg.)	BAZ (deg.)
98	86/05/26	19:48:36.3	20.726S	177.814E	623	5.5	87.00	235.21
99	86/06/16	10:48:25.7	22.037S	178.925W	547	6.3	86.26	231.99
100	86/06/28	05:03:47.4	20.037S	176.056W	211	6.1	83.09	230.93
101	86/07/02	04:16:57.7	22.038S	179.534W	598	5.6	86.59	232.45
102	86/07/16	12:41:28.3	19.511S	169.165E	111	6.2	91.12	242.33
103	86/07/19	05:59:36.2	47.264N	151.127E	141	5.9	56.56	305.35
104	86/07/27	10:43:26.0	25.848S	177.490W	147	5.8	88.60	228.72
†105	86/08/30	21:28:35.4	45.547N	26.316E	132	6.4	83.46	22.45
106	86/09/13	15:17:21.0	31.827S	179.937W	215	5.9	94.70	227.02
107	86/10/22	08:59:28.8	10.569S	166.040E	165	5.9	86.31	250.40
108	86/10/30	01:28:54.5	21.702S	176.616W	188	6.4	84.75	230.42
109	86/11/23	01:39:23.9	3.342S	77.411W	106	6.4	63.08	129.47
110	87/01/14	11:03:48.7	42.565N	142.850E	102	6.5	64.08	305.24
111	87/01/21	11:26:36.6	20.608N	144.885E	118	5.6	77.93	287.16
112	87/02/10	00:59:28.5	19.489S	177.456W	395	6.2	83.40	232.33
113	87/02/11	17:42:50.9	43.169N	132.286E	499	5.5	69.33	311.50
114	87/02/14	13:38:22.7	17.926S	178.632W	566	5.7	82.77	234.15
115	87/03/19	22:51:39.2	20.397S	176.134W	214	5.9	83.43	230.78
116	87/04/07	00:51:36.6	22.782S	66.074W	205	5.5	85.28	130.72
117	87/04/29	14:27:35.7	19.013S	177.736W	385	5.9	83.16	232.82
118	87/05/07	03:05:49.1	46.736N	139.232E	430	6.0	63.30	310.65
119	87/05/18	03:07:34.1	49.282N	147.693E	542	6.1	57.26	308.89
120	87/05/19	00:14:33.1	29.862N	139.067E	417	5.5	75.01	297.65
121	87/07/14	23:46:03.5	49.631N	147.828E	576	5.7	56.99	309.17
122	87/08/26	06:56:46.2	20.749S	178.464W	569	5.7	84.97	232.38

(continued)

Event #	Date (y/m/d)	UTC (h:m:s.dsec)	Lat (deg.)	Long (deg.)	Z (km)	m_b	Dist. (deg.)	BAZ (deg.)
123	87/09/01	04:26:07.4	23.052S	66.529W	199	6.0	85.27	131.22
124	87/09/14	10:17:15.0	30.488N	139.671E	171	5.7	74.20	297.72
125	87/09/23	07:15:43.2	45.960N	149.519E	131	5.9	58.22	304.86
126	87/09/24	06:03:19.8	21.841S	179.454W	593	5.5	86.39	232.50
127	87/10/02	07:38:27.8	27.346N	139.942E	464	5.5	76.27	295.28
128	87/10/03	03:35:10.6	17.950S	69.247W	149	5.8	79.63	130.53
129	87/10/07	00:51:36.6	22.845S	68.030W	106	5.6	84.33	132.26
130	87/10/24	14:37:16.4	10.913S	166.154E	171	5.5	86.50	250.09
131	87/10/27	12:57:59.4	21.360S	178.805W	534	5.5	85.65	232.29
132	87/10/27	21:58:17.0	28.676S	62.929W	605	6.0	91.72	131.75
133	87/11/06	18:47:35.0	22.801S	63.583W	538	5.8	86.61	128.84
134	87/11/12	00:24:40.0	17.209S	177.306W	393	5.5	81.46	233.53
135	87/12/04	19:51:35.7	5.777S	154.555E	145	5.9	90.40	262.03
136	87/12/12	04:51:50.5	29.692N	140.025E	164	6.3	74.55	296.91
137	88/01/02	12:42:02.5	43.295N	142.419E	177	6.0	63.84	306.09
138	88/01/15	08:40:23.9	20.789S	175.993W	214	6.2	83.68	230.45
139	88/01/24	16:00:04.5	17.763S	178.737W	566	5.7	82.70	234.33
140	88/02/06	18:03:54.7	17.756S	66.958W	285	6.0	80.68	128.58
141	88/02/06	21:30:04.3	16.195S	173.820W	126	5.8	78.74	231.31
142	88/02/18	13:52:36.0	23.513S	67.706W	142	5.7	85.05	132.38
143	88/03/04	03:08:15.4	17.993S	178.521W	590	5.5	82.76	234.03
144	88/03/09	21:41:10.8	18.313S	69.543W	119	5.4	79.78	130.97
145	88/03/10	10:25:05.3	20.917S	178.645W	623	6.1	85.20	232.42
146	88/04/11	22:36:25.0	21.460S	179.336W	619	5.6	86.01	232.63
147	88/05/04	23:47:02.4	18.512N	145.858E	123	5.9	78.79	285.00

(continued)

Event #	Date (y/m/d)	UTC (h:m:s.dsec)	Lat (deg.)	Long (deg.)	Z (km)	m_b	Dist. (deg.)	BAZ (deg.)
148	88/05/13	04:44:39.8	15.378S	174.965W	272	5.7	78.68	232.71
149	88/05/20	03:19:54.1	17.473S	69.470W	125	5.5	79.12	130.45
150	88/05/28	16:27:24.1	17.852S	178.662W	559	5.7	82.73	234.22
151	88/06/10	03:10:22.1	12.724S	166.744E	113	5.7	87.48	248.47
152	88/07/02	10:01:30.4	14.251S	167.209E	156	5.8	88.34	247.14
153	88/07/03	05:09:43.2	24.569S	179.262E	534	5.5	89.28	231.86
154	88/07/06	01:10:53.0	17.593S	178.929W	546	5.5	82.67	234.58
155	88/07/09	15:10:48.9	29.693S	179.045W	177	5.6	92.53	227.64
156	88/07/28	17:12:32.7	22.292S	65.847W	285	5.8	85.00	130.27
157	88/08/14	10:56:57.5	54.601N	152.657E	644	5.5	51.80	312.37
158	88/09/07	11:53:25.4	30.335N	137.363E	499	6.0	75.70	299.09
159	88/09/13	00:58:45.9	29.805N	138.363E	447	5.8	75.48	298.07
160	88/09/14	22:14:07.6	23.386S	67.944W	124	5.8	84.82	132.49
161	88/09/15	18:48:03.2	1.403S	77.895W	189	5.8	61.19	128.78
162	88/09/30	03:23:47.3	19.727S	69.115W	113	5.3	81.18	131.41
163	88/11/07	03:24:30.6	26.574N	126.336E	118	5.6	84.94	303.94
164	88/12/24	04:26:57.5	23.385S	66.391W	223	5.9	85.61	131.30
165	89/01/02	01:52:08.0	18.589S	174.559W	109	6.1	81.11	230.56
166	89/01/18	17:32:11.6	7.025S	74.598W	147	5.4	67.67	129.00
167	89/02/01	10:22:41.5	31.561N	140.155E	119	5.5	73.15	298.20
168	89/02/28	13:01:57.6	23.113S	61.465W	569	5.6	88.00	127.43
169	89/03/11	05:05:00.6	17.766S	174.761W	230	6.4	80.53	231.19
170	89/03/30	20:39:29.3	19.589S	175.848W	230	5.8	82.61	231.02
171	89/04/05	23:47:49.3	20.857S	69.028W	112	5.7	82.17	131.96
172	89/04/16	19:48:14.6	21.039S	178.942W	610	5.7	85.46	232.58

(continued)

Event #	Date (y/m/d)	UTC (h:m:s.dsec)	Lat (deg.)	Long (deg.)	Z (km)	m_b	Dist. (deg.)	BAZ (deg.)
173	89/04/18	12:33:52.1	23.834S	179.944E	524	5.8	88.32	231.79
174	89/05/05	18:28:39.4	8.281S	71.381W	594	6.4	70.45	126.87
175	89/05/08	14:28:30.9	23.427S	179.953W	548	5.6	87.94	231.95
176	89/05/21	21:56:48.6	17.952S	178.593W	584	5.7	82.77	234.11
177	89/06/14	10:17:35.2	12.875N	143.351E	126	5.5	84.51	282.86
178	89/06/16	23:42:35.1	31.807N	137.982E	360	5.9	74.27	299.75
179	89/06/19	16:00:47.9	22.113S	67.559W	189	5.5	83.96	131.49
180	89/06/21	23:51:01.9	21.785S	176.493W	182	5.6	84.76	230.28
181	89/08/08	23:44:04.4	22.723S	68.478W	102	5.3	84.00	132.54
182	89/08/21	18:25:41.0	4.104S	154.459E	494	5.8	89.25	263.23
183	89/10/23	13:08:25.6	25.645S	179.809E	441	5.7	89.85	230.83
184	89/10/30	23:46:30.6	21.104S	178.684W	582	5.6	85.37	232.34
185	89/11/01	06:40:30.3	20.995S	67.954W	140	5.9	82.83	131.18
186	89/11/16	08:39:42.7	17.760S	178.990W	538	5.7	82.84	234.53
187	89/11/29	05:48:59.8	25.374S	179.629E	487	5.7	89.73	231.12
188	89/12/23	11:24:02.6	17.401N	145.788E	162	5.9	79.63	284.27
189	90/01/02	20:21:32.6	13.408N	144.439E	136	5.7	83.40	282.45
190	90/01/18	20:57:49.2	20.760S	178.487W	586	5.7	84.99	232.39
191	90/02/25	22:51:09.1	18.042S	69.135W	141	5.5	79.76	130.49
192	90/03/13	19:40:33.6	3.429S	76.913W	112	5.7	63.42	129.05
193	90/03/21	16:46:05.4	31.092S	179.093W	145	6.2	93.69	226.87
194	90/03/30	00:42:06.9	20.231N	122.038E	124	5.5	92.34	303.10
195	90/04/11	20:51:12.1	35.474N	135.451E	362	5.6	73.12	303.98
196	90/04/14	08:00:13.8	27.296N	139.924E	458	5.6	76.32	295.26
197	90/05/11	13:10:20.2	41.820N	130.858E	579	5.7	71.03	311.32

(continued)

Event #	Date (y/m/d)	UTC (h:m:s.dsec)	Lat (deg.)	Long (deg.)	Z (km)	m_b	Dist. (deg.)	BAZ (deg.)
198	90/05/17	11:03:24.7	18.080S	69.626W	106	5.6	79.54	130.91
199	90/05/17	15:59:56.5	25.398S	178.101E	614	5.8	90.57	232.22
200	90/05/20	07:32:37.2	18.102S	175.130W	232	5.9	81.01	231.29
201	90/06/08	15:05:09.5	18.874S	178.789W	499	5.6	83.63	233.72
202	90/06/23	21:38:18.7	21.568S	176.483W	181	6.4	84.57	230.39
203	90/06/24	08:35:24.9	21.610S	176.502W	193	5.6	84.62	230.38
204	90/06/26	12:08:29.3	22.015S	179.473W	587	6.0	86.54	232.41
205	90/07/04	02:24:41.9	25.372N	124.473E	133	5.6	86.92	304.49
206	90/07/22	09:26:14.6	23.622S	179.893W	531	5.9	88.06	231.79
207	90/07/27	12:37:59.5	15.355S	167.464E	126	6.4	89.01	246.24
208	90/08/05	01:34:55.8	29.551N	137.630E	496	6.0	76.10	298.36
209	90/08/12	21:25:21.9	19.435S	169.132E	140	6.3	91.08	242.40
210	90/08/20	00:03:52.7	46.189N	142.289E	309	5.9	62.04	308.64
211	90/09/04	23:15:11.3	31.262S	69.063W	112	5.5	90.87	137.60
212	90/09/07	16:09:19.6	24.260S	66.957W	161	5.5	86.05	132.22
213	90/10/10	01:00:05.5	19.503S	66.618W	266	5.8	82.30	129.30
214	90/10/10	05:54:53.5	23.497S	179.029E	549	6.0	88.54	232.66
215	90/10/21	15:10:43.7	3.989S	77.274W	116	5.7	63.70	129.72
216	90/12/07	08:25:03.0	16.993S	177.268W	414	5.6	81.26	233.62
217	91/02/10	14:15:19.8	14.005N	144.743E	156	5.5	82.76	282.64
218	91/02/28	13:30:13.5	20.118S	175.830W	220	5.6	83.04	230.70
219	91/03/01	17:30:26.0	10.939N	84.637W	197	6.1	47.25	127.55
220	91/04/09	06:02:24.5	9.788S	74.702W	124	5.9	69.94	130.66
221	91/04/18	09:41:20.1	22.924S	179.342W	471	5.7	87.20	231.79
222	91/05/03	02:14:14.4	28.080N	139.585E	433	6.0	75.97	296.04

(continued)

Event #	Date (y/m/d)	UTC (h:m:s.dsec)	Lat (deg.)	Long (deg.)	Z (km)	m_b	Dist. (deg.)	BAZ (deg.)
223	91/05/06	22:50:45.3	20.871S	177.868W	497	5.5	84.74	231.85
224	91/05/08	19:53:21.6	13.875S	74.458W	107	5.6	73.53	132.68
225	91/05/24	20:50:55.8	16.506S	70.701W	128	6.3	77.67	130.93
226	91/06/09	07:45:02.1	20.252S	176.218W	266	6.1	83.35	230.93
227	91/06/11	14:32:47.9	18.209S	178.409W	628	5.5	82.88	233.81
228	91/06/12	20:11:35.0	42.789N	143.329E	109	5.7	63.66	305.18
229	91/07/02	06:08:09.2	23.233S	179.126W	429	5.7	87.34	231.44
230	91/07/05	10:58:28.5	47.892N	145.796E	468	5.6	59.10	308.46
231	91/07/09	05:54:07.1	20.599S	68.803W	101	5.3	82.07	131.64
232	91/09/30	00:21:46.4	20.878S	178.591W	566	6.3	85.14	232.40
233	91/09/30	00:42:25.3	20.941S	178.713W	591	5.6	85.26	232.46
234	91/10/06	16:48:21.1	7.358S	74.827W	143	5.4	67.83	129.40
235	91/10/08	03:31:15.6	45.587N	149.049E	146	6.0	58.70	304.73
236	91/10/26	02:27:31.5	18.506N	145.668E	192	5.5	78.92	285.13
237	91/11/07	05:59:35.5	26.309S	177.877W	200	5.6	89.18	228.75
238	91/12/03	10:33:39.9	26.483S	178.715E	561	6.0	91.11	231.13
239	91/12/15	18:56:05.6	17.521S	70.422W	104	5.6	78.66	131.26
240	91/12/17	06:38:17.3	47.393N	151.499E	157	5.8	56.27	305.30
241	92/01/13	09:37:43.7	20.930S	178.717W	575	5.7	85.25	232.47
242	92/01/20	13:37:03.0	27.983N	139.405E	499	5.8	76.15	296.09
243	92/01/22	01:06:55.5	38.470N	140.308E	116	5.6	68.25	303.34
244	92/02/01	19:04:04.5	35.106N	139.644E	100	5.6	70.96	301.15
245	92/02/09	22:01:58.4	48.014N	152.968E	123	5.6	55.10	305.25
246	92/03/03	01:18:31.2	14.384S	167.179E	148	5.9	88.46	247.08
247	92/03/27	20:28:14.7	47.863N	147.128E	454	5.5	58.40	307.80

(continued)

Event #	Date (y/m/d)	UTC (h:m:s.dsec)	Lat (deg.)	Long (deg.)	Z (km)	m_b	Dist. (deg.)	BAZ (deg.)
248	92/04/03	06:07:38.8	28.929S	69.612W	110	5.5	88.65	136.75
249	92/04/04	01:11:12.3	17.949S	178.365W	574	5.6	82.64	233.93
250	92/04/16	18:33:05.3	20.004S	68.479W	122	5.6	81.74	131.05
251	92/05/16	14:58:38.9	19.119S	169.079E	165	5.6	90.87	242.64
252	92/06/16	05:51:03.7	45.704N	142.263E	317	5.7	62.36	308.23
253	92/07/11	10:44:19.7	22.483S	178.413W	377	6.2	86.35	231.34
254	92/07/18	21:36:24.4	30.770N	137.306E	475	5.5	75.42	299.44
255	92/08/04	06:58:32.5	21.738S	177.214W	253	5.7	85.10	230.86
256	92/08/07	11:11:41.6	35.728N	135.152E	358	5.6	73.11	304.35
257	92/08/15	19:02:09.1	5.111N	75.607W	119	5.7	57.09	122.36
258	92/08/24	06:59:39.9	41.977N	140.660E	121	6.2	65.68	305.94
259	92/08/29	19:19:05.5	33.190N	137.975E	289	6.0	73.29	300.76
260	92/08/30	20:09:05.7	17.918S	178.710W	565	5.8	82.81	234.22
261	92/09/15	21:03:59.9	14.053S	167.269E	184	6.3	88.15	247.22
262	92/10/11	19:24:26.2	19.247S	168.948E	129	6.4	91.05	242.65
263	92/10/11	23:20:34.7	50.458N	153.167E	285	5.6	53.67	307.69
264	92/11/01	09:36:42.5	28.907S	69.544W	110	5.6	88.66	136.69
265	92/11/12	22:28:57.5	22.401S	178.104W	360	5.9	86.11	231.15
266	93/01/18	01:18:06.3	18.414N	145.734E	151	5.6	78.94	285.02
267	93/01/19	14:39:26.1	38.649N	133.465E	448	6.0	71.94	307.49
268	93/02/09	14:25:38.9	45.709N	141.938E	307	5.6	62.54	308.40
269	93/02/24	22:21:37.8	24.931S	68.386W	119	5.8	85.89	133.68
270	93/03/10	21:56:27.8	48.383N	152.987E	141	5.5	54.89	305.62
271	93/03/21	05:04:59.1	18.042S	178.528W	589	6.1	82.81	234.00
272	93/04/16	14:08:38.9	17.778S	178.864W	565	6.0	82.78	234.42

(continued)

Event #	Date (y/m/d)	UTC (h:m:s.dsec)	Lat (deg.)	Long (deg.)	Z (km)	m_b	Dist. (deg.)	BAZ (deg.)
273	93/04/18	09:16:23.2	11.652S	76.530W	106	6.0	70.60	133.31
274	93/04/20	16:26:19.5	20.883S	178.699W	592	5.6	85.20	232.48
275	93/04/24	09:54:21.0	17.871S	179.849E	599	5.5	83.58	235.36
276	93/05/02	15:26:02.5	21.151S	175.883W	120	5.7	83.92	230.16
277	93/05/06	13:03:18.1	8.472S	71.485W	573	5.8	70.56	127.07
278	93/05/18	10:19:33.7	19.914N	122.450E	169	6.4	92.35	302.60
279	93/05/24	23:51:28.2	22.671S	66.543W	221	6.6	84.95	131.02
280	93/05/27	08:51:59.5	29.359S	178.271W	119	5.9	91.87	227.29
281	93/06/08	23:17:41.4	31.560S	69.234W	113	6.5	91.04	137.88
282	93/07/09	15:37:53.6	19.782S	177.486W	398	6.0	83.65	232.19
283	93/07/22	12:15:36.1	21.760N	144.261E	127	5.6	77.52	288.40
284	93/07/24	20:24:50.1	13.060S	167.056E	194	5.8	87.53	248.02
285	93/08/07	00:00:37.0	26.585N	125.612E	155	6.0	85.34	304.45
286	93/08/07	17:53:24.2	23.866S	179.846E	523	6.0	88.40	231.84
287	93/08/21	09:42:35.9	21.278S	178.023W	427	5.7	85.16	231.74
288	93/09/11	06:14:27.7	4.689S	76.318W	121	5.6	64.80	129.23
289	93/10/11	13:07:29.5	17.845S	178.726W	555	5.8	82.76	234.27
290	93/10/11	15:54:21.2	32.020N	137.832E	351	6.4	74.21	300.00
291	93/10/12	19:51:25.3	4.196N	76.638W	103	5.5	57.25	123.99
292	93/10/30	17:59:02.7	31.704S	68.232W	107	5.9	91.62	137.24
293	93/11/27	06:11:22.6	38.625N	141.164E	104	5.9	67.66	302.97
294	93/12/10	06:31:54.1	2.210S	179.575W	605	5.6	86.73	232.39
†295	94/03/09	23:28:06.7	18.039S	178.413W	563	6.6	82.74	233.92
†296	94/03/31	22:40:52.1	22.057S	179.533W	580	6.1	86.60	232.43

† denotes events added after original data selection process.

Vita

Shawn Robert Dewberry

Birth Date: May 17, 1962 **Birthplace:** Los Angeles, California

Education: Calabasas High School, Calabasas, California, Diploma, 1980
Whitworth College, Spokane, Washington, B.S. Physics, 1987
University of Washington, Ph. D. Geophysics, 1996